CARDIFF UNIVERSITY
PRIFYSGOL CAERDYDD

DECLARATION

This work has not previously been accepted in substance for any degree and is not concurrently submitted in candidature for any degree.

Signed ..... (candidate) Date 31/1/11

STATEMENT 1

This thesis is being submitted in partial fulfillment of the requirements for the degree of PhD (insert MCh, MD, MPhil, PhD etc, as appropriate)

Signed ..... (candidate) Date 31/1/11

STATEMENT 2

This thesis is the result of my own independent work/investigation, except where otherwise stated. Other sources are acknowledged by explicit references.

Signed ..... (candidate) Date 31/1/11

STATEMENT 3

I hereby give consent for my thesis, if accepted, to be available for photocopying and for inter-library loan, and for the title and summary to be made available to outside organisations.

Signed ..... (candidate) Date 31/1/11

The neuro-ophthamological syndrome 3-methylglutaconic aciduria – a molecular and functional study of the B6; C3-Opa3^{L122P} mouse model

A thesis submitted to Cardiff University for the degree of Doctor of Philosophy

Jennifer Rhian Davies

Supervisors: Dr Marcela Votruba, Prof Andrew Quantock

Visual Neuroscience & Molecular Biology Group
School of Optometry and Vision Science
Cardiff University
2010

ProQuest LLC
789 East Eisenhower Parkway
P.O. Box 1346
Ann Arbor, MI 48106-1346

It is the man of science, eager to have his every opinion regenerated, his every idea rationalized, by drinking at the fountain of fact, and devoting all the energies of his life to the cult of truth, not as he understands it, but as he does not yet understand it, that ought properly to be called a philosopher.

~Charles Peirce

Acknowledgements

I would like to thank the many people who have been instrumental in the completion of this work. I am especially grateful to Dr. Marcela Votruba for her endless encouragement, expertise, and dedication to the project. I would like to thank Dr Andrew Quantock and my advisor Dr Jez Guggenheim for their support and guidance. I thank Professor Paul Sharpe for his continued help and collaboration with craniofacial work, Dr Ron Douglas for the mouse pupillometry testing and Dr Timothy Wells for his collaboration on the metabolic chapter. I would also like to thank everyone in my group for their help. I gratefully acknowledge funding from the MRC and the BBSRC.

Finally, a special thanks to my family, my parents, Robert and Janet, my brother, Andrew, for being ever supportive and always believing in me. None of this would have been possible without them.

Summary

Introduction: *OPA3* is the causative gene of the autosomal recessive, multi-systemic neuro-ophthalmological syndrome, 3-methylglutaconic aciduria Type III (MGA-III) and Autosomal Dominant Optic Atrophy and Cataract (ADOAC). Early onset bilateral optic atrophy is a common characteristic of both disorders where retinal ganglion cells (RGCs) are lost.

Purpose: To investigate the pathophysiology of the disease and function of the OPA3 protein we generated a novel ENU-induced mutant mouse carrying the missense mutation p.L122P in exon 2 of *Opa3* which is predicted to alter tertiary protein structure.

Methods: Visual function was assessed using optokinetic nystagmus and pupillary light reflex. Histology explored retinal degeneration and metabolic dysfunction. Rotarod, wirehang and open field analysed neurological, neuromuscular and behavioural aspects of the disease. Genomic structure of *Opa3* was re-examined using RT-PCR and bio-informatic programs characterized possible upstream transcription factor binding sites (TFBS).

Results: *Opa3*$^{-/-}$ mice displayed a multi-systemic disease, including decreased life span and weight, extra-pyramidal dysfunction, neuro-muscular defect, craniofacial defects, reduction in intra-abdominal white adipose tissue, elevated marrow adiposity and severe hepatic steatosis. *Opa3*$^{-/-}$ are functionally blind but pupillary function was essentially intact. Histology showed loss of RGCs and other cell types through postnatal development onwards. RT-PCR identified a third exon and analysis of 53 TFBS identified suggests a role for *Opa3* in retinal and craniofacial development, cellular stress response/apoptosis and adipogenesis.

Conclusions: *Opa3*$^{-/-}$ display many aspects of human MGA-III syndrome and phenotypes not observed such as craniofacial defects and a profound disturbance in lipid metabolism. *Opa3* is thought to be involved in the mevalonate shunt and leucine degradation metabolic pathways. Defects in these pathways can cause a build up of 3-methylglutaconic acid and 3-methylglyaric acid in the inner mitochondrial membrane which may have a profound affect on mitochondrial metabolism particularly in high energy demand tissues such as retina, heart and neurons.

Table of Content

	Page
Declaration	1
Acknowledgements	4
Summary	5
Content	6
List of Figures	13
List of Tables	16
Abbreviations	17

CHAPTER I: Introduction

1.1 General Introduction	21
1.2 *OPA3* is associated with syndromic optic neuropathies	22
1.2.1 3-Methylglutaconic aciduria syndromes	22
1.2.2 3-Methylglutaconic aciduria Type III or Costeff syndrome	25
1.2.3 Symptoms and genetics of the other syndromes of 3-Methylglutaconic aciduria	25
1.2.3.1 3-Methylglutaconic aciduria Type I	25
1.2.3.2 3-Methylglutaconic aciduria Type II or Barth syndrome	26
1.2.3.3 3-Methylglutaconic aciduria Type IV	27
1.2.3.4 3-Methylglutaconic aciduria Type V	27
1.2.4 *OPA3*-Autosomal Dominant Optic Atrophy and Cataract	28
1.2.5 Cataracts as part of ADOAC	28
1.2.5.1 What is a cataract?	28
1.2.5.2 Causes of cataract	28
1.2.5.3 Genetics of cataract	29
1.3 Pathophysiology of the non-syndromic optic neuropathies	29
1.3.1 *OPA1*- Autosomal dominant optic atrophy and neurological defects	29
1.3.2 *OPA2*- X-linked optic atrophy	30
1.3.3 Leber's hereditary optic atrophy	31
1.4 The Mitochondrion: a unifying theme	32
1.4.1 Structure	32
1.7.1.1Fusion and Fission	33
1.4.2 Function	34
1.4.2.1 ATP production- Electron transport chain and oxidative phosphorylation	35
1.4.2.2 Mitochondrial mediated apoptosis	38
1.4.2.3 Heat production	39
1.5 The Vertebrate Retina	41
1.5.1 The Retinal Ganglion Cell Layer	42
1.5.2 The Optic Nerve	43
1.5.3 RGCs vulnerability to physiological and biochemical insult	44
1.5.3.1 Energy deficits	44
1.5.3.2 Lamina cribrosa	45

1.5.3.3 Spatial distribution of mitochondria along the optic nerve 46
1.5.3.4 Light exposure 48

1.6 Mechanisms of retinal ganglion cell degeneration 49
1.6.1 Axoplasmic transport block 49
1.6.2 Glutamate induced excitotoxicity 50
1.6.3 Free radical generation 51
1.6.4 Nitric oxide neurotoxicity 51
1.6.5 Apoptosis 52

1.7. The Human homologue *OPA3* 54
1.7.1 Function of human *OPA3* 56
1.7.2 Mutations of the human *OPA3* gene 58

1.8 Hypothesis 60

1.9 Mouse model of *Opa3* 60

CHAPTER II: General Materials and Methods

2.1 DNA preparation and purification 62
2.1.1 Sample preparation 62
2.1.2 Purification of genomic DNA from lysate using microcentrifuge 62
2.2 RNA isolation 62
2.2.1 RNA purification and quantification 63
2.3 cDNA synthesis (reverse transcription) 63
2.4 Agarose gel electrophoresis 64
2.5 Tissue fixation for wax embedding 65
2.5.1 Fixation of eyes for wax embedding 65
2.5.2 Fixation of other tissues for wax embedding 66
2.6 Frozen tissues for cryostat sectioning 66
2.7 Histology 66
2.7.1 Haematoxylin & eosin 66
2.7.2 Oil red-O stain 67
2.7.3 Toluene Blue stain 68
2.8 Perfusion fixation 68
2.9 Embryo collection 69

CHAPTER III: Splicing, expression and putative functional analysis of optic atrophy gene *Opa3*

3.1 Introduction 71
3.1.1 Use of bio-informatic analysis 72
3.1.2 Multispecies DNA sequence comparison for phylogenic footprinting-What species to select? 73
3.1.3 Identification of TFBS for insight into gene function 74
3.1.4 Predictive programmes for identification of TFBS 75
3.1.4.1 Mulan/MultiTF 75

3.1.4.2 Genomatix- MatInspector 75
3.1.4.3 TFSEARCH 76
3.1.4.4 PReMod 76
3.1.5 Use of TRANSFAC and PWM 76

3.2 Materials and Methods 78
3.2.1 Conserved region identification of *Opa3* using comparative genomics 78
3.2.2 Detection of mouse *Opa3* exon 3 expression and novel splice variant by RT-PCR 78
3.2.3 Sequencing of mouse exons and transcripts 79
3.2.4 Sequencing of human *OPA3* 80
3.2.4.1 Individuals and Pedigrees 80
3.2.4.2 Sequencing of OPA3 80
3.2.4.3 Mutation analysis 81
3.2.4.4 Statistics 81
3.2.5 Bio-informatics analysis of the 5' region 82
3.2.5.1Mulan/MultiTF for evolutionary conserved TFBS search upstream of Opa3 82
3.2.5.2 TFBS searches with other programs 83

3.3 Results 84
3.3.1 *Opa3* third exon and splice variant 84
3.3.2 Revised genomic structure of murine *Opa3* 86
3.3.3 Murine Opa3 protein 88
3.3.4 Sequencing of human *OPA3* and mutation analysis 88
3.3.5 The evolutionary conservation of regions upstream of *Opa3* exon 1 92
3.3.6 Analysis of the *Opa3* gene proximal sequence using phylogenetic footprinting and TRANFAC PWM searches 93

3.4 Discussion 95
3.4.1 Alternate splicing of *Opa3* 95
3.4.2 Determination of *OPA3* genetic variants in patients with optic atrophy 95
3.4.3 Mutations of *OPA3* 96
3.4.4 Using TFBS as an insight into *Opa3* function 97
3.4.4.1 Retinal development and neuron development/survival 99
3.4.4.2 Cellular stress response/Apoptosis 99
3.4.4.3 Bone/Craniofacial Development 100
3.4.4.4 Adipogenesis 100

3.5 Conclusions 102

CHAPTER IV: Genotype/phenotype correlations and development of the mutant B6; C3- *Opa3*^{L122P} mouse line

4.1 Introduction 104
4.1.1 Generation of *Opa3* mutant mice: the L122P mutation 105
4.1.2 Strain background disease characteristics 105
4.1.2.1 C3H/HeJ Strain 106

4.1.2.2 C57BL/6J Strain 106

4.2 Materials and Methods 108
4.2.1 Mouse strains and husbandry 108
4.2.2 Genotyping offspring 108
4.2.2.1 Opa3 genotyping 108
4.2.2.2 Rd1 genotyping 109
4.2.2.3 Nnt genotyping 109
4.2.3 Histology of mouse tissues on C57BL/6JCrl and C3H background strains 110
4.2.4 Embryology 110
4.2.5 Craniofacial Analysis 110
4.2.5.1 Skeletal preparations 111
4.2.5.2 MicroCT analysis 111
4.2.5.3 Bone and cartilage analysis 111
4.2.6 Statistics 111

4.3 Results 112
4.3.1 Phenotypic manifestations of *Opa3* mutation in G1 mice 112
4.3.2 Phenotypic manifestations of *Opa3* mutation in G3/4 mice 113
4.3.2.1 Opa3 mouse viability 115
4.3.2.2 General Tissue Histology 118
4.3.2.3Embryology 121
4.3.3 Phenotypic manifestations of *Opa3* mutation in G3/4 mice on a C3H background 122
4.3.3.1 General Tissue Histoloy 123
4.3.4 Craniofacial Malformations 125
4.3.4.1 MicroCT scan analysis of G1 adult mice 125
4.3.4.2 Summary of the mutant phenotype on CT 126
4.3.4.3 Embryonic bone and cartilage analysis in G4 mice 128
4.3.4.4 Bone (Alizarin red) and Cartilage (Alcian blue) analysis at 18.5 dpc 129

4.4 Discussion 132
4.4.1 Craniofacial malformations 134

4.5 Conclusions 135

CHAPTER V: The *Opa3*^{L122P} mouse displays neurological and behavioural deficits

5.1 Introduction 137
5.1.1 Testing motor behaviour and co-ordination 138
5.1.2 Exploratory and emotional behaviour 139

5.2 Materials and Methods 141
5.2.1 Body weight 141
5.2.2 SHIRPA 141
5.2.2.1 Above Arena 143
5.2.3 Walking Pattern 145
5.2.4 Rotarod 145

5.2.5 Wire Hang 146
5.2.6 Open Field activity 147
5.2.7 Magnetic resonance imaging (MRI) 148
5.2.7.1 Volumetric measurements 148
5.2.8 Dual COX-SDH muscle histochemistry 148
5.2.9 Statistics 149

5.3 Results 150
5.3.1 Body Weight 150
5.3.2 Primary SHIRPA screening on Generation 3 and 4 151
5.3.2.1 Primary SHIRPA screening on aged heterozygous 'founders' 153
5.3.3Walking Pattern 154
5.3.4 Rotarod 155
5.3.5 Wire Hang 157
5.3.6 Open field Testing 158
5.3.6.1 Latency to reach the periphery 158
5.3.6.2 Total Activity 158
5.3.6.3 Exploration and Rearing 160
5.3.7 Muscle COX-SDH 162
5.3.8 Cerebellar MRI imaging 162

5.4 Discussion 165

5.5 Conclusions 170

Chapter VI: The *Opa3*^{L122P} mouse model of MGA-III displays a profound disturbance in lipid metabolism

6.1 Introduction 172
6.1.1 Adipose tissue in mammals 172
6.1.2 Energy homeostasis 173
6.1.3 Thermogenesis 176

6.2 Materials and Methods 178
6.2.1 Mice used 178
6.2.2 Tissue collection 178
6.2.3 Blood plasma biochemistry 178
6.2.3.1 Measurement of 3-methylglutaconic acid 178
6.2.3.2 Liver triglycerides 179
6.2.4 Bone histology 179
6.2.4.1 Analysis of bone marrow adiposity using ImageJ 179
6.2.4.2 Using Image J 179
6.2.5 Adiposity profiling of Liver 180
6.2.5.1 Analysis of liver steatosis using QWin 180
6.2.6 Thermal imaging 180
6.2.7 Statistics 181

6.3 Results 182
6.3.1 General Physiology and Plasma Biochemistry of *Opa3* mutant mice 182
6.3.2 *Opa3*$^{-/-}$ display profound leanness 182
6.3.3 Bone Marrow adiposity 185

6.3.4 Hepatic steatosis 185
6.3.5 Thermal imaging 188

6.4 Discussion 190
6.4.1 Hepatic steatosis 192
6.4.2 Bone Marrow Adiposity 194
6.4.3 Thermoregulation 194

6.5 Conclusions 196

CHAPTER VII: Pupillary and Visual function are dissociated in the *Opa3* ^{L122P} mouse model

7.1 Introduction 198
7.1.1 Image and non-image forming pathways 199
7.1.2 Testing the mouse visual system 199
7.1.2.1 Optokinetic Nystagmus 200
7.1.2.2 Pupillary light reflex 200

7.2 Materials and Methods 202
7.2.1 Optokinetic Nystagmus 202
7.2.2 Pupillometry 203
7.2.3 Histology of the retina 204
7.2.3.1 Quantification of thicknesses of the retina and GCL counts 204
7.2.4 Statistics 205

7.3 Results 206
7.3.1 Loss of visual acuity in the *Opa3*$^{-/-}$ mice 206
7.3.1.1 Optokinetic drum testing on G1 cohort 206
7.3.1.2 Optokinetic drum testing on aged 'founders' 207
7.3.1.3 Optokinetic drum testing on G3/4 cohort 208
7.3.2 Retention of pupillary light reflex 211
7.3.2.1 Optokinetic drum testing of the mice used in pupillometry 212
7.3.3 GCL counts and retinal layer thicknesses for mice used in pupillometry testing 213

7.4 Discussion 215
7.4.1 OKN 215
7.4.2 Pupillometry 217
7.4.2.1 Why should ipRGCs be less susceptible to mitochondrial impairment than those ganglion cells going to the LGN? 218

7.5 Conclusions 220

CHAPTER VIII: Retinal degeneration in *Opa3*^{L122P} mouse is associated with increased postnatal apoptosis

8.1 Introduction 222
8.1.1 Development and degeneration of the mouse retina 223

8.2 Materials and Methods 226
8.2.1 Histology of the retina 226
8.2.2 TUNEL Technique 226
8.2.2.1 *Preparation and permeabilization of wax embedded retinas* 226
8.2.2.2 TUNEL Assay 227
8.2.2.3 Positive control 227
8.2.3 Statistics 227

8.3 Results 228
8.3.1 Postnatal and adult changes in retinal morphology 228
8.3.2 Retinal degeneration in *Opa3*$^{-/-}$ mouse associated with increased apoptosis in GCL and INL 230

8.4 Discussion 233

8.5 Conclusions 237

Chapter IX: Final Discussion, future work and conclusions

9. Final Discussion 239
9.1 Summary of results- Overview of mouse phenotype 239
9.1.1 Opa3^{L122P} *as a model of MGA-III* 240
9.2 Possible mechanisms and causes of MGA-III 241
9.2.1 Possible origin and effect of 3-methylglutaconic aciduria 241
9.2.2 OPA3 and mitochondria 242

9.3 Conclusions 247

9.4 Future work 248

References 249

Appendix I 269
1) Chemicals and enzymes
2) Kits
3) Solutions buffers and media
4) Software

Appendix II 273

Appendix III 278

List of Figures

Chapter I
Figure 1.1. The Mitochondrion structure.
Figure 1.2. Schematic representation of mitochondrial metabolism.
Figure 1.3. The electron transport chain in the mitochondrion is the site of oxidative phosphorylation in eukaryotes.
Figure 1.4. Mitochondrial mediated apoptotic sigmalling.
Figure 1.5. UCP-1 and mitochondrial proton leak.
Figure 1.6. A simplistic wiring diagram of the retina emphasizes only the sensory photoreceptors and the ganglion cells with a few interneurons connecting the two cell types.
Figure 1.7. Scheme showing central connections of the optic nerve and optic tracts.
Figure 1.8. The terminal portion of the optic nerve and its entrance into the eyeball.
Figure 1.9. The retinal ganglion cell system.
Figure 1.10. Schematic flow diagram showing the mechanisms that would result into the non-maintenance of the sharp mitochondrial gradient at the optic nerve head.
Figure 1.11. Schematic diagram showing the major apoptotic signalling pathways.
Figure 1.12. Northern blot analysis by 619 bp probe to human *OPA3* cDNA.

Chapter III
Figure 3.1. Page from murine Ensembl (version 50) showing *Opa3* and EST 3727961.
Figure 3.2. A phylogenetic tree generated by Mulan depicting the evolutionary relationship of the seven species used in analyses of *Opa3* based on the similarities of their genomes.
Figure 3.3. Mulan sequence conservation profile for the human and murine *Opa3* loci.
Figure 3.4. RT-PCR showing tissue expression of alternately splice variants of *Opa3*.
Figure 3.5. Comparison of murine Opa3a (exon1-2) and Opa3b (exon1-3) transcripts.
Figure 3.6. Amino acid sequence alignment of murine Opa3a (exon1-2) and Opa3b (exon1-3).
Figure 3.7. Electropherograms showing the two genotype patterns for the *OPA3* c.227 C>T p.A76V SNP in (A) the control patients (C/C) and (B) the affected patient (C/T).
Figure 3.8. Standard stacked-pairwise visualization (smooth graph) of Mulan alignments of murine *Opa3* loci with 6 orthologous species.

Chapter IV
Figure 4.1. Peptide sequence of Opa3 showing the L122P mutation in exon 2.
Figure 4.2. Agarose gel of PCR products for genotyping the *Opa3* colony.
Figure 4.3. Mouse genotyping for selection of *Rd1* $^{+/+}$ and *Rd1* $^{+/-}$ mice by multiplex PCR for *Rd1* alleles.
Figure 4.4. PCR genotyping for selection of *Nnt*$^{+/+}$ mice.
Figure 4.5. Visible traits associated with G1 *Opa3* homozygous mice.
Figure 4.6. Visible traits associated with the G3/4 *Opa3* homozygous mice.
Figure 4.7. Kaplan Meier survival curve showing decreased survival rate of G3 homozygotes compared to heterozygote and wildtype mice from birth to 50 days of age.
Figure 4.8. Kaplan Meier survival curve showing decreasing survival rates of mice at each generation from birth to 21 days of age as they progressively become more congenic to C57BL/6JCrl.
Figure 4.9A. Heart histopathology of 30 day old G3/4 C57BL/6JCrl homozygote mice compared to wildtype controls.
Figure 4.9B. Histological examination of G3/4 C57BL/6JCrl mouse tissues.
Figure 4.10. Embryonic viability of the *Opa3* mice at 13.5dpc, 18.5dpc and P0.
Figure 4.11. Visible traits associated with G3/4 C3H mice.

Figure 4.12. Histological examination of G3/4 C3H mouse tissues.
Figure 4.13. CTscan of the cranium of wildtype, heterozygote and homozygote littermates.
Figure 4.14. CTscan of three other homozygotes showing the craniofacial phenotype.
Figure 4.15. Bone (Alizarin red) and Cartilage (Alcian blue) analysis of G4 embryos at 18.5dpc.
Figure 4.16. Bone and cartilage analysis of 18.5 dpc embryos fixed in NBF.

Chapter V

Figure 5.1. SHIRPA is a semi-quantitative protocol designed to characterize the phenotype of mice in three stages.
Figure 5.2. Perspex viewing jar for 5 mins of behavioural observation.
Figure 5.3. Arena for observations of motor behaviour.
Figure 5.4. Supine Restraint.
Figure 5.5. Rotarod apparatus.
Figure 5.6. Wire Hang apparatus.
Figure 5.7. Growth curves of wildtype, heterozygote and homozygote G3/4 *Opa3* mice from birth to 50 days of age.
Figure 5.8. Box plot of final body weight at 50 days of age.
Figure 5.9. Footprint pattern analysis in (A) homozygote and (B) wildtype mice.
Figure 5.10. Accelerating rotarod performance.
Figure 5.11. Box plot of final rotarod performance in 87 day old mice.
Figure 5.12. Hanging wire test.
Figure 5.13. Latency to reach perimeter squares of $Opa3^{-/-}$ and $Opa3^{+/-}$ and $Opa3^{+/+}$ mice in open field testing.
Figure 5.14. Graph showing total locomotor activity for each 30 sec period during the 5 min testing.
Figure 5.15. Total locomotor activity of $Opa3^{-/-}$ and $Opa3^{+/-}$ and $Opa3^{+/+}$ mice in open field testing.
Figure 5.16. The number of rears during 5 min of $Opa3^{-/-}$ and $Opa3^{+/-}$ and $Opa3^{+/+}$ mice in open field testing.
Figure 5.17. Percentage of time spent in various areas of the arena of $Opa3^{-/-}$ and $Opa3^{+/-}$ and $Opa3^{+/+}$ mice in open field testing.
Figure 5.18. Dual COX-SDH staining in (A) homozygote and (B) wildtype muscle sections.
Figure 5.19. Cerebellar volume is reduced in $Opa3^{-/-}$ mice.

Chapter VI

Figure 6.1. Adipose tissue, which is the main energy storage site, is responsive to both central and peripheral metabolic signals by regulating lipid storage and mobilization.
Figure 6.2. Model of lipid flux through the liver
Figure 6.3. Quantification of (A) epididymal, (E) retroperitoneal and (F) inguinal WAT depots from male 30 day old $Opa3^{-/-}$ and age-matched control mice.
Figure 6.4. Quantification of bone marrow adiposity in toluidine blue stained proximal tibiae from male 30 day old $Opa3^{-/-}$ and age-matched control mice.
Figure 6.5. The effect of the *Opa3* mutation on hepatic TAG production and storage.
Figure 6.6. The $Opa3^{-/-}$ mice display defects in thermoregulation.
Figure 6.7. Metabolic defects leading to the development of hepatic steatosis.

Chapter VII

Figure 7.1. Diagram of the pathways taken by melanopsin ganglion cells to the brain.
Figure 7.2. Images of mouse pupils showing full dilation of pupil in dark adapted eye and full constriction of pupil in bright light.

Figure 7.3. Optokinetic drum set up for visual acuity testing.
Figure 7.4. Graph showing the visual acuity of heterozygous 'founders' and their wildtype controls on the 1° and 2° grating at two years of age.
Figure 7.5. Graphs showing the visual acuity of *Opa3* wildtypes, heterozygotes and homozygotes on the (A) 1°, (B) 2° and (C) 4° grating from 18 days of age up to 31 days of age.
Figure 7.6. The average minimum pupil area expressed as a percentage of maximum dilation following illumination with various intensities of white light for mice homozygous for mutations of the *Opa3* gene.
Figure 7.7. Graph showing the visual acuity of wildtypes and homozygotes used in the pupillometry testing on the optokinetic drum.
Figure 7.8 $Opa3^{-/-}$ adult mice display panretinal degeneration.

Chapter VIII
Figure 8.1. Temporal and spatial heterogeneity of developing retinal progenitor cells.
Figure 8.2. Apoptosis throughout the development of the C57BL/6J mouse retina.
Figure 8.3. Morphological demonstrations of retinal degeneration in $Opa3^{-/-}$ mice.
Figure 8.4. Individual GCL counts of four adult homozygote mice.
Figure 8.5. TUNEL staining in the $Opa3^{-/-}$ and $Opa3^{+/+}$ P8 and adult retina.
Figure 8.6. Percentage of cells in GCL and INL of homozygote mice as a proportion of the wildtype.

Chapter IX
Figure 9.1. Metabolic pathway diagram showing branched-chain organic acid 3-MGC as an intermediate of leucine degradation and the mevalonate shunt pathway that links sterol synthesis with mitochondrial acetyl-CoA.
Figure 9.2. Schematic summary of the common themes linking mitochondrial optic neuropathies.

Appendix III
Figure 79. Total number of peripheral and central squares entered during 5 mins of $Opa3^{-/-}$ and $Opa3^{+/-}$ and $Opa3^{+/+}$ mice in open field testing.
Figure 80. Percentage of time spent in various areas of the arena (after the mice had reached the periphery) of $Opa3^{-/-}$ and $Opa3^{+/-}$ and $Opa3^{+/+}$ mice in open field testing.

List of Tables

Chapter I
Table 1.1. Genes associated with hereditary forms of optic atrophy.
Table 1.2. Overview of all 5 methylglutaconic aciduria syndromes.
Table 1.3. Both morphologic and biochemical characteristics are distinctive between apoptotic and necrotic cells.
Table 1.4. Mutations reported in the OPA3 gene.

Chapter II
Table 2.1. Genomic DNA elimination reaction components.
Table 2.2. Reverse transcription reaction components.

Chapter III
Table 3.1. Oligonucleotide primers used to amplify *Opa3* exons.
Table 3.2. Oligonucleotide primers used to amplify *Opa3* for exon and transcript sequencing.
Table 3.3. Oligonucleotide primers used to amplify *Opa3* exons for mutation analysis sequencing.
Table 3.4. Allelic frequencies of the OPA3 gene in patients with optic atrophy and health controls.
Table 3.5. Putative transcription factor binding sites identified upstream of *Opa3* using the databases Mulan, Matinspector, TFsearch and PReMod.
Table 3.6. List showing common functional themes in the TFBSs found upstream of *Opa3* and which TFBSs are known to play a role in these processes.

Chapter IV
Table 4.1. Obtained and predicted genotype viability of *Opa3* G1 heterozygote inter-crosses.
Table 4.2. Obtained and predicted genotype viability of *Opa3* G3 heterozygote inter-crosses.
Table 4.3. Obtained and predicted genotype viability of *Opa3* G3/4 C3H heterozygote inter-crosses.

Chapter V
Table 5.1. List of all tests performed in the SHIRPA protocol.

Chapter VI
Table 6.1. General physiology and plasma biochemistry in male $Opa3^{-/-}$ mice.

Chapter VII
Table 7.1. The visual acuity of G1 *Opa3* wildtype, heterozygote and homozygote mice on the 1°, 2°, 4° and 8° gratings at 2 months of age.

Chapter IX
Table 9.1. Classification by phenotype of disease progression in the *Opa3* homozygote mouse.
Table 9.2. Human MGA-III syndrome and the $Opa3^{L122P}$ mouse model: diagnosis and phenotypic comparisons.

Appendix III
Table 10.1 Quantification of retinal thickness in adult homozygote and wildtype mice used in pupillometry testing.
Table 10.2 Percentage thickness of retina in adult homozygote and wildtype mice used in pupillometry testing.

Abbreviations

aa- amino acid
AD- Autosomal dominant
ADOA- Autosomal dominant optic atrophy
ADOAC- Autosomal dominant optic atrophy and cataract
AIF- Apoptosis inducing factor
AR- Autosomal recessive
ATP- Adoesine triphosphate
BAT- Brown adipose tissue
bp- base pairs
cDNA- Complementary DNA
cms- centimetres
CNS- Central nervous system
COX -Cytochrome oxidase
CRM- Cis regulatory module
DFF- DNA fragmentation factor
DNA- Deoxyribonucleic acid
dNTP- Deoxyribonucleotide triphosphate
DOA- Dominant optic atrophy
dpc- Days post coitum
E- Embryonic day
ECR- Evolutionary conserved regions
EDTA- Ethylenediaminetetraacetic acid
EM- Electron microscope
ENU-*N*-ethyl-*N*-nitrosourea
EPW- Epiphyseal plate width
ES- Esterase
ES-ARA- Esterase
EST- Expressed sequence tag
FA- Fatty acids
FADH
g- Grams
G- Generation
GCL- Ganglion cell layer
gDNA- Genomic DNA
GFP- Green flourescent protein
H&E- Hematoxylin and eosin stain
HET- Heterozygote
HMG-CoA- 3-hydroxy-3-methyl-glutaryl-Coenzyme A
hrs- Hours
IAP- Inhibitor of apoptosis protein
i.d- Internal dimensions
IF- Image forming pathway
IMM- Inner mitochondrial membrane
INbL- Inner neuroblastic layer
INL- Inner nuclear layer
IPL- Inner plexiform layer
ipRGCs- Intrinsically photoreceptive retinal ganglion cells
kb- kilobase
kD- kilodalton

LGN- Lateral genticulate nucleus
LHON- Leber's hereditary optic neuropathy
LPL- Lipoprotein lipase
MGA - Methylglutaconic aciduria
MGA III- Methylglutaconic aciduria Type III
mins- Minutes
mm- Millimetres
MNDA- N-methyl D-aspartate
MRC- Medical research council
MRI- Magnetic resonance imaging
mRNA- Messenger RNA
mtDNA- Mitochondrial DNA
mtPTP- Mitochondrial permeability transition pore
MULAN- MUltiple sequence Local AligNment and conservation visualization tool
m/z- Mass to charge ratio
NADH- Nicotinamide adenine dinucleotide
NBF- Neutral buffered formalin
NBL- Neuroblastic layer
NCBI- National Center for Biotechnology Information
nDNA- nuclear DNA
NFL- Nerve fibre layer
NIF- Non-image forming pathway
Nnt- Nicotinamide nucleotide transhydrogenase
NO- Nitric oxide
OCT- Optimal Cutting Temperature compound
OKN- Optokinetic nystagmus
OMIM- Online Mendelian Inheritance in Man
OMM- Outer mitochondrial membrane
ONbL- Outer neuroblastic layer
ONL- Outer nuclear layer
OPL- Outer plexiform layer
ORF- Open reading frame
OXPHOS- Oxidative phosphorylation
P- Postnatal day
PBDs- Peroxisome biogenesis disorders
PBS- Phosphate buffered solution
PCR- Polymerase chain reaction
PFA- Paraformaldehyde
PLR- Pupil light reflex
PMB- Papillomacular bundle
PPAR- Peroxisome proliferator activated receptor
psi- Pounds per square inch
PWM- Position weight matrix
Rd1- Retinal degeneration 1
RGC- Retinal ganglion cells
RNA- Ribonucleic acid
ROS- Reactive oxygen species
RPE- Retinal pigment epithelium
rpm- Revolutions per minute
RT- Reverse transcription
SCN- Super chiasmic nucleus

secs- Seconds
S.E.M- Standard error of mean
SDH- Succinate dehydrogenase
SHIRPA- Smithkline, Harwell, Imperial, Royal London hospitial Phenotype Assesment
SNP- Single nucleotide polymorphisms
TAG- Triacylglycerol
TCA- Tricarboxylic acid cycle
TF- Transcription factor
TFBS- Transcription factor binding sites
TMS- Trimethylsilyl
TUNEL- Terminal deoxynucleotidyl transferase-mediated dUTP-biotin nick end labeling
UCP-1- Uncoupling protein 1
µg- micro gram
UK- United Kingdom
µl- micro litre
µm- micro metre or micron
UTR- Untranslated regions
UV- Ultra violet
V-Volts
VLDL –Very low density lipoprotein
W- Watts
WT- Wildtype
WAT- White adipose tissue
XLOA- X-linked optic atrophy
XR- X-linked recessive
ZS- Zellweger disorders

CHAPTER I

Introduction

1.1 General Introduction

Hereditary optic atrophies comprise a group of disorders in which the cause of optic nerve dysfunction appears to be hereditable based on familial expression or genetic analysis [Newman, 1999; Biousse and Newman, 2001] (Table 1.1.). They typically present as symmetric, bilateral, central visual loss caused by degeneration of retinal ganglion cells (RGCs) that form the optic nerve fibres and/or loss of the supporting microvascular tissue surrounding the optic nerve. Optic nerve damage is usually permanent and, in many diseases, progressive. Once optic atrophy is observed, substantial nerve injury has already occurred.

Leber's hereditary optic neuropathy (LHON) [Leber, 1871; Wallace *et al*, 1988] and dominant optic atrophy (DOA) [Kjer, 1959; Alexander *et al*, 2000] are the two most frequent hereditary optic neuropathies with monosymptomatic expression [Yu-Wai-Man *et al*, 2009]. Autosomal DOAs are the most common form (prevalence 1: 50,000) and three loci have been reported: *OPA1* (3q28–q29; OMIM 165500), *OPA4* (18q12.2–q12.3; OMIM 605293), and *OPA5* (22q12.1–q13.1; OMIM 610708). *OPA1* accounts for about 90% of DOAs and is due to mutations in the OPA1 protein (OMIM 605290). LHON (OMIM 535000) is a maternally inherited mitochondrial disorder.

In contradistinction, optic neuropathy can also be part of a more complex syndrome. The autosomal recessive optic atrophies are often multi systemic diseases involving the central nervous system (CNS) and other organs. Loci of syndromic recessive optic atrophy include: *OPA3* (3-methylglutaconic aciduria Type III (MGA-III) or Costeff syndrome; OMIM 606580), and *WFS1* (Wolfram syndrome; OMIM 606201).

There are also acquired types of optic atrophy which may be due to blood supply changes in the eye or optic nerve (anterior ischaemic optic neuropathy or posterior ischemic optic neuropathy), maybe secondary to inflammation or swelling within the optic nerve (optic neuritis), maybe a result of pressure against the optic nerve (such as from a tumour), or maybe related to metabolic diseases e.g., diabetes, trauma, glaucoma, or toxicity caused by alcohol, tobacco or other poisons.

Only the sequence of *OPA1* and *OPA3* are known. The locus position of *OPA2, OPA4, OPA5* and *OPA6* has been refined to a critical disease region but none of them have been identified as yet.

Disorder	Locus	Inheritance	Gene Location
Autosomal dominant optic atrophy	*OPA1* *OPA4* *OPA5*	AD	3q27-q29 18q12.2-q12.3 22q12.1-q13.1
Autosomal recessive optic atrophy	*ROA1 (OPA6)*	AR	8q21-q22
X-linked optic atrophy	*OPA2*	XR	Xp11.4-p11.21
Wolfram syndrome	-	AR	4p16.1 4q22-q24
Behr's syndrome	-	AR	?
MGA-III Autosomal dominant optic atrophy and cataract	*OPA3*	AR AD	19q13.2-q13.3
Leber's optic neuropathy	-	mtDNA	Mutations at bp 11778,3460,14484
Abbreviations: AD=Autosomal dominant, AR= Autosomal recessive, XR= X-linked recessive, mtDNA= mitochondrial DNA, DNA= Deoxyribonucleic acid, bp=base pair.			

Table 1.1. Genes associated with hereditary forms of optic atrophy.

1.2 *OPA3* is associated with syndromic optic neuropathies

OPA3 mutations have been associated with the recessive neuroopthamalogical syndrome MGA-III and autosomal dominant optic atrophy and cataract (ADOAC). A common characteristic of both disorders is early onset bilateral optic atrophy where RGCs are lost and visual acuity is impaired from an early age.

1.2.1 3-Methylglutaconic aciduria syndromes

3-methylglutaconic aciduria (MGA) is used to describe a group of heterogenous disorders that impair the body's ability to make energy in the mitochondria. This impairment is characterised by an abnormal organic acid profile of 3-methylglutaconic acid and 3-methylglutaric acid which can be detected in the urine. To date, five different types of MGA have been described (Table 1.2.). MGA seems to be most prevalent amongst the Jewish population of Iraq. However, a high concentration of Type V is found in the Saguenay region

of Canada. This tends to show that the disease is more frequent in insular areas where there is an increased chance that both parents are carriers, a higher birth rate and higher numbers of consanguineous marriages. As all types of MGA show recessive inheritance it is likely that consanguineous marriages where both parents are carriers increase the chances of having a sick child.

	Common Name	OMIM	Mutated Gene	Gene Location	Mode of Inheritance	Urinary Metabolites	Symptoms
MGA-I		*AUH* 600529, MGA-I 250950	*AUH*	Chr 9	Autosomal Recessive	Very high levels of 3-methylglutaconic and 3-hydroxyisovaleric acids.	Speech delay, delayed development of both mental and motor skills (psychomotor delay), abnormal muscle tone (dystonia), and spasms and weakness affecting the legs (spastic quadriparesis) and metabolic acidosis.
MGA-II	Barth Syndrome	*TAZ* 300394, Barth 302060	*TAZ*	Xq28	X-linked Recessive	Moderate increase in 3-methylglutaconic and 3-methylglutaric acid, normal levels of 3-hydroxyisovaleric acid.	Dilated cardiomyopathy, neutropenia, skeletal myopathy, and abnormal mitochondria. By electron microscopy, the mitochondria showed concentric, tightly packed cristae and occasional inclusion bodies.
MGA-III	Costeff Optic Atrophy Syndrome	*OPA3* 606580, MGA-III 258501	*OPA3*	19q13.2-13.3	Autosomal Recessive	Urinary excretion of 3-methylglutaconic and of 3-methylglutaric acid is increased.	It is characterized mainly by degeneration of the optic nerve. Other nervous system problems occur such as an inability to maintain posture, poor muscle tone, the development of certain involuntary movements (extrapyramidal dysfunction) and a general decrease in brain function.
MGA-IV		MGA-IV 250951	Genetic factors unknown		Inheritance unknown		A clinically heterogenous group of disorders with variable psychomotor retardation, hypertonicity, hypotonia, optic atrophy, dysmorphic features, seizures, cardiomyopathy and hepatic dysfunction. Some patients have elevated lactic or citric acid cycle intermediates, and some have abnormalities of the mitochondrial electron transport chain.
MGA-V		MGA-V 610198, *DNAJC19* 608977	*DNAJC19*	3q26.3		5-10 fold increase in both plasma and urine 3-methylglutaconic and 3-methlyglutaric acid.	Early-onset dilated cardiomyopathy with conduction defects, nonprogressive cerebellar ataxia, testicular dysgenesis, and growth failure in addition to 3-methylglutaconic aciduria [Chitayat *et al*, 1992; Davey *et al*, 2006].

Table 1.2. Overview of all five methylglutaconic aciduria syndromes. The syndromes were divided into four different disease categories by Gibson *et al,* 1993. In 2006 Davey *et al,* added MGA-V to the list.

1.2.2 3-Methylglutaconic aciduria Type III or Costeff syndrome

MGA-III (OMIM 258501) presents with early-onset bilateral optic atrophy, late-onset spasticity, extrapyramidal dysfunction, and cognitive deficit. Urinary excretion of 3-methylglutaconic acid and of 3-methylglutaric acid is increased. The disease was first reported by Costeff *et al*, in [1989]. Disease characteristics include, infantile optic atrophy sometimes associated with infantile-onset horizontal nystagmus; extrapyramidal movement disorder, dominated by chorea, with onset before age ten years, which is often severe enough to restrict ambulation. Some are confined to a wheelchair from an early age. About half the patients developed spastic paraparesis during the second decade of life. Ataxia and cognitive defects are common, but usually of mild degree. Nine of the 10 families described by Costeff, including all of those with multiple affected siblings, belonged to the Iraqi Jewish community in Israel, a group with an estimated minimal prevalence rate of 1:10,000, with a carrier rate estimated to be 1:10 [Anikster *et al*, 2001]. The disorder bore some similarity to Behr syndrome (OMIM 210000) but the neurological aspects were distinctive.

The occurrence of MGA in this disorder was discovered by Chitayat *et al*, [1992], only then was it designated MGA-III. Elpeleg *et al*, [1994] reported 11 new patients of Iraqi Jewish origin with the same clinical syndrome associated with MGA and reviewed the clinical and biochemical findings in 36 patients. The report defined a homogeneous group of patients with MGA-III. They differed from patients with MGA-I by the normal 3-methylglutaconyl-CoA hydratase activity in their fibroblasts and differed from patients with MGA-II by the absence of cardiomyopathy, short stature, and neutropenia. In addition, the mode of transmission in MGA-III is autosomal recessive, whereas MGA-II appears to be X-linked.

1.2.3 Symptoms and genetics of the other syndromes of 3-Methylglutaconic aciduria

1.2.3.1 3-Methylglutaconic aciduria Type I (MGA-I)

MGA-I is a very rare autosomal recessive disorder where fewer than 20 cases have been reported. The clinical features are nonspecific and variable, ranging from minimal to severe symptoms. The characteristic features include speech delay, delayed development of both mental and motor skills (psychomotor delay), dystonia, spasms and weakness affecting the arms and legs (spastic quadriparesis) and metabolic acidosis [Shoji *et al*, 1999; Ijlst *et al*, 2002; Arn and Funanage, 2006; Di Rosa *et al*, 2006]. Furthermore, tissues with higher

requirement for oxidative metabolism, such as the CNS, cardiac and skeletal muscle, are predominantly affected [Gunay-Aygun, 2005]. Patients with MGA-I excrete higher levels of 3-methylglutaconic acid and of 3-methylglutaric acid than those affected by other variants of MGA.

The excretion of organic acids in MGA-I is due to mutations in the AU-specific RNA-binding enoyl-CoA hydratase (*AUH*) gene. This gene provides instructions for producing 3-methylglutaconyl-CoA hydratase, an enzyme that is involved in processing the amino acid (aa) leucine. This aa is broken down in the mitochondria during the process of energy production. The isolated deficiency of 3-methylglutaconyl-CoA hydratase [Duran *et al*, 1982] leads to a build up of 3-methylglutaconic acid, which is eliminated in the urine. It is believed that other genes or environmental factors also contribute to the development of this disorder.

The precise etiology of the increased organic acid excretion in MGA II-V has not been elucidated.

1.2.3.2 3-Methylglutaconic aciduria Type II (MGA-II) or Barth syndrome

Barth syndrome was first reported by Barth *et al*, [1981, 1983]. He described a large pedigree showing X-linked inheritance of a disorder characterized by dilated cardiomyopathy associated with skeletal myopathy, neutropenia and growth retardation [Walsh *et al*, 1999; Ijlst *et al*, 2002; Barth *et al*, 2004]. Dilated cardiomyopathy presents within first year of life or even prenatally [Barth *et al*, 2004]. Cognitive development is normal, although an associated learning disorder has been described. Abnormal mitochondria have been observed by electron microscopy which showed concentric, tightly packed cristae and occasional inclusion bodies. The incidence of Barth syndrome is approximately 1 in 200,000 male infants. Female carriers of the Barth syndrome gene appear to be healthy. This could be due to a selection against cells that have the mutant allele on the active X chromosome.

Mutations in the tafazzin (*TAZ*) gene cause Barth syndrome. This gene provides the instructions for making a protein called tafazzin which is thought to be involved in the metabolism of cardiolipin. Barth syndrome was the first identified inborn error of metabolism that directly affects cardiolipin. Cardiolipin is a component of the inner mitochondrial membrane (IMM) and is required for the optimal function of many proteins within the mitochondria, particularly the electron transport chain. It is also involved in mitochondrial-

mediated apoptotic process. The appropriate content of cardiolipin appears to be critical for these functions. Cardiolipin is synthesized *de novo* in mitochondria and is rapidly remodelled to produce cardiolipin enriched in linoleic acid. Mutations in *TAZ* result in a decrease in tetra-linoleoyl species of cardiolipin and an accumulation of monolysocardiolipin within cells from Barth syndrome patients. This results in abnormalities in the structure and function of mitochondria, leading to the heart defects and other problems seen in this disorder.

1.2.3.3 3-Methylglutaconic aciduria Type IV (MGA-IV)

Only one case of MGA-IV (autosomal recessive, with severe psychomotor phenotype and cerebellar dysgenesis) has been described. Chitayat *et al*, [1992] described an 18 year old male proband with MGA, severe psychomotor retardation, and cerebellar dysgenesis, which they designated MGA-IV. He was the offspring of consanguineous Italian parents. At birth, he was hypotonic, with absent reflexes and respiratory distress. Congenital deformities included bilateral inguinal hernia, undescended testes, subaortic stenosis with biventricular hypertrophy and right simian crease with left bridged simian crease. The signs and symptoms of MGA-IV are variable and overlap with Types I-III. The incidence of MGA-IV and the genetic factors involved in causing MGA-IV are unknown.

1.2.3.4 3-Methylglutaconic aciduria Type V (MGA-V)

The fifth type of MGA is a novel autosomal recessive disorder that shares some clinical similarity with X- linked Barth syndrome and the other MGAs. It was described by Davey *et al*, [2006], who reported 18 patients with dilated cardiomyopathy and ataxia from 11 consanguineous Canadian Dariusleut Hutterite families. Disease phenotype is characterized by early onset dilated cardiomyopathy with conduction defects, non-progressive cerebellar ataxia causing significant motor delays, testicular dysgenesis, prenatal and postnatal growth failure and MGA. Urine and plasma samples consistently showed a 5- to 10-fold increase in 3-methylglutaconic acid and 3-methylglutaric acid. Additional features included normochromic microcytic anaemia in 12 patients, mild to borderline nonprogressive mental retardation in 10, a mild increase in hepatic enzymes with microvesicular hepatic steatosis in 5 and optic atrophy in 4. The onset of cardiomyopathy was always before the age of 3 years, and over 70% of affected individuals died from either progressive cardiac failure or sudden cardiac death. Candidate genes were sequenced and identified homozygosity for a splice-site mutation in the *DNAJC19* gene in all 16 patients for whom DNA samples were available. The

protein encoded by DNAJC19 shares sequence similarity with Tim14, an integral IMM protein that participates in mitochondrial protein import.

1.2.4 *OPA3*- Autosomal Dominant Optic Atrophy and Cataract (ADOAC)

More recently *OPA3* has also been associated with ADOAC (OMIM 165300). This optic atrophy, cataract and neurological disorder was first described by Garcin *et al*, in [1961]. The disorder was found in 14 persons in 7 sibships of 4 generations with several instances of male-to-male transmission. A blue-dot cerulean cataract was usually recognised in the first decade. However, mutations causing this disorder were not identified until Reynier *et al*, [2004] found two different mutations of the *OPA3* gene in another family: gly93 to ser and gln105 to glu, respectively. No abnormalities were found in the respiratory chain, the mitochondrial membrane potential, or in the organisation of the mitochondrial network of fibroblasts obtained from one affected patient. However, the fibroblasts showed increased susceptibility to staurosporine-induced apoptosis. Although Garcin *et al*, [1961] described the phenotype as a neurodegenerative disorder, Reynier *et al*, [2004] noted that the neurological signs are mild or even absent in affected patients. They suggested the disease would be more appropriately designated ADOAC.

1.2.5 Cataracts as part of ADOAC

1.2.5.1 What is a cataract?

A cataract is a clouding of the crystalline lens or its surrounding transparent membrane, which lies behind the iris and the pupil. The lens is mostly made of water and protein. The protein is arranged in a precise way that keeps the lens clear and allows light to pass through it. Either through age or disease, cataracts can result from changes in lens architecture, from disruption of intracellular ordered arrangement of proteins or from changes in organisation of lens fibres due to aberrations in growth or differentiation. These changes will obstruct the passage of light and cause a reduction in vision.

1.2.5.2 Causes of cataract

Cataracts are the leading cause of blindness in the world. It is also the most treatable cause of visual problems both in childhood (congenital cataract) and in adults (age-related cataract). The incidence of congenital cataract is approximately 1-6/10,000 live births, and the condition can occur in isolation or as part of a more complex syndrome. There are also certain factors

that can increase your risk of getting cataracts e.g., exposure to UV light, exposure to radiation, diabetes, hypertension and advanced age.

1.2.5.3 Genetics of cataract

Hereditary cataracts that have been characterized so far show Mendelian inheritance and either result from single-gene mutations or from chromosomal translocations. They can be inherited in an autosomal dominant, recessive or X-linked mode. Over 26 of the 39 mapped loci for isolated congenital or infantile cataracts have been associated with mutations in specific genes. Of the cataract families for whom the mutant gene is known, about half have mutations in crystallins, about a quarter have mutations in connexins, with the remainder divided among the genes for heat shock transcription factor-4, aquaporin-0, and beaded filament structural protein-2. There is often some correlation between the pattern of expression of the mutant protein and the morphology of the resulting cataract. However, inheritance of the same mutation in different families or even the same mutation within the same family can result in radically different cataract morphologies and severities. This suggests that additional genes or environmental factors might modify the expression of the primary mutation associated with the cataracts. Conversely, cataracts with similar or identical clinical presentations can result from mutations in completely different genes.

1.3 Pathophysiology of the non-syndromic optic neuropathies

The non-syndromic optic neuropathies are by definition limited to a single cellular target, i.e., the RGCs. LHON and DOA are non-syndromic with early and preferential involvement of the small axons that form the papillomacular bundle (PMB) [Yu-Wai-Man *et al*, 2009]. Loss of these cells leads to a reduction of optic nerve tissue and thinning of the nerve along its length. Pupil function is less affected than visual function suggesting that the retinotectal fibres responsible for the pupil light reflex (PLR) are less susceptible to damage than the retinogeniculate fibres. Visual field defects, including diffuse or sectorial scotomas, can usually be observed but are highly variable.

1.3.1 OPA1- Autosomal dominant optic atrophy and neurological defects

Autosomal dominant optic atrophy (ADOA) is the most common form of non-glaucomatous optic atrophy and in the general population has an incidence of 1/50,000 [Votruba *et al*, 1998] and a prevalence of 1/10,000 [Kjer *et al*, 1996]. Generally it presents in childhood as slowly progressive bilateral loss of visual acuity, constriction of peripheral visual fields, central

scotomas, and colour vision abnormalities. ADOA is caused by mutations in the optic atrophy 1 gene (*OPA1*) [Alexander *et al*, 2000, Delettre *et al*, 2000] mapped to chromosome 3q28–q29 and has variable clinical expression and penetrance [Toomes *et al*, 2001].

OPA1 comprises 30 exons and is ubiquitously expressed, with highest expression in the retina, but also abundantly in brain and muscle [Alexander *et al*, 2000; Wang *et al*, 2006]. Common to all isoforms of OPA1 are a GTPase, dynamin-like domain; a central domain; a C-terminal coiled coil domain presumably involved in protein–protein interaction; and an N-terminal mitochondrial targeting sequence that directs the protein to the IMM, facing the intermembrane space [Olichon *et al*, 2002]. *OPA1* has been linked to two important mitochondrial activities: fusion [Cipolat *et al*, 2004], that in equilibrium with fission regulates mitochondrial morphology [Ishihara *et al*, 2006], and caspase-dependent apoptosis through mitochondrial cristae remodelling [Frezza *et al*, 2006; Olichon *et al*, 2003]. The equilibrium between mitochondrial fusion and fission appears very dynamic and links mitochondrial morphology to mitochondrial function [Ishihara *et al*, 2006] and vice versa. Recent reports have also associated common *OPA1* mutations, predicted to generate a truncated *OPA1* protein and typical of uncomplicated ADOA phenotypes, to impaired oxidative phosphorylation with mitochondrial fragmentation in fibroblasts, and increased susceptibility to apoptosis [Zanna *et al*, 2008; Olichon *et al*, 2007].

1.3.2 OPA2- X-linked optic atrophy

The first report of X-linked optic atrophy (XLOA) appeared in 1947 and described eight males in a four generation kinship [Lysen and Oliver, 1947]. The next report appeared in 1967 where two brothers and a nephew with apparent XLOA displaying progressive optic atrophy, sensorineural hearing loss, and a polyneuropathy [Rosenberg and Chutorian, 1967].

A Dutch pedigree with XLOA was described by Volker-Dieben *et al*, [1974] and Went *et al*, [1975]. Age of onset was early childhood, and the progressive loss of visual acuity was very slow. Optic discs were sharply outlined and completely pale. Some affected males were mentally retarded and showed minor abnormalities on neurologic examination including, hyperactive knee jerks, absent ankle jerks, extensor plantar reflexes, dysarthria, tremor, dysdiadochokinesia, difficulty with tandem gait. Female carriers showed no abnormalities and no abnormality was described in obligatory heterozygotes. Four males from this Dutch

kindred were subsequently studied and linkage analysis placed the gene in the Xp11.4-Xp11.2 interval [Assink *et al*, 1997].

Katz *et al*, [2006] reported 6 males with decreased visual acuity from early childhood; visual acuities ranged from 20/30 to 20/100, and all had significant optic nerve pallor all from a 3-generation family in Idaho. Obligate female carriers were clinically unaffected. Linkage analysis suggested the *OPA2* locus.

1.3.5 Leber's hereditary optic neuropathy

LHON was first described by Leber in 1871 and is the first disease to be associated with the mitochondrial genome. The condition is inherited through the female line by maternal transmission of mtDNA. The majority of patients with LHON are males in their 20s, but atypical cases may be found in females who may present at any age between 10 and 60 years.

The condition appears suddenly and usually affects both eyes. There is often an acute, severe, painless loss of vision; both eyes may either be affected simultaneously or sequentially, with a gap of a few days or weeks between the onset of symptoms. Visual field defects usually affect central field vision, the peripheral field being spared. The optic disc may appear normal in the acute stage. Colour vision problems may be present affecting the red-green axis and there may be some pain during eye movements. There is considerable variation in symptoms between patients, but most typically cases show disc hyperaemia, dilated capillaries on the disc surface, deformed blood vessels and swelling of the peripapillary nerve fibre layer (NFL). There is a modest degree of disc elevation and no dye leakage on fluorescein angiography. Visual prognosis is poor although there is often some visual recovery. The majority of patients will exhibit permanent loss of vision with a final visual acuity 6/60, although this will vary with the type of mutation.

There are three primary mutations of mtDNA in LHON, *viz* at bp 11778, 3460, and 14484. The mutation at bp 11778 causes a change in the NADH hydrogenase sub-unit four of complex I in the respiratory chain, and is present in 64% of cases of LHON. The mutation at bp 3460 is present in 10% of patients while that at 14484 bp is found largely in the United Kingdom (UK) and Netherlands accounting for 25% of cases.

The majority of these mutations result in partial defects of the respiratory chain function leading to deficits in ATP and an increase in oxidative stress. The presence of myelin pathology and a multiple sclerosis likeness in some patients, especially those with the 11778 mutation, supports the suggestion that oxidative stress is important in LHON. The visual prognosis of the condition appears to depend on the type of mutation, with the 11778 mutation patients having the worst prognosis.

A commonality to all these diseases is the selective loss of RGCs within the retina.

1.4 The Mitochondrion – a unifying theme

The prevalence of neuronal diseases associated with abnormalities of mitochondrial proteins encoded by the mitochondrial or the nuclear genomes indicates an important functional relationship between mitochondria and neurons. In 1988 Wallace identified the first substitution in the mtDNA causing LHON which was originally described by Leber in 1871, thereby beginning the list of optic neuropathies linked to mitochondrial dysfunction [Newman, 2005]. The discovery in the year 2000 that the genetic cause of the most common group of ADOA is *OPA1*, a nuclear gene encoding a mitochondrial dynamin [Alexander *et al*, 2000; Delettre *et al*, 2000], together with the finding that *OPA3,* the third gene identified as involved in primary optic neuropathies, encodes a mitochondrial protein [Da Cruz *et al*, 2003; Ryu *et al*, 2010] definitively demonstrates that the optic nerve is highly dependent on mitochondrial functions.

1.4.1 Structure

Mitochondria are bacterium size, membrane-bound organelles in the eukaryotic cell and were descended from prokaryotic endosymbionts about two billion years ago. Mitochondria do not exist stably as distinct, individual, autonomous organelles but form a highly dynamic semi-tubular network. They are 0.5μm-1.0μm across and exhibit a complex internal architecture (Fig 1.1.).

The organelle is encompassed by two membranes, an outer mitochondrial membrane (OMM) that defines the external boundary of the organelle and an IMM exhibiting numerous folds, known as cristae, that project into the mitochondrial interior. The outer and inner membranes divide the mitochondrion into two distinct compartments, the inner membrane space, which is located between the inner and outer membranes and the mitochondrial matrix, which is enclosed by the IMM.

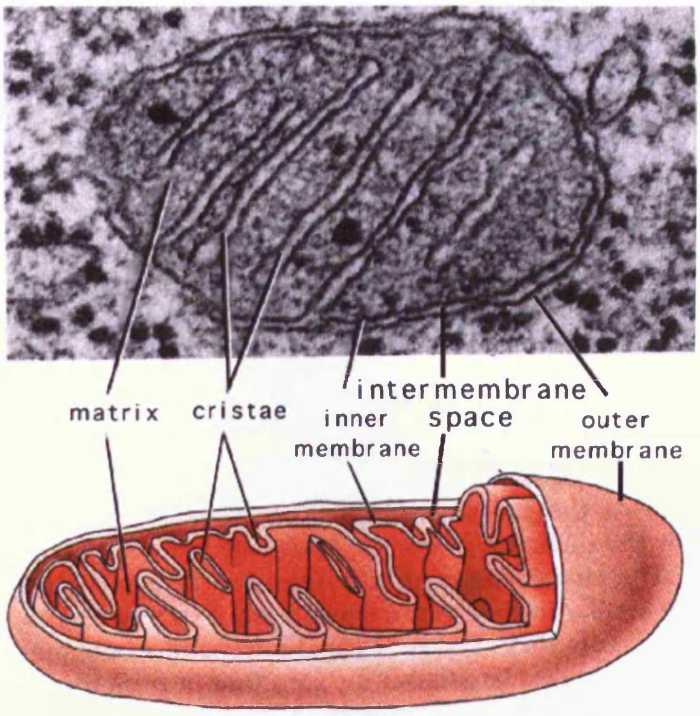

Figure 1.1. The Mitochondrion structure.
[http://academic.brooklyn.cuny.edu/biology/bio4fv/page/mito.htm – accessed 10.6.10]

The mitochondrion is especially complex as it is the only cellular organelle under the dual control of both the nuclear and its own (mitochondrial) genomes. The mitochondrial genome is a multicopy, maternally inherited, 16,596bp circular double stranded DNA that encodes for 13 polypeptides, all of which are structural components of the respiratory chain complexes, along with two ribosomal RNAs and 22 transfer RNAs, which are needed for the translation of the 13 mtDNA specified proteins.

1.4.1.1 Fusion and Fission

In the past decade a new concept of mitochondrial presence and spatial distribution in the host cell was articulated based on microscopy observation, which suggested the fusion and fission of different mitochondria: the mitochondrial network concept. Mitochondria form a highly dynamic semi-tubular network in the cell, the morphology of which is regulated by movements along the cytoskeleton and the balance of mitochondrial fusion and fission events. Equilibrium between fusion and fission controls the morphology of the mitochondria which is necessary for maintaining normal mitochondrial function. They can appear as dots or elongated tubules depending on the prevailing forces.

Recent studies have indicated that mitofusins (*MFN1* and *MFN2*) and *OPA1* are essential for mitochondrial fusion whereas *FIS1* and *DRP1* are essential for mitochondrial fission. The overall morphology of the mitochondrial population depends on the relative activities of these two sets of proteins. In addition to the regulation of mitochondrial shape, these molecules also play important roles in cell and tissue physiology. Perturbation of mitochondrial fusion results in defects in mitochondrial membrane potential and respiration, poor cell growth and increased susceptibility to cell death. These cellular observations may explain why mitochondrial fusion is essential for embryonic development. Two inherited neuropathies, Charcot-Marie-Tooth Type 2A and ADOA are caused by mutations of *MFN2* and *OPA1*, suggesting that proper regulation of mitochondrial dynamics is particularly vital to neurons. Mitochondrial fission accompanies several types of apoptotic cell death and appears important for progression of the apoptotic pathway.

1.4.2 Function

Mitochondria are the driving force behind life and serve four fundamental biological roles (i) provision of ATP, (ii) mediation of cell death by apoptosis, (iii) heat production, and (iv) contribute to the genetic pool. In addition mitochondria play a crucial role in:- β-oxidation, citrate cycle (tricarboxic cycle, Krebs cycle), degradation of aa, parts of the haem-biosynthesis, parts of the steroid metabolism, parts of the uric acid cycle, mitochondrial protein synthesis, the pyruvate dehydrogenase complex and are responsible for the decarboxylation of pyruvate. The main metabolic functions of mitochondria are shown in Fig 1.2.

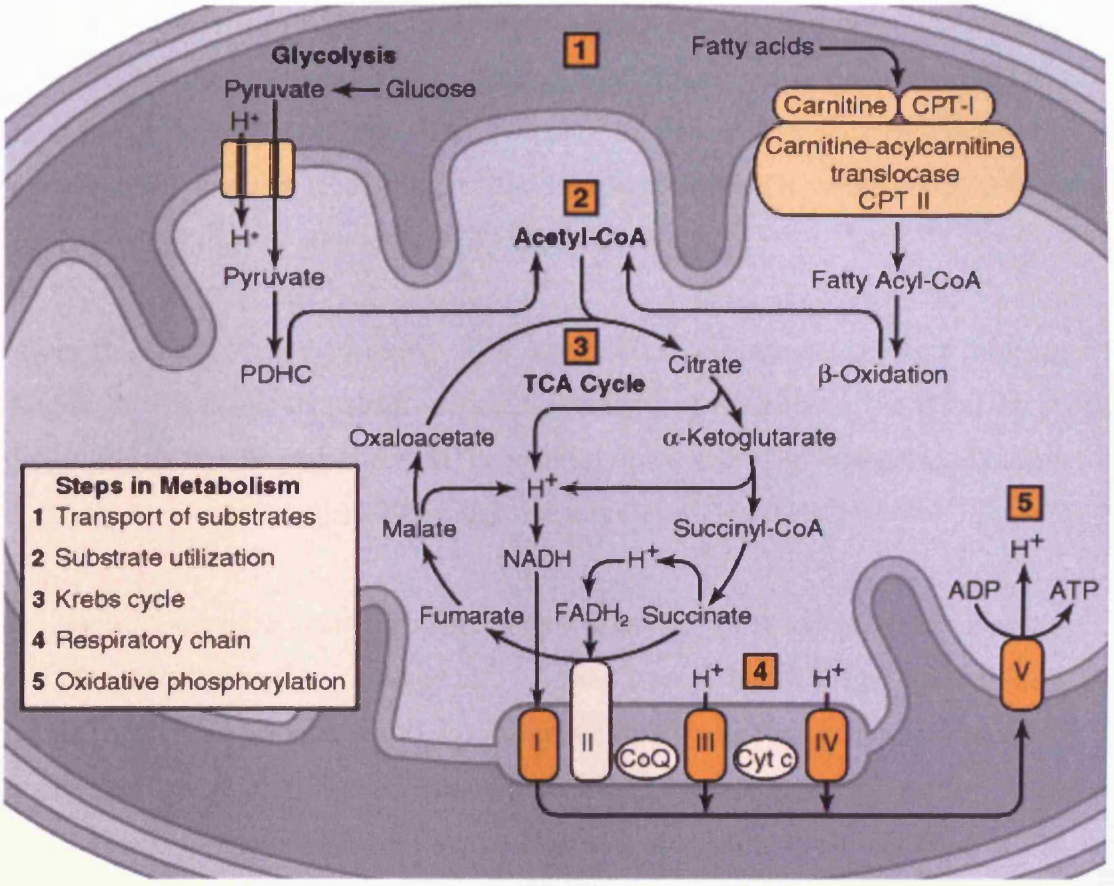

Figure 1.2. Schematic representation of mitochondrial metabolism. Respiratory chain complexes or components encoded exclusively by the nuclear genome are light orange. Complexes containing some subunits encoded by the nuclear genome and others encoded by mitochondrial DNA are dark orange. *CPT,* carnitine palmitoyltransferase; *PDHC,* pyruvate dehydrogenase complex; *CoA,* coenzyme A; *TCA,* tricarboxylic acid; *CoQ,* coenzyme Q; *Cyt c,* cytochrome c [Siegel *et al*, 2006].

1.4.2.1 ATP production - Electron transport chain and oxidative phosphorylation

Mitochondria generate most of the cellular energy by OXPHOS, and produce most of the toxic reactive ROS as a by-product. Genetic defects that inhibit OXPHOS also cause the redirection of OXPHOS electrons into ROS production, thus increasing oxidative stress. A decline in mitochondrial energy production and an increase in oxidative stress can impinge on the mitochondrial permeability transition pore (mtPTP) to initiate programmed cell death (apoptosis). The interaction of these three factors appears to play a major role on the pathophysiology of degenerative diseases.

The electron transport chain is located in the IMM and comprises some 80 proteins organized in four enzymatic complexes (I-IV). Complex V generates ATP but has no electron transfer

activity. Electron transfer between these complexes is accomplished by two electron shuttle molecules; Coenzyme Q (also known as ubiquinone) from Complexes I and II to Complex III and cytochrome *c* from Complex III to Complex IV. These enzymes are encoded by either mitochondrial or nuclear DNA (Fig 1.2.). Therefore a deficit of either mitochondrial or nuclear DNA may lead to malfunction of OXPHOS.

Metal centres and other co-factors in these complexes act, in essence, as a molecular wire, carrying electrons from the strongly reducing products of the Kreb cycle (NADH, succinate) to highly oxidizing dioxygen which is reduced to water. The *direct* oxidation of these substrates by O_2 would release a great deal of energy as useless heat.

Instead, *indirect* oxidation occurs, whereby during a series of redox reactions, electrons travel down the chain releasing their energy in controlled steps (Fig 1.3.). These reactions drive the active transport of H^+ ions from the mitochondrial matrix, through the inner membrane to the intermembrane space, creating an electrochemical proton gradient across the IMM. Complex I (NADH coenzyme Q reductase) accepts electrons from the Krebs cycle electron carrier nicotinamide adenine dinucleotide (NADH), and passes them to Coenzyme Q, which also receives electrons from complex II (succinate dehydrogenase). Coenzyme Q passes electrons to complex III (cytochrome bc_1 complex), which passes them to cytochrome *c*. Cytochrome *c* passes electrons to Complex IV (cytochrome *c* oxidase), which uses the electrons and hydrogen ions to reduce molecular oxygen to water. This electrochemical proton gradient allows ATP synthase (ATP-ase) to use the flow of H^+ through the enzyme back into the matrix to generate ATP from ADP and inorganic phosphate. Although electron transport occurs with great efficiency, a small percentage of electrons are prematurely leaked to oxygen, resulting in the formation of the toxic free-radical superoxide.

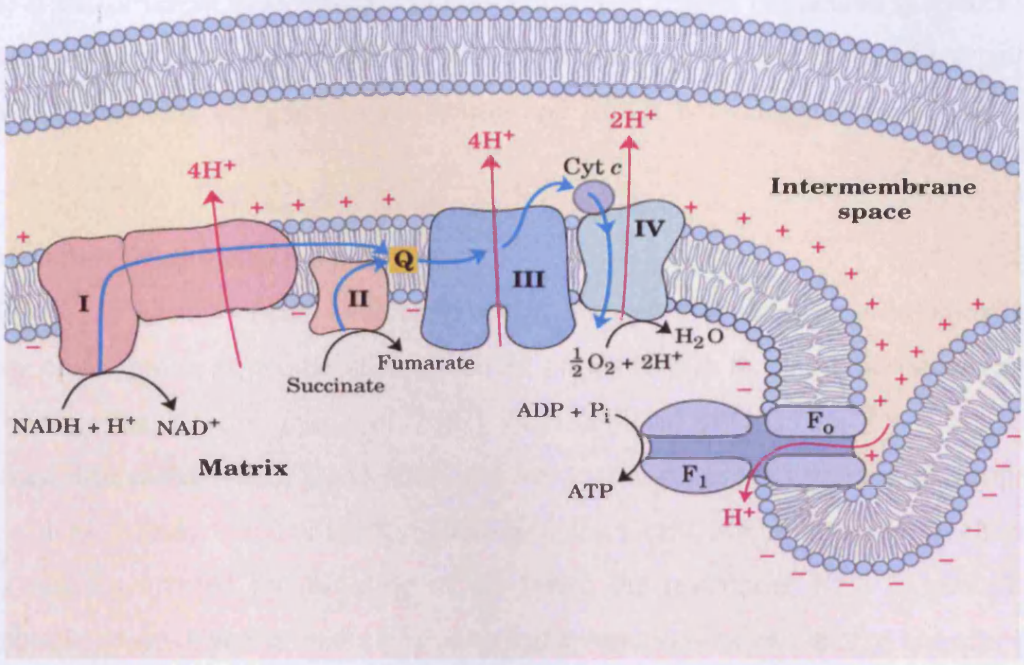

Figure 1.3. The electron transport chain in the mitochondrion is the site of oxidative phosphorylation in eukaryotes. The NADH and succinate generated in the citric acid cycle is oxidized, providing energy to power ATP synthase. [http://inoxx.net/?p=26 – accessed 10.6.10]

Fibroblasts from patients with ADOA (*OPA1*), ADOAC (*OPA3*) and LHON have a common coupling defect of OXPHOS associated with reduced efficiency of ATP synthesis [Chevrollier *et al*, 2008]. Their fibroblasts showed that in the routine respiratory state a greater proportion of their respiratory capacity was used compared to controls (80% versus 60%), thus retaining a low 'reserve' capacity to face greater energy requirements. In LHON this defect is associated with mtDNA point mutations that affect various subunits of Complex I. Fibroblasts from DOA patients carrying frame shift/stop codon/splicing (haploinsufficiency) mutations in the *OPA1* gene have recently been shown to display a defective ATP synthesis mainly when driven through complex I substrates [Zanna *et al*, 2008].

The consequences of complex I dysfunction may go beyond the immediate effects on energy conservation and ROS production. There is mounting evidence tightly linking complex I dysfunction with predisposition to apoptosis [Zanna *et al*, 2005; Porcelli *et al*, 2009]. There is also a tight connection between fission/fusion, mitochondrial network dynamics, control and regulation of apoptosis [Olichon *et al*, 2003; Frezza *et al*, 2006; Suen *et al*, 2008]. There are many intricacies of how different genetic defects, in the nuclear and in the mitochondrial

genomes, affect different biochemical systems and cell functions implicated in mitochondrial homeostasis. However, in many cases these may converge towards common final pathways, one of which may link complex I dysfunction and RGCs neurodegeneration [Carelli *et al*, 2007].

1.4.2.2 Mitochondrial mediated apoptosis

Death of RGCs in LHON occurs in an apoptotic manner, so that changes in the mitochondrial respiratory chain and/or in oxidative stress could play a role in the induction of apoptosis in LHON [Wong *et al*, 2002; Ghelli *et al*, 2002]. Cells depleted of Opa3 and Opa1 are sensitive to apoptosis. The IMM where Opa3 and Opa1 are expressed is also the site of apoptogenic proteins such as cytochrome c or the apoptosis-inducing factor. About 90% of cytochrome c is stored in vesicles created by infolding of the IMM; the remaining 10% is located in the intermembrane space. Cytochrome c physiologically functions as an electron transfer protein in many different redox processes.

The mitochondrial pathway of apoptosis (Fig 1.4.) functions in response to various types of stress such as ultraviolet light, pro-oxidants, viral infections, chemotherapeutic agents, ischaemia, inflammatory cytokines, neurotoxins, and many others can induce a variety of intracellular changes, such as increased calcium levels, NO release, ceramide activation, and antioxidant depletion. Those alterations cause damage to mitochondrial inner and outer membranes causing (i) the release of cytochrome c into the cytosol in the first phase of apoptosis, activating caspase 9 [Bossy-Wetzel *et al*, 1999]; (ii) the Bcl-2 family proteins (located in the OMM) to form complexes and enter the mitochondrial membrane, regulating the release of cytochrome c and other proteins [Adachi *et al*, 1997]; (iii) the decrease of IMM potential, mediated by opening of the mitochondrial permeability transition pore [Susin *et al*, 1996]; (iv) electron transport alterations, oxidative phosphorylation dysfunction, and storage of free radicals [Greenlund *et al*, 1995]. An alternative pathway may induce swelling and rupture of mitochondrial membranes, which may lead not only to caspase activation and apoptosis but also to necrosis due to a breakdown of ATP production and the creation of ROS. But the crucial step toward irreversible death commitment in many systems is the release of cytochrome *c*.

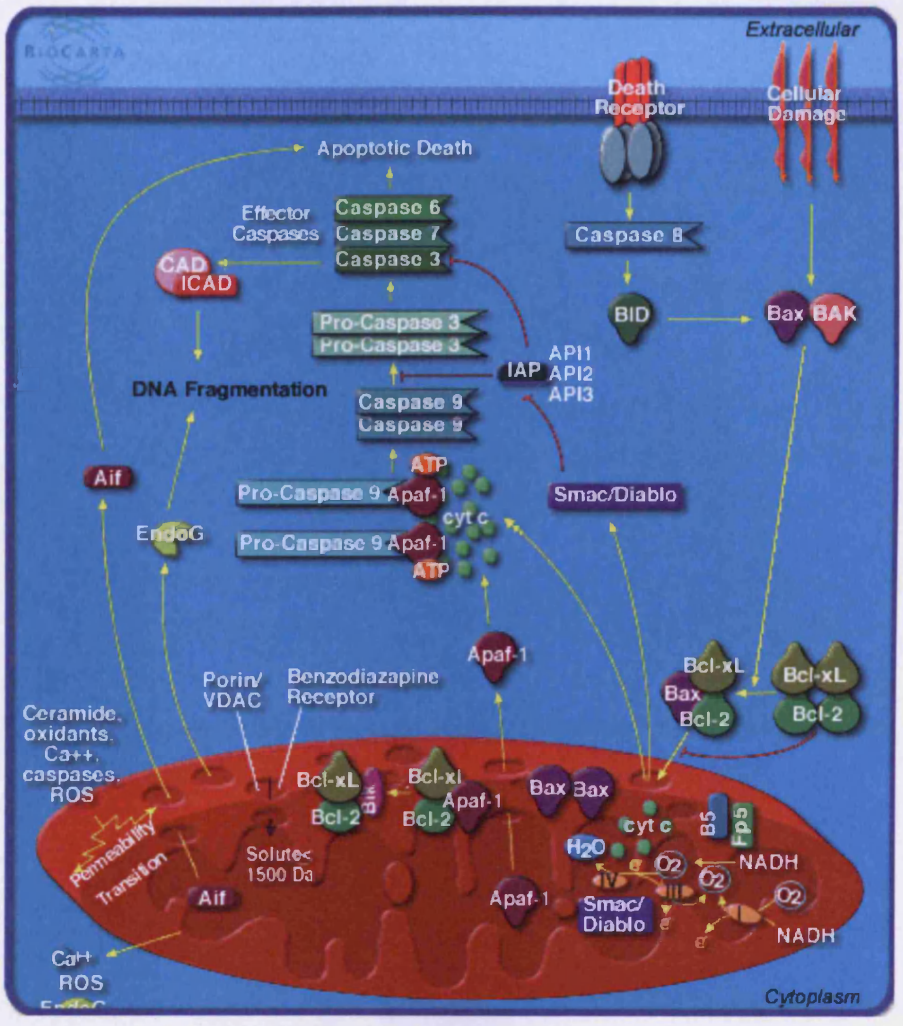

Figure 1.4. Mitochondrial mediated apoptotic signalling.
[http://www.biocarta.com/pathfiles/h_mitochondriaPathway.asp – accessed 10.6.10]

1.4.2.3 Heat production

Non-shivering thermogenesis in brown adipose tissue (BAT) is the main mechanism for thermoregulatory heat production in small mammals and newborns. BAT is highly specialized for this non-shivering uncoupling protein 1 (UCP-1) mediated thermogenesis. UCP-1 is restricted to brown fat, where it provides a mechanism for the enormous heat-generating capacity of the tissue. UCP-1 mediated thermogenesis uncouples the respiratory chain, allowing for fast substrate oxidation with a low rate of ATP production (Fig 1.5.)

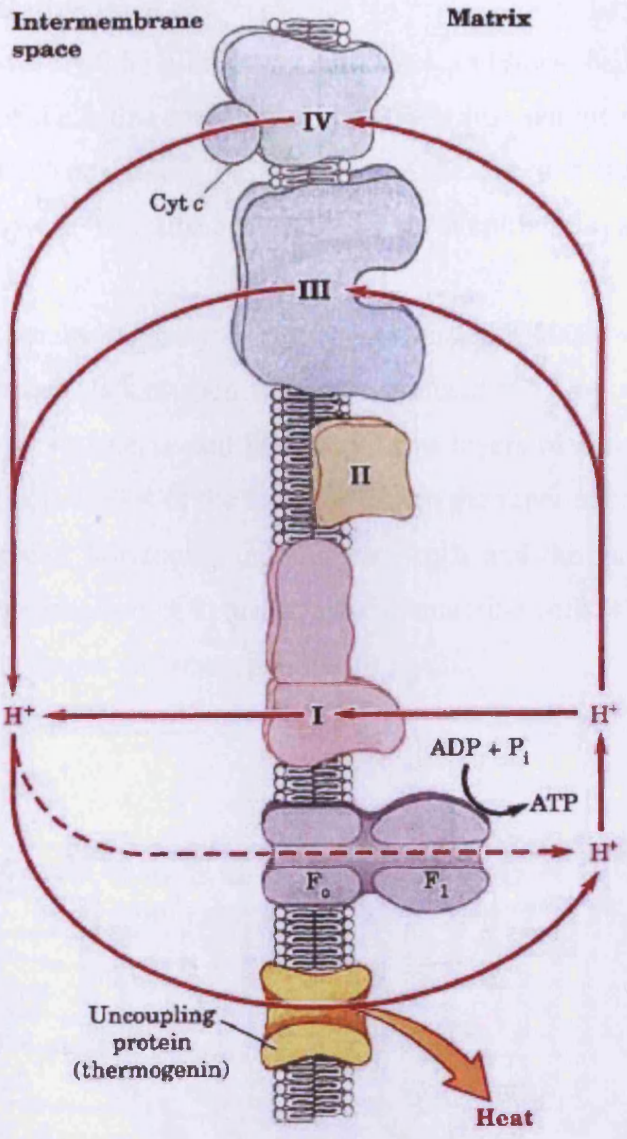

Figure 1.5. UCP-1 and mitochondrial proton leak.
[www.fucotin.com/Portals/8/images/Figure03.jpg- accessed 10.6.10]]

Despite known defects in the electron transport chain no patients with MGA-III or ADOAC are known to suffer from any thermoregulation defects.

1.5 The Vertebrate Retina

The retina is approximately 0.5 millimetres (mm) thick and lines the back of the eye. A radial section of a portion of the retina reveals that the RGCs (the output neurons of the retina) lie innermost in the retina closest to the lens and front of the eye, and the photo sensors (the rods and cones) lie outermost in the retina against the pigment epithelium and choroid (Fig 1.6.).

Mammalian retinas contain a variety of cell types [Masland, 2004] which are packaged into highly ordered anatomical layers each with a specialized function. The vertebrate retina is composed of three layers of nerve cell bodies and two layers of synapses. The outer nuclear layer (ONL) contains cell bodies of the rods and cones, the inner nuclear layer (INL) contains cell bodies of the bipolar, horizontal and amacrine cells and the ganglion cell layer (GCL) contains cell bodies of ganglion cells and displaced amacrine cells. Dividing these nerve cell layers are two synaptic (inner and outer plexiform) layers.

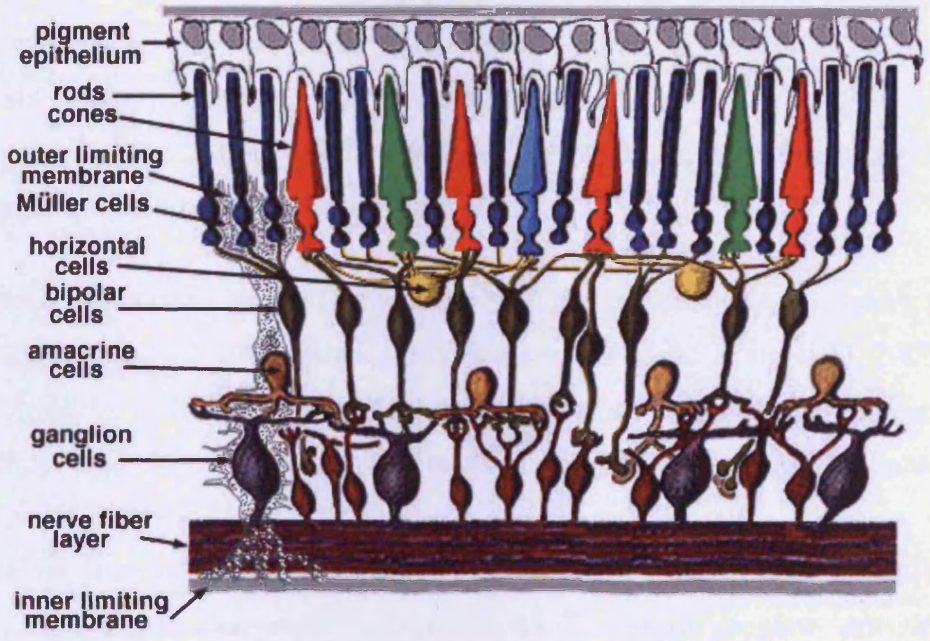

Figure 1.6. A simplistic wiring diagram of the retina emphasises only the sensory photoreceptors and the ganglion cells with a few interneurons connecting the two cell types. [www.webvision.med.utah.edu/sretina.html- 10.6.10]

In the retina, the photoreceptors synapse directly onto bipolar cells, which in turn synapse onto ganglion cells, which will then conduct action potentials to the brain. A significant amount of visual processing arises from the patterns of communication between neurons in the retina. About 130 million photoreceptors absorb light, yet roughly 1.2 million axons of ganglion cells transmit information from the retina to the brain. The processing in the retina includes the formation of center-surround receptive fields of bipolar and ganglion cells in the retina, as well as convergence and divergence from photoreceptor to bipolar cell. In addition, other neurons in the retina, particularly horizontal and amacrine cells, transmit information laterally (from a neuron in one layer to an adjacent neuron in the same layer), resulting in more complex receptive fields that can be either indifferent to color and sensitive to motion or sensitive to color and indifferent to motion.

1.5.1 The Retinal Ganglion Cell Layer

Adult RGCs are a heterogeneous, finite population of post mitotic neurons. Though mainly located within the innermost nucleated layer of the mature retina, the somata of some RGCs are displaced from this GCL to the inner plexiform layer (IPL) [Dann *et al*, 1988]. The distribution of RGCs is very non-linear. In the perifoveal macula the RGCs are concentrated and stacked six or seven cells deep [Polyak, 1941; Fine and Yanoff, 1979]. Further from the fovea the numbers of RGCs decreases becoming relatively sparse in the periphery with each of the cells quite distant from the others.

RGCs have been categorised into different classes in a number of species including the mouse [Doi *et al*, 1995; Sun *et al*, 2002a; Badea and Nathans, 2004 and Kong *et al*, 2005]. RGCs can be categorized by their morphology, such as soma size and dendritic field dimensions. As the morphology of RGCs is a direct reflection of the underlying neural connectivity, it remains the most common way of identifying and classifying retinal neurons. However, studies of the rat [Huxlin and Goodchild, 1997; Sun *et al*, 2002b] and mouse [Sun *et al*, 2002a] retina have shown that with the exception of the largest ganglion cells, considered homologous to the alpha cells first identified in the cat [Peichl, 1991], there is considerable overlap in both soma and dendritic field measurements of RGCs in these rodents.

More recent cell-filling methods to assess types of RGCs include: a single cell injection with diffusible markers, such as Lucifer yellow or neurobiotin; a sparse delivery of lipophilic dyes by particle bombardment; expression of genetically encoded histochemical or fluorescent

reporters; and a photofilling method [Badea and Nathans, 2004; Masland and Raviola, 2000]. The systematic surveys indicate that the human, monkey, cat, rabbit, and mouse each contain approximately 10 to 15 types of RGCs.

RGCs have also been classified based on their processing of visual (image-forming and non-image-forming) information that is sent to the brain: (i), M-cells, with large center-surround receptive fields that are sensitive to depth, indifferent to colour, and rapidly adapt to a stimulus. (ii), P-cells, with smaller center-surround receptive fields that are sensitive to colour and shape. (iii), K-cells, with very large center-only receptive fields that are sensitive to colour and indifferent to shape or depth. (iv), Intrinsically photosensitive RGCs (ipRGCs) and (v), a population that is used for eye movements.

Among the different cell types in the retina, RGCs are the only ones whose axons leave the retina, transmitting visual information to the brain.

1.5.2 The Optic Nerve

Visual information is transmitted from the retina to the brain via the optic nerve, also called the cranial nerve II. The optic nerve is the second of twelve paired cranial nerves but is considered to be part of the CNS as it is derived from an out pouching of the diencephalons during embryonic development. Consequently, the fibres are covered with myelin produced by oligodendrocytes rather than Schwann cells of the peripheral nervous system. Similarly, the optic nerve is ensheathed in all three meningeal layers (dura, arachnoid, and pia mater) rather than the epineurium, perineurium, and endoneurium found in the peripheral nerves. This is an important issue, as fibre tracks of the mammalian CNS (as opposed to the peripheral nervous system) are incapable of regeneration and hence optic nerve damage produces irreversible blindness. The fibres from the retina run along the optic nerve to nine primary visual nuclei in the brain, from whence a major relay inputs into the primary visual cortex (Fig 1.7.).

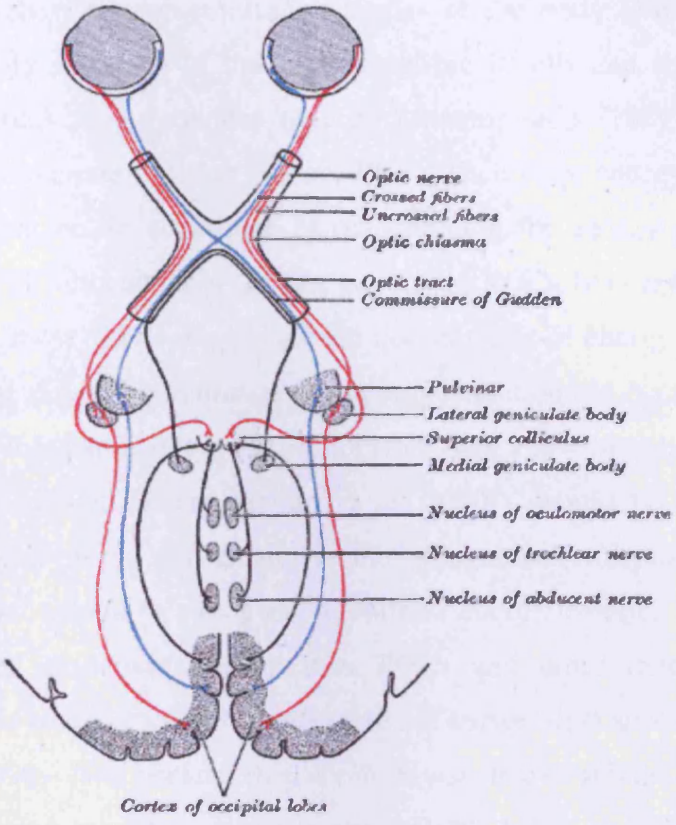

Figure 1.7. Scheme showing central connections of the optic nerve and optic tracts. [Henry Gray (1825–1861). Anatomy of the Human Body. 1918.]

RGCs integrate signals within the retina and are the point at which these are converged to action potentials. Since these activities are highly energy dependent and the axon path to the CNS is long, these cells are vulnerable to a range of metabolic and ischaemic insults that can act within the retina and along the course of the axon.

1.5.3 RGCs vulnerability to physiological and biochemical insult

It is interesting that despite OPA3 and OPA1 mutant proteins being ubiquitously expressed and therefore defective in every cell, the optic nerve is the major clinically affected organ. There must therefore be some aspects of its structure and/or function that make it uniquely vulnerable to certain physiological and biochemical insults – below some of these aspects are discussed.

1.5.3.1 Energy deficits

By virtue of their unmyelinated stretches, RGC axons are bioenergetically weak elements of the CNS. The relative oxygen consumption of the retina is higher than that of the brain and so

being one of the highest oxygen-consuming tissues of the body [Yu and Cringle, 2001]. RGCs are also mainly made up of the smaller calibre P-cells and these have the lowest volume (energy source) to surface area (energy demand) ratio. They also have a thinner myelin sheath and a rapid rate of firing [Sadun, 1998]. Their large energy consumption makes them highly dependent on an abundance of mitochondria for energy production, although there is a high level of mitochondrial enzyme activity in RGCs [Andrews *et al*, 1999]. Thus these fibres have the most disadvantageous condition in terms of energy requirements among the axons of the optic nerve. Therefore, if any energy depletion did occur the PMB which is composed mostly of these smaller type axons together with a few M-cells (which in the PMB are of considerably smaller calibre [Sadun *et al*, 2000]), would be a highly vulnerable component of the optic nerve particularly at the prelaminar (unmyelinated) portion. This vulnerability, however, cannot be explained by a simple energetic deficit since photoreceptors have a much higher oxidative demand than RGCs and other mitochondrial disorders characterised by more severe complex I defects do not universally cause optic atrophy. RGCs may be preferentially involved because they are more sensitive to subtle imbalances in cellular redox state or increased reactive oxygen species (ROS) levels or vulnerable due to their unique structure.

1.5.3.2 Lamina cribrosa

The pathway taken by the optic nerve axons as they cover the five centimetres (cms) between the eye and the visual centres is stressful for the cells. On leaving the eye, axons turn through 90 degrees to enter the optic nerve head. At the optic nerve head, about 1.2 million unmyelinated RGC axons exit through an opening in the sclera approximately 1.5 mm across (Fig 1.8.). In doing so, they pass through the lamina cribrosa which is a series of successive perforated collagen plates that mark the anatomical transition from the unmyelinated (pre-laminar) to the myelinated (post-laminar) segment of the human optic nerve.

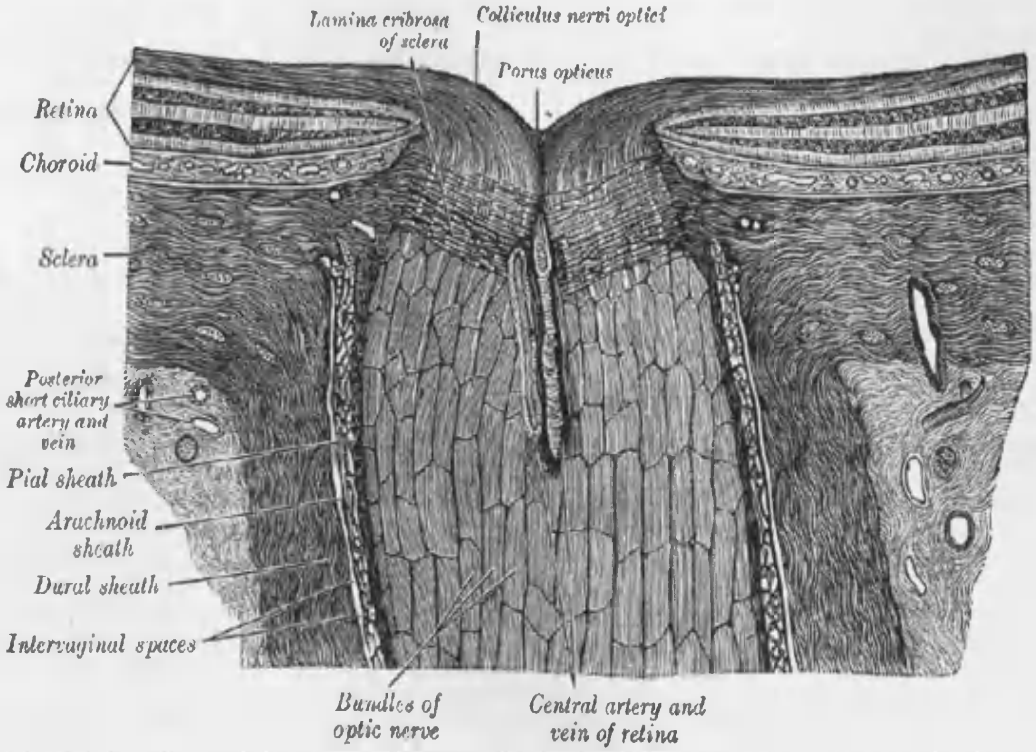

Figure 1.8. The terminal portion of the optic nerve and its entrance into the eyeball. [Henry Gray (1825–1861). Anatomy of the Human Body, 1918.]

The pre-laminar section has a much higher concentration of mitochondria to support the higher energy demands of unmyelinated nerve conduction and it is likely that active processes involving the cytoskeletal architecture are needed to maintain this sharp mitochondrial gradient [Bristow *et al*, 2002; Barron *et al*, 2004]. Pathological mechanisms which disrupt this unique structural feature would lead to impaired axonal transport and set up a vicious circle with fragmentation of the mitochondrial network at the lamina cribrosa, exacerbating even subtle mitochondrial energy deficits and eventually precipitating apoptotic cell death.

1.5.3.3 Spatial distribution of mitochondria along the optic nerve

At the ultrastructure level a high mitochondrial density level can be seen in the prelaminar NFL and a low density in the postlaminar region. This difference has previously been attributed to mechanical compression of RGC axons or a hold up of the axoplasmic flow of organelles at the lamina cribrosa [Hollander *et al*, 1995]. However, no reduction in axonal diameter has been found in the laminar region. A potential explanation for the hold up of axoplasmic flow is the small size of the P-cells in the PMB. The small size of axons in the PMB may impart anatomical constraints for the axoplasmic transport of mitochondria. Mitochondria are typically about 0.5*u*m – 1.0 *u*m across. Their biogenesis is carried out

within the RGC soma and they are replicated through organelle splitting and budding. Hence the RGCs must transport the mitochondria along their very long axons to distribute them along strategic, energy dependent locations in the optic nerve. These are mainly the unmyelinated portions of the axons within the eye (Fig 1.9.).

Myelination confers a great advantage for the cell since it allows saltatory conduction of action potentials that reduces the energy demand for the cell. The unmyelinated portion of the RGC axons has much slower conduction velocities and requires far greater energy to restore the electrical potential, as compared to the posterior myelinated portion of these same axons, which are energy and temporally efficient because of saltatory conduction [Waxman, 1978]. Recent studies of human retina and optic nerve specimens using electron microscopy and histochemical stains for the mitochondrial respiratory complexes, such as COX, elegantly showed an inverse relationship between the mitochondrial activities and myelination [Minckler *et al*, 1976; Andrews *et al*, 1999; Bristow *et al*, 2002].

These findings indicated an asymmetric distribution of mitochondria along the RGC axons that matches the energy and functional requirements of the axons related to their state of myelination (Fig 1.9.). Some particular areas that require high concentrations of mitochondria are the gap junctions; the prelaminar and laminar regions of the optic nerve head (where mechanical and hydrostatic factors come into play); under the nodes of Ranvier in the post-laminar portion of the optic nerve (where most of the sodium/potassium pump work occurs); and finally the synaptic terminals (Fig 1.9.).

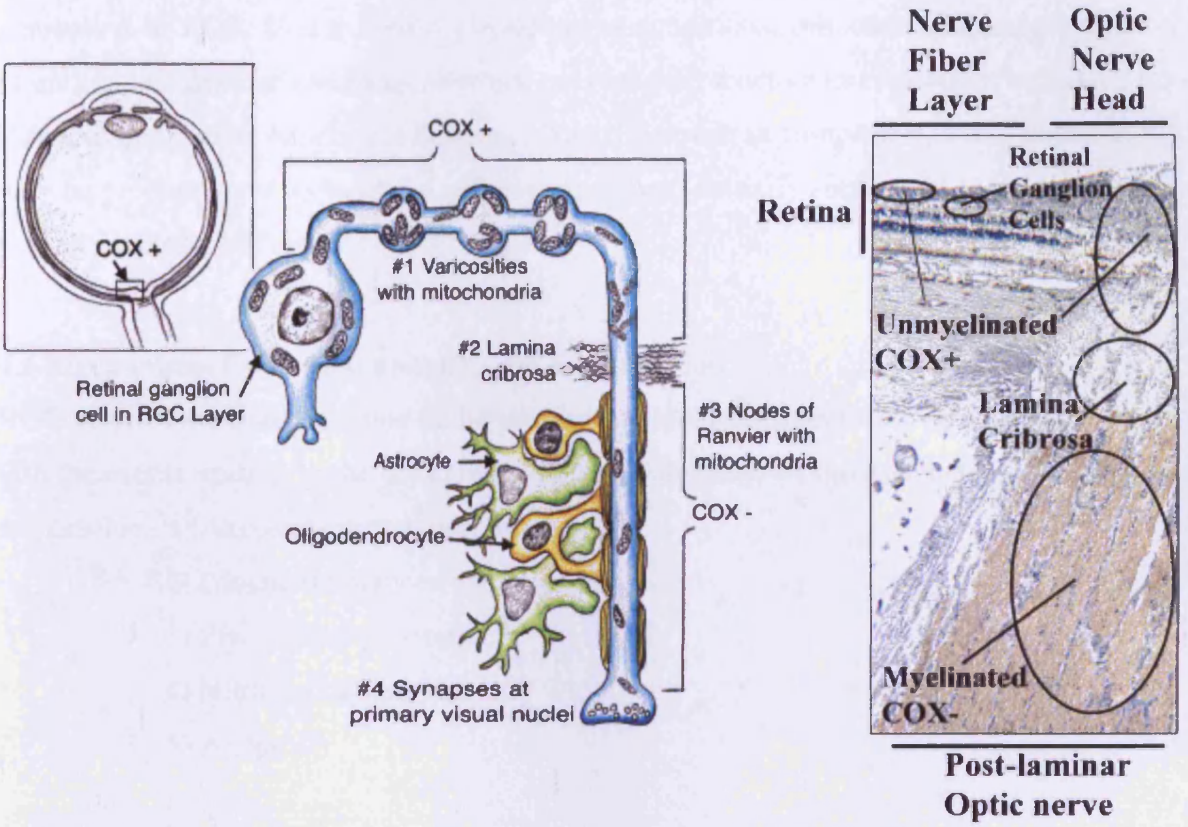

Figure 1.9. The retinal ganglion cell system. Diagrammatic view of pattern for staining of COX. On the left side is a sagittal view of the human eye. The boxed part is enlarged and schematically illustrated, with emphasis on the RGC cellular system. Mitochondrial distribution is shown from the RGC somata through the unmyelinated (COX+) portion of the axon in the nerve fibre layer (NFL), NFL and penetrating the lamina cribrosa at the optic nerve head. Mitochondrial accumulations are represented within the varicosities within the NFL, and in the prelaminar region. There is a drastic decrease in mitochondrial numbers within the postlaminar portion (COX-). Mitochondria, in this part of the RGC axon, are mostly located under the unmyelinated nodes of Ranvier. On the right side is illustrated a histological sagittal section of a normal human eye showing a parallel transition from the retina to the optic nerve head, the lamina cribrosa and a portion of the myelinated postlaminar optic nerve. The ocular tissue was stained by a method using immunoperoxidase for myelin basic protein [Carelli, 2004].

1.5.3.4 Light exposure

RGCs are unusual in that they are the only portion of the CNS exposed to light. It has been suggested that light, particularly blue light, has a detrimental influence on mitochondria which already exist in a compromised energetic state [Osbourne *et al*, 2006] but not on mitochondria in healthy ganglion cells. Ganglion cell mitochondria are particularly prevalent in the non-myelinated intraocular portions of the axon when compared with the myelinated extraocular regions [Bristow *et al*, 2002; Barron *et al*, 2004; Carelli *et al*, 2004] and these intraocular portions are unprotected from light (400–760 nm) impinging onto the retina. Light can be absorbed by mitochondrial enzymes such as cytochrome and flavin oxidases causing the

generation of ROS. Under normal physiological conditions, mitochondria possess a number of antioxidant defence mechanisms which prevent such reactive intermediates becoming toxic [Lin and Beal, 2006; Morin and Nicolas, 2006]. However, in compromised mitochondria ROS may be produced in excess of the cellular capacity to detoxify such species and this can then lead to apoptotic cell death.

1.6 Mechanisms for retinal ganglion cell degeneration

RGC death is the final common pathway of virtually all diseases of the optic nerve. Research into the events leading to the death of RGCs has delineated several mechanisms that might be responsible. 1) Axoplasmic transport block

2) Glutamate induced excitotoxicity

3) Free radical generation

4) Nitric oxide neurotoxicity

5) Apoptosis

1.6.1 Axoplasmic transport block

An axons length can be 1,000 or 10,000 times the diameter of the cell body but no protein synthesis takes place in the axon. Only the cell body and proximal dendrites contain ribosomes, the protein manufacturing organelles. Therefore, mitochondria, lipids, synaptic vesicles, proteins and other cell parts are constantly transported from the cell body down the length of the axon to maintain normal axonal function. Transport of molecular inclusions and organelles within axons occurs both away from the cell body (anterograde direction) and towards the cell body (retrograde direction) by processes that require energy, microtubules and certain protein motors.

The energy for axonal transport is generated by mitochondrial OXPHOS. Mitochondria are transported bi-directionally (antero-retrograde) with the 'fast component' of the axonal transport [Grafstein, 1995; Hollenbeck, 1996]. Their 'saltatory' movements are based on motor proteins. Essentially, the microtubule based motility is supported by kinesin for anterograde transport and by dynein for retrograde. Moreover, mitochondria can also use actin microfilaments which represent, most likely, an auxillary system involved in local transport [Grafstein, 1995; Hollenbeck, 1996]. Both kinesin and dynein present an ATPase activity that is activated by microtubule binding.

The hypothesis holds that mammalian neuronal growth and maintenance depends upon the viability of this axoplasmic flow. It is therefore conceivable that any energy depletion due to mitochondrial dysfunction has the potential of affecting axonal transport, including that of mitochondrial transport itself (Fig 1.10.).

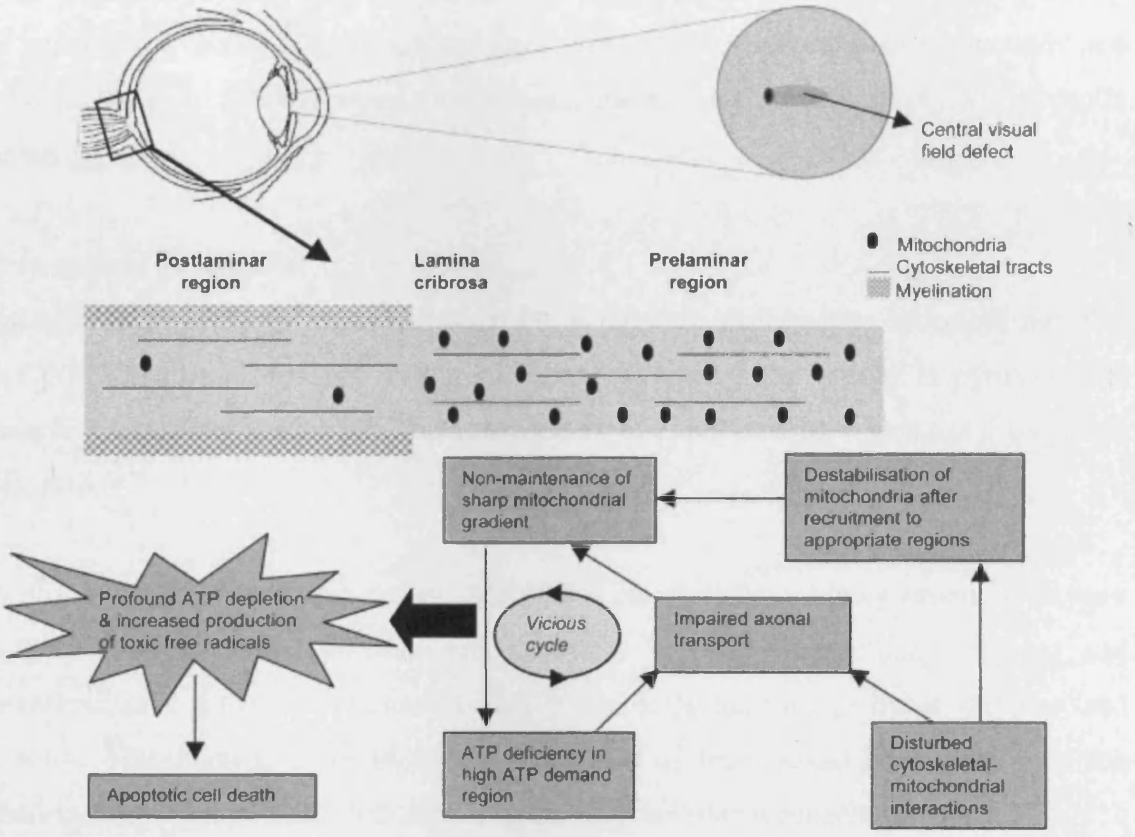

Figure 1.10. Schematic flow diagram showing the mechanisms that would result into the non-maintenance of the sharp mitochondrial gradient at the optic nerve head and how this constitutes the first step in a vicious cycle of events that would eventually lead to apoptotic cell death [Yu–Wai-Man *et al*, 2005].

1.6.2 Glutamate induced excitotoxicity

Glutamate is the main fast excitatory neurotransmitter in the mammalian nervous system and is present in very high concentrations. At chemical synapses, glutamate is stored in vesicles. Nerve impulses trigger release of glutamate from the presynaptic cell, glutamate receptors, such as the *N*-methyl *D*-aspartate (NMDA) receptor bind glutamate and are activated. Because of its role in synaptic plasticity it is believed that glutamic acid is involved in cognitive functions like learning and memory in the brain.

Glutamate induced excitotoxicity occurs when extracellular glutamate levels are increased either due to increased release or decreased uptake from the synapse. High glutamate

concentrations activate several types of cell receptors, including MNDA receptors that can allow entry of excessive amounts of calcium leading to neuronal damage and eventual cell death by inappropriate activation of complex cascades of nucleases, proteases and lipases. They directly attack cell constituents including the mitochondria and this leads to the generation of highly reactive free radicals and activation of the nitric oxide (NO) pathway [Naskar and Dreyer, 2001]. The resulting interaction between intermediate compounds and free radicals leads to DNA nitrosylation, fragmentation and activation of the apoptotic programme.

1.6.3 Free radical generation

Free radicals are not only generated through the activation of glutamate receptors but also through OXPHOS, the process by which mitochondria capture the energy in pyruvate and fatty acids (FA) and store it as ATP. This is especially true in the retina which has a very high metabolic rate.

A small proportion of oxygen that enters OXPHOS is converted to toxic by-products, oxygen radicals (free radicals). Most of these are detoxified by protective cellular enzymes and vitamin antioxidants. If they are not neutralized, free radicals can damage lipids, proteins, and nucleic acids. This damage is more severe at the site of free radical generation, i.e., the mitochondria. Mitochondria are deficient in protective cellular mechanisms, most of which reside in the cytosol. OXPHOS dysfunction increases free radical production. This creates a vicious cycle which increases mitochondrial DNA damage and causes more OXPHOS dysfunction and more free radical generation. Cellular damage in mitochondrial disorders is due to free radicals and energy deficiency. Both these factors can also trigger necrosis and apoptosis.

1.6.4 Nitric oxide neurotoxicity

Another important activated enzyme is nitric oxide synthase, which catalyses the production of NO from L-arginine. NO synthase is an enzyme in the body that contributes to transmission from one neuron to another, to the immune system and to dilating blood vessels. It does so by synthesis of NO from the terminal nitrogen atom of arginine in the presence of NADPH and dioxygen (O_2). NO is found through out the body and is particularly abundant in the central and peripheral nervous system. NO mediates a diverse range of physiological functions associated with neurons. Studies have also identified skeletal muscle as a major

source of NO in the body [Kobzik *et al* 1994] where NO regulates both metabolism and muscle contractility.

NO neurotoxicity occurs through the reaction of NO with superoxide anion to form peroxynitrite and other more reactive free radical species. Peroxynitrite is extremely toxic and acts by S-nitrosylating both proteins and nucleic acids, thus destroying them. NO can also have a profound effect on mitochondria inhibiting mitochondrial respiration, which in turn would create more free radicals and cause additional membrane depolarization. It has been reported by Barsoum *et al*, [2006] that mitochondria undergo fission in response to NO in cortical neurons of primary cultures. This fission by NO occurs long before any neurite injury or neuronal cell death is observed. Furthermore, fission is accompanied by ultrastructural damage of mitochondria, autophagy, ATP decline and generation of free radicals. The NO–initiated neurotoxic cascades are important components of the mechanism of cell death in many neurodegenerative disorders [Christopherson *et al*, 1997].

1.6.5 Apoptosis

There are two morphologically distinct types of cell death- necrosis and apoptosis (Table 1.3.).

Apoptosis	Necrosis
Morphologic Criteria	
Membrane blebbing	Loss of membrane integrity
Cell shrinkage and formation of apoptotic bodies	Cell swelling and lysis
Lack of inflammatory response	Significant inflammatory response
Lysosomal preservation	Lysosomal leakage
Biochemical Criteria	
Induction by physiological stimuli	Induction of non-physiological disturbances
Energy requirement	Lack of energy requirement
Macromolecular synthesis requirement	Lack of macromolecular synthesis requirement
De novo gene transcription	Lack of *de novo* gene transcription
Nonrandom fragmentation of DNA	Random digestion of DNA

Table 1.3. Both morphologic and biochemical characteristics are distinctive between apoptotic and necrotic cells.

Necrosis is classically marked by cellular swelling, disruption of organelle and plasma membranes, random DNA fragmentation, and uncontrolled release of cellular constituents into extra-cellular space usually resulting in inflammation. The process of apoptosis which is a process rather than an event is characterised by an orderly pattern of inter-nucleosomal DNA fragmentation, chromosome clumping, cell shrinkage and membrane blebbing [Kaushik, 2003]. This is followed by disassembly of cells into multiple membrane-enclosed vesicles that are engulfed by neighbouring cells without inciting inflammation.

All animal cells are programmed for carrying out self-destruction when they are not needed, or when damaged. It has been labelled a programmed cell death, or cell suicide. It is not unique to RGCs alone. Under either physiological or pathological conditions, apoptosis is driven by interactions among several families of protein i.e., caspases, Bcl-2 family proteins, and inhibitor of apoptosis proteins (IAP). Other proteases such as granzyme B, calpain and cathepsin have also been demonstrated to play a vital role in apoptosis occurring under certain physiological states.

Apoptosis occurs via two main signalling pathways (Fig 1.11.) the extrinsic (death receptor) pathway or intrinsic (mitochondrial) pathway. The extrinsic pathways involve the delivery of Granzyme B through perforin to the cells as well as receptor ligation that triggers caspase-8 activation. In the intrinsic pathways, caspase-9 is activated following release of mitochondrial components to form the Apaf complex. Some forms of intracellular stress can also induce the activation of caspase-12. Both the extrinsic and intrinsic pathways converge on the activation of caspase-3 or caspase-7. IAPs can suppress these pathways either by blocking the activation of caspase-9 or by directly inhibiting caspase-3 activity.

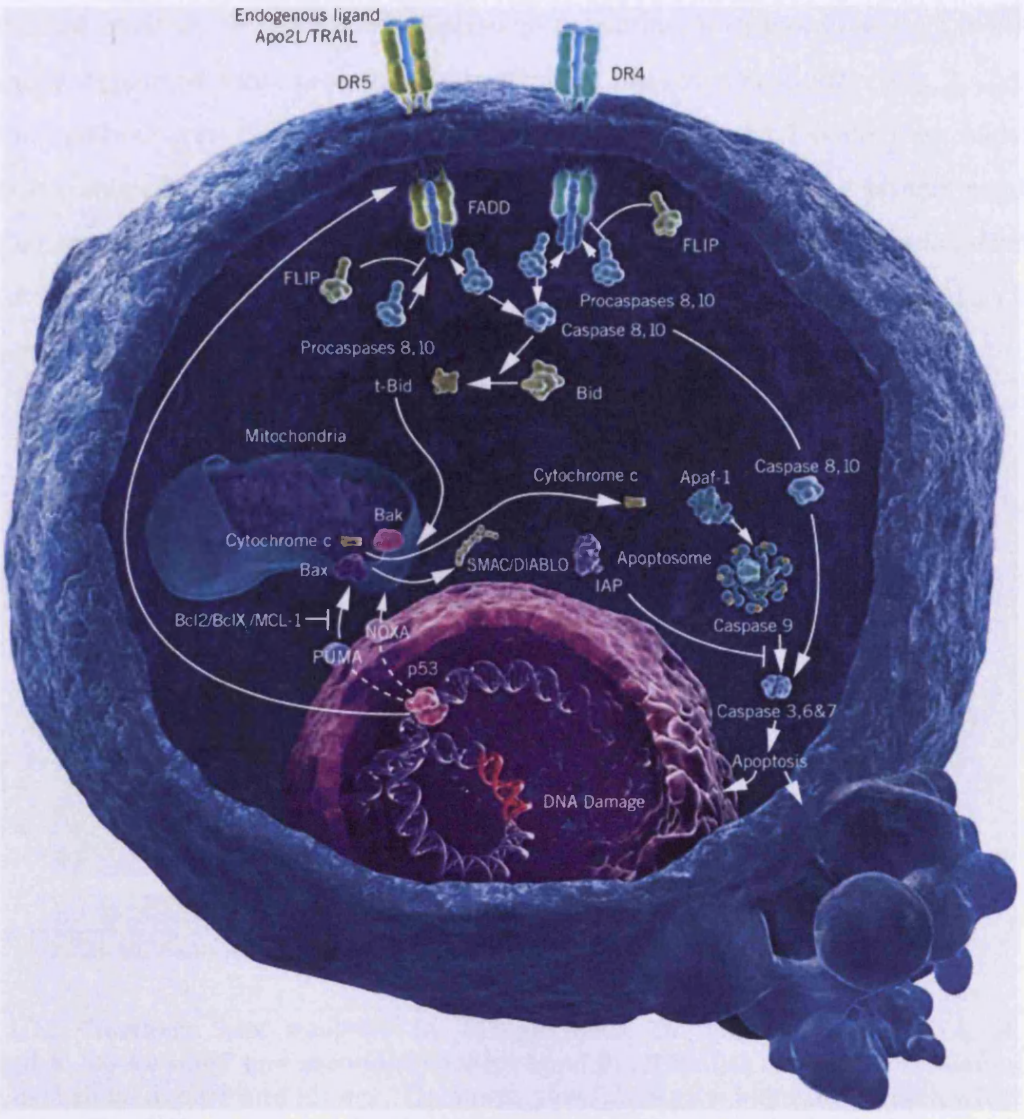

Figure 1.11. Schematic diagram showing the major apoptotic signalling pathways. [http://www.biooncology.com/pipeline/apoptosis/index.html – accessed 10.6.10]

1.7 The Human homologue *OPA3*

Linkage analysis, undertaken by Nystuen *et al*, in [1997] in MGA-III affected families, originating from inbred Iraqi Jewish populations, allowed the mapping of the causative gene (*OPA3*) to chromosome 19q13.2-13.3. Anikster *et al*, [2001] sought candidate genes within the minimal disease region [D19S412-D19S918, Nystuen *et al*, 1997]. They sequenced four genes and identified an intronic G-to-C mutation of a gene, designated *OPA3,* corresponding to complementary DNA (cDNA) clone FLJ22187 which segregated with the MGA-III phenotype. The patients exhibited a homozygous intronic G-to-C (-1 position of intron 1 in the 3′ (acceptor) splice site) change that abolished messenger ribonucleic acid (mRNA) expression in fibroblasts from affected patients.

Northern blot analysis demonstrated a primary transcript of approximately 5.0 kb that is ubiquitously expressed most prominently in skeletal muscle and kidney (Fig 1.12.). In the brain, the cerebral cortex, the medulla, the cerebellum, and the frontal lobe had slightly increased expression compared to other parts [Ankister *et al*, 2001]. The protein product is a 20 kiloDalton (kD) peptide which is predicted to contain an N-terminal mitochondrial leader sequence (aa 1-18) followed by a sorting/cleavage signal (the peptide, NRIKE, at aa residues 25-29) and a C-terminal peroxisomal targeting signal.

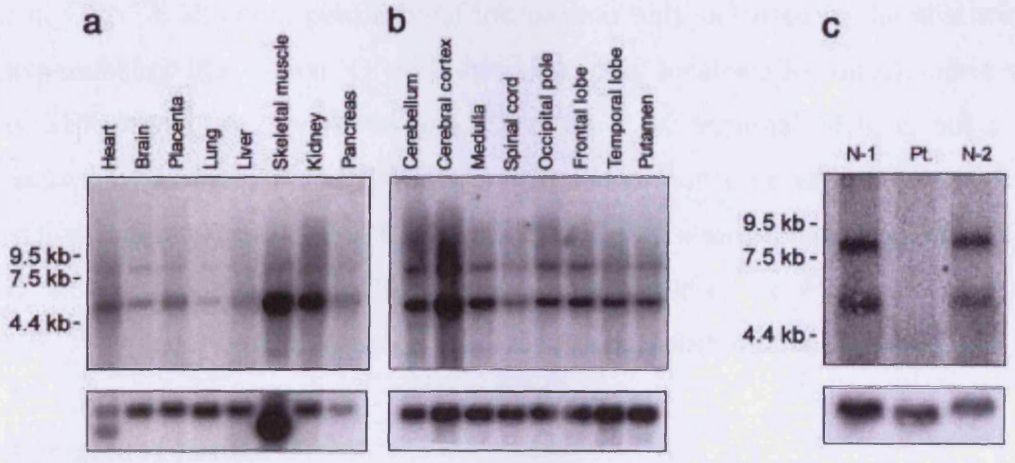

Figure 1.12. Northern blot analyses by 619-bp probe to human *OPA3* cDNA. *A*, Probe hybridised to 5.0-kb band and secondary 8.0-kb band in all tissues tested. Expression appeared greatest in skeletal muscle and kidney. The lower panel shows the band for β-actin, which served as a control for RNA loading. *B*, Same bands on human multiple-tissue northern blot, demonstrating expression in all parts of brain. *C*, 5.0-kb and 8.0-kb bands of RNA from normal fibroblasts (N-1 and N-2), which hybridised with *OPA3*-cDNA probe, whereas no bands appeared on use of RNA from fibroblasts from one Iraqi Jewish patient [Ankister *et al*, 2001].

At present the mitochondrial location of OPA3 is debatable. Proteomic profiling of IMM proteins extracted by alkali treatment [Da Cruz *et al*, 2003] and sequence analysis [Ankister *et al*, 2001; Reynier *et al*, 2004] suggest that OPA3 is localised to the IMM. However, Ryu *et al*, [2010] using subcellular fractionation suggests that OPA3 is localised to the OMM.

At the beginning of this thesis *OPA3* was described as a 2 exon gene consisting of a 5′ untranslated region (UTR), an open reading frame (ORF) encoding 179 aa, and >970 nucleotides of 3′ UTR sequence which spans approximately 57 kilobases (kb) on human chromosome 19q13.2-q13.3 [Anikster *et al*, 2001]. Recently however, *OPA*3 has been shown

to consist of 3 exons and is expressed in two transcripts [Huizing *et al*, 2010]. In human, both transcripts show ubiquitous expression, with transcript of OPA3A (exons 1-2) showing lower expression in the brain and transcript of OPA3B (exons1-3) showing higher expression in the testis. Huizing *et al*, [2010] also performed localisation studies of the two transcripts in normal fibroblasts. Green fluorescent protein (GFP) was fused to either the C-terminus (OPA3A-GFP, leaving the putative mitochondrial signal free), or the N-terminus (GFP-OPA3, leaving the potential peroxisomal signal free). OPA3A-GFP localised only to the mitochondria. With expression of GFP-OPA3 mitochondrial localisation was lost and GFP co-localized with a peroxisomal marker. This confirms a functional peroxisomal sorting signal in OPA3A although peroxisomal localisation only occurred in the absence of the N-terminal mitochondrial signal. OPA3B however, only localised to mitochondria whether or not its SEK signal was available indicating that its C-terminal SEK is not a functional peroxisomal targeting signal. NRIKE was also shown not to be essential for mitochondrial localisation [Huizing *et al*, 2010; Ryu *et al*, 2010]. With a mutated/deleted NRIKE signal the protein still predominantly localised to the mitochondria. It was only with the leader sequence disrupted as well that a more diffuse cellular distribution was seen.

1.7.1 Function of human *OPA3*

Whilst the function of the protein remains unknown, there are several lines of evidence that support mitochondrial function. Firstly, most primary optic atrophies are caused by mitochondrial defects [Carelli, 2004]. Secondly, most of the other MGA syndromes i.e., MGA-I and MGA-II and MGA-V are known to be associated with mitochondrial defects. Also the presence of MGA in the urine itself suggests mitochondrial involvement. Increased MGA is a common finding in many mitochondrial respiratory disorders [Gibson *et al*, 1993; Ibel *et al*, 1993].

Recent experiments in cell lines [Ryu *et al*, 2010] showed that OPA3 affects mitochondrial morphology. HeLa cells transfected with C-terminally myc-tagged OPA3 showed that overexpression of wildtype OPA3 lead to extensive ring-like fragmentation. This ring-like morphology was also seen in cells transfected with patient mutant OPA3 (G93S)-YFP. Abnormal mitochondrial morphology was also seen in HeLa cells knockdown for endogenous OPA3 using siRNA, these cells had more elongated and tubular mitochondria. This fragmentation was shown to be caused by OPA3 residues 83-102 as deletion of these residues

resulted in no morphological changes to the mitochondria. This was thought to be due to the failure of OPA3 with deleted 83-102 residues to localise to the OMM.

Ryu *et al*, [2010] also examined cells for increased sensitivity to apoptosis as altered mitochondrial morphology is closely related to apoptotic sensitivity [Youle and Karbowski, 2005]. Cells with fragmented mitochondria attributable to overexpression of wildtype OPA3 showed normal cytochrome c distribution indicating that OPA3 overexpression alone is not sufficient to induce spontaneous apoptotic cell death. However, treatment with staurosporine significantly increased the redistribution of cytochrome c from the mitochondria to the cystol in cells with OPA3-YFP compared to cells with mito-YFP showing that induced mitochondrial fragmentation augments the sensitivity to staurosporine induced apoptosis. In cells transfected with patient mutant OPA3 (G93S) cytochrome c appeared in the cytosol in the absence of external apoptotic stimuli. Reynier *et al*, [2004] also saw increased susceptibility to staurosporine induced apoptosis in fibroblasts from ADOAC patients harbouring the OPA3 mutation (G93S). However, the fibroblasts showed no abnormalities in the organisation of the mitochondrial network or in the respiratory chain or in the mitochondrial membrane potential. Contradictory to the Reynier *et al*, [2004] results, Chevrollier *et al*, [2008] showed that fibroblasts of ADOAC patients had enhanced complex V activity and reduced cytochrome c oxidase (COX) activity. However, this reduction in COX activity is unlikely to be the cause of the mitochondrial defect as respiratory chain activity was readily stimulated by adenosine diphosphate (ADP) indicating that COX activity is not the rate limiting step. Overall, the fibroblasts showed normal mitochondrial ATP production but with reduced efficiency of ATP synthesis. Wanders *et al*, [1992] also showed a reduced efficiency in ATP synthesis in digitonin-permeabilised fibroblasts of MGA-III patients. Cells exhibited a 50 % reduction in adenosine-5'-triphosphate (ATP) production and a four-fold increase in lactate:pyruvate ratio [Wanders *et al*, 1992] both of which are indicators of impaired mitochondrial function. Recently, a zebrafish model of MGA-III with a null allele of *opa3* [Pie *et al*, 2010], demonstrated normal mitochondrial oxidative phosphorylation (OXPHOS), but increased sensitivity to inhibitors of the electron transport chain. Expression of *OPA3* mRNA is also very high in tissues of high ATP production such as the cerebral cortex.

Overall, the evidence so far suggests that OPA3 is localised to the mitochondria with mutations causing disturbances in mitochondrial dynamics, respiratory chain activity and an increased sensitivity to apoptosis

1.7.2 Mutations of the human *OPA3* gene

Mutations in *OPA3* can cause diseases with recessive as well as dominant modes of inheritance. All cases of MGA-III described to date have been caused by homozygous mutations which are predicted to abolish all protein activity. In ADOAC only one copy of *OPA3* needs to carry a missense change, which probably exhibits a dominant negative effect but manifests as a milder phenotype. Seven mutations of *OPA3* have been reported so far (Table 1.4.)

Sequence change	Protein change	Clinical designation	Mode of inheritance	Comments	Reference
IVS1–1G>C		MGA-III	Recessive	Allele frequency of 10% in Iraqi Jews.	Anikster *et al*, 2001
c.320-337del	p.Q108-E113del	MGA-III	Recessive	Reported in a boy born of consanguineous Kurdish Turkish parents.	Kleta *et al*, 2002
c.277G>A	p.G93S	ADOAC	Dominant		Reynier *et al*, 2004
c.313C>G	p.Q105E	ADOAC	Dominant		Reynier *et al*, 2004
c.–38A>G		MGA-III	Aetiology uncertain	Found in a heterozygous state, functional significance unknown.	Neas *et al*, 2005
c.231T>C		Silent polymorphism	N/A	Allele frequency in normal population 61%.	Neas *et al*, 2005
c.415C>T	p.Q139X	MGA-III	Recessive		Ho *et al*, 2008
Abbreviations: N/A= not applicable, del= deletion.					

Table 1.4. Mutations reported in the *OPA3* gene.

1. MGA III- IVS1-1G-C mutation

Anikster *et al*, [2001] identified the acceptor splice site mutation, IVS1-1G-C, a homozygous G-C change at -1 position of *OPA3* intron 1 in the 3' acceptor splice site resulting in the obliteration of the intron 1 splice site. This mutation abolishes mRNA expression in fibroblasts in several Iraqi Jewish patients and accounts for 100% of disease-causing alleles in the Iraqi Jewish population.

2. MGA III- 320-337 deletion

Kleta *et al*, [2002] reported a novel mutation in *OPA3* in a Kurdish–Turkish patient with optic atrophy and 3-methylglutaconic and 3-methylglutaric aciduria previously carrying a diagnosis of MGA-IV. Sequencing revealed an in-frame deletion of 18 bp at positions 320-337 in exon 2 resulting in the deletion of the 6 aa between residues 108 and 113 i.e., QRHKEE. This was the first mutation found in an individual of non-Iraqi Jewish origin.

3. ADOAC- 227G>A mutation

In affected members of a French family with ADOAC first described by Garcin *et al*, [1961], Reynier *et al*, [2004] identified a heterozygous 277G-A transition in exon 2 of the *OPA3* gene, resulting in a gly93-to-ser (G93S) substitution.

4. ADOAC- 313C>G mutation

In affected members of a family with ADOAC, Reynier *et al*, [2004] identified a heterozygous 313C-G transversion in exon 2 of the *OPA3* gene, resulting in a gln105-to-glu (Q105E) substitution.

5. MGA III- c.–38A>G

Neas *et al*, [2005] screened 13 patients with neurological abnormalities and MGA for mutations in the *OPA3* gene. In a single patient a sequence variation in the 5' UTR was identified c.–38A>G. The significance of the 5' UTR sequence variation remains open to speculation.

6. MGA III- c.231T>C

Neas *et al*, [2005] also detected the sequence variation c.231T>C in 12 out of the 13 patients. This is a silent polymorphism and therefore does not appear to have any pathological significance.

7. MGA III- c.415C>T

This was a nonsense mutation, found in the homozygous state in an individual of Indian origin with MGA-III. It is the second mutation found to date in an individual of non-Iraqi Jewish origin [Ho *et al*, 2008].

In 2009, 980 patients were screened for suspected hereditary optic neuropathies [Ferre *et al*, 2009]. The entire coding sequence of *OPA3* was screened in 14 patients belonging to three unrelated families. They presented with bilateral optic atrophy and posterior cataract which was inherited as an autosomal dominant trait. Two mutations were found in exon 2: 227G>A and 313C>G both of which have been previously reported by Reynier *et al,* [2004]. Both mutations segregated with the disease and were absent in healthy relatives and 400 control chromosomes.

At present the limited number of mutations found does not permit any genotype-phenotype correlations. Even in the Iraqi Jewish population which all have the same mutation there is variability in the phenotype, sometimes within the same family.

1.8 Hypotheses

1) That *OPA3* is an important gene and its characterization will help us better understand retinal development and ganglion cell survival.
2) That RGCs die through compromised mitochondrial function which initiates cell death either by apoptotic or non-apoptotic signalling.
3) Its normal function is important for the health of organs with high energy requirements.
4) Peroxisomal dysfunction plays a role in the disease phenotype.
5) That the $Opa3^{L122P}$ mouse mutant will be a clinically relevant model of MGA-III.

1.9 Mouse model of *Opa3*

This thesis made use of an *N*-ethyl-*N*-nitrosourea (ENU) induced point mutation in the murine *Opa3* gene creating the first model of the human disorder MGA-III. The pathophysiology of the mouse model was assessed using a range of visual, neurological, behavioural and metabolic tests. Findings were compared with those from clinical studies of patients with an MGA-III/ADOAC disease in the hope of producing a clinically relevant model.

CHAPTER

II

General Materials and Methods

2.1 DNA preparation and purification

2.1.1 Sample preparation

Genomic DNA was prepared from tail biopsy and tissue samples using two different methods depending on the experimental procedure.

For genotyping of mice from tail biopsies a DirectPCR lysis reagent (Viagen) was used. This is a quick and crude DNA preparation method. Genomic DNA was isolated from biopsy of mouse tail tissue in 200µl of Viagen lysis solution containing 2mg/ml of Proteinase K. This was incubated at 55°C for 5-6 hrs followed by 45 mins in a water bath at 85°C to inactivate the Proteinase K. Samples were then spun down to minimise uptake of debris into PCR preparation.

For PCR or sequencing where a pure DNA sample was required the Wizard SV genomic purification kit was used. The tail biopsy or tissue sample was added to the Digestion Solution Master Mix made up as follows:- 200µl nuclei lysis solution, 50µl 0.5M EDTA, 20µl of 20mg/ml Proteinase K and 5µl of 4mg/ml RNase A solution. This was incubated for 16-18 hrs in a 55°C oven. Then 250µl of SV lysis buffer was added and vortexed.

2.1.2 Purification of genomic DNA from lysate using microcentrifuge

While the lysate was still warm it was transferred to a minicolumn assembly and then centrifuged at 13,000g for 3 mins. The liquid in the collection tube was discarded and 650µl of SV wash solution was added to the minicolumn and centrifuged at 13,000g for 1 min. This step was repeated four times. After which the minicolumn was centrifuged at 13,000g for 1 min with no solution in it to dry out the binding matrix. The minicolumn was then placed in a new collection tube. 250µl of room temperature nuclease free water was added and incubated at room temperature for 2 mins. The minicolumn was then centrifuged at 13,000g for 1 min. The eluted water contains the DNA. For a more concentrated solution of DNA the eluted water can be put back into the minicolumn and centrifuged again.

2.2 RNA isolation

Heart, muscle, brain, kidney, liver and eye tissue of wildtype *Opa3* animals were collected in RNALater.

2.2.1 RNA purification and quantification

Total RNA was purified using an RNeasy Mini Kit (Qiagen). As the tissue was stabilised in RNALater it can be cut up for homogenisation at room temperature. RNA is very unstable so frozen samples should not be allowed to thaw and fresh samples should be homogenised immediately. The tissue was disrupted and homogenised in 600µl of RLT buffer using a rotor-stator homogeniser until it was uniformly homogenised. The lysate was then centrifuged for 3 mins at full speed. The supernatant was removed and transferred to a new microcentrifuge tube. It is this supernatant that is used in all subsequent steps. To this supernatant one volume of 70% ethanol was added and was immediately mixed by pipetting. 700µl of the sample was then added to an RNeasy spin column and placed in a 2ml collection tube. This was then centrifuged for 15 secs at 10,000 revolutions per minute (rpm). The flow through was discarded and 700µl of RWI buffer was added to the RNeasy spin column. The column was then spun again for 15 secs at 10,000 rpm and the flow through discarded. After which 500µl of RPE buffer was added to the spin column and centrifuged for 15 secs at 10,000 rpm to wash the spin column membrane. This was repeated with the RPE buffer but centrifuged for 2 mins. The spin column was then placed in a new centrifuge tube and centrifuged for 1 min on full speed. This step eliminates the carry-over of any residual RPE buffer. The spin column was then placed in a new centrifuge tube and 50µl of RNase free water was added and this was centrifuged for 1 min at 10,000 rpm to elute the RNA. The sample can then be stored at -20°C short term or -80°C long term.

RNA was quantified using the Picodrop spectrophotometer (Picodrop, UK).

2.3 cDNA synthesis (reverse transcription)

cDNA was synthesised from 0.5µg total RNA using Qiagen's Quantitect Reverse Transcription Kit. This kit is an RT-PCR method for efficient reverse transcription and removal of genomic DNA. A detailed protocol can be found in the instructions with the kit. So, briefly, while the tube of RNA template thawed on ice, the Genomic DNA Elimination Reaction Components were mixed in a tube comprising of (Table 2.1.).

Component	Volume/reaction	Final concentration
gDNA wipeout buffer 7X	2 µl	1x
Template RNA	Variable (up to 1µg)	
RNase free water	Variable	
TOTAL VOLUME	**14µl**	

Table 2.1. Genomic DNA elimination reaction components.

This solution was incubated for 7 mins at 42°C then placed immediately on ice. During this incubation a reverse transcription master mix was prepared on ice (Table 2.2.).

Reverse transcription master mix	Volume/reaction	Final concentration
Quantiscript reverse transcriptase	1µl	
Quantiscript TR buffer 5x	4µl	1x
RT Primer mix	1µl	
Entire genomic DNA elimination reaction	14µl	
TOTAL VOLUME	**20µl**	

Table 2.2. Reverse transcription reaction components.

This solution was incubated for 30 mins at 42°C then for a further 3 mins at 95°C to inactivate the Quantiscript reverse transcriptase. The solution can then be stored at -20°C and used for PCR.

2.4 Agarose gel electrophoresis

Agarose gel electrophoresis was the method selected for the visualisation of the PCR products. The 2% gel was prepared by dissolving 3g of agarose (molecular biology grade, Sigma) in 150 mls of 1x TBE buffer. Agarose solution was heated in a microwave for 2-3 mins until the agarose was completely dissolved. Then 5µl ethidium bromide solution (10mg/ml) was added to the agarose. The solution with ethidium bromide was poured into a casting tray with a comb to form wells. After a 40 min delay for the gel to solidify, 20µl of PCR product was loaded into each well. DNA hyperladder IV (Bioline) was used for estimation of band sizes.

The gel was electrophoresed at 120V until adequate separation of the bands. The gel was visualised on a UV transilluminator (UVP, England) and the image of the gel was captured with BioDoc-It and visiDoc-It system (UVP, England) equipped with a thermal printer (Sony, Japan).

2.5 Tissue fixation for wax embedding

Tissue fixation and subsequent wax embedding are routinely used techniques of histology procedures for morphological studies. The purpose of the fixation is to preserve the structure and components of the tissue. Two different length protocols were used for the fixation of tissues for embedding in wax depending on the tissue type. All tissues were processed for the xylene embedding wax method.

After dissection, tissues from all mice ages were fixed in a solution of 4% PFA pH 7.4 (Sigma, Germany) for 24 hrs at 4°C. Tissues were then washed twice in PBS for 30 mins, placed in a new tube with fresh PBS and left overnight at 4°C. The following day they were processed by one of the two protocols below.

2.5.1 Fixation of eyes for wax embedding

A longer fixation protocol was used for eyes as the lenses were not removed for sectioning. If the lens is not fixed sufficiently it can move in the block and cannot be sectioned properly. However, if the lens is fixed for too long it will shatter spreading debris over the slide. This is preferable to being under-fixed.

The first step in the process is dehydration. This process is carried out using a series of increasing grades of ethanol (Fisher solutions, UK). Eyes were first soaked in 50% ethanol solution for 30 mins, then 70% ethanol for 1hr, 90% ethanol for 2 hrs (twice) then 90% for another hr. Finally, in 100% ethanol for 2 hrs and again in 100% ethanol for one more hr.

Once the eyes are dehydrated it is important to carry out a clearing step. The eyes were put in a new glass vial and soaked for 15 mins in a solution of 50% xylene/50% ethanol. The solution was then changed and the eyes were left in 50% xylene/50% ethanol overnight. Eyes were then soaked in 100% xylene for 1 hr (twice). After the clearing step, the excess of xylene was removed and the eyes were put in warm wax in glass vials in a histology oven at 56°C. After 2

hrs the wax was removed and new wax was added to the eyes for another 2 hrs. The eyes were then collected, orientated in a plastic mould and embedded in new wax. The samples in the mould with the wax were left for 30 mins on a -12°C cold plate to solidify then stored at 4°C. Blocks were sectioned at 7μm in a Microm microtome (Microm, Germany) using a sharp blade (Nakura systems, Japan).

2.5.2 Fixation of other tissues for wax embedding

For the lung, skeletal muscle, heart, liver and kidney the same protocol was used, except the dehydration step was shorter. The tissues were first soaked in 50% ethanol solution for 30 mins, then 70% ethanol for 1hr, 90% ethanol for 1hr (twice), then 100% ethanol for 1hr (twice). The samples then continued with the clearing step as in the protocol for the eyes.

2.6 Frozen tissues for cryostat sectioning

Fresh tissue samples were collected and cut to an appropriate size and orientation. A small cup was made out of foil (just big enough to hold the tissue and be filled with OCT). Then the tissue was placed in the OCT. A cold-resistant plastic beaker was filled with iso-pentane. The foil cup was placed in the beaker containing iso-pentane and then the beaker was placed into liquid nitrogen. When the OCT had solidified the foil cup was removed from the iso-pentane and placed in liquid nitrogen. Samples were stored at -80°C.

2.7 Histology

Histochemistry is the science that uses different chemistry on cells or tissues to show and identify their microscopic structure. The basic nature of histology slide staining is to stain with two or more contrasting dyes that will highlight specific areas or entities with one colour, and leave a counterstaining background colour.

All histologically stained sections were observed via bright field microscopy using Leica DMRA2 microscope (Leica, Germany).

2.7.1 Haematoxylin and eosin

The most routine stain used is the haematoxylin and eosin (H&E) stain. The H&E stain uses two separate dyes, haematoxylin is a dark purplish dye that will stain the chromatin (nuclear material) within the nucleus, leaving it a deep purplish-blue colour. Eosin is an orange-pink to red dye that stains the cytoplasmic material including connective tissue, and leaves an orange-

pink counter stain. This counter stain acts as a sharp contrast to the purplish-blue nuclear stain of the nucleus, and helps identify other entities in the tissue such as cell membranes.

The process of performing the H&E stain is relatively simple. Slides were selected then taken through 2 changes of 100% xylene for 2 mins each and then put in decreasing concentrations of ethanol. Two washes were carried out in 100% ethanol for 1min each, then 1 min in 95% ethanol followed by 1 min in 70% ethanol. The slides were then washed under the tap for 1 min before being immersed in Harris's haematoxylin (BDH, England) for 2 mins. Harris haematoxylin stains everything on the slide and holds fast to the tissue when rinsed. Therefore, after staining and before using the eosin stain, it is necessary to rinse under the tap for 5 mins until the excess haematoxylin has been removed from everything except the nucleus.

After that the slides were stained in 1% eosin (Surgipath, UK) for 10 mins. The slides were then washed for 15 secs under the tap before running in a reverse manner through the ethanol series. 15 secs in 70% ethanol, 30 secs in 90% ethanol then two washes for 2 mins each in 100% ethanol and finally two washes in 100% xylene for 2 mins each for clearing. The slides were mounted with D.P.X permanent medium for microscopy (BDH, England).

2.7.2 Oil red-O stain

Oil red-O is a lysochrome (fat-soluble dye) diazo dye used for staining of neutral triglycerides and lipids on frozen sections and some lipoproteins on paraffin sections.

Unfixed frozen sections must first be fixed in 10% buffered formal saline for 5 mins. After which they are rinsed in water for 2 mins then rinsed in 60% isopropyl alcohol (prepared with distilled water) for a further 1 min. Slides are then stained for 10 mins with Oil red-O (Sigma-Aldrich) in an air tight container, then washed in 60% isopropyl alcohol for 30 secs. After which they are transferred to a water bath flat on the bench (no running water) for 5 mins. Slides are then counterstained with Mayer's haematoxylin solution for 5 secs and then washed in running water for 5 mins. The slides should then be kept in the water before mounting with an aqueous mounting medium.

Staining should show unsaturated hydrophobic lipids (i.e. triglycerides, cholesterol esters) in red, phospholipids in pink and the nuclei in blue.

2.7.3 Toluidine Blue stain

Toluidine Blue is a metachromatic dye used in staining bone and cartilage.

Bone sections were rinsed in 100% xylene twice for 2 mins, then through an alcohol series, of 100% alcohol for 2 mins (twice), 2 mins in 95% alcohol then 2 mins in 70% alcohol. Sections were then washed in running tap water until clear. Sections were then transferred into toluidine blue dye for 30 secs and again washed in running tap water until clear. They were then drained, blotted dry with filter paper and allowed to air dry for a few minutes. After which they were transferred into 100% xylene for 2 mins (twice) before being mounted under a coverslip using D.P.X mountant.

Staining should show Meta chromatic substances in red, pink or purple and nuclei and other components in blue.

2.8 Perfusion fixation

Transcardial perfusion under terminal anaesthesia is a method commonly used for tissue fixation in immunohistochemical localization protocols. This method takes advantage of the subjects circulatory system to deliver the fixative solution evenly throughout the body tissue, with optimal penetration of the brain. This is the optimal method of tissue preservation because the tissues are fixed before autolysis begins and are less susceptible to artefacts caused by handling. Fixation preserves the ultrastructure, and stabilizes protein and peptide conformation. The perfusion process should take place in a fume hood for best personal protection.

The mouse is anaesthetised using 0.2 ml euthatal. The withdrawal reflex must not be present before procedure begins to ensure adequate depth of anaesthesia. The chest cavity is opened to expose the heart. A needle is inserted into the left ventricle and clamped in place. A scissor incision is then made into right atrium to allow perfusate to exit circulation. Blood can then be flushed from the body using 0.2M phosphate buffer for about 30 sec. When the fluid exiting the mouse is clear of blood the flush line should be removed and a new one with 4% PFA should be added. 4% PFA must be made up fresh on the day of procedure. Muscle contractions and blanching of the liver and mesenteric blood vessels are signs of good perfusion. Perfusion is complete when all muscle contractions have stopped, the liver and mesenteric vessels are blanched and the desired amount of preservative has passed through the circulatory system.

2.9 Embryo collection

To generate embryos for analysis, heterozygous *Opa3* males and females were selected for inter cross matings. All mice were maintained on a 12/12-hr light-dark cycle the mid-point of the dark cycle being 2am and for the timed mates 2pm on the day of the appearance of the vaginal plug is designated 0.5 days post coitum (dpc). All embryos were dissected from maternal tissue and Reichert's membrane removed in PBS with 10% newborn calf serum. The recovered embryos were staged according to Mouse Atlas [Kaufman, 1994]. The tails of the embryos were added to 200μl of Viagen lysis solution. Samples were digested and genotyped as described for genotyping offspring. Embryos were either fixed in 10% NBF for sectioning or 95% ethanol of skeletal analysis.

CHAPTER III

Splicing, expression and putative functional analysis of optic atrophy gene *Opa3*

3.1 Introduction

Aims of chapter

- Use of RT-PCR to confirm a 3rd exon of *Opa3* and assess for alternative splicing.
- To analyse the expression of splice variants in various adult mouse tissues.
- To screen British adult patients with optic atrophy but without *OPA1* mutations, for mutations in the *OPA3* gene by direct genomic sequencing.
- To use biological databases for gene sequence analysis, protein structure predictions and effects of mutations on human protein structure.
- Use of bio-informatic programs for characterisation of putative transcription factor binding sites (TFBS) to enable further functional predictions of *Opa3*.

At the beginning of this project in 2006 the mouse orthologue of *Opa3* was considered to be a 2 exon gene located on chromosome 7 at 19,813,753 bp – 19,833,210 bp with a single transcript length of 3,289 bp and a translation length of 179 residues. However, the appearance of a novel expressed sequence tag (EST) in the murine Ensembl database (version 50) indicated the possible presence of a 3rd exon (Fig 3.1.) prompting a re-examination of the genomic structure of the *Opa3* locus. The C57BL/6JCrl mouse was used to further characterise the *Opa3* gene structure.

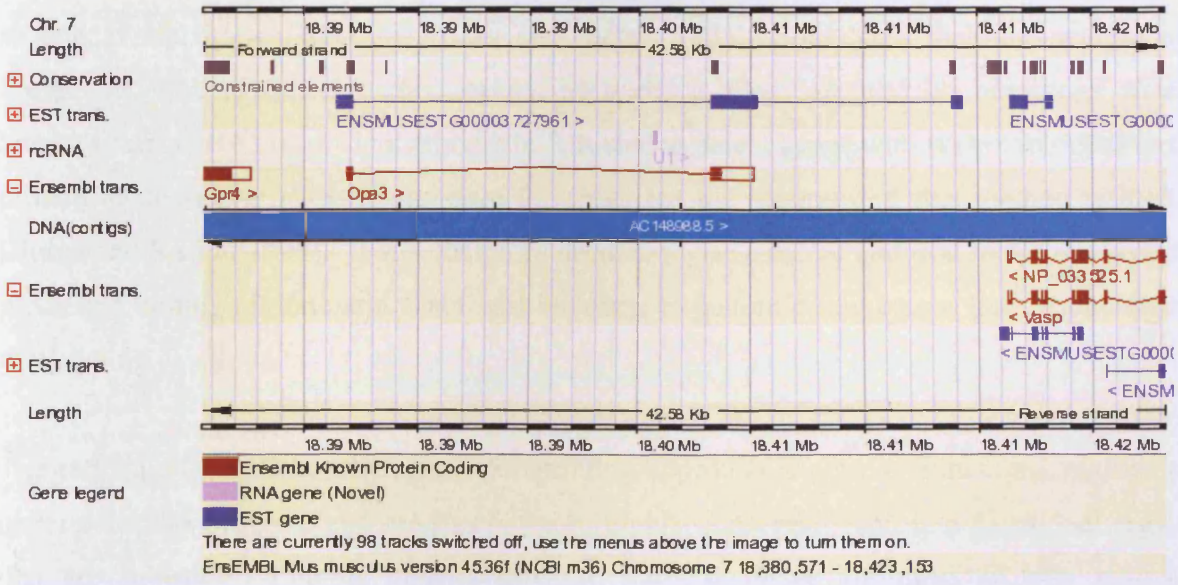

Figure 3.1. Page from murine Ensembl (version 50) showing *Opa3* and EST 3727961.

The function of *Opa3* remains unknown, so with the use of bio-informatic databases the 5 kb proximal sequence of the mouse *Opa3* gene was compared with other mammalian orthologous sequences to look for highly conserved regions. Searches for TFBS that are conserved are important evidences of which proteins may be involved in *Opa3* gene transcriptional regulation. Identification of transcription factors that regulate *Opa3* expression is a step forward to better understand its transcription rules and its function.

This chapter reports the confirmation of a 3rd exon of *Opa3* which creates a novel splice variant of murine *Opa3*. This finding prompted the screening of a panel of patients with optic atrophy in whom mutations in the gene for ADOA (*OPA1*), mapping to chromosome 3q28-qter, had not been found in a previous survey of mutations. Bio-informatic programs were also used to characterise possible upstream TFBS for putative functional analysis.

3.1.1 Use of bio-informatic analysis

With the increasing availability of bio-informatic tools the genomic sequence of *Opa3* was first assessed to determine if there was a 3rd exon of *Opa3*. Traditionally there would have been two possible methods for the prediction of a 3rd exon. An intrinsic method, which uses statistical features such as codon frequencies, open reading frame lengths and the location of potential splice sites to distinguish coding from non-coding sequences of the genome [Burge and Karlin, 1997] or an extrinsic method, which tries to find similarities between genomic sequences and known proteins [Gish and States, 1993]. Both have their advantages and limitations. The extrinsic method cannot be used, as *Opa3* showed no homology to any known proteins. The intrinsic method which is able to detect genes with no homologues in the protein database would be appropriate for *Opa3* but the accuracy of this method is limited [Burge and Karlin, 1998]. It was therefore decided to use a recent addition to the methods for predicting coding regions and functional elements in genomic sequences, that of phylogenic footprinting.

The rationale behind the phylogenic footprinting approach is simple: functional regions are under selective pressure and tend to be more highly conserved than non-functional regions that are subject to random genetic drift, so local sequence similarity usually indicates biological functionality. Several recent studies have used cross-species sequence comparison to identify functional regions in large genomic sequences [Sandelin, 2008; Chen *et al*, 2006]. It is now widely accepted that comparative sequence analysis is a universally applicable tool

for genome analysis and annotation, therefore, being a powerful approach for understanding phylogenetic relationships, annotating genes, and detecting functional regulatory elements.

3.1.2 Multispecies DNA sequence comparison for phylogenic footprinting- What species to select?

Phylogenic footprinting is not only useful for gene annotation, e.g., to look for undiscovered exons but can also be used to detect regulatory regions to shed light on gene function. A range of species were compared to reveal conserved non-coding sequences upstream of *Opa3*. These sequences can then be used to search for TFBS for putative functional analysis. Before this, species selection and the number of species selected for comparison is an important step to consider.

Comparing the genomic sequences of species at different evolutionary distances one can identify coding sequences and conserved non-coding sequences with regulatory functions and determine which sequences are unique for a given species. DNA sequences of species that diverged ~40–80 million years ago from a common ancestor, such as humans and mice reveals conservation in both coding sequences and a significant number of non-coding sequences. Those whose functions have been assigned have been transcriptional regulatory elements of nearby genes [Gumucio *et al*, 1996; Hardison *et al*, 1997] or genes as much as 200 kb away [Loots *et al*, 2000]. A question remains as to whether most of the conserved non-coding sequences are present because of functional constraints or are the result of a lack of divergence time. Comparing species with a larger evolutionary related distance, such as humans and pufferfish, which diverged approximately 450 million years ago, primarily reveals coding sequences as conserved [Aparicio *et al*, 2002]. This is due to the fact that protein coding sequences are tightly constrained to retain function and thus evolve slowly, resulting in readily detectable sequence homology even over this large phylogenetic distance. Therefore, the addition of distantly related organisms (~450 million years) to a multi-species sequence comparison improves the ability to classify conserved elements into coding sequences and non-coding sequences. However, one should be aware that at such large evolutionary distances it is difficult to definitively distinguish between yet undiscovered coding sequences and functional non-coding sequences.

At the other end of the scale comparing sequences from closely related species, such as humans and chimpanzees, identify sequences that have changed and genomic rearrangements

that have occurred in recent evolutionary history [Frazer *et al,* 2003]. Some of these recent genomic events identified by comparison of orthologous sequences between closely related species may be responsible for gene differences between the organisms and are of interest because of their potential functional consequences. Thus, by adding a closely related organism to a multispecies comparative sequence analysis, one can identify not only coding sequences and functional non-coding sequences but also those genomic sequences which may be responsible for traits that are unique to the reference species.

A range of species was therefore chosen that were closely related, such as human and chimpanzee, and more evolutionary divergent species such as the dog and cow (Fig 14.). Frog was initially added to the list but showed no conservation with any of the other species.

3.1.3 Identification of TFBS for insight into gene function

Control of transcription initiation is a pivotal mechanism for determining whether or not a gene is expressed and how much mRNA and consequently protein is produced. A promoter is a sequence that initiates and regulates the transcription of a gene. Protein binding sites in a promoter represent the most crucial elements and the corresponding proteins are called transcription factors (TFs). Understanding a regulatory system requires detailed knowledge of both the trans-acting TFs and the respective promoter *cis*-elements (binding sites). TFs work by binding to specific DNA sites among a vast excess of structurally similar non-specific sites to either increase or decrease the affinity of RNA polymerase for the sequence, thereby altering the rate of mRNA production [Alberts *et al*, 1989].

The identification of DNA regulatory regions is one of the most important and challenging problems in the functional annotation of genomes. Traditionally, DNA binding specificity was determined experimentally primarily with *in vitro* techniques such as DNase I footprinting and electromobility shift assay. However, these processes are very costly and time consuming. With the availability of working draft genomes of many species computational identification of regulatory elements becomes a valuable alternative to *in vitro* techniques.

3.1.4 Predictive programmes for identification of TFBS

Computational TFBS prediction provides reliable results in application to prokaryotes and yeast. However, in higher eukaryotes accurate and reliable TFBS prediction is a huge challenge.

Online applications, such as MatInspector, MATCH and ConSite have been built to predict TFBSs embedded in promoter sequences. However, it should be noted that TFBS searches only identify sites where the TF could bind, but not necessarily will bind. Several different methods and predictive programmes were used.

3.1.4.1 Mulan- MultiTF

Mulan (MUltiple sequence Local AligNment and conservation visualisation tool), is a novel method and a network server for comparing up to 20 draft and finished-quality sequences of different species to identify functional elements conserved over evolutionary time. Mulan brings together several novel algorithms: the threaded blockset aligner (TBA) multi-aligner program for rapid identification of local sequence conservation, and the multiTF program for detecting evolutionarily conserved TFBS in multiple alignments. In addition, Mulan supports two-way communication with the GALA database; alignments of multiple species dynamically generated in GALA can be viewed in Mulan, and conserved TFBS identified with Mulan/multiTF can be integrated and overlaid with extensive genome annotation data using GALA.

3.1.4.2 Genomatix- MatInspector

MatInspector is a tool for TF analysis. It utilises Genomatixs' MatBase the comprehensive TF knowledge database which locates TFBS in sequences of unlimited length. MatInspector assigns a quality rating to matches (called matrix similarity) and thus allows similarity based filtering and selection of results. For every single matrix, an individually optimised similarity score is specified, minimising the number of false positive hits in non-regulatory sequences. Each matrix definition is quality tested, resulting in superior usability for functional analysis of regulatory regions. MatInspector is described in Quandt *et al*, [1995].

3.1.4.3 TFSEARCH

The TFSEARCH program was written by Yutaka Akiyama in 1995. The TFSEARCH searches highly correlated sequence fragments against TFMATRIX TFBS profile database in the 'TRANSFAC' databases by GBF-Braunschweig. There has been no publication on the TFSEARCH program yet.

3.1.4.4 PReMod

PReMod is a database of genomewide *cis*-regulatory module (CRM) predictions for both the human and the mouse genomes. The prediction algorithm, described previously in Blanchette *et al*, [2006], exploits the fact that many known CRMs are made of clusters of phylogenetically conserved and repeated TFBS. Contrary to other existing databases, PReMod is not restricted to modules located proximal to genes, but in fact mostly contains distal predicted CRMs. TFBS can occur everywhere in the genome and are by no means restricted to regulatory regions. Sites outside regulatory regions are known to bind their TFs [Kodadek *et al*, 1998], and it is the context that differentiates a functional binding site affecting gene regulation from a mere physical binding site [Elkon *et al*, 2003].

3.1.5 Use of TRANSFAC and PWM

Numerous DNA footprinting and biochemical studies carried out over the last decade have identified close to 500 vertebrate-specific TFs and information regarding the DNA sequences they recognise. The TRANSFAC database (http://transfac.gbf.de/TRANSFAC/) [Wingender *et al.* 1996; Matys *et al.* 2003] represents the most comprehensive collection of TF binding specificities and has been increasingly linked with other databases such as TFSEARCH and PReMod (transfac 7.2). TRANSFAC summarises TF as position weight matrices (PWMs) for review, see Stormo, [2000].

A weight matrix pattern definition is superior to a simple IUPAC (International Union of Pure and Applied Chemistry) consensus sequence as it represents the complete nucleotide distribution for each single position. It also allows the quantification of the similarity between the weight matrix and a potential TFBS detected in the sequence.

A major limitation in using PWMs to computationally identify functional TFBS is that many TFs bind to short degenerate sequence motifs (6–12 bp in length). More problematic in this

evaluation is that the TF can be shown to bind *in vitro* even if they show no *in vivo* activity. This suggests that there exist other conformational factors that regulate whether a given sequence in the DNA is available for binding. TFBS prediction programs like MatInspector can infer the binding potential, although not the functionality of a site. Functionality can ultimately be proven only by a wet-lab experiment with defined settings, particularly since potential binding sites in a promoter can be functional in certain cells, tissues or developmental stages and non-functional under different conditions.

Study of the molecular basis of diseases by experimental methods is laborious and time-consuming, and at the structural level often nearly impossible, especially in cases where there are several missense mutations causing the disease. By involving advanced bioinformatics strategies like detailed promoter analysis of, for instance, orthologous or co-regulated genes can significantly reduce the number of test candidates. Precise and useful information about the effects of mutations on protein structure and function can readily be obtained by theoretical methods.

3.2 Materials and Methods

3.2.1 Conserved region identification of *Opa3* using comparative genomics

The identification of conserved regions around the *Opa3* locus which may indicate the presence of a 3rd exon was facilitated by comparing the chromosomal regions spanning the human (Ensembl Chr 19 50780462-50722397 bp) and mouse (Ensembl version 50 ENSMUSESTG00000010990 Chr 7 19813232-19841673 bp) gene locus using the Mulan software (mulan.dcode.org) [Ovcharenko *et al*, 2005]. The Evolutionary Conserved Region (ECR) Browser within Mulan was used to visualise phylogenetically core ECRs. To be core ECRs the sequences must be orthologous for 350 bp or more with greater than 77% sequence identity and would therefore be considered as highly likely to be functional. The human *OPA3* gene sequence was used as the reference sequence for annotation in Mulan.

3.2.2 Detection of mouse *Opa3* exon 3 expression and novel splice variant by RT-PCR

To determine whether the core ECR downstream of exon 2 is transcribed, a series of RT-PCR reactions on six different types of wildtype C57BL/6JCrl mouse tissue were performed with the primers listed in Table 3.1. The primers were designed using the primer3input program (website frodo.wi.mit.edu/cgi-bin/primer3/primer3_www.cgi) using the mouse *Opa3* gene sequence in Ensemble. Primers were designed in the exon coding sequences close to the exon/intron boundaries (Fig 3.5.).

Primers	Sequence 5'-3'	Location	Annealing Temp	Product
F1	GGCGAAGCTGTTCTACTTGG	exon 1		
R2	TTATTGCGCTGCTGAGTCTG	exon 2	63oC	309bp
R3	GCGGTGTTTCGATGACTTCT	exon 3	63oC	307bp

Table 3.1. Oligonucleotide primers used to amplify *Opa3* exons.

Total RNA was isolated from heart, skeletal muscle, brain, kidney, liver and eye tissue of adult C57BL/6JCrl wildtype animals (n=3) and collected in RNALater (Sigma). Total RNA was isolated using an RNeasy Mini Kit (Qiagen). RNA was quantified using the Picodrop machine. cDNA was synthesised from 0.5 μg total RNA using Qiagen Quantitect Reverse Transcription Kit (see Chapter II). RT-PCR was performed in 25 μl reactions for exon 1-2 and exon 1-3 transcript detection. RT-PCR contained 2μl template DNA, 1.5 μl of F1 and 1.5 μl

of R2 or R3, 13 µl Taq polymerase mastermix (BioMix Red; BioLine, UK) and dH20 to make up volume.

The general PCR conditions used were as follows: initial denaturation cycle of 15 mins at 95°C; followed by 38 cycles of 45 secs at 95°C, 45 secs at 63°C, and 1 min at 72°C; and a final extension of 10 mins at 72°C. PCR products were visualised on 2% agarose gels stained with ethidium bromide.

3.2.3 Sequencing of mouse exons and transcripts

Genomic DNA and cDNA were isolated as per protocols in Chapter II. PCR products were amplified from genomic DNA and cDNA using primers located in flanking intron and UTR sequences (Table 3.2.). PCR amplification was performed in 25 µl reactions containing 100-200 ng template DNA, 1.25 µl of forward and reverse primers, 12.5 µl Taq polymerase mastermix (BioMix Red; BioLine, UK) and dH20 to make up volume.

Primers	Sequence 5'-3'	Location	Annealing Temp	Product size
F1	AGGCAAGTCCTTCCTTACGC	Exon 1	60°C	341bp
R1	CCGTTCCCCTGAACTAGAAA			
F2	AAGTATTGGGGGTGGAGCTT	Exon 2	63°C	571bp
R2	GCCACATGGTCACAAACAAG			
F3	GTGTTTGCAGTGGGGTGAG	Exon 3	63°C	660bp
R3	ACAAGCCCAGACAACAGTCC			
F1-2	CGCCCAGTCAGCAAGGTT	Exon1-2	60°C	1080bp
R1-2	TCAGAGACTGGATGGGCTCT			
F1-3	CCATGGCGAAGCTGTTCTAC	Exon1-3	60°C	622bp
R1-3	TCAGGACACTGGAGTTCAGG			

Table 3.2. Oligonucleotide primers used to amplify *Opa3* for exon and transcript sequencing.

PCR conditions had to be optimised for each primer pair. Samples were placed in a Techne thermocycler. PCR conditions for exon 1 (F1,R1), transcript 1-2 (F1-2, R1-2) and transcript 1-3 (F1-3, R1-3) were an initial denaturation of 95°C for 5 mins, followed by 35 cycles of 94°C for 30 secs, 60°C for 30 secs, 72°C for 30 secs, with a final extension of 72°C for 5 mins. For exon 2 (F2, R2) and exon 3 (F3, R3) PCR conditions were an initial denaturation of 95°C for 5 mins, followed by 35 cycles of 92°C for 1 min, 63°C for 1 min, 72°C for 1 min, with a final extension of 72°C for 5 mins.

The PCR products were purified for sequencing using QuickClean (Bioline). QuickClean is a method for removing proteins (such as restriction enzymes, polymerases, etc.), primers, primer-dimers and dNTPs. The protocol allows the precipitation of nucleic acids ≥75bp without the need for organic solvents, glass milk or expensive spin-columns. All PCR products were sequenced in forward and reverse to confirm the sequence.

Mouse exon alignments were performed by ClustalW2 [Larkin *et al*, 2007].

3.2.4 Sequencing of human *OPA3*

3.2.4.1 Individuals and Pedigrees

With appropriate ethical approvals, up to 74 British adult patients with optic atrophy but without *OPA1* mutations, were screened for mutations in the *OPA3* gene by direct genomic sequencing. A panel of up to 46 controls (92 chromosomes) was also assessed. All the patients had been previously analysed to exclude mutations in the *OPA1* gene. The patients came from two groups: 1. Patients with ADOA from families too small for linkage data and 2. Individuals with presumed sporadic optic atrophy.

All of the patients studied were adults, over the age of 21 years, with a mean age of 43 years (range 24 to 66 years). Although none had formal audiometry or neuroimaging, none had any neurological symptoms or physical signs on clinical examination. Whilst it is possible that some of the patients may have had mild neurological deficits, it appeared unlikely. There was no sign of late-onset spasticity, extrapyramidal dysfunction or cognitive deficit. The clinical diagnosis of optic neuropathy was based on visual loss, colour vision defects including a tritan defect, temporal pallor of the optic disc and familial occurrence, where a family history was available. Visual fields and visual evoked potentials were documented where possible. Blood samples were obtained from patients, with informed consent, and genomic DNA was prepared from these samples using standard methods [Thiselton *et al*, 2002].

3.2.4.2 Sequencing of OPA3

In order to reduce the probability of screening error the entire coding region of the *OPA3* gene and associated intron-exon boundaries were sequenced by direct bi-directional sequencing of DNA from all individuals. PCR products were amplified from patient DNA using primers located in flanking intron and UTR sequences (Table 3.3.). Standard 50 µl PCR reactions

were performed for direct sequencing using 100-200 ng template DNA, 50 mM KCl, 10 mM Tris pH 8.8, 15 mM $MgCl_2$, 1% Triton X-100, 0.2 mM each dNTP, 0.1 μM each primer and 0.2 μl *Taq* polymerase (Bioline). Typical cycling conditions were initial denaturation of 95°C for 5 mins, followed by 35 cycles of 95°C for 30 secs, 54-60°C for 30 secs (temperature optimized for each primer pair), 72°C for 30 secs, with a final extension of 72°C for 5 mins.

Primers	Sequence 5'-3'	Location	Annealing Temp	Product size
F1 R1	CGTACATACGTACTGACGCA AAGCAACCACCTGACAGG	Exon1	55°C	317bp
F2 R2	TCCCAGAGCGCAGCCTGAC GCCAAGTTGCATCAAGATCCT	Exon2	54°C	555bp
F3a R3a	GGGACATCGAAGCACAGAGG ACGTCGCTCCTTTTCCTTGCG	Exon3	60°C	285bp
F3b F3b	TGCCTGATGCTGGAGTATTGG AGGCCAAGACAGAGACTTCG	Exon3	60°C	323bp

Table 3.3. Oligonucleotide primers used to amplify *Opa3* exons for mutation analysis sequencing.

3.2.4.3 Mutation analysis

Sequence homologues were obtained by PSI-BLAST [Altschuler *et al*, 1997], and homologues for the *OPA3* domain sequence were collected from the Pfam database (seed: 6, full: 59 sequences). Multiple sequence alignments were performed by ClustalW2. Structural disorder in the protein and the effects of mutations on disordered regions were studied using three predictors, DisEMBL [Linding *et al*, 2003a], GlobPlot [Linding *et al*, 2003b] and PONDR [Romero *et al*, 1997]. The wildtype sequences were compared to the polymorphic sequences. The effects of mutations on aggregation propensities were studied by TANGO [Fernandez-Escamilla *et al*, 2004]. The damaging effects of point mutations were analysed using SNPs3D [Yue *et al*, 2006], PolyPhen [Sunyaev *et al*, 2001] and Pmut [Ferrer-Costa *et al*, 2005]. The effects of mutations on protein stability were predicted by SCpred [Dosztányi *et al*, 1997]. No structural analysis could be performed, due to the lack of tertiary structure predictions for the OPA3 protein.

3.2.4.4 Statistics

95% confidence intervals were calculated for control allele frequencies based on sample size. The analysis used a two-tailed estimation of significance. Hardy-Weinberg equilibrium (HWE) was also assessed using a $\chi 2$ test for patient and control groups. The Hardy-Weinberg calculator (scienceforall.org/2010/06/.../hardy-weinberg-equilibrium-calculator/) was used for statistical analysis.

3.2.5 Bio-informatics analysis of the 5' region

As a part of efforts to understand the physiological functions of the *Opa3* gene the 5' untranslated region of *Opa3* was studied. Comparative genomics and pattern-recognition programs were used to characterise possible binding sites and to determine which TF could be relevant for *Opa3* gene expression.

3.2.5.1 Mulan/MultiTF for evolutionary conserved TFBS search upstream of Opa3

The sequences from an evolutionary and taxonomically divergent range of species were aligned using Mulan (Fig 3.2.) to compare the *Opa3* 5' untranslated region to identify ECRs.

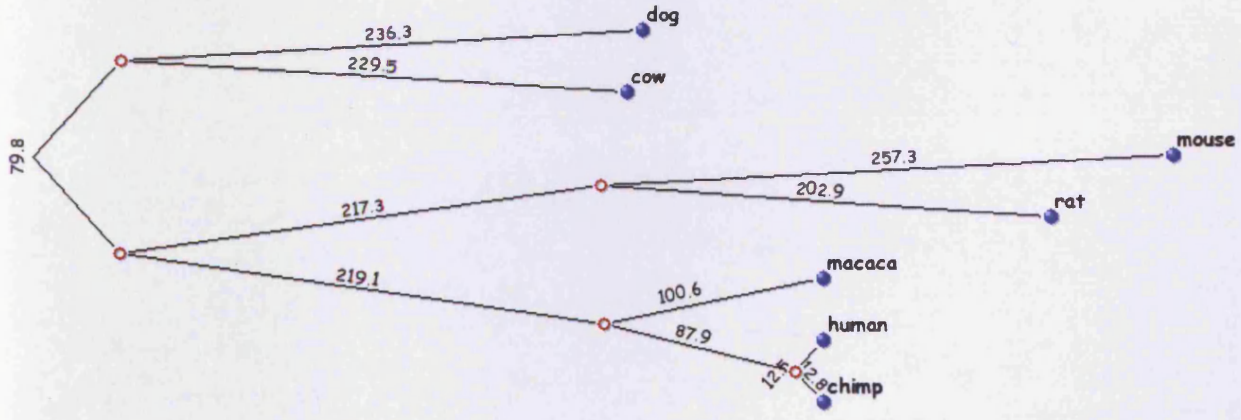

Figure 3.2. A phylogenetic tree generated by Mulan depicting the evolutionary relationship of the seven species used in analyses of *Opa3* based on the similarities of their genomes. The open circles represent common ancestors, and the numbers represent nucleotide substitutions per one kilobase of genomic sequence.

The -5000 bp to +280 bp genomic sequence of mouse *Opa3* was compared with the corresponding human, rat, dog, cow, macaca and chimp sequences. The region analysed was 5 kb as this is the approximate distance between *Opa3* and the upstream gene *Grp4* in mouse. Mulan's graphical alignment used the mouse sequence as the reference. The results were

submitted to MultiTF (multitf.dcode.org) to identify conserved TF consensus sequences. The "optimised for function" search option in multiTF was used which weights PWM differently by minimising and balancing out the abundance of false-negative hits from different matrices.

3.2.5.2 TFBS searches with other programs

With the large number of TFBS produced from predictive programs when the whole 5 kb upstream sequence was used it was decided to use only the sequences that are evolutionary conserved upstream of *Opa3*. As this infers possible functionality it is hoped to reduce the number of false positives. The sequence from the conserved regions found from the alignment of the seven species in Mulan was used as the input sequence for Genomatix software MatInspector [Quandt *et al*, 1995] and TFsearch [http://www.rwcp.or.jp/papia/] with a core similarity cut-off value of ≥ 0.9. PReMod Mouse Mar. 2005 assembly (mm6, Build 34) was used for genome-wide CRM predictions. The selection of programs and high stringencies were chosen to complement each other for a richer and more accurate prediction of TFs in the 5' region.

3.3 Results

3.3.1 *Opa3* third exon and splice variant

Mulan analysis of the mouse and human *Opa3* loci revealed the presence of a core ECR downstream of exon 2 (Fig 3.3.).

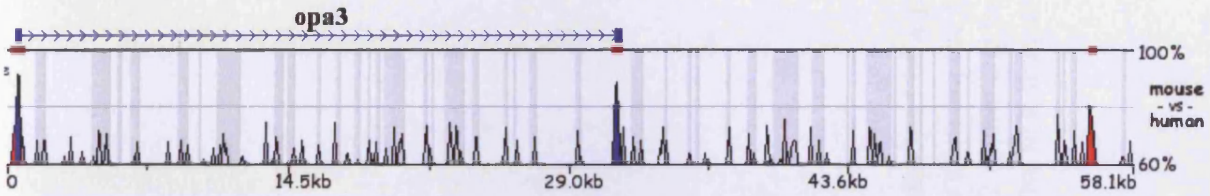

Figure 3.3. Mulan sequence conservation profile for the human and murine *Opa3* loci. The horizontal axis displays the input sequence. Core evolutionary conserved regions (ECRs, > 77% identity; ≥ 350 bp) are depicted as dark red bars above each pairwise alignment. *Opa3* coding exons 1 and 2 (blue), intergenic elements (red) and intron sequence (pink) are marked and the vertical axis shows the percent similarity of the human *Opa3* orthologue to the mouse sequence. A conserved intergenic region, upstream of exon 1 of the *Opa3* gene, can be seen in red (in addition to the one downstream of exon 2 corresponding to exon 3).

To confirm that the conserved region is an exon of *Opa3,* RT-PCR was performed on cDNA from seven different tissues. Primer pairs spanning exons 1 to 2 and exons 1 to 3 yielded the expected product sizes in all tissue cDNAs, showing that the conserved region was indeed transcribed (Fig 3.4B.). Primer pairs spanning exons 2 to 3 did not yield a product in any cDNA sample indicating that exon 2 and 3 do not splice together (Fig 3.4B.). These results demonstrate that exons 2 and 3 are alternatively spliced. This produced two different transcripts that are ubiquitously expressed in all adult mouse tissues tested.

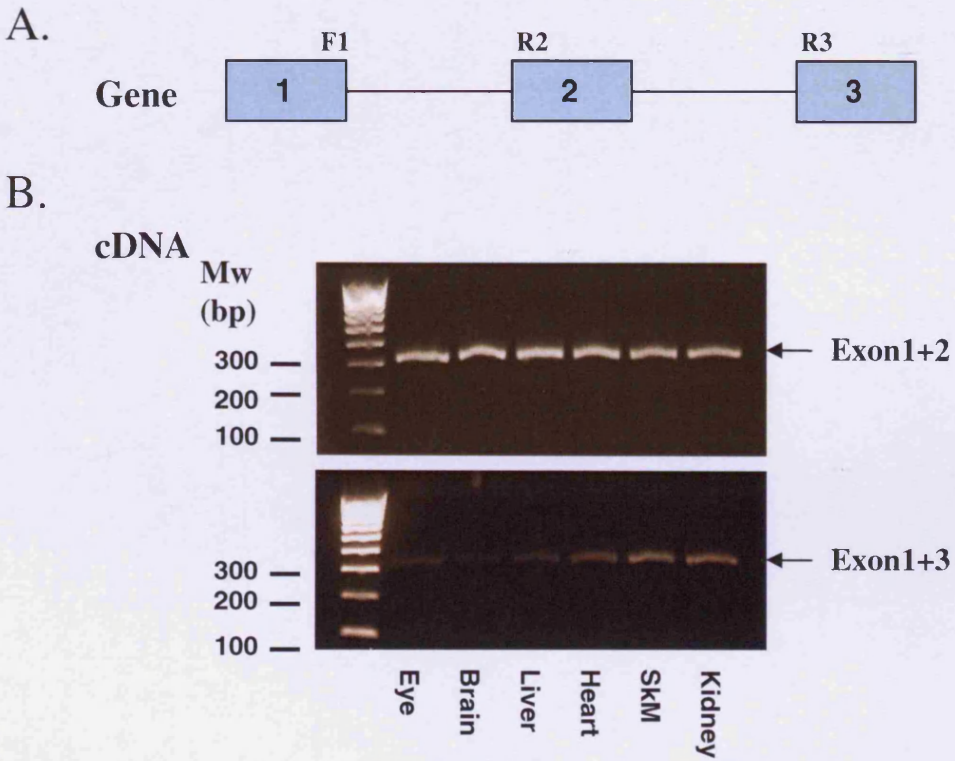

Figure 3.4. RT-PCR showing tissue expression of alternately splice variants of murine *Opa3* in a panel of tissues (eye, brain, liver, heart, skeletal muscle, kidney). (A) Schematic diagram of *Opa3* gene showing the location of RT-PCR primers used to verify 3rd exon and splice variant. (B) Exon 1 splices to exon 2 giving a product of 310 bp (1+2), or to exon3 giving a product of 307 bp (1+3). Primers F1 and R3 did not give rise to a transcript product of Exons 1+2+3 suggesting they do not splice together.

3.3.2 Revised genomic structure of murine *Opa3*

The nucleotide sequence results of the three exons were aligned with the genomic DNA sequences reported in Ensembl and both sequences agreed (Genomic DNA sequences in Ensembl are from the C57BL/6JCrl mouse). Forward and reverse sequences can be seen in Appendix II. RT-PCR confirmed that the EST downstream of *Opa3* is a 3rd exon. Therefore, the revised structure of murine *Opa3* now consists of three exons and produces two transcripts Opa3a (exon1-2) and Opa3b (exon1-3) (Fig 3.5.). The nucleotide sequences of mouse exon 2 and exon 3 highly resemble each other, suggesting a common evolutionary origin (Fig 3.5.).

```
                                  >>>>>>>>>>>>>>>>>>>>F1
Exon1-2  ATGGTGGTGGGCGCGTTCCCCATGGCGAAGCTGTTCTACTTGGGCATCCGGCAGGTTAGC 60
Exon1-3  ATGGTGGTGGGCGCGTTCCCCATGGCGAAGCTGTTCTACTTGGGCATCCGGCAGGTTAGC 60
         ************************************************************

Exon1-2  AAGCCGCTGGCCAACCGTATCAAGGATGCTGCCCGCCGCAGCGAGTTCTTCAAGACCTAC 120
Exon1-3  AAGCCGCTGGCCAACCGTATCAAGGATGCTGCCCGCCGCAGCGAGTTCTTCAAGACCTAC 120
         ************************************************************

Exon1-2  ATCTGCCTACCGCCAGCCCAGCTGTACCACTGGGTGGAGATGCGGACGAAGATGCGCATA 180
Exon1-3  ATCTGCCTACCGCCAGCCCAGCTGTACCACTGGCTAGAGATGCGGACCAAGATGCGCATC 180
         ********************************* * ********** **********

Exon1-2  ATGGGTTTCCGGGGCACTACCATCAAGCCACTGAATGAGGAGGCAGCAGCAGAGCTGGGT 240
Exon1-3  ATGGGCTTCCATGCTGAGGCCATCAAGCCACTGAATGAGGATGCAGCGGCTGAGCTGGGT 240
         ***** ****  *      ********************** ***** ** *********

Exon1-2  GCTGAGCTGCTGGGCGAGGCCACCATCTTCATTGTGGGCGGAGGCTGCCTGGTCCTGGAG 300
Exon1-3  GCGAACCTGCTGGGTGAAGCCATCATCTTTGCTGCTGCGGGCAGCTGTCTGCTGCTGGAG 300
         **  * ******** ** **** ******   **  *  **  **** *** * ******

                 R2<<<<<<<<<<<<<<<<<<<<
Exon1-2  TACTGGCGCCACCAGACTCAGCAGCGCAATAAGGAGGAGGAACAGCGGGCAGCCTGGAAC 360
Exon1-3  TTCTGGCGCCAGAAGTCATCGAAACACCGCAGGGAAGTGGCGCAGGTGGC--CACGGTGC 358
         * *********  ** *   * * * *   * *** * **  ***  ***  *  **  *
                 R3<<<<<<<<<<<<<<<<<<<<
Exon1-2  GCTC--TGCAGGATGAGGTGGGCCGCCTGGCACTGGCCTTAGAGGCGCTGCAGGCTCAGG 418
Exon1-3  TGTCGCTGCGGGAGGATGTGGAATACCTGGAGAACATGCTGGACGAGGTGCAGGTGCAGG 418
           **  *** *** ** ****    *****          * ** * * ******  ****

Exon1-2  CACAAGCGA---TGCCC------TCCTTGAGTGCCCTGGAGG---AGCTGCGGGAGGAGC 466
Exon1-3  TGCAGGCAGCATTGCCCAGGAACTCACTGGATGAGCTGCGGGCAGAGCTGCGGGCAGAGC 478
           ** **     *****       **  **  **  ***  **   *********  ****

Exon1-2  TGCAGGAGGTGC-GTGGTCAGGTCTGCAA-------TGC----------TCA-------- 500
Exon1-3  TGCGGGCGGAGCTGCGGACAGAGTTGCAAGCAGAGTTGCGGGCAGAGCTTCAAGATGAGC 538
         *** ** ** ** * ** ***   *****       ***          ***

Exon1-2  ----------------------CTGTA----CTTCCAAGTGCCAGG-------------- 520
Exon1-3  TACAGAAGTTCAGAACCCAGATCTGTAAAGATTGCTATGAGCCAGAGCTTAAGCCTGAAC 598
                                    *****     * * * * *****

Exon1-2  --CAGCATCTT-------CCAAGAAATAG 540
Exon1-3  TCCAGTGTCCTGAGGCCCCCAAGGAGTAG 627
           ***  ** *       ***** * ***
```

Figure 3.5. Comparison of murine Opa3a (exon1-2) and Opa3b (exon1-3) transcripts. Transcripts show an 81% sequence identity. Exon1 is blue. Alternative second exons are in black. Red shows first stop codon in each transcript. Alignment was generated by the ClustalW2 program."*" means that the residues or nucleotides in that column are identical in all sequences in the alignment. ":" means that conserved substitutions have been observed, according to the colour table in CLUSTALW2. "." means that semi-conserved substitutions are observed. F1, R2 and R3 show position of primers for identification of splice variants in section 3.3.1.

Alignment of the amino acid sequences of the two transcripts (Fig 3.6.) show that the two proteins are 61% homologous and the protein sequences contain 96 mismatches.

```
Exon1-2         MVVGAFPMAKLFYLGIRQVSKPLANRIKDAARRSEFFKTYICLPPAQLYHWVEMRTKMRI 60
Exon1-3         MVVGAFPMAKLFYLGIRQVSKPLANRIKDAARRSEFFKTYICLPPAQLYHWLEMRTKMRI 60
                ************************************************:********

Exon1-2         MGFRGTTIKPLNEEAAAELGAELLGEATIFIVGGGCLVLEYWRHQTQQRNKEEEQRAAWN 120
Exon1-3         MGFHAEAIKPLNEDAAAELGANLLGEAIIFAAAGSCLLLEFWRQKSSKHRREVAQVATVL 120
                ***:. :******:*******:***** ** ..*.**:**:**:::.:::.:*  * *:

Exon1-2         ALQDEVGRLALALEALQAQAQAMPSLSALEELR-----------------------EEL 156
Exon1-3         SLREDVEYLENMLDEVQVQVQAALPRNSLDELRAELRAELRAELRTELQAELRAELQDEL 180
                :*:::*  *   *: :*.*.**  . .:*:***                        :**

Exon1-2         QEVRGQVCN----AHCTSKCQAASSKK- 179
Exon1-3         QKFRTQICKDCYEPELKPELQCPEAPKE 208
                *:.* *:*:    .. ..: *...: *
```

Figure 3.6. Amino acid sequence alignment of murine Opa3a (exon1-2) and Opa3b (exon1-3). Peptides show a 61% sequence identity. Alignment was generated by the ClustalW2 program."*" means that the residues or nucleotides in that column are identical in all sequences in the alignment. ":" means that conserved substitutions have been observed, according to the colour table in CLUSTALW2. "." means that semi-conserved substitutions are observed.

3.3.3 Murine Opa3 protein

The Opa3 protein is of unknown structure and function. NCBI Blast was used for a protein-protein homology search of *Opa3*. There were no homologies to any other proteins except to Opa3 like proteins in other species. There are no other proteins in the human genome that contain the domain (PFamA) and using the conserved domain architecture program CDART to find sequences with similar conserved domains, none were found.

3.3.4 Sequencing of human *OPA3* and mutation analysis

Of the human DNA samples sequenced 97.6% amplified well and were analysed successfully. From the screening of the three exons in human *OPA3,* seven polymorphisms were detected. These were: one polymorphism in exon 2 T>C (231 bp), three polymorphisms in exon 3 which were C>T (227 bp), G>A (379 bp) and G>A (389 bp), two intronic polymorphisms in the 5' UTR sequence, which were -38 bp A>G (-38 bp) and -80 bp G>A (-80 bp) and one intronic deletion c.143-23. The polymorphisms A>G (-38 bp) and T>C (231 bp) have previously been reported [Neas *et al*, 2005]. Therefore, five novel polymorphisms were identified (Fig 3.7.).

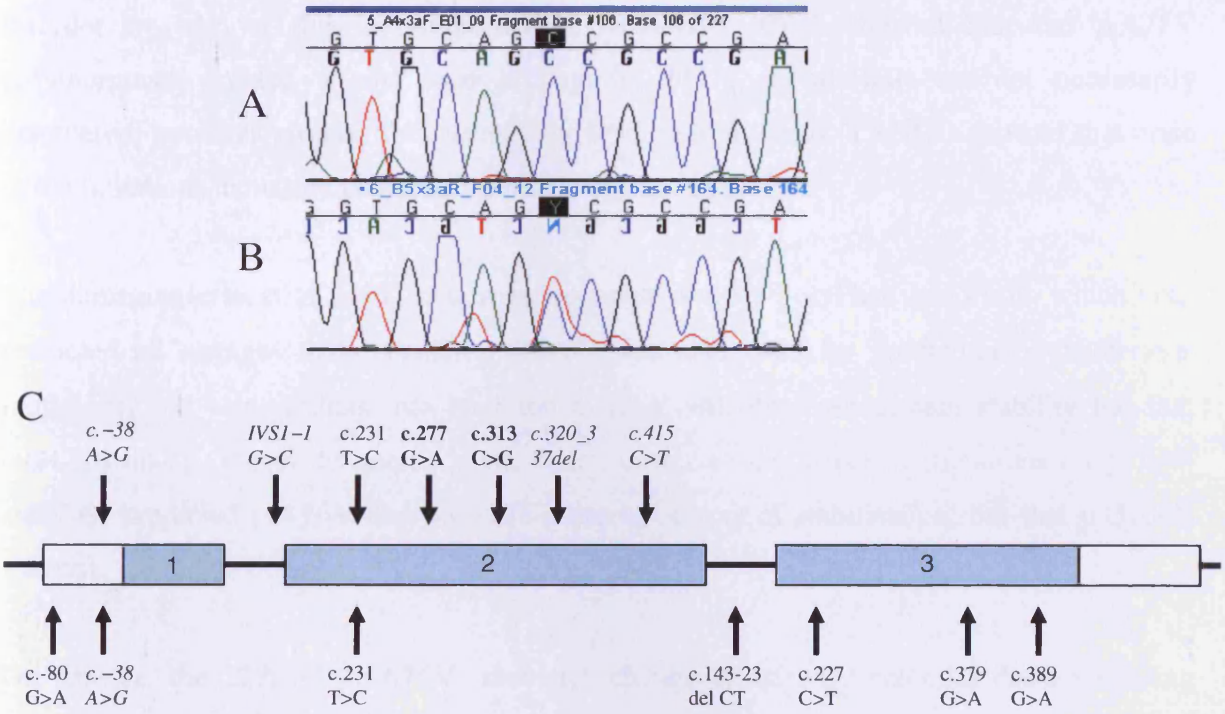

Figure 3.7. Electropherograms showing the two genotype patterns for the *OPA3* c.227 C>T p.A76V SNP in (A) the control patients (C/C) and (B) the affected patient (C/T). (C) Genomic organization of human *OPA3* gene showing all previously reported polymorphisms above the genomic structure with bold text showing mutations that cause ADOAC and *italic text* showing mutations that cause MGA III. All polymorphisms found in this report from genetic screening of British adult patients with optic atrophy are shown below the genomic structure. Grey box - coding regions, White box- untranslated regions (not to scale).

Disease causing mutations are typically located at conserved positions within a protein family, since these positions are usually essential for the structure and/or function of the protein [Miller and Kumar, 2001; Mooney and Klein, 2002; Shen and Vihinen, 2004]. All four of the exonic SNPs are located in the *OPA3* protein domain and variants 227C>T (p.A76V) and 379G>A (p.G127S) are highly conserved in human, mouse, rat, chimp and dog, whereas variant 389G>A (p.G130E) and 231T>C (which is a silent polymorphism) are not conserved.

The introduction of charged and polar aa, as well as residues that may change the orientation of the main chain such as prolines, are likely to have a destabilising effect at these positions. All aa and their SNPs are neutral and non-polar except threonine (T) which is polar neutral.

The effect of mutations on structural disorder was investigated by three different methods (Globplot, DisEMBL and PONDR). None of the exonic mutations were predicted to increase

disorder by any of the programs except DisEMBL which showed that the p.A76V polymorphism created a new loop at peptides 65-73. Loops/coils are not necessarily disordered, however protein disorder is only found within loops. TANGO showed that none of the mutations increased propensity for beta aggregation.

The damaging effects of point mutations were analysed by PolyPhen and Pmut, which both predicted all changes to be benign. SNP3D was also used for prediction of deleterious mutations, and this predicts that mutation p.A76V will decrease protein stability but that p.G127S and p.G130E do not. SCpred, which evaluates the effect of mutations on protein stability, predicted p.A76V and p.G127S were in centres of stabilisation, but that p.G130E was not.

On balance, the 227C>T (p.A76V) sequence change is the only potential disease causing mutation. However, since the tertiary structure of *OPA3* is unknown this bio-informatics inference is speculative. The frequency of this change in our panel of normal chromosomes is 0 (Table 3.4.), but it is not possible to carry out 227C>T (p.A76V) segregation analysis in order to support the pathology of the mutation since the patient identified is a sporadic case of optic atrophy.

A goodness-of-fit $\chi 2$ test was used to test for Hardy-Weinberg Equilibrium (HWE) by comparing the observed number of subjects for each genotype with the expected number of subjects assuming HWE. Some of the control and patient groups depart from HWE (Table 3.4.). Departure from HWE may indicate sequencing errors or factors that disrupt HWE such as small N number.

cDNA change	Allelic Frequency		Statistics HWE		95% CI for control alleles
	Patients N (frequency)	Controls N (frequency)	Patients	Controls	
c.-80 G>A	G: 19/22 (0.86) A: 3/22 (0.14) G/A: 0	G: 45/50 (0.9) A: 5/50 (0.1) G/A: 0	*P*=0.00	*P*=0.00	G: 90 ± 8.32% A: 10 ± 8.32%
c.-38 A>G	A: 19/22 (0.86) G: 0 A/G: 3/22 (0.14)	A: 39/50 (0.78) G: 1/50 (0.02) A/G: 10/50 (0.2)	*P*=0.73	*P*=0.22	A: 78± 11.48% G: 2 ± 3.88% A/G: 20 ± 11.09%
c.231 T>C	T: 3/21 (0.14) C: 4/21 (0.19) C/T: 14/21 (0.67)	T: 5/50 (0.1) C: 10/50 (0.2) C/T: 35/50 (0.7)	*P*=0.12	*P*=0.003	T: 10 ± 8.32% C: 20 ± 11.09% C/T: 70 ± 12.7%
c.143-23 del CT	WT: 61/74 (0.82) Het: 12/74 (0.16)) Homo: 1/74 (0.02)	WT: 76/92 (0.83) Het: 14/92 (0.15) Homo: 2/92 (0.02)	*P*=0.64	*P*=0.18	WT: 83 ± 7.68% Het: 15 ± 7.3% Homo: 2 ± 2.86%
c.227 C>T	T: 0 C: 73/74 (0.98) C/T: 1/74 (0.02)	T: 0 C: (92/92) (1) C/T: 0	*P*=0.95	--	--
c.379 G>A	A: 0 G: 73/74 (0.98) G/A: 1/74 (0.02)	A: 0 G:92/92 (1) G/A: 0	*P*=0.95	--	--
c.389 G>A	A: 0 G: 73/74 (0.98) G/A: 1/74 (0.02)	A: 0 G:92/92 (1) G/A: 0	*P*=0.95	--	--

Table 3.4. Allelic frequencies of the OPA3 gene in patients with optic atrophy and health controls. HWE= Hardy Weinberg Equilibrium. If the p-value obtained is higher than 0.05 then the sample respects the equilibrium and is a good example of the whole population. CI= confidence interval, WT= wildtype, Het= heterozygote and Homo= Homozygote.

3.3.5 The evolutionary conservation of regions upstream of *Opa3* exon 1

Multi-species Mulan conservation analysis of exon 1 and the 5 kb region upstream of *Opa3* revealed three discrete elements of non-coding ECRs that are conserved in all seven vertebrate lineages (Fig 3.8.) when using a >100 bp and >70% identity cut off, the classically defined stringency for the identification of functional mammalian regulatory elements [Pennacchio and Rubin, 2001]. These three elements are: -3538 bp to -3236 bp, -1326 bp to -1015 bp and -420 bp to -143 bp. When using a more stringent cut off (>200 bp and 77% identity) only the -1326 bp to -1015 bp region remains.

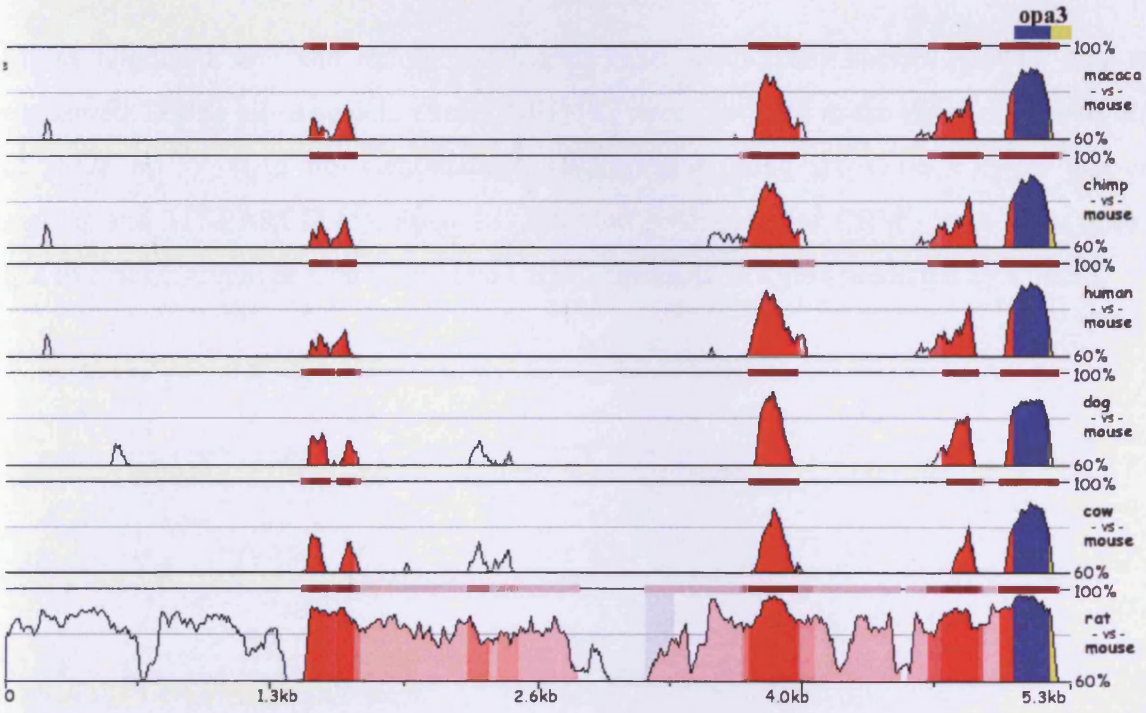

Figure 3.8. Standard stacked-pairwise visualization (smooth graph) of Mulan alignments of murine *Opa3* loci with 6 orthologous species. The mouse sequence was selected as the reference sequence. The horizontal axis displays the input sequence which was -5000bp to +280bp. The graphical representations of the other sequences are displayed according to their similarity to the base sequence: the closer they are to mouse, the higher is the conservation. Evolutionary conserved regions set as (ECRs >70% identity, >100bp. Lower ECR cut off was 60%). Figure shows regions of conserved sequence that are present in all species. Colour density by interspecies conservation (the darker the colour the more species the conserved region is in). Red indicates regions upstream of exon 1. Blue region shows conservation of *Opa3* exon1 sequence.

To assess if any of the ECRs are exons of *OPA3* all upstream human ESTs between *OPA3* and *GRP4* (of which there are three: DW461756, DW420344 and DW461531) were aligned with the 5 kb upstream sequence of human *OPA3*. None of the ESTs aligned with the conserved regions and do not overlap with *OPA3* at the mRNA level, suggesting they are not

exons of *OPA3*. However, DW414756 does have a small ORF and upstream ORFs of a gene are known to influence translation [Chatterjee and Pal, 2009] and therefore could potentially have a regulatory effect on the expression of *OPA3*.

3.3.6 Analysis of the *Opa3* gene proximal sequence using phylogenetic footprinting and TRANFAC PWM searches

The results produced 53 TFBS's (Table 3.5.) in the mouse *Opa3* 5 kb upstream region and consequently suggest many putative regulatory proteins that could potentially modulate *Opa3* expression.

Mulan alignment between mouse and the six other mammalian species showed nine multi conserved TFBSs all of which, except RBP-JK, were clustered in the most conserved region of -1326 bp to -1015 bp. Genomatixs' MatInspector found six TFBS's in the conserved regions and TFSEARCH identified 18. PReMod produced four CRM's, two were upstream and two downstream of *Opa3*. The two CRM's upstream of *Opa3* predicted 29 TFBS's.

TFBS	Official mouse Symbol	Bioinformatic Program	NCBI Gene ID
P53 & P53 decamer	Trp53	Mulan, Genomatix, PReMod	22059
HFH8	Foxf1a	Mulan , PReMod	15227
Fox01		Mulan, PReMod	56458
Fox04		Mulan, PReMod	54601
XFD1		Mulan, TFsearch	
VDR		Mulan, PReMod	22337
OLF1	EBF1	Mulan	13591
RBPJK	Rbpj	Mulan	19664
CRE-BP	Atf2	TFsearch, PReMod	11909
CREB	Creb1	TFsearch, PReMod	12912
SP1		Genomatix,	20683
AP2F	Tcfap2a	Genomatix,	21418
CAAT		Genomatix	
EBOX		Genomatix	
E2F1		Genomatix	13555
Oct-01	Pou2f1	TFsearch	18986
SRY		TFsearch	21674
Stat		TFsearch	
HLF		TFsearch	217082
Gata 1		TFsearch	14460
Gata2		TFsearch	14461
Gata3		TFsearch	14462
NRF2	Nfe212	TFsearch	18024
MZF1		TFsearch	109889
C/EBP a		TFsearch	12606
C/EBP b		TFsearch	12608

TFBS	Official mouse Symbol	Bioinformatic Program	NCBI Gene ID
Aml-1a	Runx1	TFsearch	12394
v-MYB		TFsearch	17863
Nkx 2		TFsearch	
S8	Prrx2	TFsearch	20204
Tel2	Telo2	PReMod	71718
E4F1		PReMod	13560
Pax2		PReMod	18504
Pax3		PReMod	18505
Pax4		PReMod	18506
Pax8		PReMod	18510
HfH1	Foxq1	PReMod	15220
GR	Nr3c1	PReMod	14815
Freac-7	Foxl1	PReMod	14241
ATF		PReMod	
ATF3		PReMod	11910
ATF4		PReMod	11911
ATF6		PReMod	226641
TCF11	Nfe2l1	PReMod	18023
Cart1	Alx1	PReMod	216285
E4BP4	Nfil3	PReMod	18030
Chx10	Vsx2	PReMod	12677
Muscle initiator		PReMod	
Muscle initiator 19		PReMod	
Muscle initiator 20		PReMod	
PolyA downstream element		PReMod	
Cre-bp1/c-jun		PReMod	

Table 3.5. Putative TFBSs identified upstream of *Opa3* using the databases Mulan, MatInspector, TFSEARCH and PReMod. The official mouse symbol was added where they differed from the TFBS gene name given in the databases. NCBI gene IDs were omitted where they were unknown.

3.4 Discussion

3.4.1 Alternate splicing of *Opa3*

The *Opa3* gene was previously believed to contain 2 exons and produce one transcript. The results here demonstrate that the murine *Opa3* gene consists of three exons which produce two transcripts, similar findings were recently reported in human [Huizing *et al*, 2010]. The 2nd transcript consists of the common exon 1 spliced directly to a third exon and skipping exon 2 altogether. No transcript was found containing all 3 exons. Exon 3 is conserved in all other species studied (mouse, human, rat, cow, dog, macaca and chimp) and closely resembles exon 2 suggesting a duplication event. Both isoforms are naturally expressed in a variety of tissues and are highly conserved between human, mouse and orthologs in other vertebrate species. The third exon of *Opa3* was found to be expressed in heart, lung, muscle, brain, kidney, liver and eye tissue of adult C57BL/6JCrl wildtype mice. This revised intron-exon structure spans around 27 kb of genomic DNA, adding approximately 8 kb to the previously defined region.

Recent quantitative PCR assessment by Kate Powell, Cardiff University of the relative expression of isoform a to isoform b in wild type and homozygous mutant *Opa3*$^{-/-}$ mice at P7 and P30 shows that transcript b is expressed at less than ten-fold levels compared to transcript a in lens or retina, and that the presence of the mutation does not disturb this ratio. *OPA3A* deficiency in patients causes up-regulation of *OPA3B* in MGA-III patients [Huizing *et al*, 2010].

3.4.2 Determination of OPA3 genetic variants in patients with optic atrophy

The three intronic and the exon 2 polymorphisms reported in this study were found with comparative frequencies in 50 unrelated control chromosomes from patients from the UK. This, together with the bio-informatic analysis, predicts that they do not change functionally important residues and are benign. The exon 3 polymorphisms were only found in one patient and in none of the unrelated control chromosomes. Polymorphisms G>A (379 bp) and G>A (389 bp) are unlikely to affect protein structure, while the polymorphism C>T (227 bp) may potentially be disease causing but as the protein structure of OPA3 is unknown and there are no other members of the protein family, results are inconclusive. We thus report five novel sequence changes in the *OPA3* gene.

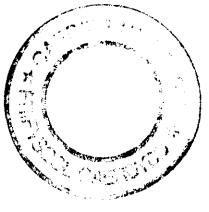

The absence of homozygous or heterozygous mutations in the *OPA3* gene in this group of patients suggests that the optic atrophy seen in a cohort of patients without *OPA1* mutations is not commonly caused by mutations in the *OPA3* gene. The heterozygous mutation in *OPA3* reported by Anikster *et al*, [2001], may be excessively rare in an out bred population, such as that from the UK. Both Anikster *et al*, [2001] and Ho *et al*, [2008], suggest that *OPA3* mutations should be sought in samples from patients with optic atrophy which are atypical for the recessively inherited condition *OPA3*.

The sequence changes reported do not affect the coding region of the *OPA3* gene. In particular, the 22 highly conserved aa of *OPA3* (aa 10 to 32) at bp 28 to 91 are not affected. This region contains the mitochondrial targeting peptide, NRIKE, at aa residues 25-29. The sequence changes detected are not predicted to alter the splice sites. The mutation detection rate for sequence based screening is the highest of all methods currently in use. In this study direct bidirectional sequence analysis was performed in an attempt to avoid screening errors.

3.4.3 Mutations of *OPA3*

Mutations in *OPA3* can cause diseases with recessive as well as dominant modes of inheritance. This bimodal effect of *OPA3* mutations is not common but is also not unique. In general, disorders that have both dominant and recessive modes of inheritance are caused by mutations at different gene loci.

In Costeff syndrome autosomal recessive loss-of-function *OPA3* mutations lead to severe multisystem disease with optic atrophy, 3-methylglutaconic aciduria, and psychomotor retardation [Anikster *et al*, 2001; Kleta *et al*, 2002]. The complete loss of *OPA3* expression as a result of both copies of the *OPA3* gene carrying a mutation results in a disorder that has a recessive mode of inheritance. Indeed, all cases of MGA-III described to date have been caused by homozygous mutations IVS1−1G>C or c.320_337del or the nonsense mutation we have identified (p.Q139X), and all of which are predicted to abolish all protein activity. However, heterozygous parents of patients with Costeff syndrome are not affected by optic atrophy or cataract, suggesting that haploinsufficiency of the *OPA3* gene might have milder effects.

However, a different mode of inheritance of optic atrophy was reported by Reynier *et al*, [2004], whereby *OPA3* mutations were responsible for ADOAC in two of the families studied. The two missense mutations p.G93S and p.Q105E segregated with disease in each

family and were absent in healthy relatives and normal controls. Therefore, for ADOAC only one copy of *OPA3* needs to carry a missense change, which probably exhibits a dominant negative effect but manifests as a milder phenotype. It appears therefore that either complete absence of OPA3 protein or an abnormal peptide will lead to disease.

3.4.4 Using TFBS as an insight into *Opa3* function

During the analysis of the 53 predicted TFBS upstream of *Opa3* several common functional themes emerged. Many of the TFs are involved in (1) retinal development and neuron development/survival, (2) cellular stress response/apoptosis, (3) bone/craniofacial development and (4) adipogenesis (see Table 3.6.).

TFBS	Neuronal / Retinal	Cellular stress response/Apoptosis	Craniofacial/ Bone	Adipogenesis
P53 & P53 decamer	+	+	+	+
CRE-BP	+	+	+	+
AP2F	+	+	+	+
CREB	+	+	+	+
Stat	+	+		+
Oct-01	+	+		
Pax2	+		+	+
AML-1a	+		+	
Chx10	+		+	
RBPJK	+			+
Gata3	+			+
Fox01		+	+	+
E2F1		+	+	+
Fox04		+		+
C-EBP a+b		+		+
NRF 2		+		+
MZF1		+		
VDR			+	+
OLF1			+	+
SP1			+	+
Pax3			+	+
ATF(inc 3,4,6)			+	
Cart1			+	
HFH8			+	
Gata2				+
GR				+

Table 3.6. List showing common functional themes in the TFBSs found upstream of *Opa3* and which TFBSs are known to play a role in these processes. TFBS were omitted where no evidence was found for their involvement in any of the functional themes listed.

Interestingly, these functional themes coincide with many of the phenotypic aspects observed in our mouse model (B6; C3-*Opa3*^{L122P} [Davies *et al*, 2008]. The homozygote mice have reduced visual acuity consistent with the thinning of various retinal layers and a significant reduction in RGCs, extending to a distinct degeneration of axons within the optic nerve. Magnetic resonance imaging (MRI) scans show a considerable lack of visceral adipose tissue and the phenotype shows clinically apparent dysmorphic features in the bones of the head.

3.4.4.1 Retinal development and neuron development/survival.

Adult *Opa3* homozygote mice have a significant loss of cells from the retinal ganglion cell/nerve fibre layer and inner nuclear layer. Many of the predicted TFBSs upstream of *Opa3* (Table 3.6.) are known to be expressed in the retina. For example, during retinogenesis, all STAT (Signal Transducers and Activator of Transcription) proteins are expressed in the neuronal retina in distinct cell populations at different embryonic stages. Other proteins expressed during retinogenesis are Runx1, a novel marker for a restricted amacrine cell subtype and the homeobox gene CHX10 which is required for retinal progenitor cell proliferation early in retinogenesis and subsequently for bipolar neuron differentiation. RBP-JK is a key mediator of Notch signalling and this Notch signalling pathway is important at several stages of retinal development including the differentiation of RGCs and Müller glia. Mutant mice with reduced CREB expression show loss of refinement of retinogeniculate projections. Oct-1 is co-expressed with Sox2 and Pax6 during lens and nasal placode induction and during subsequent developmental stages. Other TFs are known to be involved in regulation of neuron development and survival e.g. GATA binding protein 3 (GATA3).

3.4.4.2 Cellular stress response/Apoptosis

Previous studies have indicated that *OPA3* may play a role in promoting increased cell death. Reynier *et al*, [2004] showed that human fibroblasts carrying the 227G>A (G93S) mutation were more susceptible to apoptosis induced by staurosporine than wildtype counterparts. The cellular stress response is a defence reaction of cells to damage that environmental forces inflict on macromolecules. In addition, cells can quantify stress and activate a death program (apoptosis) when tolerance limits are exceeded.

Some of the TFs identified here are involved in apoptotic response to DNA damage, such as Oct-1, E2F1 and STAT-1, which interacts with p53 to enhance DNA damage-induced apoptosis. FOXO1 and FOXO4, are implicated in the regulation of a variety of cellular processes, including the cell cycle, apoptosis, DNA repair, stress resistance, and metabolism. Pax3 is involved in anti-apoptotic cell survival. The Nrf2 transcription factor plays a key role in the cellular defense against oxidative and xenobiotic stresses through its capability to induce the expression of genes which encode detoxifying enzymes and antioxidant proteins.

3.4.4.3 Bone/Craniofacial Development

The *Opa3* homozygote mice are smaller than their wildtype littermates even during embryogenesis [Davies *et al*, 2008]. They show dysmorphic facial features and suffer from overgrown teeth possibly from a misalignment of the jaw. These phenotypes are suggestive of defects in bone and craniofacial development. Of the TFs identified to associate with *Opa3* in this study a number are involved in wide ranging aspects of bone and craniofacial development.

Genes involved in craniofacial development can be categorised by their malformations: (A) Neural-tube defects, which are described as exencephaly when they occur in the cranial region, for example mice that are null for Pax3 (paired box gene 3); Tcfap2a (transcription factor AP-2α) and Cart1 (cartilage homeoprotein 1). (B) Mice null for Pax2, Chx10 and AP-2 show sensory organ defects, usually of the eye or ear. (C) Neural-crest defects which affect neural-crest specification, migration, proliferation and epithelial–mesenchymal induction. This large group includes many members of the Prrx (Paired-related) homeodomain families and Pax3. (D) Other TFs involved in skeletal development, e.g., ATF-2 mouse mutants have been shown to display chondrodysplasia and neurological abnormalities [Reimold *et al*, 1996] or Runx1 which is expressed in various types of bone formation. The pattern of Runx1 expression suggests that it could be potentially involved in incipient intramembranous bone formation during craniofacial development.

3.4.4.4 Adipogenesis

Many of the predicted TFs are proteins known to be involved in adipogenesis (the development of fat cells from preadipocytes). Interestingly, MRI scans of our *Opa3* mouse model [Davies *et al*, 2008] show a striking lack of visceral adipose tissue in the *Opa3* homozygotes. Adipogenesis is a complex process that involves the integration of many different signalling pathways and TFs. The coordinated action of the peroxisome proliferator-activated receptor (PPAR) and the CCAAT/enhancer binding protein (C/EBP) family of TFs regulate the adipocyte differentiation program. C/EBP can induce many adipocyte genes directly, and *in vivo* studies indicate its important role in the development of adipose tissue. Other pro-adipogenic proteins include EBF1, which stimulates adipogenesis in NIH-3T3 fibroblasts, STAT5a [Floyd and Stephens, 2003] and CREB [Zhang *et al*, 2004].

By contrast, many TFs are anti-adipogenic including several members of the GATA-binding and forkhead families. Murine GATA-2 and GATA-3 are specifically expressed in white adipocyte precursors and their down-regulation sets the stage for terminal differentiation. Foxo1 inhibits adipogenesis at least partially by repressing PPARγ gene transcription [Armoni *et al*, 2006]. Sp1 mediates repression of the C/EBPα promoter [Tang *et al*, 1999]. VDR, P53 and NRF2 are also known to inhibit adipogenesis.

The disease-related TFBS clusters described mirror major phenotypic features seen in the B6;C3-*Opa3*^{L122P} mouse. Identification of such TFBS may provide important future insight into factors which regulate *Opa3* gene transcription, elucidating its transcriptional rules and providing important further clues to the function of the Opa3 protein.

3.5 Conclusions

- *Opa3* is a 3 exon gene where exons 2 and 3 are alternately spliced to produce two transcripts both of which are expressed in a wide variety adult mouse tissue and throughout embryonic development. Full characterisation of *Opa3* may prove valuable for elucidating function and will be useful for carrier detection, genetic counselling, and for detecting mutations in individuals with optic atrophy.

- Five novel polymorphisms have been identified in humans, of which one may potentially be disease causing.

- Opa3 shows conservation between species but has no homology to any other known proteins.

- 53 TFBS have been identified which may be responsible for control of *Opa3* expression and these fall into four functional categories: retinal development and neuron development /survival; cellular stress response/apoptosis; bone/craniofacial development and adipogenesis. These themes support studies of our mouse model, as they coincide with observed phenotypes of mice homozygous for the *Opa3* mutation and are in line with the phenotypic features in patients with MGA-III. These TFBS provide useful clues as to the function of the Opa3 protein and suggest new areas of research into the pathophysiology of MGA-III and optic atrophy.

CHAPTER IV

Genotype/phenotype correlations and development of the mutant B6; C3- *Opa3*^{L122P} mouse line

4.1 Introduction

Aims of Chapter

- To develop the B6; C3-*Opa3*^{L122P} mutant mouse on an appropriate background strain and generation that minimises phenotype variability and with an appropriate severity that allows for ease of analysis of disease phenotype.
- Assess gross morphological defects and tissue pathology in adult homozygote and wildtype mice.
- To dissect at a range of embryonic time points to look for any pathology and embryonic lethality.
- Analysis of craniofacial dysmorphia observed in homozygotes and heterozygotes.

The mouse is an ideal model organism for the study of human disease. The similarities between the mouse and human are striking; both the mouse and human genomes are approximately the same size, both contain the same number of genes, both show an extensive conserved gene order and conserved gene function and mice are physiologically similar to humans.

A large genetic reservoir of potential models of human disease has been generated through the identification of >1000 spontaneous, radiation or chemically induced mutant loci. In the vast majority of these models, the mouse mutant phenotype very closely resembles the human disease phenotype and these models therefore provide valuable resources to understand how diseases develop.

This chapter deals with the development of the B6; C3-*Opa3*^{L122P} mutant mouse on two background strains and assesses gross morphological defects in adult, embryo and tissue pathology. Since there are no reports of craniofacial and skeletal anomalies in the corresponding human conditions, one of the aims was to characterise these malformations in this mouse model.

4.1.1 Generation of *Opa3* mutant mice: the L122P mutation.

The *Opa*3 mouse model was created by screening a panel of over 10,000 ENU mutagenised C3H mouse sperm DNAs for mutations in *Opa*3 by sequencing exons 1 and 2 of *Opa3*. This was carried out for our laboratory by Ingenium Pharmaceuticals (www.ingenium-ag.com). A heterozygous missense mutation was found in exon 2 coding for T to C transition at position 365 in the open reading frame (c.365T>C) which changes a leucine into a proline within the peptide (Fig 4.1.).

MVVGAFPMAKLFYLGIRQVSKPLANRIKDAARRSEFFKTYICLPPAQLYHWVEMRTK
MRIMGFRGTTIKPLNEEAAAELGAELLGEATIFIVGGGCLVLEYWRHQTQQRNKEEE
QRAAWNALtoPQDEVGRLALALEALQAQAQAMPSLSALEELREELQEVRGQVCNAH
CTSKCQAASSKK

Figure 4.1. Peptide sequence of Opa3 showing the L122P mutation in exon 2. L= leucine (wildtype), P= proline (mutant)

The mutation is not the same as any of the published human disease causing mutations, but is highly predicted to be disease causing. The missense mutation affects an aa which is very highly conserved across human, mouse, rat and even insects and plants. The exon 2 mutation is located in a long helical secondary structure region, and the introduction of a helix breaking proline severely changes the predicted tertiary structure of the protein. *Opa3* mRNA was present in all mouse tissues examined and its transcription was unaffected by the presence of the mutation [Davies *et al*, 2007]

Sperm were used (*in vitro* fertilisation with C57BL/6J females) to generate heterozygous hybrid $Opa3^{+/-}$ 'founders' (the B6; C3-$Opa3^{L122P}$ mouse line). For ease of writing the nomenclature, homozygote mice throughout this thesis are referred to as $Opa3^{-/-}$, heterozygotes as $Opa3^{+/-}$ and wildtypes as $Opa3^{+/+}$.

4.1.2 Strain background disease characteristics

When using an inbred strain for the phenotypic characterisation of a chosen mutation it is important to be aware of any background diseases that the strain might carry so as not to confuse them with any induced genetic defects. There are four types of background diseases that could influence ocular phenotypes; (i) systemic diseases that might affect the eye, (ii)

known genetic defects, (iii) congenital abnormalities that might be polygenic and (iv) susceptibility genes that alter the response to an external stimulus.

The 'founder' mice were a hybrid of C57BL/6J and C3H/HeJ mouse strains. The 'founders' were bred to more congenic backgrounds on both of these strains.

4.1.2.1 C3H/HeJ Strain

C3H/HeJ mice are used as a general purpose strain in a wide variety of research areas including cancer, immunology and inflammation, sensorineural, and cardiovascular biology research. C3H/HeJ mice are homozygous for the retinal degeneration 1 mutation (*Pde6b*^{rd1}), which causes blindness by weaning age. There is also a high incidence of hepatomas in C3H mice. Despite the lack of exogenous mouse mammary tumor virus, virgin and breeding females may still develop some mammary tumors later in life. C3H/HeJ mice spontaneously develop alopecia areata at a reported incidence of approximately 0.25% by 18 months of age.

A spontaneous mutation occurred in C3H/HeJ at lipopolysaccharide response locus (mutation in toll-like receptor 4 gene, Tlr4Lps-d) making C3H/HeJ mice endotoxin resistant. C3H/HeJ (Tlr4Lps-d) mice are highly susceptible to infection by Gram-negative bacteria, such as Salmonella enterica. The C3H/HeJ substrain is homozygous for an inversion on Chromosome 6 named In(6)1J. The inversion covers 20% of Chromosome 6 between *D6Mit124* (~30.3 cM) and *D6Mit150* (~51.0 cM) but has no apparent effect on phenotype.

The C3H/HeJ mice used by Ingenium carry the *Pde6b*^{rd1} mutation which would affect the retinal phenotype. Therefore, *Rd1* allele-specific PCR genotyping was used to direct breeding with wild-type C57Bl/6JCrl and the removal of the *Rd1* allele of *PdeB* (carried by the C3H paternal line) was thus ensured. For breeding the *Opa3*^{L122P} mutation to a more congenic C3H/HeJ background a C3H strain from Medical Research Council (MRC), Harwell that does not carry the *Pde6b*^{rd1} mutation was used.

4.1.2.2 C57BL/6J Strain

C57BL/6J mice have been widely used as an inbred control strain in many studies. However, they also represent an important model of diet-induced diabetes, and they exhibit glucose intolerance, which is independent of obesity. Blood glucose levels of non-obese C57BL/6J

mice, measured using an intraperitoneal glucose tolerance test, reveal that plasma glucose levels rise much higher and take longer to regain the resting level than in other mouse strains.

The C57BL/6J mouse has a deletion of the nicotinamide nucleotide transhydrogenase (*Nnt*) gene on chromosome 13, a nuclear-encoded mitochondrial protein involved in β-cell mitochondrial metabolism. This deletion is an in-frame five-exon deletion in *Nnt* that removes exons 7–11. This results in a complete absence of Nnt protein in these mice.

Nnt is located in the IMM and involved in β-cell mitochondrial metabolism. It was therefore thought prudent to genotype the mice for *Nnt* and breed the mutation out of the colony as *Opa3* is also thought to be expressed in the IMM.

4.2 Materials and Methods

4.2.1 Mouse strains and husbandry

The founder mice were 50:50 C3H/C57BL/6J hybrids originating from the screening of *Opa3* by Ingenium Pharmaceuticals as outlined in section 4.1.1. The colony was maintained by crossing mice heterozygous for *Opa3* (genotyped by PCR) to C57BL/6JCrl (Charles River, UK) or C3H/HeJ (MRC, Harwell) mice to create two separate lines on different backgrounds. $Opa3^{+/-}$ mice at each generation were inter-crossed to obtain homozygous $Opa3^{-/-}$ mice for analysis. Mice used in this study were from generation 1 (G1) (strain background 50:50 C3H/C57BL/6JCrl), generation 3 (G3) (background approx 95% C57BL/6JCrl or C3H/HeJ) and generation 4 (G4) (background approx 97.5% C57BL/6JCrl or C3H/HeJ).

Mice were housed in hard bottomed polypropylene experimental cages in groups of same sex siblings with mixed genotype. Lighting was controlled on a 12 hr light: 12 hr dark cycle and all mice were tested during the light phase. The housing facility temperature was maintained at 21°C and the relative humidity was also controlled at 60%. The mice had *ad libitum* access to water and standard dry laboratory food.

4.2.2 Genotyping offspring

All mice were genotyped for *Opa3* and initially for *Rd1* and *Nnt.*

4.2.2.1 Opa3 genotyping

Opa3 PCR genotyping was carried out to distinguish wildtype and mutant alleles using a forward primer mOPA3 exon 2: 5'-GGACGAAGATGCGCATAATGG-3' and a reverse primer mOPA3 exon 2: 5'-GTACAGTGAGCATTGCAGACC-3'. PCR amplification was performed in 25 µl reactions containing 0.2 mg genomic DNA, 20 pmol of forward and reverse primers, 10mM Tris-Hcl pH 8.3, 50 mM KCl, 1.5 mM $MgCl_2$, 200 µM of each dNTP and 1µl of *Taq* DNA polymerase (Bioline). The samples were placed in a Techne thermocycler for 35 cycles of 1 min denature at 92°C, 1 min anneal at 63°C and 1 min extension at 72°C with a final extension at 72°C for 5 mins. This provided a product size of 343bp. An enzyme digest using Pst1 enzyme (sequence CTGCAG; 10µl) on the 343bp product from the wild type (T allele) provides a major product of 205bp and on the recessive type (C allele) it provides a major product of 247bp (Fig 4.2.).

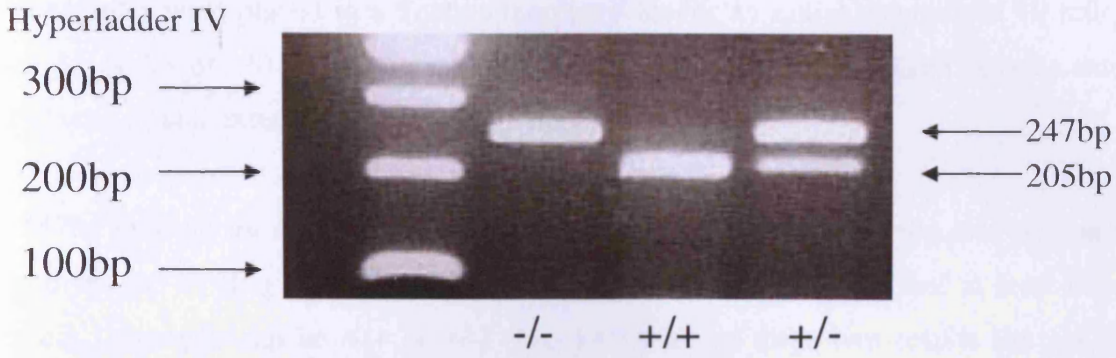

Figure 4.2. Agarose gel of PCR products for genotyping the *Opa3* colony

4.2.2.2 Rd1 genotyping

Rd1 genotyping was carried out as a multiplex reaction, with the following three primers in equal combination: RD3: 5'-TGACAATTACTCCTTTTCCCTCAGTCTGA-3', RD4: 5'-GTAAACAGCAAGAGGCTTTATTGGGAAC-3', and RD6: 5'-TACCCACCCTTCCTAA TTTTTCTCAGC-3' [Gimenez and Montoliu, 2000; Qiao *et al*, 2003]. The samples were placed in a Techne thermocycler for 35 cycles of 30 secs denature at 95°C, 30 secs anneal at 55°C and 30 secs extension at 72°C with a final extension at 72°C for 5 mins. The wild type *Rd1* allele was 300bp and the mutant allele was 450bp (Fig 4.3.) [Davies *et al*, 2007].

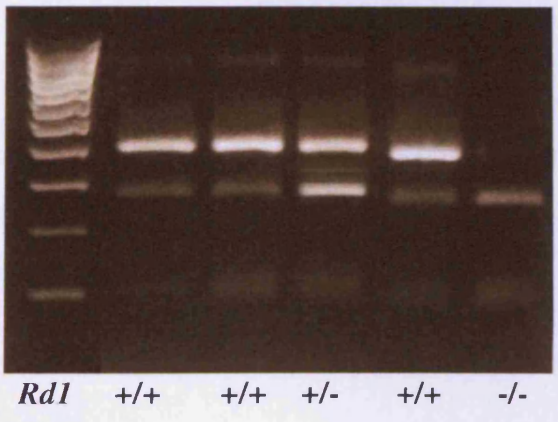

Figure 4.3. Mouse genotyping for selection of *Rd1* +/+ and *Rd1* +/– mice by multiplex PCR for *Rd1* alleles. The wild-type fragment is 300 bp and the mutant allele is 450 bp.

4.2.2.3 Nnt genotyping

Mice were genotyped by PCR for missing *Nnt* exons 7 to 11. Primers for *Nnt* exon 7 are: NntXn7 forward: 5'-GTGCATTGAACCCTCAAAGG-3' and NntXn7 reverse: 5'-CAGGTAAGAAAGCTCCTGTTTT-3' [Freeman *et al*, 2006]. Primers for *Nnt* exons 6 -12 are: Nnt6L4 forward: 5'-TCCCCTCCCTTCCATTTAGT-3' and Nnt12L1 reverse: 5'-GTAGGGCCAACTGTTTCTGC-3' [Huang *et al*, 2006].

The samples were placed in a Techne thermocycler for an initial denature of 10 mins at 95°C then 35 cycles of 30 secs denature at 94°C, 30 secs anneal at 60°C and 30 secs extension at 72°C with a final extension at 72°C for 5 mins.

A 547bp product for exon 6-12 primers indicate that exons 7-11 of the *Nnt* gene are missing (genotype is -/-) (Fig 4.4A.). A 250bp product for exon 7 indicate that at least one allele is present (genotype can be +/+ or +/-) (Fig 4.4B.). From these two results the genotype of a mouse can be deduced.

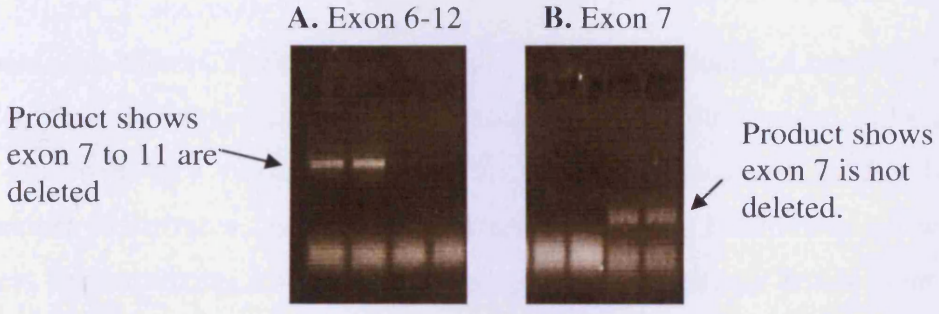

Figure 4.4. PCR genotyping for selection of *Nnt* +/+ mice. (A) Product for exon 6-12 primers indicates presence of deletion in at least one allele of *Nnt* (genotype can be -/- or +/-). (B) Product for exons 7 indicate that at least one allele is present (genotype can be +/+ or +/-).

All PCR products were visualized on a 2% agarose gel run at 120V.

4.2.3 Histology of mouse tissues on C57BL/6JCrl and C3H background strains

Tissues from G3/4 adult C57BL/6JCrl and C3H mice (*Opa3*$^{-/-}$ n=3, *Opa3*$^{+/+}$ n=3) were taken at 30 days old to assess for abnormal pathology. Retina, heart, lung, liver, kidney and muscle were taken from homozygote and wildtype animals and placed in 4% PFA. The tissues were fixed, dehydrated and processed as per protocols in Chapter II.

4.2.4 Embryology

Animals were paired/ mated and plugging was recorded. Embryos were collected and processed as per protocols in Chapter II.

4.2.5 Craniofacial Analysis

Craniofacial analysis was carried out by Prof Paul Sharpe, King's College, London, using the following three techniques.

4.2.5.1 Skeletal preparations

Skeletons were harvested, fixed in 95% ethanol and stained with Alcian blue (0.03% w/v in 95% ethanol with 20% acetic acid) overnight. After several washes with 95% ethanol, the skeletons were rehydrated, treated with 2% KOH for 12 hrs and then stained in 1% KOH containing 75 μg/ml Alizarin red S (Sigma-Aldrich) for 24 hrs. Excess stain was removed by clearing in 1% KOH / 20% glycerol and, after washing in 0.2% KOH / 20% glycerol, skeletons were stored in 50% glycerol.

4.2.5.2 MicroCT analyses

Specimens for microCT were scanned using a General Electric Locus SP microCT scanner (GE Healthcare). The specimens were immobilised using cotton gauze and scanned to produce 14-28 μm voxel size volumes. The specimens were characterised further by making three-dimensional isosurfaces, generated and measured using Microview software (GE). Skull thickness measurements and bone histomorphometry on femur heads were made using the Direct Measures component of the Advanced Bone Analysis package of Microview.

4.2.5.3 Bone and cartilage analyses

For differential staining of bone and cartilage, 18.5dpc mice were fixed overnight in 95% ethanol, skinned, and eviscerated. Cartilage staining was carried out by soaking in a solution of 76% ethanol, 20% glacial acetic acid, and 0.015% Alcian blue 8GX (Sigma-Aldrich) for 24 hrs, differentiating for 7 days in 95% ethanol, macerating in 1% KOH for 24 hrs, and washing overnight under running tap water. Bone staining was carried out by transferring the heads to a freshly made 0.1% aqueous solution of Alizarin red S, with the addition of several drops of 1% KOH to enhance the darkness of the red colour. The samples were then washed for 30 mins under running tap water, decolourised in 20% glycerol in 1% KOH for 1–2 weeks, and prepared for storage in increasing concentrations of glycerol in 70% ethanol to a final concentration of 100% glycerol. Skeletal preparations were photographed in light-field, using a Leica stereomicroscope, while submerged in 100% glycerol.

4.2.6 Statistics

1 tailed, binomial exact test was used for all genotyping results. P values ≤ 0.05 were considered statistically significant.

4.3 Results

4.3.1 Phenotypic manifestations of *Opa3* mutation in G1 mice

In the heterozygous state, mice are phenotypically indistinguishable from their wildtype littermates and have no difference in survival rates. The homozygote mice show no gross abnormalities at birth except being usually smaller than their littermates. They display a phenotype which has a highly variable time of onset and variable lifespan. Some of the characteristics displayed include: 'runted' appearance at birth, frail weak appearance, craniofacial abnormalities, splayed gait and tremor (Fig 4.5.).

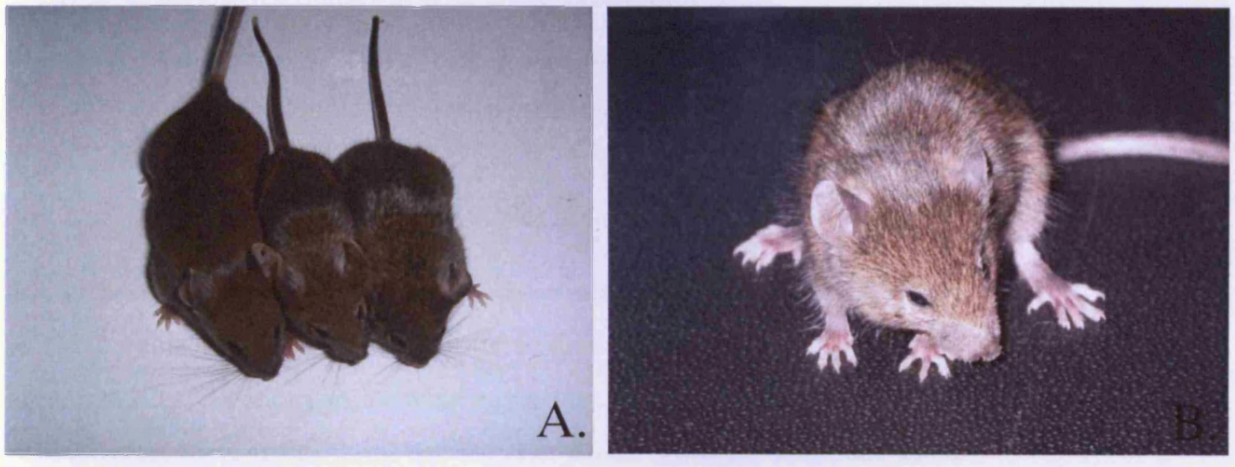

Figure 4.5. Visible traits associated with G1 *Opa3* homozygous mice. (A) Wildtype on left, middle and right are homozygotes. Homozygote on the far right has a craniofacial defect. (B) Homozygote showing splayed gait [Davies *et al*, 2008].

Genotyping at around 21 days of age when they are weaned from their mothers showed a loss of homozygotes by this time. However, the proportion was not significantly different from the expected 25% (see Table 4.1.). The majority die within 12-16 weeks of postnatal age but in a few isolated instances animals have survived to seven months of age. It was not possible to investigate the progeny of *Opa3* homozygote intercross or outcross matings due to the frail state of the homozygotes in terms of health and size. Intercrosses and outcrosses were set up, but pregnancy was never established.

Generation1	Expected	Observed
genotype (n=105)		
+/+	26.25 (25%)	22 (21%)
+/-	52.5 (50%)	62 (59%)
-/-	26.25(25%)	21 (20%)

Table 4.1. Obtained and predicted genotype viability of *Opa3* G1 heterozygote inter-crosses (n = 105). Number of homozygotes observed was 80% that of the expected number (1 tailed, binomial exact test; P = 0.141).

The highly variable longevity and onset of phenotype seen in the G1 mice is in part due to the mixed genetic background which made analysis of the phenotype difficult. It was therefore decided to breed the mutation to a more congenic C57BL/6JCrl background in the hope of reducing the variability in the time of disease onset. The time scale to make mice congenic (which would be 20 generations) was considered too long so the phenotype was again studied at G3 and G4.

4.3.2 Phenotypic manifestations of *Opa3* mutation in G3/4 mice

In G3/4 mice there was no obvious perinatal difference between the *Opa3* wildtypes and heterozygotes. Homozygotes were generally smaller at birth. Some of the litter were very pale at birth, these usually did not survive the next 24 hrs. These are known to occasionally be heterozygotes, as well as homozygotes.

Visible traits observed in the homozygote mice include: stunted growth, craniofacial abnormalities and splayed gait (Fig 4.6.). As the *Opa3* homozygote mice become compromised they display, tremor, hunched physique (Fig 4.6D.), reduced body fat and have reduced locomotor activity. By G3/4 a very small number of heterozygotes displayed various aspects of the homozygote phenotype. Phenotype was assessed in-depth in Chapter V.

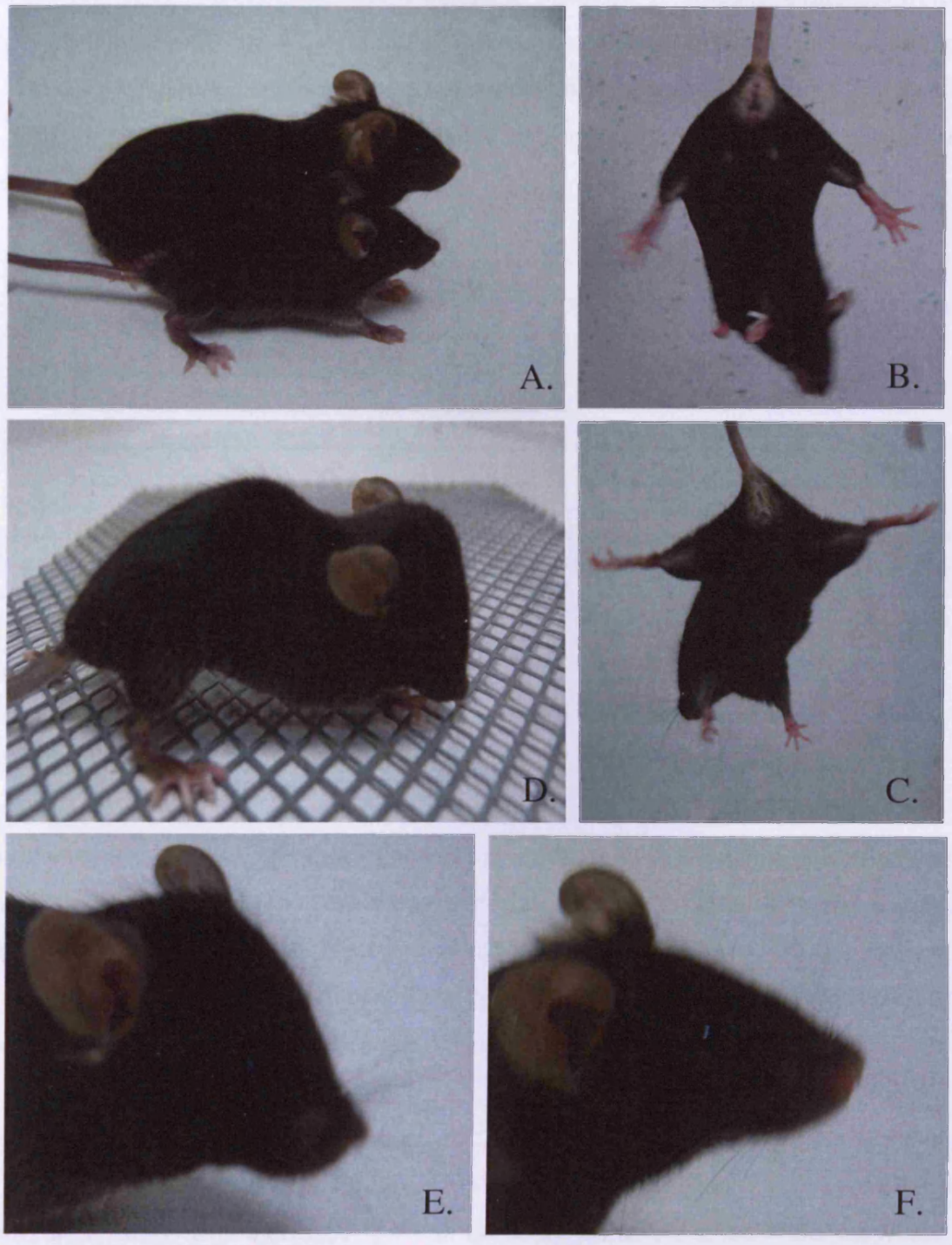

Figure 4.6. Visible traits associated with the G3/4 *Opa3* homozygous mice. (A) Homozygote in the foreground showing smaller size with wildtype sibling behind. (B) Wildtype showing normal leg postion. (C) Homozygote showing hind limb extension phenotype. (D) Homozygote showing hunching, splayed gait and craniofacial defects. Craniofacial phenotype has incomplete penetrance with (E) homozygote displaying craniofacial defects and (F) homozygote displaying normal cranium.

4.3.2.1 Opa3 mouse viability

Matings were set up and progeny were observed to assess survival rates. Wildtypes were seen in expected numbers (Table 4.2.). Of the 42 heterozygotes observed three died within the first two days after birth and a further three heterozygotes were found dead at days 24, 29 and 41. This again suggests the presence of congenital defects in the heterozygotes as well as the homozygotes.

Generation 3 genotpye (n=73)	Expected	Observed
+/+	18.5 (25%)	19 (26%)
+/-	37 (50%)	42 (57%)
-/-	18.5 (25%)	12 *(17%)

Table 4.2. Obtained and predicted genotype viability of *Opa3* G3 heterozygote inter-crosses (n = 73). Number of homozygotes observed was 68% that of the expected number (1 tailed, binomial exact test; $*P < 0.05$).

By G3 there is a statistically significant loss of homozygotes by weaning at 21 days of age (Table 4.2.). This is a 12% increase compared to the G1 mice. Loss maybe more than this as many pups die very quickly around birth and DNA could not be procured quickly enough for a genotyping result. Also, the mothers were observed to eat dead/dying newborns so exact loss is difficult to estimate. The survival rate of each genotype at G3 is portrayed as a Kaplan-Meier survival curve (Fig 4.7.). The survival rate of the homozygotes at G3 can be seen to be to be statistically significantly different form that of the wildtype controls (P=0.000). Survival of the heterozygotes was not significantly different for wildtypes.

As the C57BL/6JCrl component of the genetic background increases, a greater percentage of mice are lost in the first few weeks of life. By G4 there is greater than 40% loss of the litter by weaning at 21 days. This increased loss can be portrayed as a Kaplan-Meier survival curve, which shows survival of the mice as they progressively become more congenic to C57BL/6JCrl with each generation (Fig 4.8.). The curves show the loss of all mice at each generation during the first 21 days, not just the homozygotes. The survival rate of mice at G4 is significantly less compared to previous generations (P=0.000). At G4 the severity spectrum of the phenotype seems to have remained the same as at G1 but life span has decreased and

onset of disease phenotype is less variable and earlier. This indicates the potential presence of a strain-specific modifier(s) on C57BL/6JCrl.

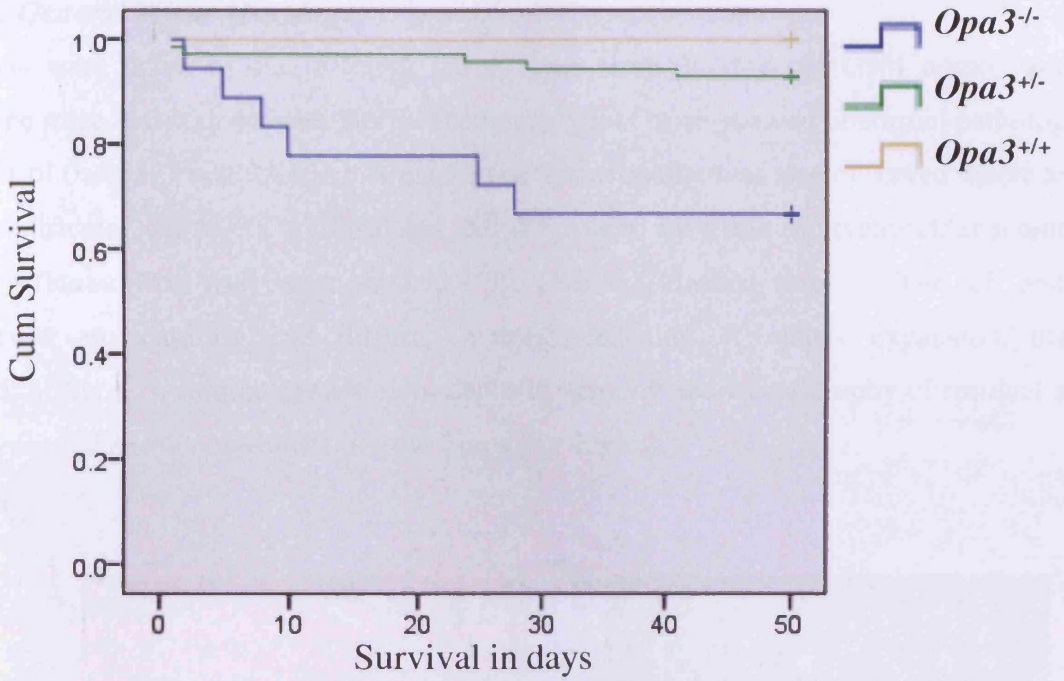

Figure 4.7. Kaplan Meier survival curve showing decreased survival rate of G3 homozygotes compared to heterozygote and wildtype mice from birth to 50 days of age. The survival rate of the homozygotes was statistically significantly less compared to wildtype controls (Long Rank (Montel-Cox) *P*=0.00).

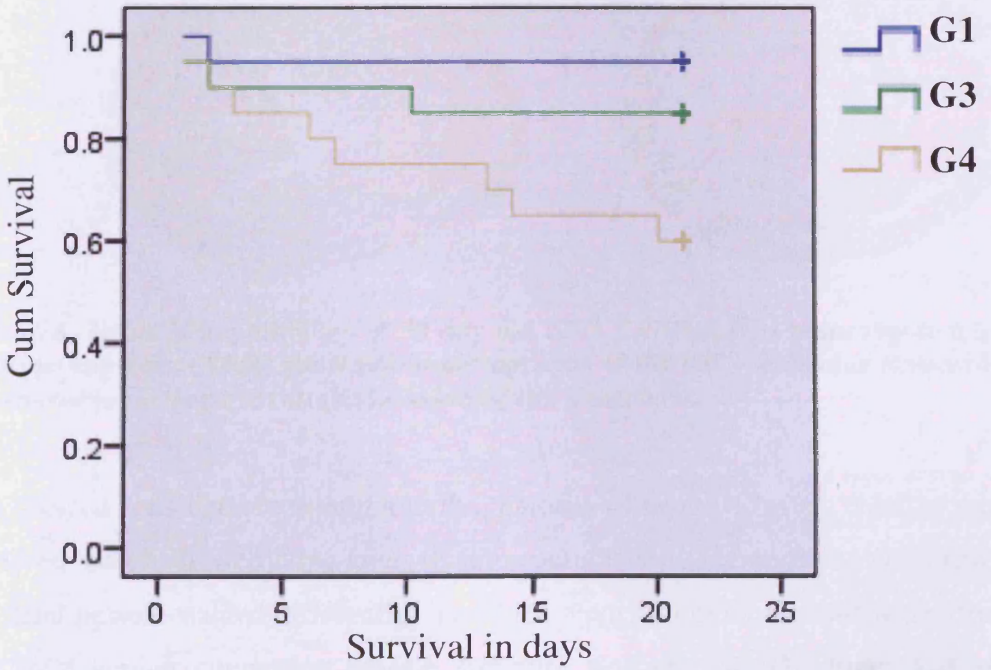

Figure 4.8. Kaplan Meier survival curve showing decreasing survival rates of mice at each generation from birth to 21 days of age as they progressively become more congenic to C57BL/6JCrl. The survival rate of the G4 generation was statistically significantly less compared to the G1 genertion (Long Rank (Montel-Cox) *P*=0.00).

4.3.2.2 General Tissue Histology

Sections were taken of six different tissue types from 30 day old G3/4 homozygote and wildtype mice and stained with H&E. The homozygote mice showed abnormal pathology in a number of tissues (Fig 4.9A&B.). A marked cardiomyopathy was also observed where left and right ventricular chambers were dilated (solid arrows). Both the interventricular septum and left ventricular free wall were thinned (Fig 4.9A.D.) (dashed arrows). The left and right ventricular myocardium had diffuse changes consisting of matrix expansion, inducing interstitial fibrosis, cardiac muscle fibre deposits, atrophy and hyperatrophy of residual muscle fibres, as well as vacuolation of muscle fibres (fig 4.9A.B.).

A.

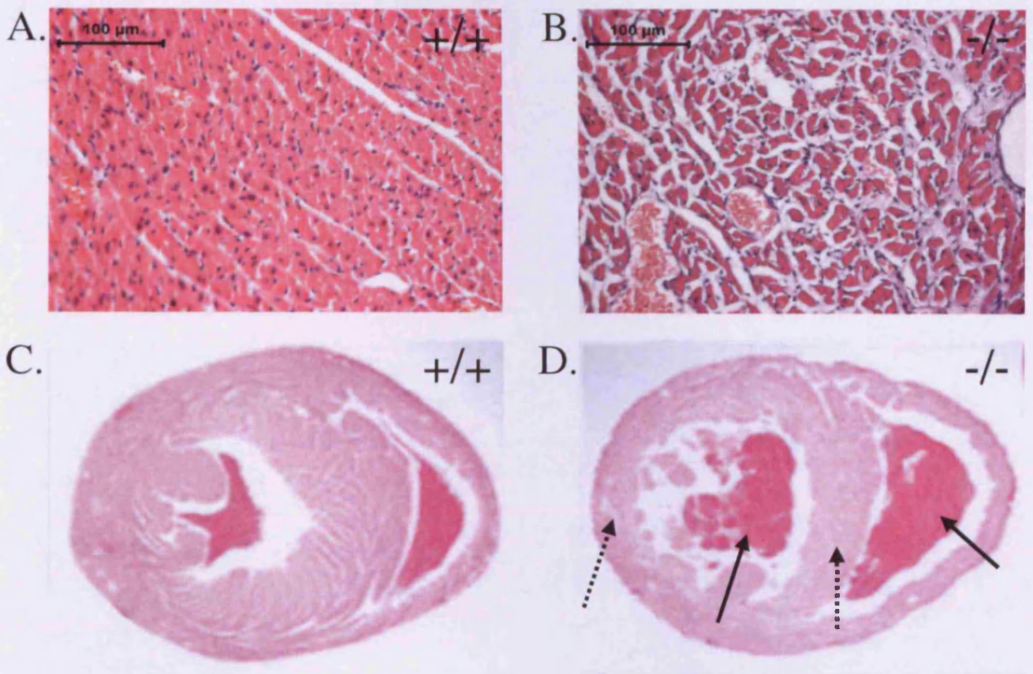

Figure 4.9A. Heart histopathology of 30 day old G3/4 C57BL/6JCrl homozygote mice compared to wildtype controls. (A&B) show photomicrographs of the left ventricular myocardium. (C&D) are transverse sections through the base of the ventricles.

Retina showed considerable thinning in the majority of layers. Chronic changes were observed in the liver, which showed large areas of fat accumulation (Fig 4.9B.) (solid arrow). Although the skeletal muscle stained differently, the fibres were of similar size/shape and the number of nuclei were similar suggesting muscle structure was normal. The lungs and kidneys also appeared to be normal by H&E histology. This analysis will only detect gross pathology, but is very useful as a starting point for indicating abnormalities that require further investigation.

Hepatic steatosis was analysed in Chapter VI and retinal thinning was further assessed in Chapters VII and VIII.

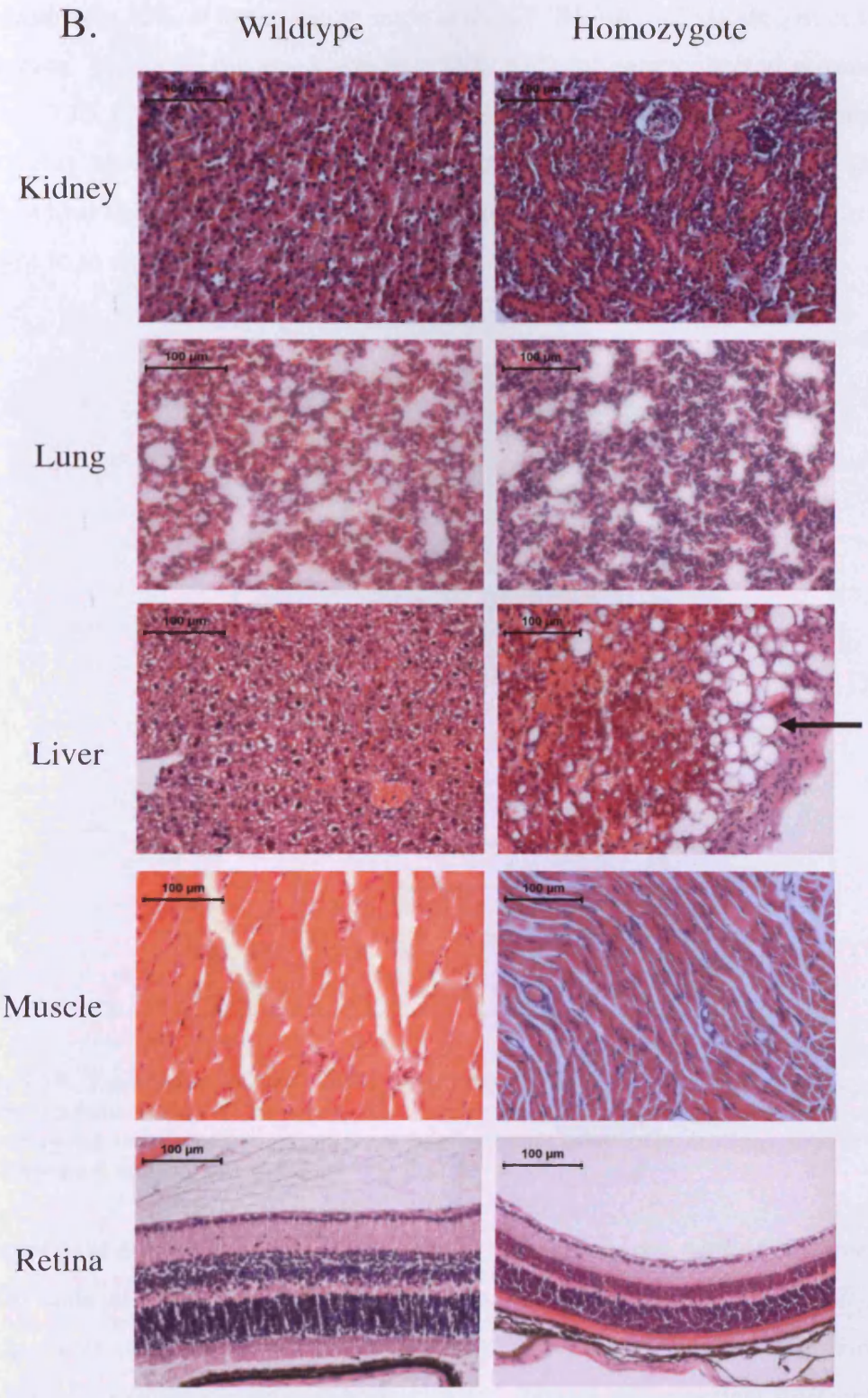

Figure 4.9B. Histological examination of G3/4 C57BL/6J mouse tissues. Magnification x20

4.3.2.3 Embryology

Approximately 35% of homozygote mice in the C57BL/6JCrl G3/4 are lost at some point prior to weaning. To assess for any embryonic loss, embryos were collected at various time points between 13.5 dpc and birth. Of the homozygote embryos observed none showed any gross abnormality except being slightly smaller than the wildtypes (Fig 4.10A.). The heterozygote embryos also showed no outward abnormalities but their size was variable, from as large as a wildtype to as small as a homozygote.

A.

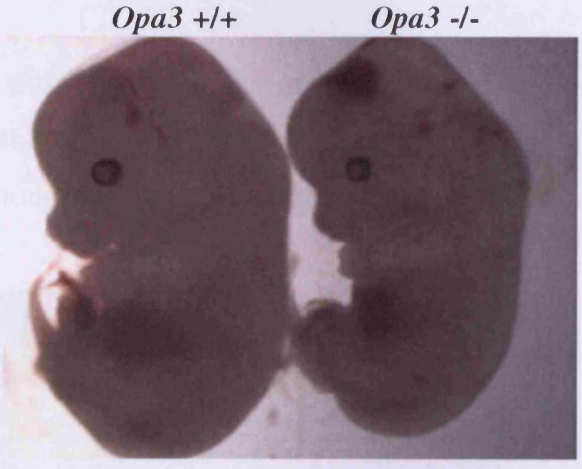

B.

	+/+	+/-	-/-
P0	**10** (9.25)	**19** (18.5)	**8** (9.25)
18.5dpc	**3** (3.75)	**9** (7.5)	**3** (3.75)
13.5dpc	**3** (3.25)	**8** (6.5)	**2** (3.25)

Figure 4.10. Embryonic viability of the *Opa3* mice at 13.5 dpc, 18.5 dpc and P0. (A) Micrograph showing 13.5dpc embryos. Homozygotes display no gross abnormalities except smaller size. (B) Table showing viability of embryos from heterozygote inter-cross matings. Observed numbers in bold. Expected numbers in brackets.

The number of embryos collected did not allow for an accurate estimate of time of lethality but no dead embryos or empty/absorbing deciduas were observed at any time points between 13-18.5 dpc. This suggests that no homozygotes were being lost between approximately 11.5 dpc and birth. Genotyping results of homozygotes showed no statistical difference in observed numbers from the expected numbers (Fig 4.10B.). Observations of dead pups at birth would suggest a large proportion of the loss is at birth.

4.3.3 Phenotypic manifestations of *Opa3* mutation in G3/4 mice on a C3H background

In an attempt to increase the survival rate of the *Opa3*$^{-/-}$ mice in order to improve the analysis of the phenotype a second line of mice was developed, outcrossed to a C3H background. A strain of C3H was obtained from MRC Harwell that did not carry the *Pde6b* mutation (which causes retinal degeneration). This removed the need for continued *Rd1* genotyping. By making the mouse more congenic to C3H and by removing the *Nnt* deletion, by selective breeding, a comparison of the *Opa3* mutation on two different backgrounds could be made and effects of *Nnt* on the phenotype could be analysed.

The G3/4 mice on the C3H background showed no difference in visible traits compared to the same generation C57BL/6JCrl mice (Fig 4.11.). Also, there was no improvement in longevity on this genetic background, with 38% of homozygotes lost before weaning (Table 4.3.).

Figure 4.11. Visible traits associated with G3/4 C3H mice. Wildtype behind with homozygote in forefront displaying craniofacial defect, splayed gait, hunched posture and tail kink.

Generation 3/4 genotype (n=163)	Expected	Observed
+/+	40.75 (25%)	48 (29%)
+/-	81.5 (50%)	86 (53%)
-/-	40.75 (25%)	29 *(18%)

Table 4.3. Obtained and predicted genotype viability of *Opa3* G3/4 C3H heterozygote inter-crosses (n = 163). Number of homozygotes observed was 72% that of the expected number (1 tailed, binomial exact test; *$P < 0.05$).

The G3/4 C3H mice do not carry the *Nnt* deletion. Therefore, because an almost equal number of homozygotes were lost on each background strain (G3/4 C3H-38%; G3 C57BL/6JCrl-35%) this suggests that *Opa3* does not interact with *Nnt* and therefore has no effect on the *Opa3*^{L122P} mouse phenotype. In addition, in the C57BL/6JCrl homozygote mice no correlation was ever observed between *Nnt* genotype and severity of mutant phenotype.

4.3.3.1 General Tissue Histology

Histology of G3/4 C3H tissues showed no differences in pathology when compared to the same G3/4 generation C57BL/6JCrl mice. As with the C57BL/6JCrl line, only the retina and liver (solid arrow showing fat deposits) appeared to be grossly abnormal (Fig 4.12.). Yet again, the muscle seems structurally normal but stains a different colour despite being processed in the same batch as the wildtype tissue.

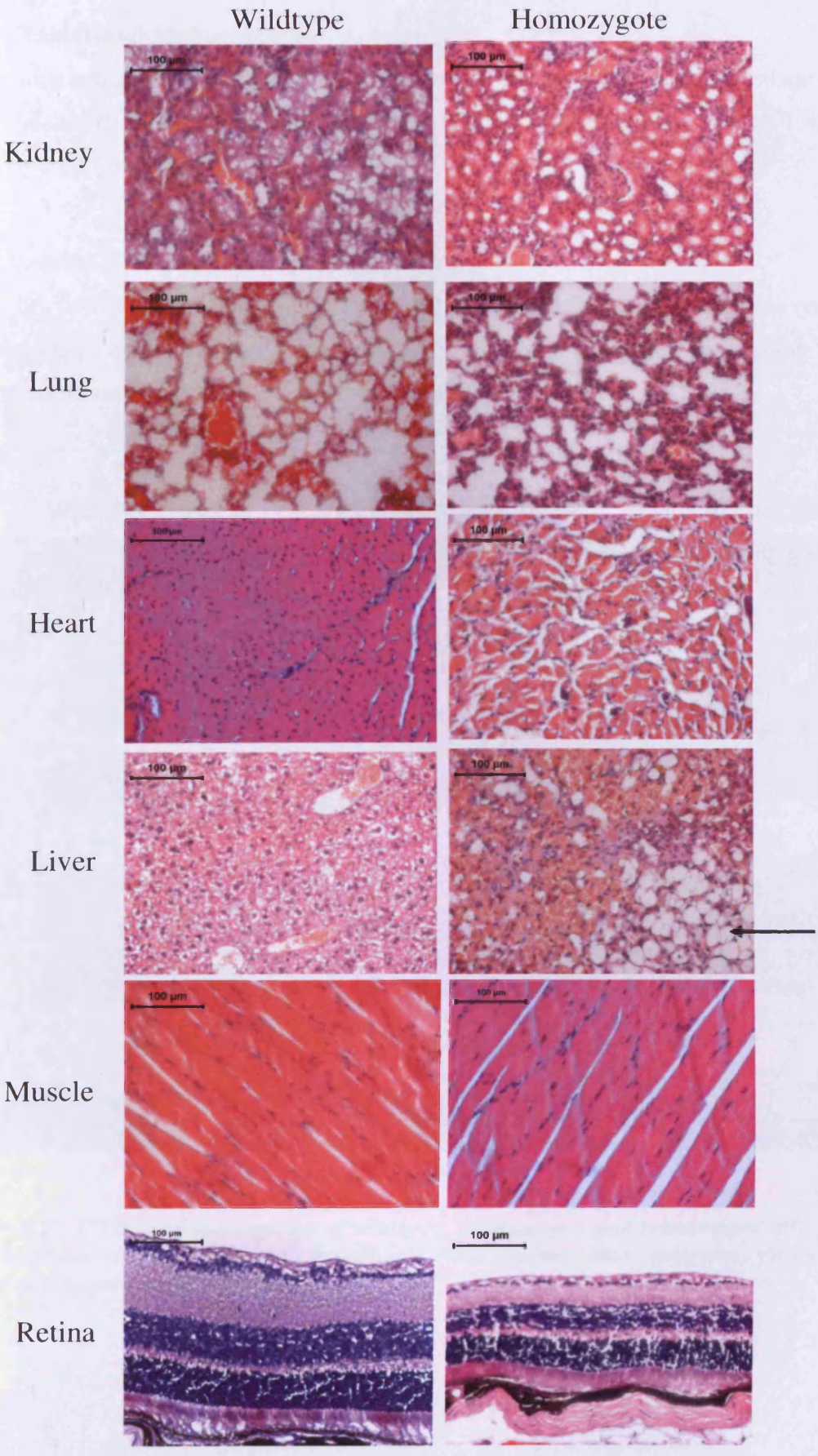

Figure 4.12. Histological examination of G3/4 C3H mouse tissues. Magnification x

4.3.4 Craniofacial Malformations

Adult mice and embryos ranging from 16.5 dpc to P4 were collected in 95% ethanol or 10% NBF and sent to the craniofacial department at Guy's Hospital London. MicroCT scans were taken by Prof Paul Sharpe.

4.3.4.1 MicroCT scan analysis of G1 adult mice

Some G1 homozygotes displayed a shortened nose and broader distance between eyes and this phenotype has incomplete penetrance in the homozygotes. From observation alone there is no outward difference in the heterozygotes (Fig 4.13. & 4.14.).

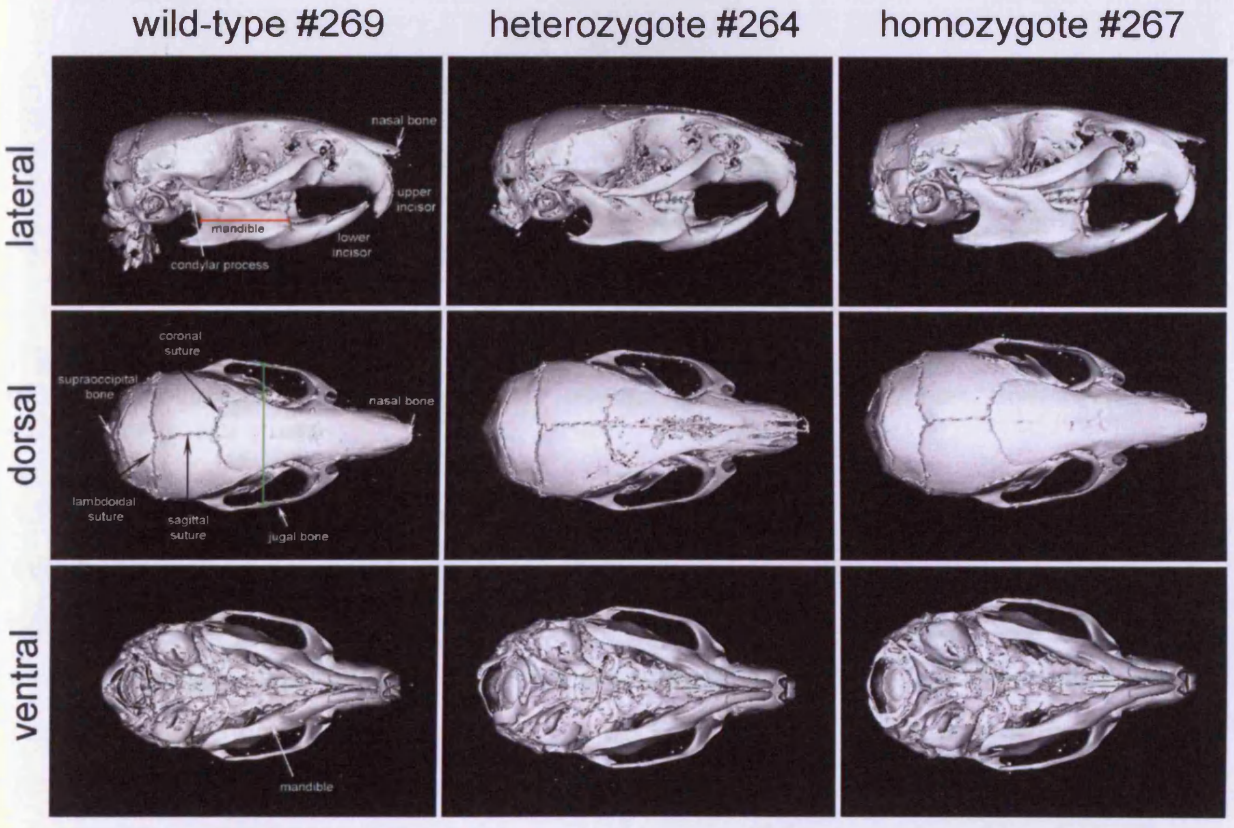

Figure 4.13. CTscan of the cranium of wildtype, heterozygote and homozygote littermates. Red line indicates measurement of mandible width. Green line indicates measurement of chondrocranium width.

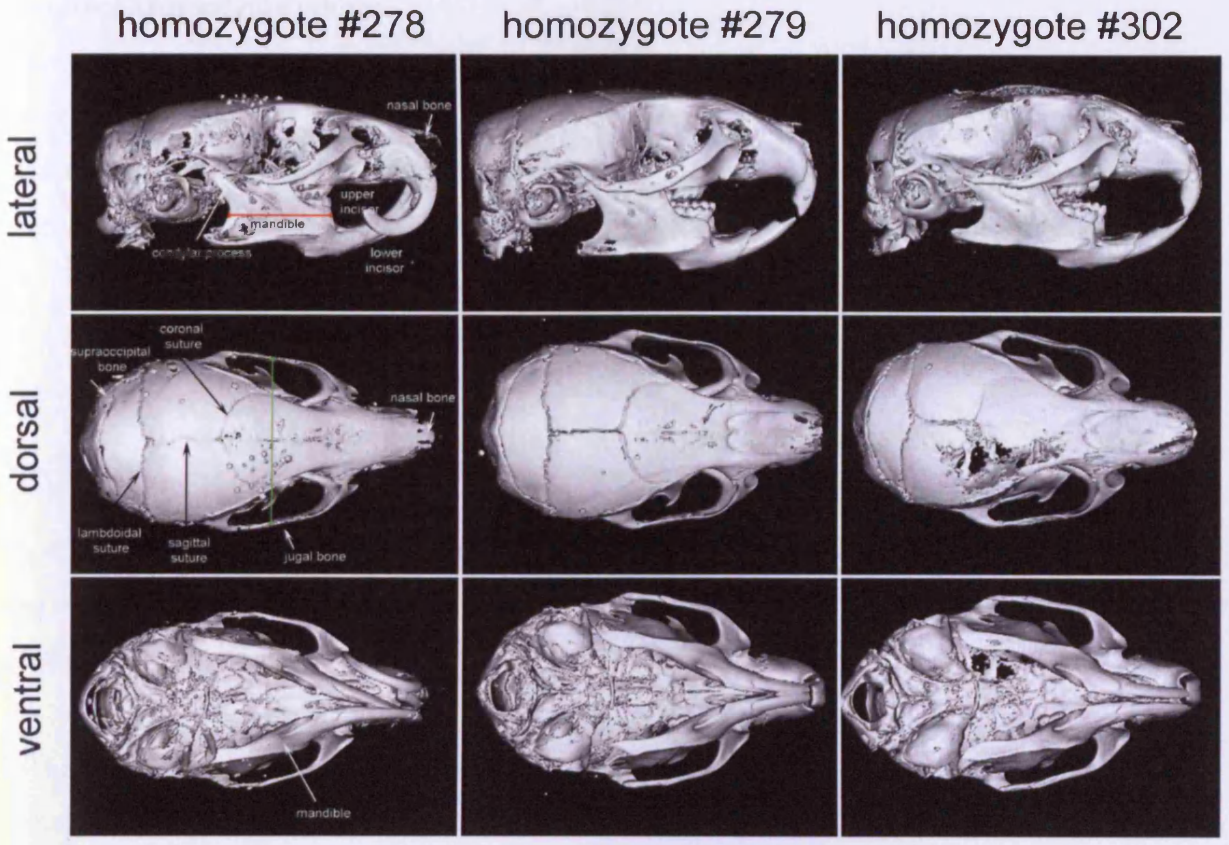

Figure 4.14. CTscan of three other homozygotes showing the craniofacial phenotype. Red line indicates measurement of mandible width. Green line indicates measurement of chondrocranium width.

4.3.4.2 Summary of the mutant phenotype on CT

The skulls of the heterozygote and homozygote mice generally appear to be larger than the skulls of wildtype mice suggesting that more bone ossification was occurring in the mutants. This correlates with analysis of bone development in the mutants at 18.5 dpc, following staining of the bone with Alizarin red. The microCT analysis also revealed that in general, the chondrocranium and dermatocranium of the homozygotes showed considerably more bone ossification than observed in the heterozygotes. The following notes highlight the changes in bone structure in the heterozygote and homozygote mutants compared to the wildtypes. It is important to bear in mind that a caveat to these conclusions is that the measurements taken are subjective to the manual positioning of individual reference points within the skull:

Skull measurements taken:

Measurements were taken from wildtype (n=1), heterozygote (n=1) and homozygote (n=4) mice.

Mandible (red line on figures 33 and 34)

Lateral view of the mandible of the heterozygote and homozygote cranial skeletons showed that it was consistently broader than the lateral view of the wildtype mandible (red line):

Wt (#269): 4.47mm

Het (#264): 5.59mm

Hom (#267): 5.97mm, Hom (#278): 5.83mm, Hom (#279): 5.14mm, Hom (#302): 4.82mm

Homozygotes displayed an average mandible width of 5.44mm ± S.D 0.55. In particular, note the increasing width and thickening of the condylar process within the mandible of the mutants.

-Chondrocranium length

Measurements taken along the dorsal length of the chondrocranium (from the supraoccipital bone to the nasal bone) confirm the skulls of the heterozygote and homozygote mice are longer than the skull of wildtype mice.

Wt (#269): 15.50mm

Het (#264): 20.42mm

Hom (#267): 20.65mm, Hom (#278): 19.74mm, Hom (#279): 17.65mm, Hom (#302): 19.38mm

Homozygotes displayed an average chondrocranium length of 19.35mm ± S.D 1.25.

-Chondrocranium width (green line on figures 33 and 34)

Measurements taken across the dorsal view of the jugal bone (green line) provide controversial results regarding the width of the skulls of the heterozygote and homozygote mice compared to wildtype mice. These measurements do not support any consistent increase in the width of the skulls of heterozygote and homozygote mice.

Wt (#269): 11.30mm

Het (#264): 11.68mm

Hom (#267): 11.30mm, Hom (#278): 9.21mm, Hom (#279): 9.20mm, Hom (#302): 11.13mm

Homozygotes displayed an average chondrocranium width of 10.21mm ± S.D 1.16. The craniofacial phenotype observed in the G1 homozygotes has been observed in G3/4 homozygotes and heterozygotes. Embryos of G4 mice were sent to Guy's Hospital London to assess for any abnormalities in development of the skull in the heterozygotes and homozygotes.

4.3.4.3 Embryonic bone and cartilage analysis in G4 mice

The majority of bones in the cranial skeleton of the heterozygote embryo developed similarly to the wildtype embryo (Fig 4.15.). Ossification of the bones of the frontal (f), parietal (p), interparietal (i) exoccipital (e) and tympanic ring (tr) was normal in heterozygote embryos. The heterozygote embryos did however exhibit some craniofacial abnormalities; greater ossification of the mandible (md) and premaxilla (premx), while the temporal (t) bone appeared misshapened and the bones of the maxilla (mx) appeared expanded. Further analysis of the development of these specific bone anomalies in the neonatal pups will be important.

At this stage of embryonic development, cartilage development in the wildtype and heterozygote embryos was comparable. There were no obvious defects in cartilage development in the heterozygote embryos (Fig 4.15.).

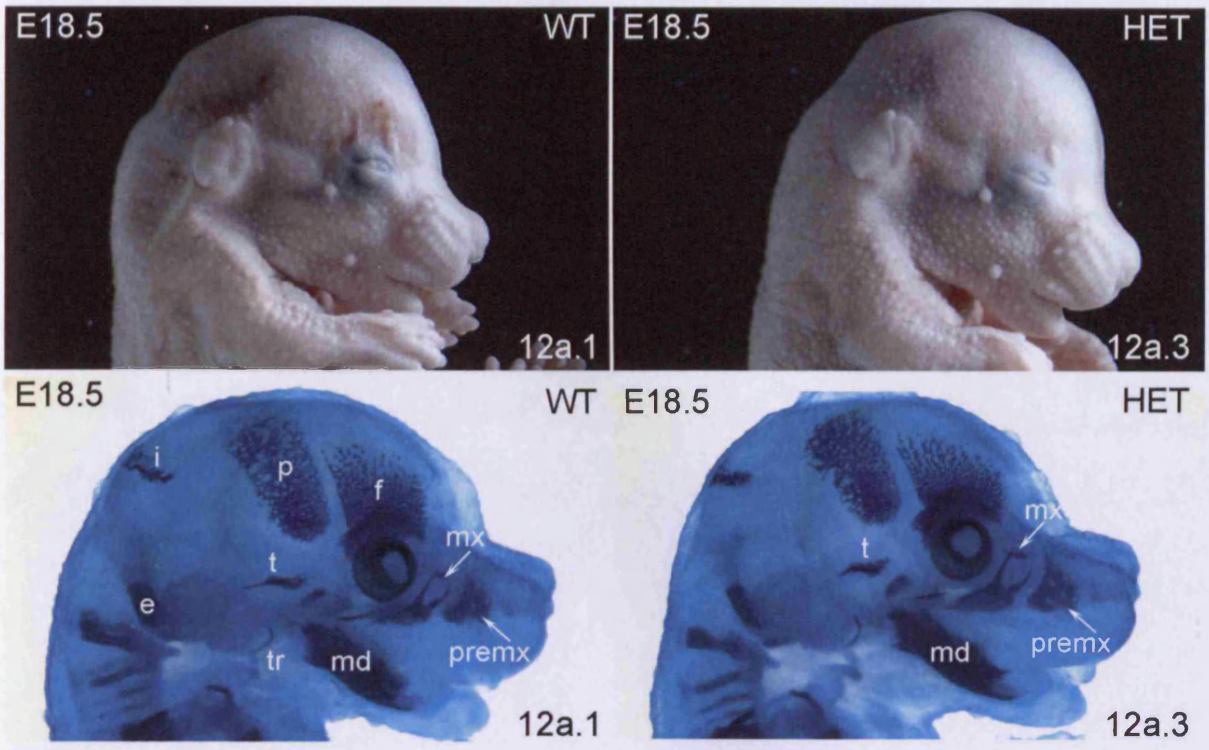

Figure 4.15. Bone (Alizarin red) and Cartilage (Alcian blue) analysis of G4 embryos at 18.5 dpc.

4.3.4.4 Bone (Alizarin red) and Cartilage (Alcian blue) analysis at 18.5 dpc (NBF fixed embryos).

These embryos were fixed in NBF (rather than 95% EtOH) prior to be sent for bone and cartilage analysis. This treatment seems to have caused the skin surrounding the forebrain, midbrain and anterior hindbrain to collapse in both the heterozygote and homozygote embryos. This resulted in the embryonic skin becoming light and difficult to remove either by gentle agitation in 1% KOH or by manually dissecting away the skin layer. For future studies, it would be better to fix the embryos in 95% EtOH rather than NBF.

The poor representation of cartilage staining in both the heterozygotes (Fig 4.16C.) and homozygotes (Fig 4.16D.) does not appear to be a result of the mutant phenotype. Rather, it appears that fixing these embryos in NBF led to the poor penetration of the Alcian blue stain and poor staining of the cartilage in these mutant embryos. Treatment with 1% KOH failed to remove the skin layer and following manual dissection of the skin from these embryos (Fig 4.16E. and F.), it was clear that the cartilage had not been sufficiently stained. Re-treating these mutant embryos with Alcian blue resulted in an overall blue tinge to the embryo (data

not shown) and did not identify cartilage typically observed at this stage of embryonic development (i.e. nasal cartilage, Meckel's cartilage).

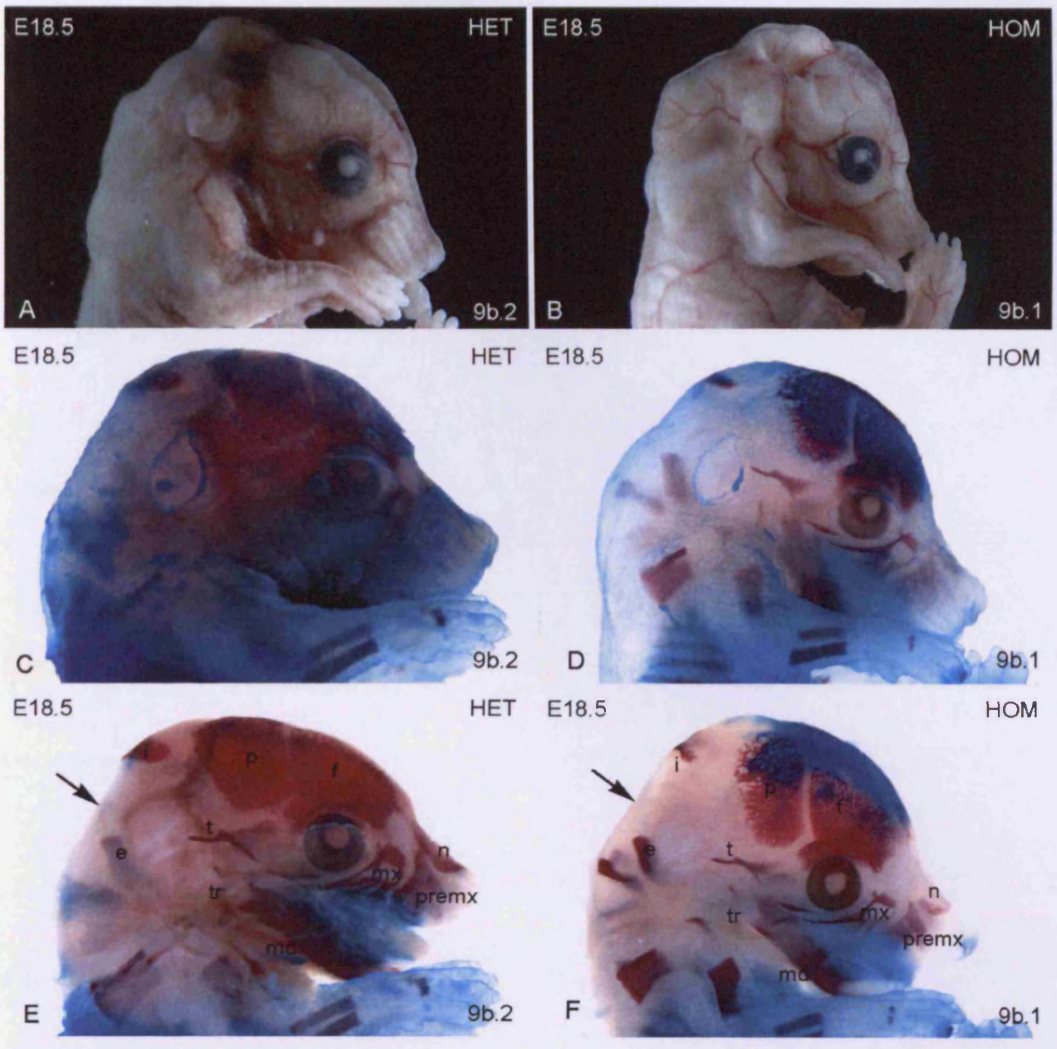

Figure 4.16. Bone and cartilage analysis of 18.5 dpc embryos fixed in NBF.

Staining of the bone with Alizarin red revealed that while both mutants exhibited abnormalities in bone ossification, these abnormalities were more severe in the homozygote embryo. Compared to the bone development in a typical 18.5 dpc embryo, in these mutants, ossification of the frontal (f) and parietal (p) bones of the cranial vault was evident but reduced and there was a marked reduction in ossification of the interparietal (i) bone in both the heterozygote (Fig 4.16E.) and homozygote (Fig 4.16F.) embryos. While staining of the exoccipital bone (e) was evident there was poor ossification of the tympanic ring (tr), mandible (md), nasal bone (n), premaxilla (premx) and maxilla (mx) and there was no ossification of the supraoccipital bone (arrow) in either of the homozygote embryos.

Analysis of the heterozygote embryo (Fig 4.16E.) also showed that while the temporal bone (t) had formed appropriately ossification of this bone was not complete. In comparison, the temporal bone (t) in the homozygote embryo (Fig 4.16F.) appeared to be abnormally shaped and with poor ossification.

4.4 Discussion

These results demonstrate that the G1 homozygote mice displayed a highly variable phenotype and longevity which made analysis of the disease phenotype difficult. By G3/4 onset of homozygote phenotype was more consistent but survival rates had decreased. *Nnt* was found to have no effect on disease phenotype and breeding the *Opa3*^{L122P} mutation on to a C3H background showed no improvement in survival rates. H&E showed severe pathology of the retina and cardiac muscle which would be consistent with a metabolic disorder affecting tissues of high energy demand. Interestingly, liver pathology showed a large accumulation of fat. Craniofacial analysis in the G1 adult mice showed an increased skull size in homozygotes and heterozygotes with increased ossification of some bones. In the G3/4 embryos the *Opa3*^{L122P} mutation was found to affect bone development but not cartilage development.

Embryo genotyping and a lack of reabsorbing deciduas during development suggests that the vast majority of homozygotes are dying at birth. Why would a P0 mouse die? The timing suggests a cardiac, circulatory, or pulmonary cause of death. At birth, the heart undergoes a critical metabolic switch from a predominant dependence on carbohydrates during fetal life to a greater dependence on postnatal oxidative metabolism. This remains the principle metabolic state throughout life, although pathologic conditions such as heart failure and cardiac hypertrophy reactivate components of the fetal genetic program to increase carbohydrate utilisation. The homozygotes do suffer with a severe cardiomyopathy, which is the likely cause of death, and *Opa3* is thought to cause defects in oxidative metabolism which might have a severe effect after the postnatal switch to oxidative metabolism. Some pups however, appear very pale at birth, this can be an indicator of problems such as anaemia or a defect in the breathing centres of the brain which can lead to perinatal lethality.

Those homozygotes that did survive past birth had a dramatically shortened lifespan. Cardiomyopathy could be the primary cause of their death, or it could be a secondary consequence of either mitochondrial dysfunction or multiple organ failure. No attempts to breed from them have been successful. It must therefore be assumed they are sterile or metabolically/ endocrinologically incapable of either conception or very early pregnancy.

The *Opa3*$^{-/-}$ mice are distinguishable from their littermates usually from birth due to their smaller size. It is often speculated that ataxic mutants are smaller than their littermates due to competition for food during the early stages of development [Lalonde and Strazielle, 2003]. This maybe a contributing factor during postnatal development. However, the homozygotes are observed to be smaller during embryonic development and therefore, postnatal ataxia/ skeletomuscular deficits cannot be solely to blame.

It can be seen from the Kaplan Meier survival curve (Fig 4.8.) that when the *Opa3* mutation was made more congenic to C57BL/6JCrl longevity is decreased. There were a few possible reasons for a decrease in lifespan and earlier onset of phenotype. As the gene-pool becomes more limited, caused by continued inbreeding, deleterious genes become widespread and the inbred strain loses hybrid vigour. It is also possible for the phenotype to not be entirely controlled by the mutation at the causative locus. A phenotype associated with a single gene mutation can be modulated by the genotype at other loci. The effect of the genetic background (i.e. different strains of mouse) can be invoked in the intermediate situation (i.e. mixed background) where phenotypic variations can be observed among individuals who carry the same mutation in the same causative gene but differ in a number of other genes. A few of these genes can control part of the phenotypic variation and hence are called 'modifier loci'. By using G3/4 (approximately 87% C57BL/6JCrl and 94% C57BL/6JCrl respectively), the mice have a variable genotype at each loci and therefore each mouse would be 'modified' in a different way, which created variability.

Another interesting point is that phenotypes associated with a mutation can vary among genetically identical individuals. This variation could be attributable either to incomplete penetrance, when a fraction of the individuals carrying the disease-associated genotype failed to develop the abnormal phenotype, or to variable expressivity, when individuals carrying the disease-associated genotype exhibit phenotypes with varying degrees of severity. The craniofacial phenotype in the heterozygotes and homozygotes is probably either incomplete penetrance or variable expressivity.

During the breeding of the Opa3^{L122P} mouse to C57BL/6JCrl it was thought prudent to breed out the deleted *Nnt* gene carried by this strain. *Nnt* is expressed in the IMM and so might interact with *Opa3*. No correlation was found between severity of disease phenotype and *Nnt*

genotype. After it was bred out of the colony no difference in phenotype or longevity was observed, suggesting *Nnt* does not interact with *Opa3*.

Changing the background to C3H had no significant effect on lifespan or onset/variability of disease phenotype. Therefore breeding to the C3H background was abandoned and all further experiments in this thesis were conducted on G3/4 C57BL/6JCrl mice.

4.4.1 Craniofacial malformations

The *Opa3* mouse has a craniofacial defect showing shorter nose, wider set eyes and longer head. Some homozygotes also had problems with overgrown teeth from a jaw misalignment, possibly from the craniofacial abnormalities. There is also the potential of deformed hind limbs, since the abnormal walking pattern of splayed gait was detected before onset of neurological symptoms.

Although MGA-III is considered to be a mitochondrial disorder, there are certain aspects of the mouse phenotype that are not found in human MGA-III or diseases of mitochondria dysfunction. One such anomalous feature is craniofacial malformations. It is therefore of some interest in this context that OPA3 has a functional C-terminal peroxisomal targeting signal, albeit only in the absence of a functional N-terminal mitochondrial leader sequence. Mitochondria share some roles with the peroxisomes, small organelles with diverse, cell dependent functions, which are scattered throughout the cell and play a part in the breakdown of long-chain fatty acids. In addition to these shared roles, other lines of evidence have hinted at the possibility that *Opa3* might have a functional role in the peroxisome.

However, expression of wildtype and mutant Opa3 in both human [Huzing *et al*, 2010] and mouse [Powell *et al.* submitted] cell lines have shown that Opa3 does not co-localization with peroxisomes. It therefore appears that Opa3 is an integral protein of the mitochondrion and that any observed differences between the human and mouse phenotype is probably due to species specific function.

4.5 Conclusions

- The *Opa3*^{L122P} mutation on a C3H and C57BL/6JCrl strain background showed no observable effect on lifespan or onset and variability of phenotype. Therefore, all future experiments were conducted on G3/4 C57BL/6JCrl mice.

- *Nnt* mutation had no observable affect on *Opa3* homozygote or heterozygote lifespan or phenotype suggesting it does not interact with *Opa3*.

- The *Opa3*^{L122P} mutation causes severe tissue pathology in the retina, heart and liver.

- G1 adult homozygote mice display craniofacial defects including shortened nose and broader distance between eyes with increased bone ossification. This phenotype however has incomplete penetrance.

- The *Opa3*^{L122P} mutation affects bone development but not cartilage development.

- The *Opa3*^{L122P} mutation probably does not cause any gestational lethality but is involved in processes required for postnatal survival.

CHAPTER V

The *Opa3*^{L122P} mouse displays neurological and behavioural deficits

5.1 Introduction

Aims of chapter

- To use a generalised behavioural and functional mouse assessment protocol to identify and characterise phenotypic variation in G3/4 *Opa3*^{L122P} mice, which can be used as a guide in the design of more in-depth studies of abberant behaviours.
- Use of a range of neurological and behaviour phenotyping paradigms for assessment of several motor parameters to cover aspects of the human MGA-III phenotype.
- Analysis of MRI head scans for gross morphological defects of the brain, in particular the cerebellum.

The mouse continues to play a vital role in the deciphering of mammalian gene function and the modelling of human diseases. There are a number of mouse models of the primary optic neuropathies but until the generation of our mouse model B6; C3-*Opa3*^{L122P} there were no models of *Opa3*.

In this chapter and the next two chapters our novel mouse carrying the L122P mutation was subjected to a systematic and comprehensive battery of tests that attempt to cover all aspects of the human disease and confirm the *Opa3*$^{-/-}$ mutant mouse as a clinically relevant model of MGA-III. From there, this model can be used to elucidate the physiological role of *Opa3* and thereby to cast light on the function of the OPA3 protein. This chapter deals with the neurological, behavioural and muscular aspects of the disease state.

When designing a battery of behavioural tests for any type of genetically, pharmacologically or physiologically manipulated mouse it is imperative to take into account any abnormalities that would impair the ability of the mouse to complete the task. Uncoordinated experimental approaches can bear a high risk of false negatives and/or false positive results. To this end it was felt that certain aspects of the human phenotype could not be analysed in our mouse model because of such impairments, for example, MGA-III patients have cognitive deficits. Behavioural tests to cover cognitive deficits generally require the ability of the mouse to memorise visual cues, which require good vision, or tests such as Morris water maze which require good motor skills. Our mouse model does not have the capability to complete such tasks due to visual and motor impairments so tests designed specifically for memory and

learning deficits were omitted from our battery. However, cognitive and learning capabilities can be inferred from behaviours observed in tasks such as open field and rotarod.

Other factors which must be taken into account as they are known to influence the behaviour of a mouse include: genetic, experimental and developmental backgrounds, biological rhythm, age, litter size, sex of the test animal, pre and post weaning treatment and observation methods [Walsh and Cummins, 1976]. It is important to keep these parameters comparable throughout a single experiment. It is recommended that all phenotyping experiments are conducted at the same time of day because psychological and biochemical parameters change throughout the day. The ideal time for testing is the first half of the lights-on period (in the morning until early afternoon). All behavioural experiments presented here were conducted at this time of day and factors influencing behaviour were taken into account where ever possible.

5.1.1 Testing motor behaviour and co-ordination

One of the characteristic manifestations in several neurodegenerative diseases, including Costeff syndrome, is the loss of voluntary motor control and the development of involuntary movements. A detailed analysis of several motor parameters is often necessary to capture accurately the essence of such neurodegenerative disease states through repeated testing at predefined time intervals over the animal's life time. Here we investigated the performance of the mice on a variety of tasks designed to identify changes in motor control.

To test for changes in the animal's motor coordination and balance, the rotorod apparatus was employed at several time periods, as it has been shown to be a sensitive tool for assessing progressive neurological deterioration in animal models of syndromes such as Friedreich ataxia [Simon *et al*, 2004]. The wire hang, which is a test of motor ability function/grip strength, can be used in conjunction with rotarod for a more detailed neuromuscular analysis.

Gait analysis can also be assessed by analysis of footprint patterns [Carter *et al*, 1999] and can provide an insight into cerebella function which is involved in the integration of sensory perception, coordination and motor control. Similarly, turning patterns (the incidence and nature of turning) inform on asymmetrical brain function [Miklyaeva *et al*, 1995]. It should be noted though that turning patterns differ between males and females [Field *et al*, 1997].

5.1.2 Exploratory and emotional behaviour

The Open Field Test [Walsh and Cummins, 1976; Crawley, 2000] was designed to measure behavioural responses such as locomotor activity and exploratory behaviours. Open field can also be used as a measure of anxiety.

Mice and rats tend to avoid areas that are brightly illuminated, novel or open, so the open field environment acts as an anxiogenic stimulus and allows for measurement of anxiety-induced locomotor activity and exploratory behaviours. The number of line crosses and the frequency of rearing are used as measures of locomotor activity and a low frequency of these behaviours indicates decreased locomotion. The number of central square entries and the duration of time spent in the central square are measures of exploration and anxiety [Podhorna and Brown, 2002]. Anxiety can be inferred by whether the majority of exploration occurs in close proximity to the walls (thigmotaxis) or in the centre of the test arena. The open space in the centre of the field is expected to induce anxiety and be more aversive than near the arena wall. A low frequency/duration of these behaviours indicates low exploratory behaviour and high anxiety levels.

Stretch attend postures are "risk-assessment" behaviours which indicate that the animal is hesitant to move from its present location to a new position [Blanchard *et al*, 2001] and thus a high frequency of these postures indicates a higher level of anxiety. Grooming behaviour is a displacement response and is expected to be displayed in a novel environment [Espejo, 1997]. Repeated exposure to the open field apparatus results in time dependent changes in behaviour [Choleris *et al*, 2001]. At first, when the apparatus is novel to the animals, more fear-related behaviours (such as stretch attends and activity in the corners and walls of the open field) are displayed. However, with repeated trials, more exploration and locomotor activity (such as rearing and line crosses as well as more central square activity) can be observed. There are, however, strain differences in behaviour after repeated testing in an open field. With repeated exposure, some strains show increased activity while others show habituation and decreased activity levels and others showed no change [Bolivar *et al*, 2000]. The C57BL/6J mice show a reduction in locomotor activity with repeated exposures to the open field and C3H mice show little difference. As locomotor activity was the main parameter of interest the mice were only tested at one time point.

The open field behaviour of mice can be affected by two behavioural dimensions; its exploratory drive and its fear drive. The interpretation of results can be confounded by these two underlying constructs and therefore the test should not be used as an individual measure of activity or anxiety but as an addition to compliment other tests in order to give a comprehensive analysis of the mouse's lomomotor activity and/or emotionality. Light is an important anxiogenic factor that will strongly influence the ambulation in a mouse and experiments under various illumination intensities and factor analysis have shown that locomotion under dim lighting is a measure of activity rather than of fear [Trullas and Skolnick, 1993]. To limit the confounding effect of fear on activity levels the experiments and video recordings were conducted under red light conditions. As mice cannot see the red end of the spectrum, it was for them essentially dark conditions.

Based on the results of the SHIRPA screening a further 7 tests were chosen to cover aspects of the MGA-III syndrome: 1) Walking Pattern (motor function), 2) Rota-rod (motor function), 3) Wire Hang (grip strength), 4) Open Field activity (emotionality, locomotor activity), 5) Metabolic testing (Chapter VI), 6) Optokinetic Drum (visual acuity Chapter VII) and 7) Pupillometry (Chapter VII).

5.2 Materials and Methods

5.2.1 Body weight

A cohort of 64 *Opa3* mice (*Opa3*$^{-/-}$ n=5, *Opa3*$^{+/-}$ n=42, *Opa3* $^{+/+}$ n=17) were weighed every day from birth until 10 days of age and then every other day after that until they were 50 days of age.

5.2.2 SHIRPA

A cohort of 30 *Opa3* mice (*Opa3*$^{-/-}$ n=10, *Opa3*$^{+/-}$ n=10, *Opa3* $^{+/+}$ n=10) were evaluated on the primary SHIRPA screen [SmithKline Beecham Pharmaceuticals, Harwell MRC Mouse Genome Centre and Mammalian Genetics Unit, Imperial College School of Medicine (St Mary's), Royal London Hospital, St Bartholomew's and the Royal London School of Medicine Phenotype Assessment] (Fig 5.1.) at 30 days of age. Heterozygote 'founders' were aged and assessed at two years of age (*Opa3*$^{+/-}$ n=4, *Opa3*$^{+/+}$ n=4). SHIRPA is a protocol that identifies a wide range of phenotypes and is a sensitive screen for mouse neurological, neuromuscular and behavioural mutants [Rogers *et al*, 1997]. This protocol does not allow for detection of vision and eye abnormalities. Vision was therefore assessed in a subsequent chapter.

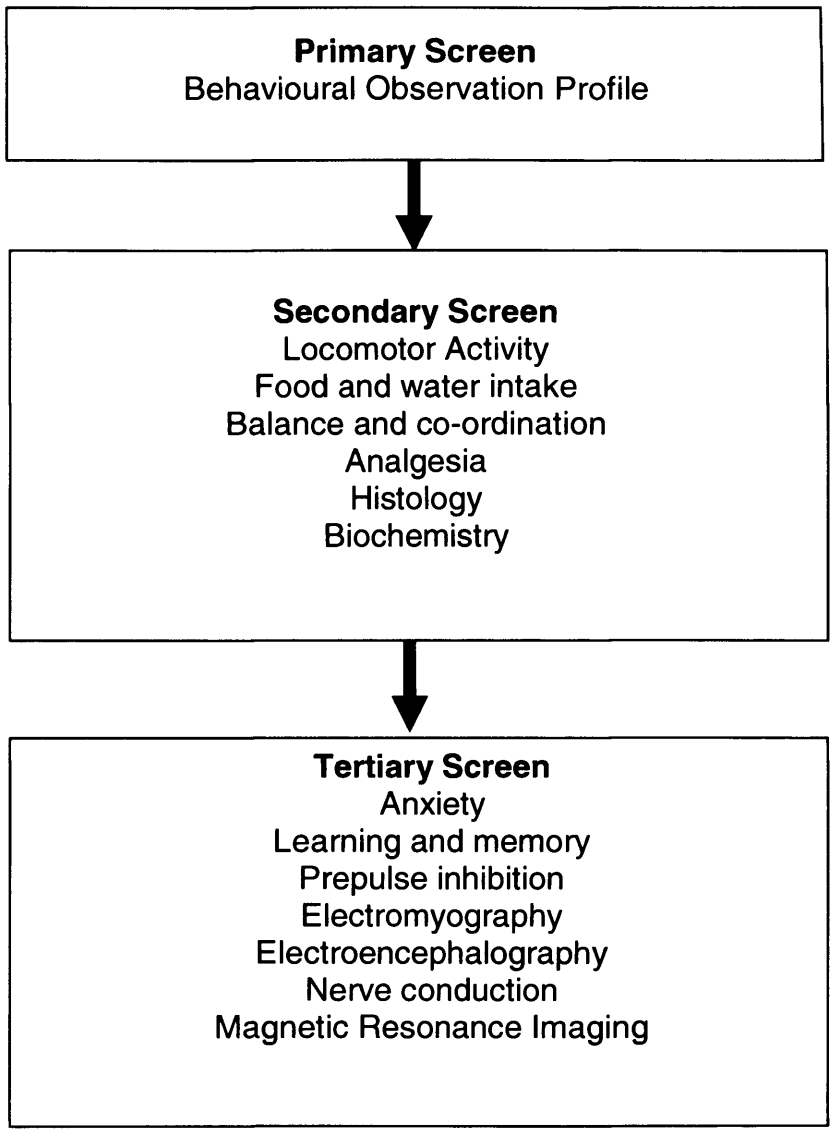

Figure 5.1. SHIRPA is a semi-quantitative protocol designed to characterise the phenotype of mice in three stages.

The first stage provides a behavioural and functional profile by observational assessment. 40 separate measurements can be taken of each animal. Assessment of each animal begins when the animal is weighed and then placed in a cylindrical clear perspex viewing jar for 5 mins for observation of undisturbed behaviour (Fig 5.2.).

This was located on top of a grid, which was suspended above a piece of white paper. Behaviours were recorded without disturbing the animal and the amount of urination or defecation was monitored at the end of the observation period. Incidents of bizarre or stereotyped behaviour and convulsions were recorded separately.

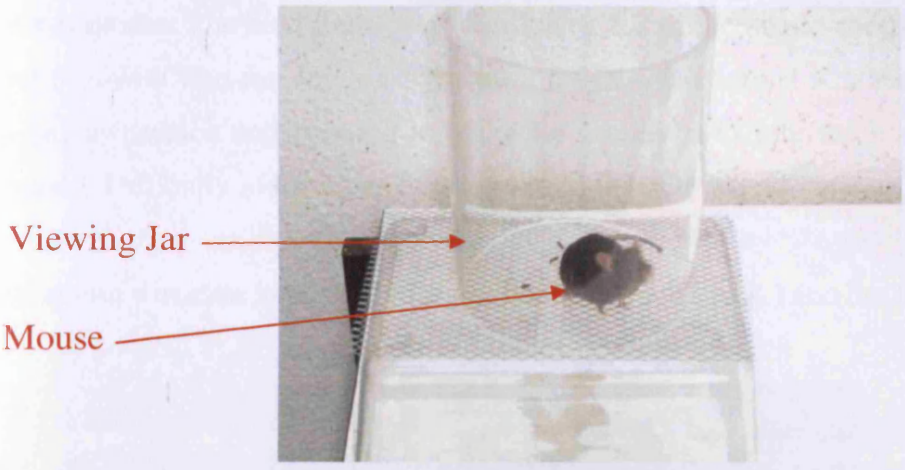

Figure 5.2. Perspex viewing jar for 5 mins of behavioural observation.

A metal plate was inserted under the viewing jar and the animal transferred and briskly dropped onto the floor of an arena without being handled (Fig 5.3.). The immediate reaction to the new environment was recorded as well as motor behaviour.

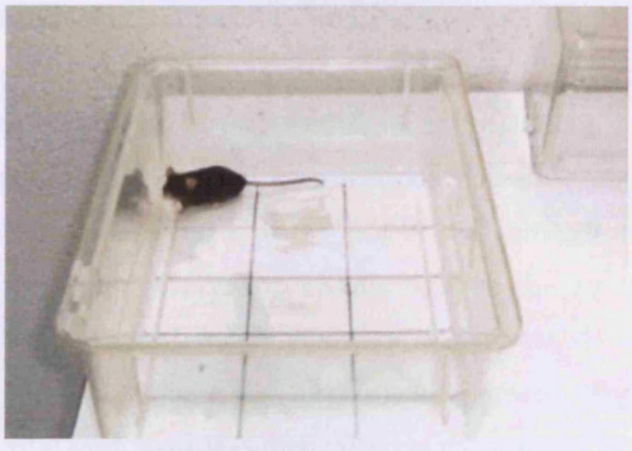

Figure 5.3. Arena for observations of motor behaviour.

5.2.2.1 Above Arena

The animal was removed from the arena and gripped by the tail. To test for vision, extension of forelimbs was observed when the mouse was lowered by base of tail from a height of approximately 15 cms above a wire grid. The mouse was then allowed to grip the grid and a gentle horizontal backwards pull was applied to assess grip strength. Whilst gently restrained on the grid the proximal part of the inner canthus was lightly touched with the tip of the fine wire probe, to look at ear retraction. Then the cornea was touched lightly, to look at eye-

blink response. The hind limbs were lifted clear for gentle lateral compression of mid digit of hind foot with fine forceps for withdrawal reflex. The animal was then held above the wire by tail suspension and lowered to allow the forelimbs to grip the horizontal wire and then released. Difficulty in lifting its back legs on to the wire would indicate muscular impairment.

The mouse was then held firmly in a supine restraint (Fig 5.4.) and the following observed.

Figure 5.4. Supine Restraint

Skin colour (gradations of plantar surface and digits of forelimbs), Heart Rate, Limb Tone, Abdominal Tone (Palpation of abdomen), Lacrimation, Salivation, Provoked Biting (a dowel rod is gently inserted between the teeth at the side of the animal's mouth), Righting Reflex (animal is held by the tail and flicked backwards through the air such that it performs a backward somersault when released - landing position was observed), Contact Righting Reflex (animal was placed into a plastic tube and turned upside down), Negative Geotaxis (animal was placed on a horizontal grid. This was then raised to the vertical with the animal facing the floor and observed for 30 secs), Fear (freezing during transfer arousal), Irritability (struggling during supine restraint), Aggression (provoked biting or attack), Vocalization (provoked during handling). Any "Bizarre Behaviour" was noted at the end. The equipment and battery is described in detail at European Mouse Phenotyping Resource of standardised Screens; EMPReSS; http://empress.har.mrc.ac.uk/.

5.2.3 Walking Pattern

Gait analysis was assessed on six *Opa3* mice (*Opa3*$^{-/-}$ n=3 and *Opa3*$^{+/+}$ n=3). To obtain footprints the hind and forefeet of the mice were coated with blue and red non-toxic paints respectively. The floor of the open field box was covered with white paper. A piece of plexiglass was used to create a lane in the open field and a play tube was placed at the other end to encourage the mouse to walk across the paper, leaving a track of footprints. In footprint analysis several step parameters are analysed; (i) Hind-base width, (ii) Front-base width which is the distance between left and right hind footprints and left and right front footprints, respectively and (iii) Distance from left or right front footprint/hind footprint overlap was used to measure uniformity of step alternation.

5.2.4 Rotarod

Balance and co-ordination (motor function) can be quantified using a rotarod (Fig 5.5.) which measures the ability of mice to remain on a rotating drum [Jones and Roberts, 1968].

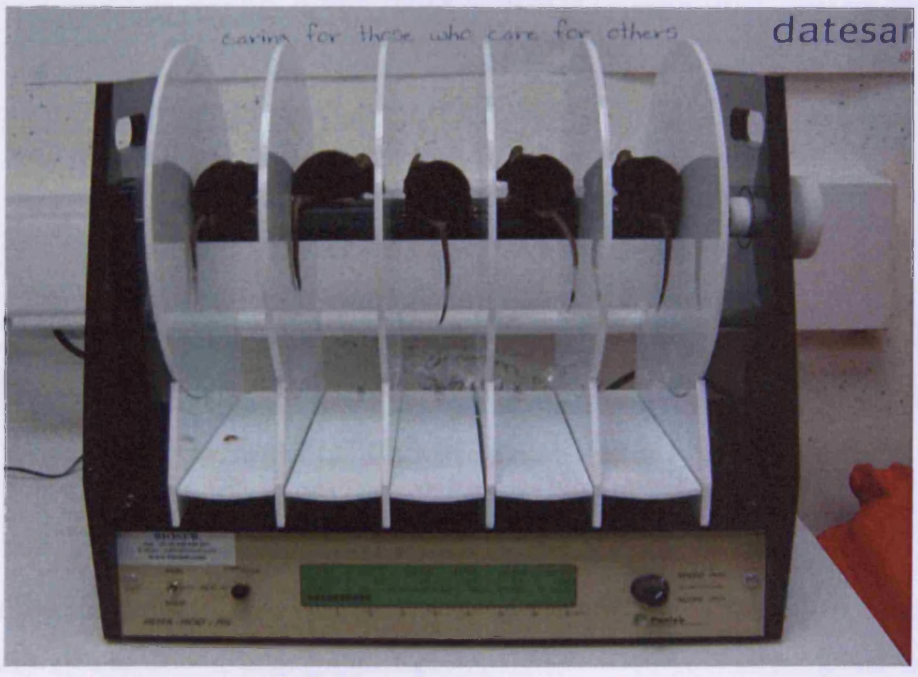

Figure 5.5. Rotarod apparatus.

The motor function of a cohort of 24 mice (*Opa3*$^{-/-}$ n=7, *Opa3*$^{+/-}$ n=10 and *Opa3*$^{+/+}$ n=7) was tested using an accelerating rotarod (Bioseb). Mice were trained to walk on the rotating drum at 21 and 22 days of age before testing began at 23 days of age and then continued every five days until the mice were three months of age. Testing commenced when the rod began to

rotate, gradually accelerating from 4 to 40 rpm over a 5 min period. Mice were given three trials on each test day with a maximum trial time of 5 mins and an inter-trial interval of 20 mins minimum. Testing ended automatically when the mouse fell off the rod. For those mice that held on to the rotating drum the latency to fall was recorded after two complete rotations. Latency to fall was taken as a measure of motor function.

5.2.5 Wire Hang

In the wire hang test, the ability to hang upside-down from a plastic mesh screen above a clear perspex box was tested. A cohort of 21 mice (*Opa3*$^{+/+}$ n=7, *Opa3*$^{+/-}$ n=7 and *Opa3*$^{-/-}$ n=7) were tested from 23 days of age and every five days thereafter until they were three months of age. After mice were placed on the screen, the screen was waved gently in the air to force the mice to grip the wires (Fig 5.6A.). The screen was then immediately turned upside down above the perspex box which was filled with bedding to allow the mice to fall safely (Fig 5.6B.).

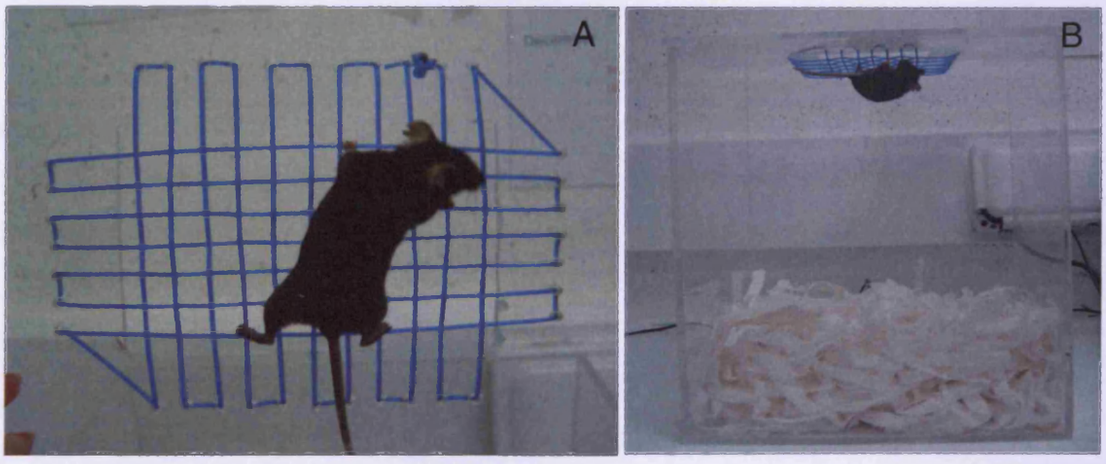

Figure 5.6. Wire Hang apparatus. (A) Each mouse was placed on the plastic mesh of a clear perspex box top. (B) The top is slowly inverted and suspended 30 cms above a clear Perspex box.

The total time the mice remained hanging on the wire was recorded as hanging time in seconds. Any mouse still gripping the cage top after 10 mins was removed and given the maximum score. Each mouse was tested four times over the test day, with an inter-trial interval of 20 mins minimum.

5.2.6 Open Field activity

A cohort of 28 mice (*Opa3*$^{+/+}$ n=9, *Opa3*$^{+/-}$ n=10 and *Opa3*$^{-/-}$ n=9) were assessed in the open field. The open field test was used to assess spontaneous locomotor activity and anxiety-related conflict [Weisstaub *et al*, 2006], i.e., the conflict that arises between the drive to explore by venturing into the centre of the arena and safety by remaining in a corner or along a wall.

The apparatus for the open field test is a 60 x 60 cm square, 30 cms high made of grey plexiglass. Each mouse was placed in a centre of the field and its behaviour recorded for five mins. All activity was recorded by a video camera mounted above the open field and scored in real-time or recorded and scored later. The open field arena is partitioned into 25 equal-size squares (12 x 12 cms); 16 border squares and 9 centre zone squares. Lighting was a 60W red light. During each test session, individual mice were placed in the centre of the open field and observed for five mins. The parameters measured were:

- Latency to reach peripheral squares
- Percentage time spent in various parts of the field e.g., peripheral squares or corners or the middle area
- Total number of central squares entered (defined as three or more paws entering into a central square)
- Total number of peripheral squares entered (defined as three or more paws entering into a peripheral square)
- Total number of squares entered
- Number of rears against a wall (standing up on hind legs using the wall for support)
- Number of rears in the periphery without using the wall (standing up on hind legs)
- Number of rears in the centre

Total activity, corresponding to the sum of the number of lines crossed and the number of rears observed during the five min trial, was calculated by averaging the single measurements obtained from each mouse within a group at each time point. The analysis was performed manually by examining the video recording. Moving time was counted with a stopwatch, distance travelled was measured counting number of squares travelled. Crossing was defined as three paws crossing one of the lines.

5.2.7 Magnetic resonance imaging (MRI)

Mice were imaged using a Bruker Biospin Advance II 9.4T (400 mHz) horizontal bore (20 mm bore) MRI system (Etlingen, Germany), equipped with S116 high performance gradient coil. Perfusion fixed mice (see Chapter II) were scanned using a 4 channel phased array mouse head surface coil (Bruker) coupled with a 750W linearly polarised 72mm ID volume coil (Bruker). For each animal a series of Turbo-RARE 3D scans with a RARE factor of 4, a FOV of 2.56 cm x 1.92 cm x 1.92 cm and a matrix of 512 x 384 x 384 giving a resolution of 50μm x 50μm x 50μm. Images were acquired for 16 hrs with 1 average, an effective TE of 50ms, a TR of 1550ms, fat suppression and a band width of 50KHz.

5.2.7.1 Volumetric measurements

The resulting MRI images were analysed using ParaVision (Bruker, Karlsruhe, Germany) a Bruker software package for multi-dimensional MRI/MRS data. Determination of the total cerebellar volume (mm^3) was taken in one *Opa3*$^{-/-}$ and one *Opa3*$^{+/+}$ mouse using Analyze region-of-interest software. Brain regions were defined manually, using atlases of the mouse brain for reference (www.hms.harvard.edu/research/brain/atlas.html). Target regions were defined in each slice, then the area of each region was calculated. These areas were converted to volumes for each slice, then summed for the whole brain to give total volume. Volumetric measurements were taken of cerebellum, brain excluding cerebellum and total brain in horizontal and plane.

5.2.8 Dual COX-SDH muscle histochemistry

The gastrocnemius muscle was harvested from 30 days of age mice (*Opa3*$^{-/-}$ n=3, *Opa3*$^{+/+}$ n=3).The muscle specimens were immediately frozen in OCT in an isopentane bath (-150°C) and stored at -80°C. Samples were raised to the sectioning temperature of -20°C. 15 μm thick serial sections were obtained using a cryostat (Microm HM560; Thermo Fisher, Walldorf, Germany) and placed on Polysine Slides (Thermo scientific). Histochemical staining for COX and SDH activity was performed using the following protocol (for solution recipes see Appendix I).

After sectioning, slides were allowed to air dry for 1 hr. During this time 0.8 ml of 5mM 3,3 diaminobenzidine tetrahydrochloride (Sigma) and 0.2 ml 500μm cytochrome c (Sigma) were rapidly thawed and mixed. A few grains of catalase (Sigma) were added. Solution was mixed, applied to the section and then incubated for 45 mins at 37°C. Slides were then

washed in 3 changes of 0.1M phosphate buffered saline pH 7.0 for 3 mins each. 0.8 ml of 1.875mM nitroblue tetrazolium (Sigma), 0.1 ml of 1.30M sodium succinate (Sigma), 0.1 ml of 2.0mM phenazine methosulphate (Sigma) and 0.01ml of 100mM sodium azide were rapidly thawed. These solutions were mixed, applied to section and incubated for 40 mins at 37°C. After slides were again washed in 3 changes of 0.1M phosphate buffered saline pH 7.0 for 3 mins each. Finally samples were dehydrated through an alcohol series. 2 mins in 50% ethanol, 2 mins in 70% ethanol, 2 mins in 90% ethanol, 2 mins in 100% ethanol and finally 10 mins in 100% ethanol. Slides were then cleared and mounted with D.P.X permanent medium for microscopy (BDH, England). Slides were examined on a Leica DMR microscope and a Leica DC500 camera. Muscle fibres were counted on five different sections for each mouse using Image J.

5.2.9 Statistics

Statistical analysis of behavioural data was carried out with SPSS 16. Statistical differences between groups in rotarod and wirehang were analyzed by one-way ANOVA, followed by Bonferroni's post hoc test or Dunnet T3 post hoc depending on equal variance or not. Paired sample *t* test for within group comparisions. SHIRPA was analysed with Mann Whitney U and Student's *t* test for open field. *P* values ≤ 0.05 were considered statistically significant.

5.3 Results

5.3.1 Body Weight

The *Opa3*$^{-/-}$ mice weighed less than the *Opa3*$^{+/+}$ and *Opa3*$^{+/-}$ mice from approximately one week old onwards and generally do not grow larger than the size of a 'weaner' (at 21 days of age a juvenile mouse is weaned from its mother to a separate cage) (Fig 5.7.). The dip off in weight gain seen around 20 days on all three curves corresponds with time of weaning from their mothers. There were very few numbers for the body weight of the homozygotes as most do not survive past weaning. Some *Opa3*$^{+/-}$ also died at birth and of the 43 *Opa3*$^{+/-}$ that went through the testing seven (16%) did not survive to 50 days of age. There also seems difference in growth rates of the homozygotes compared to the wildtypes and heterozygotes.

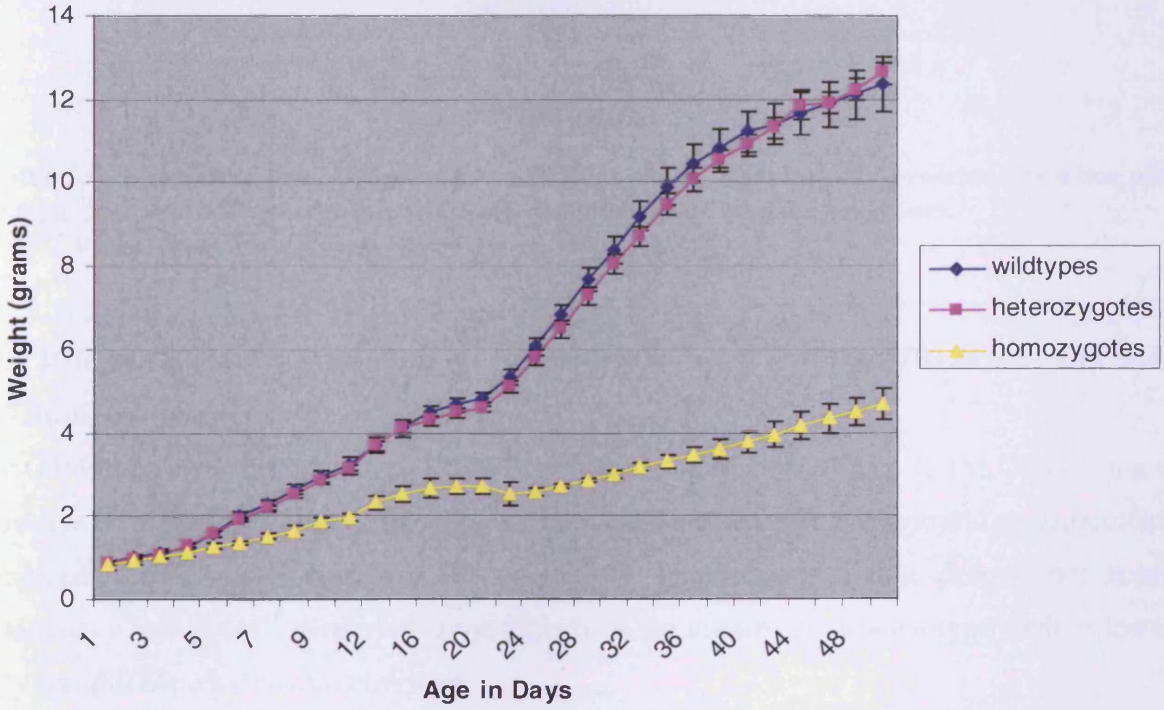

Figure 5.7. Growth curves of wildtype, heterozygote and homozygote G3/4 *Opa3* mice from birth to 50 days of age. Symbols indicate mean body weight in grams. ± S.E.M. (The maximum N for each genotype was *Opa3*$^{+/+}$ n= 17, *Opa3*$^{+/-}$ n= 42 and *Opa3*$^{-/-}$ n= 5).

However, final body weights at 50 days of age were analysed in a box plot (Fig 5.8.). Homozygote body weight was found to be statistically significantly different (P=0.000) from wildtypes and heterozygotes but, no difference was observed between the wildtypes and heterozygotes.

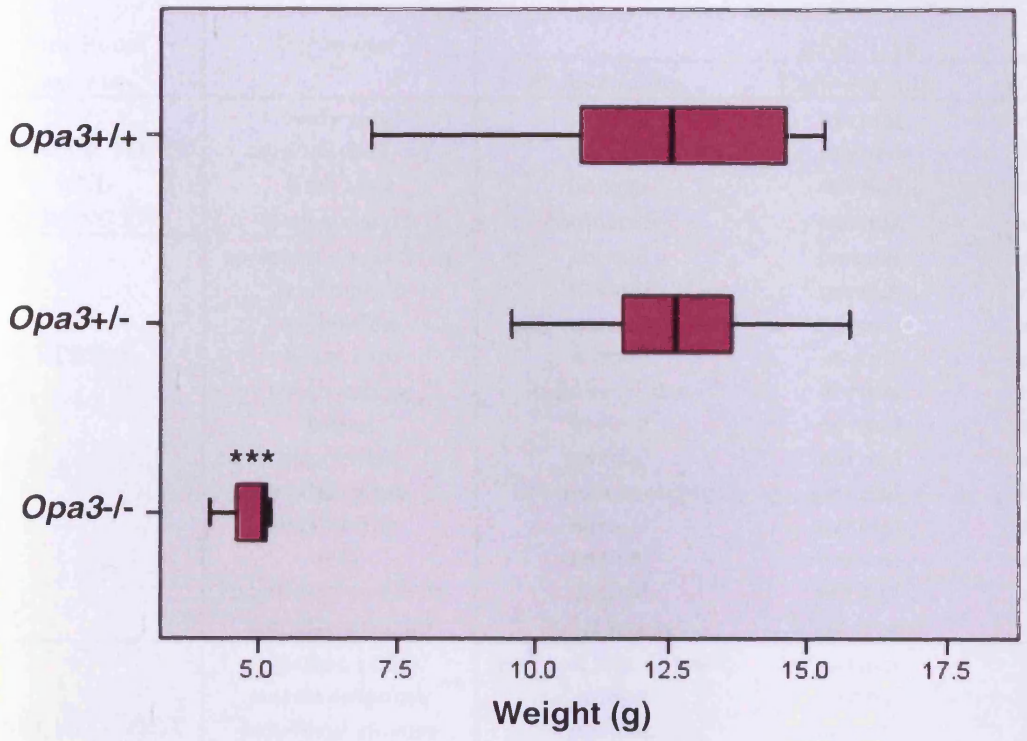

Figure 5.8. Box plot of final body weight at 50 days of age. The data are presented as a box plot (median, 25th and 75th percentile, whiskers with the highest and lowest values. (*Opa3*$^{+/+}$ n= 16, *Opa3*$^{+/-}$ n= 35 and *Opa3*$^{-/-}$ n= 3) * *P* = 0.000.**

5.3.2 Primary SHIRPA Screening on Generation 3 and 4 (87% C57BL/6JCrl and 94% C57BL/6JCrl respectively)

The G3/4 mice underwent primary SHIRPA screening at 30 days of age. In the *Opa3*$^{+/-}$ mice, there was no significant effect of genotype on all 40 of the separate behavioural measurements compared with *Opa3*$^{+/+}$ littermates. It should be noted though, that despite not being significant a few *Opa3*$^{+/-}$ displayed some aspects of the homozygote phenotype such as lower body weight, hypoactivity and tremors.

In the *Opa3*$^{-/-}$ mice, there was a significant effect of genotype on 11 of the 40 behavioural measurements compared with *Opa3*$^{+/+}$ littermates (see Table 5.1 for description).

Functional category	Parameter	RESULTS			Statistical significance
		Homozygotes	Heterozygotes	Wildtypes	
MUSCLE TONE AND STRENGTH	body tone	normal	normal	normal	N/S
	abdominal tone	normal	normal	normal	N/S
	limb tone	normal	normal	normal	N/S
	grip strength	moderate	normal	normal	N/S
STRESS	spontaneous activity	normal	normal	normal	N/S
	lacrimation	normal	normal	normal	N/S
	salivation	normal	normal	normal	N/S
	heart rate	normal	normal	normal	N/S
	touch escape	mild response	normal	normal	*P*=0.000
	biting	normal	normal	normal	N/S
	aggression	normal	normal	normal	N/S
	vocalisation	in observation jar	normal	normal	N/S
	irritability	normal	normal	normal	N/S
	fear	normal	normal	normal	N/S
	positional passivity	normal	normal	normal	N/S
	transfer arousal	brief freeze	brief freeze	normal	*P*=0.001
REFLEXOLOGY AND SENSORY FUNCTION	righting reflex	lands on side or back	normal	normal	*P*=0.013
	startle response	jumps	normal	normal	*P*=0.011
	palpebral closure	normal	normal	normal	N/S
	pineal reflex	normal	normal	normal	N/S
	corneal reflex	normal	normal	normal	N/S
	toe pinch	normal	normal	normal	N/S
	piloerection	normal	normal	normal	N/S
	negative geotaxis	normal	normal	normal	N/S
	visual placing	upon vibrassae contact	normal	normal	*P*=0.000
	tremor	mild or marked	Mild or marked	normal	*P*=0.023
MOTOR BEHAVIOUR	body position	normal	normal	normal	N/S
	tail elevation	normal	normal	normal	N/S
	pelvic elevation	elevated	normal	normal	*P*=0.023
	trunk curl	normal	normal	normal	N/S
	limb grasping	present	normal	normal	*P*=0.000
	wire manoeuvre	difficulty grasping	normal	normal	*P*=0.007
	gait	fluid but abnormal	normal	normal	*P*=0.000
	negative geotaxis	normal	normal	normal	N/S
	locomotor activity	low	low	normal	*P*=0.000
AUTONOMOUS FUNCTION	respiratory rate	normal	normal	normal	N/S
	defecation	normal	normal	normal	N/S
	urination	normal	normal	normal	N/S
	skin colour	blanched	normal	normal	N/S
	heart rate	normal	normal	normal	N/S

Table 5.1. List of all tests performed in the SHIRPA protocol. Aberrant behaviours observed in testing were not necessarily seen in all of the mice. Normal = no abnormal behaviour was observed in any of the mice. N/S= no statistically significant difference when compared to the wildtype.

In the viewing jar, *Opa3*$^{-/-}$ mice were only significantly different to *Opa3*$^{+/+}$ mice in tremor: $P < 0.05$. In the arena, the *Opa3*$^{-/-}$ mice were significantly different from *Opa3*$^{+/+}$ mice with respect to six measures: transfer arousal from the viewing jar to the arena: $P = 0.001$; locomotor activity: $P = 0.000$; startle response tested by the MRC standard click box: $P < 0.05$; gait: $P = 0.000$; pelvic elevation: $P < 0.05$ and touch escape: $P = 0.000$. For behaviours measured outside of the arena, there were significant differences between the *Opa3*$^{-/-}$ and *Opa3*$^{+/+}$ mice with respect to four measures: visual placing: $P = 0.000$; limb grasping: $P = 0.000$; wire manoeuvre: $P < 0.01$ and righting reflex: $P < 0.05$.

5.3.2.1 Primary SHIRPA screening of aged heterozygous 'founders'

Heterozygote 'founders' and their wildtype littermates were tested at two years of age, to assess whether ageing compromised the heterozygous mice. Due to deteriorating health and declining numbers it was not possible to test the *Opa3*$^{-/-}$ mice beyond four months of age. No significant differences were observed in any of the 40 parameters tested between wildtypes and heterozygotes. Therefore, at two years of age the heterozygote 'founders' remain indistinguishable from their littermate controls.

From the results of the Primary SHIRPA Screening a battery of tests from the secondary SHIRPA screening was designed to give a more in depth analysis of the aberrant behaviours observed in the *Opa3*$^{-/-}$ mice and to cover aspects of the human MGA-III phenotype.

5.3.3 Walking Pattern

Gait abnormalities were analysed by footprint patterns of mice while they walked along a narrow strip of paper. Peripheral nerve function can be assessed based on measurements made from walking tracks [De Medinaceli *et al*, 1982]. Cerebellar function can also be assessed where physiological symptoms of cerebellar dysfunction include ataxia, side-to-side truncal tremor, and an abnormal wide stance base in the gait [Gilman *et al*, 1981]. Footprint patterns of *Opa3*$^{-/-}$ and *Opa3*$^{+/+}$ mice at 30 days of age are illustrated in Fig 5.9.

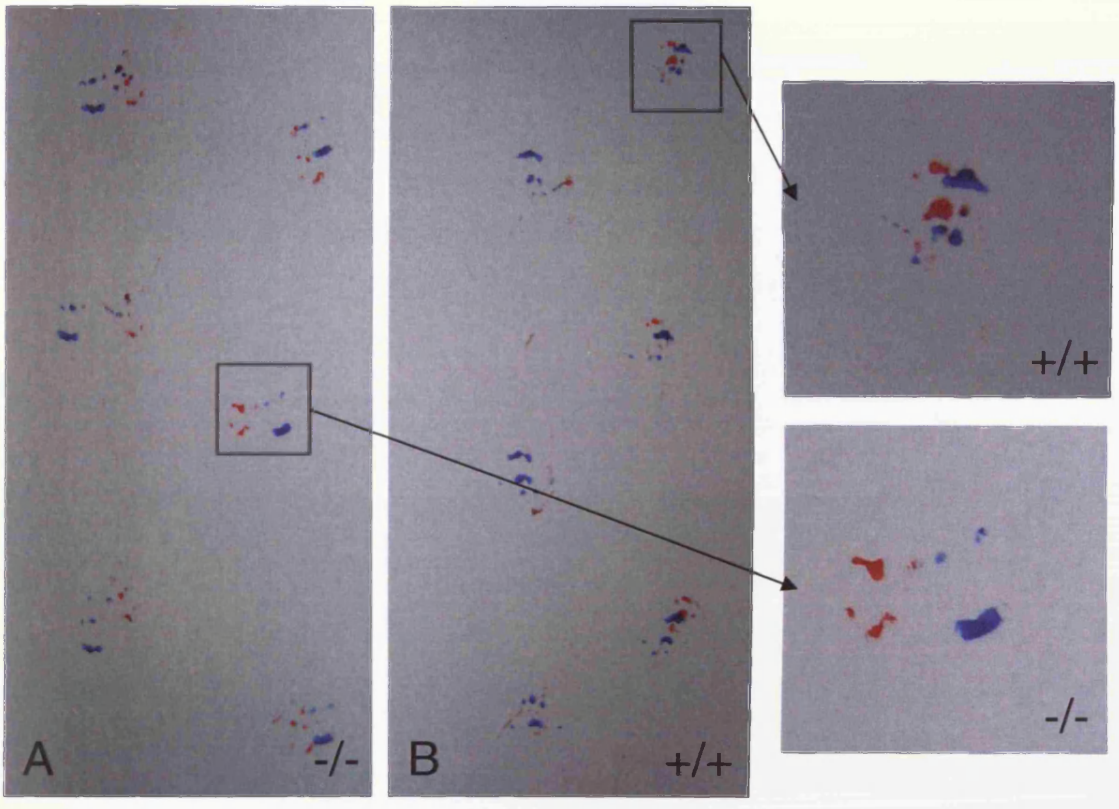

Figure 5.9. Footprint pattern analysis in (A) homozygote and (B) wildtype mice. Hindfeet were coated in blue paint and forefeet were coated in red paint. Splayed gait can be observed in the homozygote by hind foot prints not overlapping with forefoot prints.

Typically, when walking or trotting, a wildtype mouse will walk in a straight line with alternate fore and hind paw steps, lifting the fore paw on one side and the hind paw on the other together, and swinging the hind paw through to the spot from which the forepaw on the same side had previously rested (Fig 4.9B.). Consequently, a powerful measure of precision and co-ordination of walking is provided by the degree to which the forepaw and hind paw prints overlap. The homozygote mice displayed a co-ordinated walking pattern except for the hind paws being placed well outside of the fore paw step pattern (Fig 4.9A.). Footprint analysis patterns were taken before onset of tremors or ataxia.

5.3.4 Rotarod

The rotarod test was used to study motor performance/co-ordination and skill learning. From the first day of testing at 23 days of age there was a significant correlation between genotype and time spent on the accelerating rotarod. Analysis of the raw data (Fig 5.10.) showed improvements by all genotypes in time spent on the rotarod during the first few testing sessions. This either indicates their ability to learn the new skill or is an increase in muscle mass due to the immaturity of the mice at the beginning of testing. By comparing the rotarod performance of the mice at 28 and 33 days of age to their final rotarod performance at 87 days of age, the *Opa3*$^{-/-}$ and *Opa3*$^{+/-}$ showed no improvement in rotarod performance. Whereas, the *Opa3*$^{+/+}$ did show an improvement over time with a significant difference in rotarod performance (P=0.031). This suggests a deficit in cerebellar-dependent motor learning in the *Opa3*$^{-/-}$ and *Opa3*$^{+/-}$ mice. Rotarod performance is sensitive to body weight with mice of smaller strains having longer latencies to fall and mice of larger weight having shorter latencies [McFadyen *et al*, 2003]. This suggests that the *Opa3*$^{-/-}$ performance maybe poorer than results would suggest.

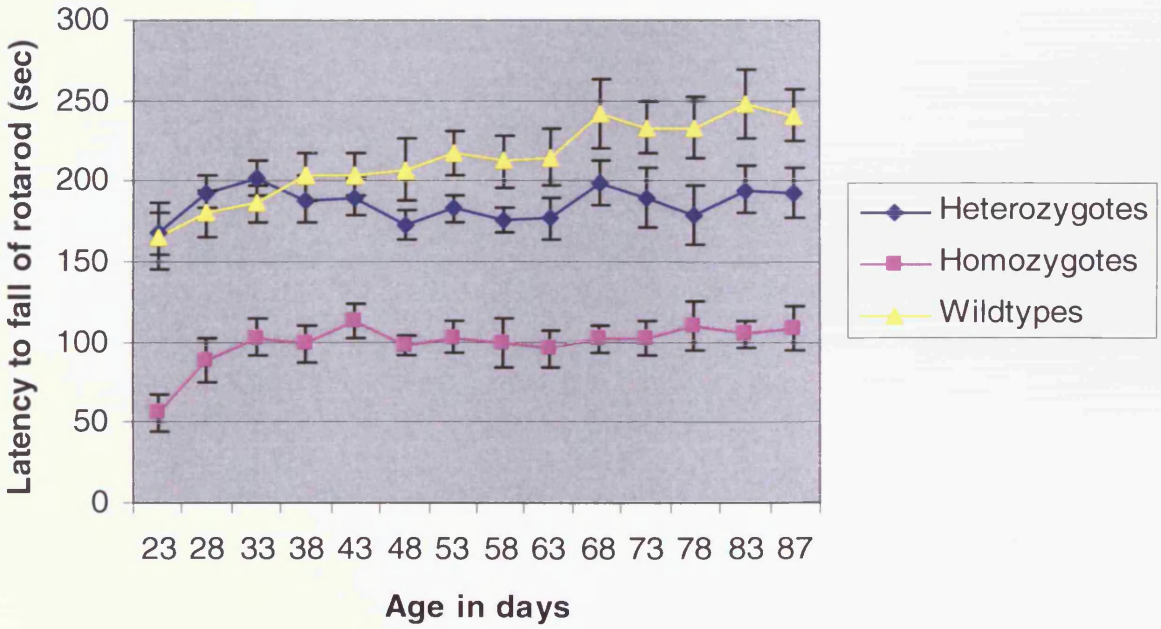

Figure 5.10. Accelerating rotarod performance. Data expressed as average latency to fall off rotarod in secs ± S.E.M. A cohort of 21 mice were tested from 23 days of age, every 5 days, until 87 days old (*Opa3*$^{+/+}$ n=7, *Opa3*$^{+/-}$ n=7, *Opa3*$^{-/-}$ n=7).

The *Opa3*$^{-/-}$ mice showed a decrease in latency to fall relative to the *Opa3*$^{+/+}$ and *Opa3*$^{+/-}$ mice (Fig 5.11.) and were statistically significantly different to the *Opa3*$^{+/-}$ and *Opa3*$^{+/+}$ on all days tested ($P< 0.005$ at all time points). There was no statistical difference between the *Opa3*$^{+/-}$ and *Opa3*$^{+/+}$ at any time points. In order to test if poor performance of *Opa3*$^{-/-}$ mice on the rotarod was due to abnormal muscle strength, they were assessed for grip strength on the wire hang.

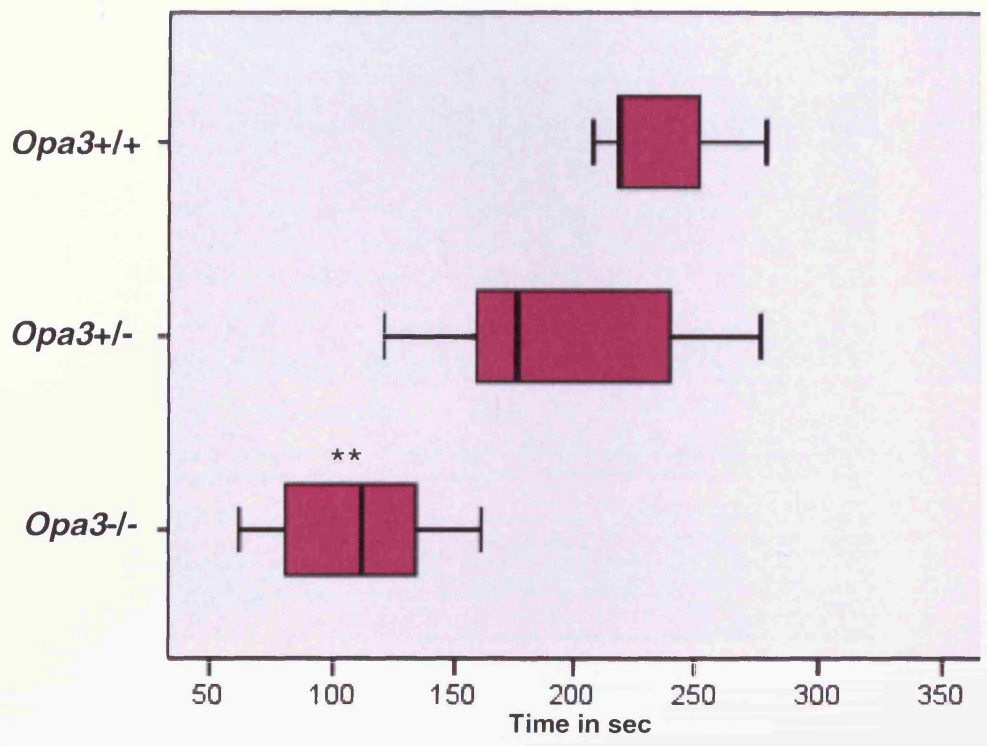

Figure 5.11. Box plot of final rotarod performance in 87 day old mice. The data are presented as a box plot (median, 25th and 75th percentile, whiskers with the highest and lowest values)
** ***P*<0.01.**

5.3.5 Wire Hang

The wire hang task (the ability to hang upside down from a wire screen) measures neuromuscular function, grip strength, and motivation.

Analysis of neurological performance on the wire hang test showed the *Opa3*$^{+/-}$ mice fell off the screen without any significant time difference from their wildtype controls (Fig 5.12.).

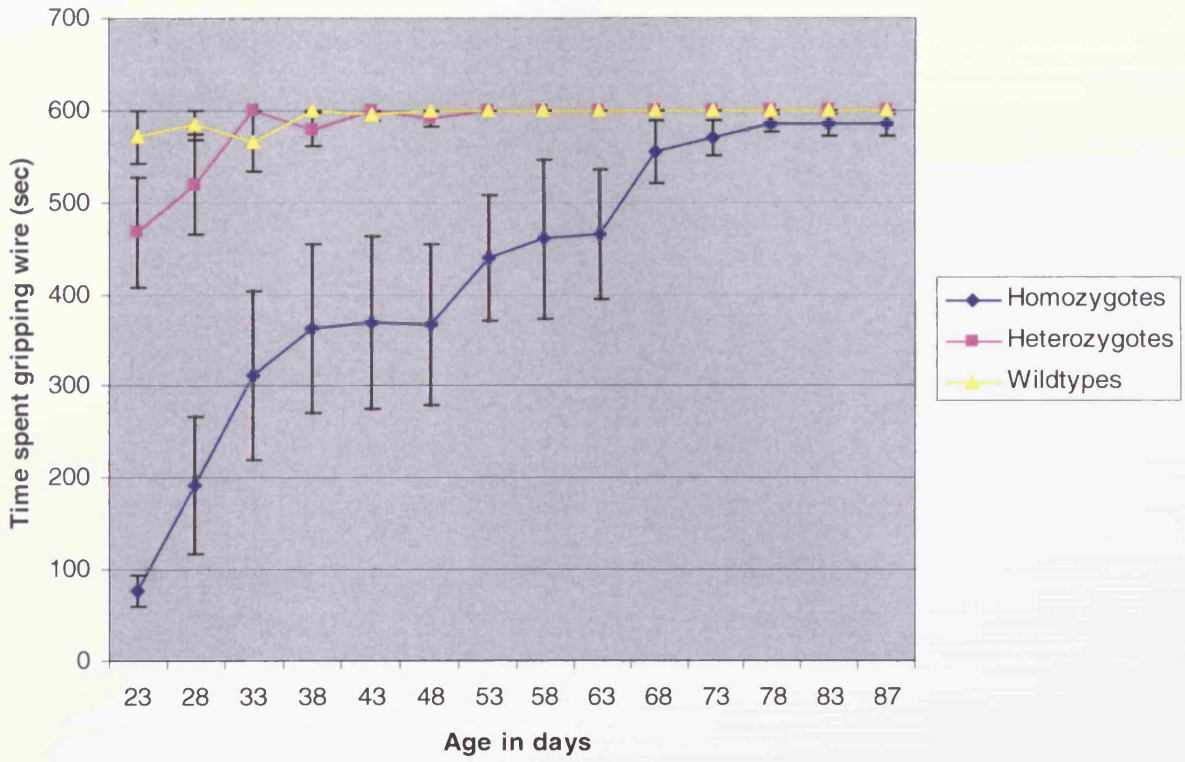

Figure 5.12. Hanging wire test to measure balance and grip strength in a cohort of 21 mice tested from 23 days of age every 5 days until 87 days of age. Time on the wire was recorded up to a maximum of 10 mins. Data expressed as average latency to fall off the wire grid in secs ± S.E.M. (*Opa3*$^{+/+}$ n=7, *Opa3*$^{+/-}$ n=7, *Opa3*$^{-/-}$ n=7).

In the *Opa3*$^{-/-}$ mice genotype effect was confirmed from 23 days of age through to 48 days of age where they were statistically significantly different. However, a global increase of performance was noted with progressive ageing in the *Opa3*$^{-/-}$ mice and from 53 days of age onwards there was no difference in genotypes. Therefore, by 53 days of age no major abnormalities in muscle strength were observed when compared with *Opa3*$^{+/+}$ mice.

5.3.6 Open Field Testing

5.3.6.1 Latency to reach the periphery.

When placed in the open field wildtype mice moved quickly to the edges of the open field apparatus, whereas the homozygote mice took significantly longer to reach the periphery (Fig 5.13.). *Opa3*$^{+/+}$ took on average of 3.1 ± 0.8 secs, *Opa3*$^{+/-}$ took 31.8 ± 13.5 secs and *Opa3*$^{-/-}$ took 69.6 ± 6.9 secs (P=0.000). A large variability was seen in time taken for the heterozygotes to reach the periphery and on average was less than half that of the wildtypes but it was not statistically significant (P= 0.166).

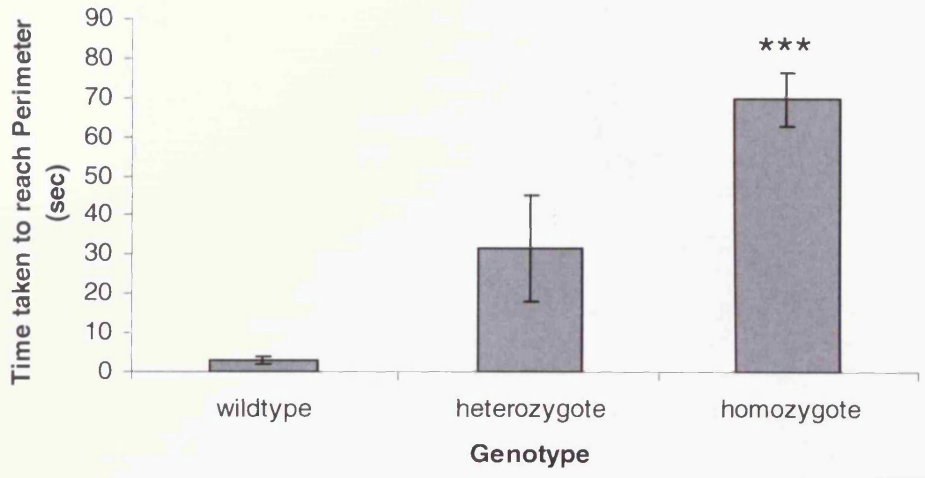

Figure 5.13. Latency to reach perimeter squares of *Opa3*$^{-/-}$ and *Opa3*$^{+/-}$ and *Opa3*$^{+/+}$ mice in open field testing. Data expressed as mean ± S.E.M. (*Opa3*$^{+/+}$ n = 9, *Opa3*$^{+/-}$ n =10, *Opa3*$^{-/-}$ n =9) ***P < 0.001.

During initial exposure to the novel environment mice normally display 'stretch attends' which is a risk assessment behaviour. All of the *Opa3*$^{-/-}$ displayed virtually no stretch attend movements suggesting a lack of anxiety and fear.

5.3.6.2 Total Activity

Study of the raw data (Fig 5.14.) which was broken into 30 sec intervals showed that total locomotor activity which included horizontal (squares entered) as well as vertical (rears) activity was significantly lower in *Opa3*$^{-/-}$ compared to the *Opa3*$^{+/-}$ and *Opa3*$^{+/+}$ mice. Comparisions were made of number of squares entered at each time point using a paired sample t test. The homozygotes showed a statistical significant increase in number of squares entered during the 5 mins. Comparisions of squares entered by the homozygotes during 0-30

sec compared to 271-300 secs (P=0.008), 31-60 secs compared to 271-300sec (P=0.032) by 61-90sec there was no significant difference (P=0.190). This suggests that the *Opa3*$^{-/-}$ mice failed to show within-session habituation. Wildtype and heterozygotes showed no statistical difference between any time points suggesting that they habituated to the open field.

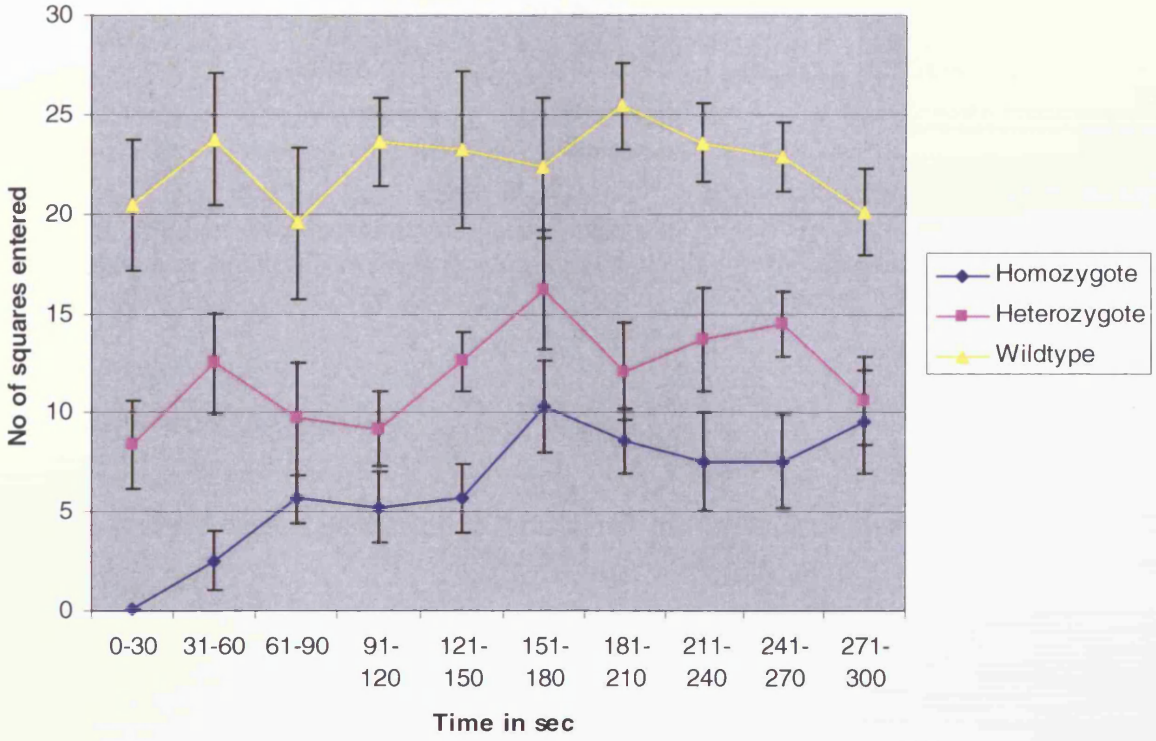

Figure 5.14. Graph showing total locomotor activity for each 30 sec period during the 5 min testing.

Analysis of total locomotor activity (Fig 5.15.) showed an effect of genotype. The *Opa3*$^{-/-}$ and *Opa3*$^{+/-}$ mice showed clear evidence of decreased locomotor activity, with total locomotor activity in *Opa3*$^{-/-}$ mice 3.6 fold less (62.77 ± 11.81, P= 0.000) and *Opa3*$^{+/-}$ mice 1.8 fold less (119.5 ± 10.43, P= 0.000) when compared with wildtype (225 ± 18.84). There was also a significant difference when comparing locomotor activity in *Opa3*$^{-/-}$ mice with *Opa3*$^{+/-}$ mice (P=0.023).

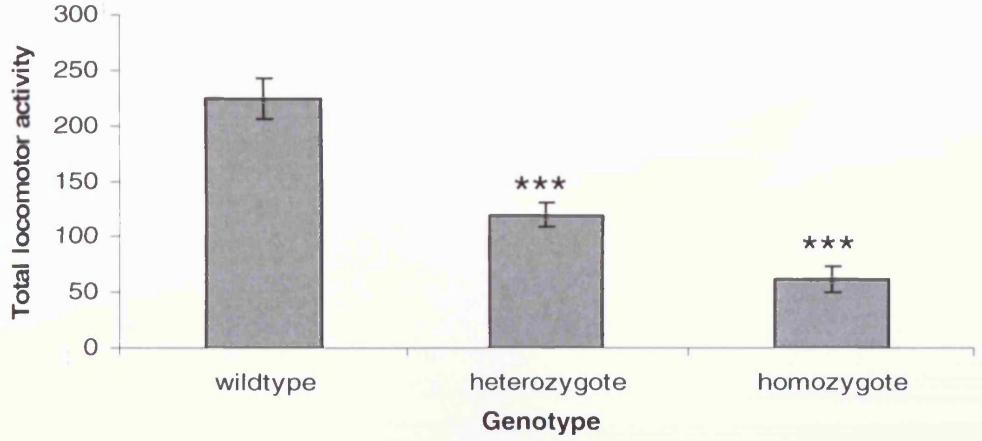

Figure 5.15. Total locomotor activity of Opa3-/- and Opa3+/- and Opa3+/+ mice in open field testing. Locomotor activity is defined as number of squares entered plus number of rears. Data are expressed as mean ± S.E.M. (Opa3+/+ n = 9, Opa3+/- n =10, Opa3-/- n =9) ***P < 0.001.

5.3.6.3 Exploration and Rearing

Number of rears is an indicator of exploratory behaviour. Reduced exploratory behaviour in *Opa3*$^{-/-}$ mice was reflected as a decreased incidence of rearing activity against the wall in the open field (Fig 5.16.).

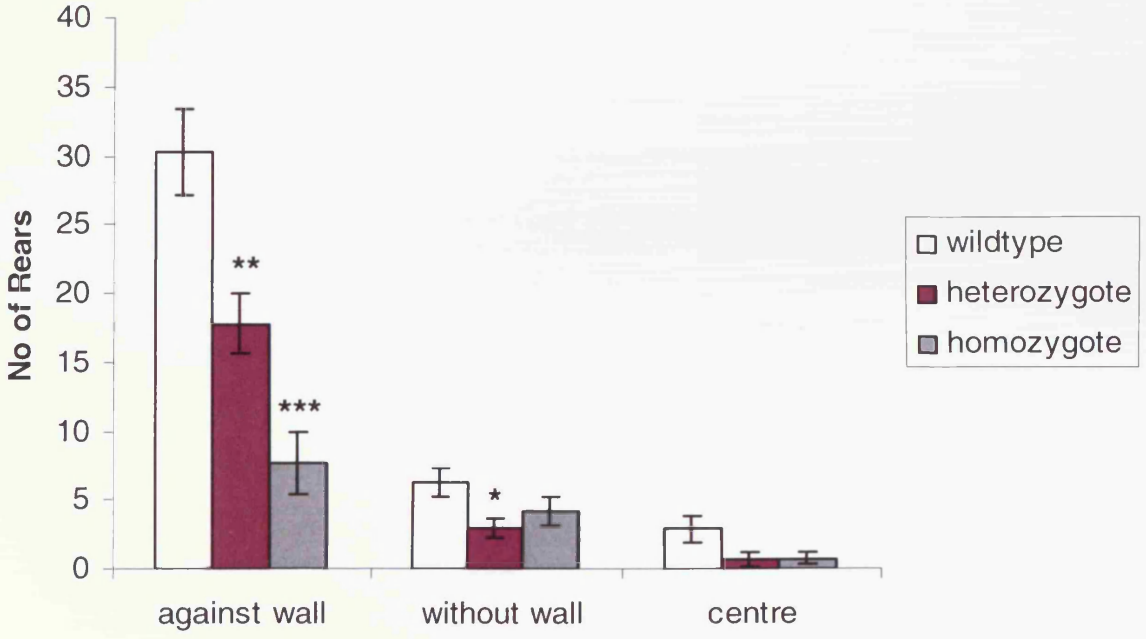

Figure 5.16. The number of rears during 5 mins of *Opa3*$^{-/-}$ and *Opa3*$^{+/-}$ and *Opa3*$^{+/+}$ mice in open field testing. Data expressed as mean ± S.E.M. (*Opa3*$^{+/+}$ n = 9, *Opa3*$^{+/-}$ n =10, *Opa3*$^{-/-}$ n =9). ***P < 0.001, **P< 0.01, *P< 0.05.

For the number of rears against the wall the *Opa3*$^{-/-}$ and *Opa3*$^{+/-}$ were statistically significantly different from their wildtype controls (*Opa3*$^{-/-}$ *P*= 0.000; *Opa3*$^{+/-}$ *P*=0.005). Without the wall only the *Opa3*$^{+/-}$ were significantly different (*P*=0.04) and in the centre of the arena there was no difference observed between any of the genotypes.

The time spent in the centre of the arenas was also measured as very little time spent in the centre can be an indication of altered anxiety especially if animals remain thigmotaxic throughout the entire test period (Fig 5.17.).

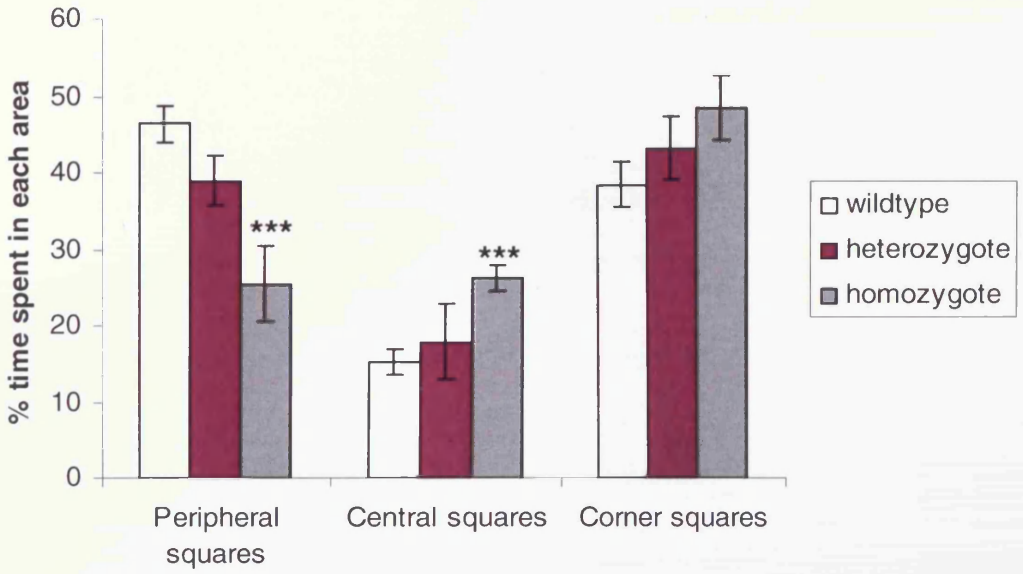

Figure 5.17. Percentage of time spent in various areas of the arena of *Opa3*$^{-/-}$ and *Opa3*$^{+/-}$ and *Opa3*$^{+/+}$ mice in open field testing. Data expressed as mean ± S.E.M. (*Opa3*$^{+/+}$ n = 9, *Opa3*$^{+/-}$ n =10, *Opa3*$^{-/-}$ n =9). ***$P < 0.001$.

The *Opa3*$^{-/-}$ mice are seen to spend considerably more time in the central squares than the heterozygotes and wildtypes. This difference was due to the long period of time taken to reach the periphery when initially placed in the open field arena Homozygotes were significantly different from wildtypes in central (*P*=0.000) and peripheral (*P*=0.001) but not corner (*P*=0.074). Difference in time spent in peripheral squares was due to reduced locomotor activity in the homozygotes. Heterozygotes were not different form wildtypes in any part of the arena. Homozygotes were only different from heterozygotes in the peripheral (*P*=0.032).

The *Opa3*$^{-/-}$ mice performed fewer complete grooming cycles than *Opa3*$^{+/+}$ mice which is consistent with the general reduction in co-ordinated activity observed in *Opa3*$^{-/-}$ mice.

5.3.7 Muscle COX-SDH

COX-SDH staining was analysed on the gastrocnemius muscle of 30 day old mice (*Opa3*$^{+/+}$ n=3, *Opa3*$^{-/-}$ n=3). Previous H&E staining (Chapter IV, Fig 4.9B.) showed normal muscle fibre morphology. No SDH staining and no COX deficient fibres were identified in any of the homozygote sections (Fig 5.18A.).

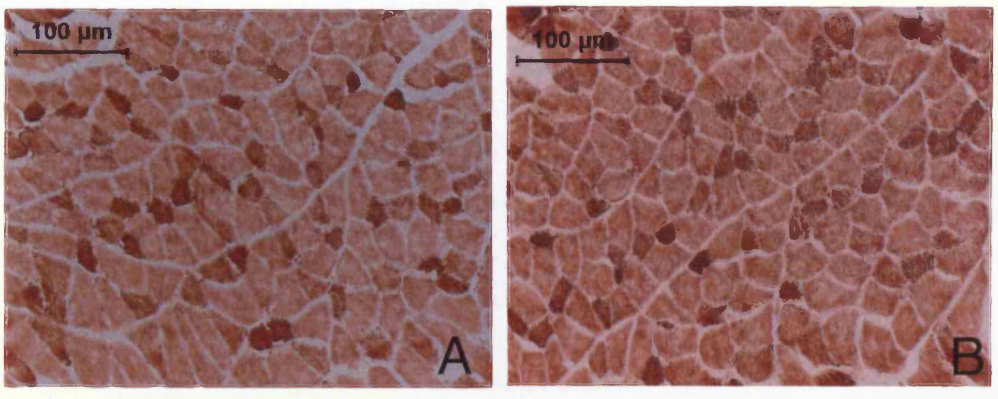

Figure 5.18. Dual COX-SDH staining in (A) homozygote and (B) wildtype muscle sections. (*Opa3*$^{+/+}$ n=3, *Opa3*$^{-/-}$ n=3). Magnification x20.

Muscle fibres were counted for any difference in light and dark stained fibres, no statistical difference was observed. The average sampling of 161 muscle fibres for each section, five section per mouse (Standard deviation = 6.88, range = 175-153).

5.3.8 Cerebellar MRI imaging

High resolution MRI allows precise measurement of volumes, and eliminates artefacts due to dehydration or paraffin embedding that can occur from histological preparation. Brains of one homozygote mouse and one control were measured with high contrast at high resolution (pixel resolution of 50 µm). The architecture of major brain regions (cortex, hippocampus, cerebellum) are clearly defined at this resolution (Fig 5.19A.) and polymicrogyria can be seen in the homozygote.

Volumes of total brain, and cerebellum only were determined for each brain in the horizontal and saggital planes. Cerebellar volume had to be estimated as a proportion of the entire brain, as overall brain size between homozygote and wildtype is different due to homozygotes being significantly smaller than wildtypes. Therefore, the cerebellum of *Opa3* homozygote mice is reduced in size and is proportionately smaller relative to the total brain size. Volumes were calculated by summing volumetric pixels (voxels) in every MRI slice. The volume of the

Opa3 homozygote cerebellum can clearly be seen to be smaller (Fig 5.19C.) and as a proportion of the whole brain was 9.71% whereas the wildtype cerebellum was 16.08% of whole brain volume. Therefore homozygote cerebellum was ~ 40% smaller than that of the wildtype.

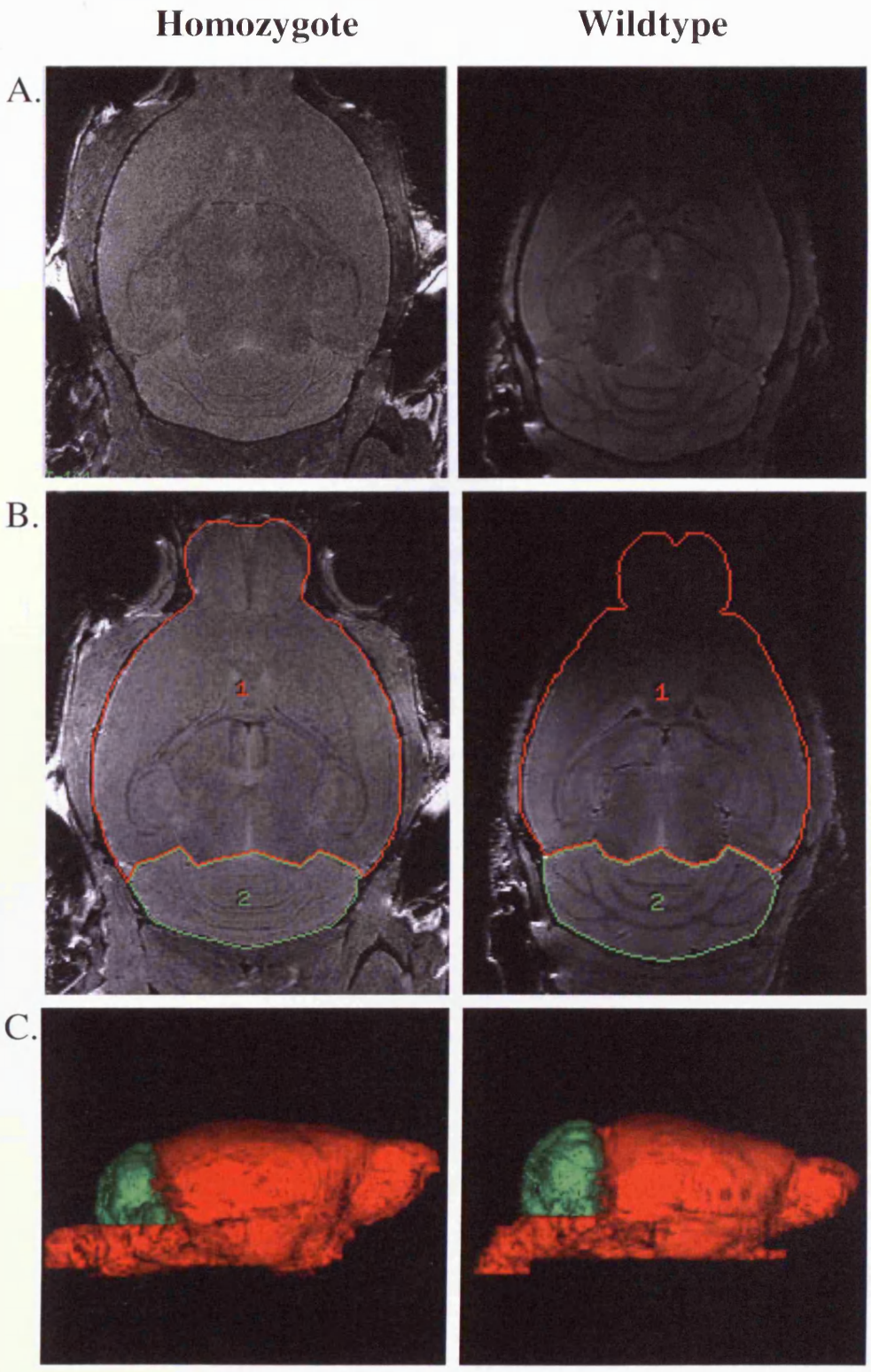

Figure 5.19. Cerebellar volume is reduced in *Opa3*$^{-/-}$ mice. (A) Representative MRI images of mouse brain in horizontal plane. (B) Manual outlining of cerebellum (green) and rest of brain (red) for volume analysis. (C) 3-D rendering of mouse brain showing cerebellum (green) and rest of brain (red). Cerebellum is visibly smaller in the homozygote.

5.4 Discussion

The present findings demonstrate that *Opa3*$^{-/-}$ mice display major changes in novelty-driven spontaneous activity characterised by hypoactivity, abnormal exploratory behaviour and impaired habituation to the test environment suggesting neuropsychiatric function maybe altered. In addition, *Opa3*$^{-/-}$ mice exhibit major impairments in motor coordination as observed in the rotarod and open field which cannot be explained by a deficit in muscle strength. This together with a splayed gait suggests cerebellar dysfunction. In rotarod testing they also exhibit poor motor learning skills which indicate deficits in cerebellum-dependent motor-learning tasks. Spinocerebellar function may also be impaired as indicated by limb grasping and splayed gait. These findings of impaired cerebellar function were strengthened by preliminary data on cerebellum volumetric analysis which showed a 40% reduction in cerebella brain mass in homozygotes.

In SHIRPA testing *Opa3*$^{-/-}$ showed clenching of the hind limbs when held by the tail and this together with the tremors and lower body weight are all signs of a neurological disorder. The leg extension reflex test evaluates the presence or absence of clasping of the hind limbs when a mouse is suspended by the tail, this is a measure of motor neuron functionality [Barneoud and Curet, 1999]. Limb clasping/extension, splayed gait and general aberrant behaviour suggest dysfunction of the cerebellum.

The homozygotes also showed a large reflexive body flinch to the acoustic startle test. This phenotype is usually considered to be a deficit in sensorimotor gating. Sensorimotor gating refers to the state-dependent regulation of transmission of sensory information to a motor system. It has been known for decades that sensory information does not have unfettered access to its targets in the CNS, as has the fact that sensorimotor gating often occurs via presynaptic inhibition of the activated sensory neuron(s). Glutamate is ubiquitously expressed in the brain and is a primary excitatory neurotransmitter. Glutamate excitotoxicity would affect the neurotransmission across the synapse and cause the high acoustic startle response and would also account for the cognitive deficits observed in MGA-III patients. This phenotype is a defect of the brain stem and since other brain stem tests were normal i.e., ear reflex, it may be that the high startle response is due to a defect in the structure of the tympanic bone which is known to be abnormal in some *Opa3*$^{-/-}$ mice (see Chapter IV). There

were neurological tests in which the homozygotes exhibited normal behaviour, such as tactile stimulus and negative geotaxis, suggesting the disease is confined to certain parts of the CNS.

The impairments in the open field task appear to reflect a deficit in motor co-ordination and the acquisition of normal patterns of adult mouse behaviour. The *Opa3*$^{-/-}$ mice displayed a reduction in horizontal as well as vertical activity. This reduction in locomotor activity may be indicative of motor impairment or weakness in the *Opa3*$^{-/-}$, particularly as little rearing behaviour was observed. As no muscle weakness was observed in the wire hang test it is more likely that lower locomotor activity was a result of motor impairment. However, it should be noted that the consistently smaller size of mutants may be masking any muscular strength deficiency on the wirehang test.

Alternatively, low activity can indicate increased anxiety or neophobia. Anxiety can be inferred by whether the majority of exploration occurs in close proximity to the walls (thigmotaxis) or in the centre of the test arena. The *Opa3*$^{-/-}$ spent significantly more time in the centre of the arena compared to the *Opa3*$^{+/+}$ and *Opa3*$^{+/-}$ mice suggesting a lack of fear. Also, when the apparatus is novel to the animals, more fear and anxiety related behaviours (such as stretch attends and activity in the corners and walls of the open field) would usually be displayed. The *Opa3*$^{-/-}$ displayed extremely few stretch attends and did not spend significantly more time in the corners of the arena compared to the *Opa3*$^{+/+}$ and *Opa3*$^{+/-}$ mice again suggesting a lack of fear and anxiety at being exposed to a novel environment.

These results for the homozygotes are unusual as time in centre is highly correlated with total locomotion these being related measures of avoidance and exploratory behaviour. However, if the raw data of the number of central and peripheral squares entered during the 5 mins is examined (Appendix III, Fig 10.1.) it can be seen that the *Opa3*$^{-/-}$ mice enter significantly less central squares than the *Opa3*$^{+/+}$ which would suggest increased anxiety. Also, if their behaviour is examined after they reach the periphery (time zero being once they have reached the periphery not when they were dropped into the arena) see Appendix III, Fig 10.2. the results would also suggest increased anxiety as the homozygotes spend significantly longer in the corner squares and significantly less time in the centre squares.

A reduction in rearing counts during the open field test strongly suggests an increase in anxiety and a deficit in exploratory behaviour. However, this discrepancy could be related to a

decrease in the balance and/or motor-coordination abilities of the *Opa3*$^{-/-}$ mice and not directly related to the exploratory behaviour or anxiety of the mice. The two legged stance used for rearing is less stable than the four legged stance used for horizontal movement. Control of body position involves the vestibular part of the inner ear, proprioreceptors in joints and muscles as well as vision. Gait abnormalities may affect the ability of animals to perform some of the tasks. Gait abnormalities can either be attributed to skeletal, muscular or neurological defects. In Costeff syndrome, patients suffer from extra-pyramidal dysfunction. The extra pyramidal system regulates posture and skeletal muscle tone. An inability to maintain posture and poor muscle tone may explain the footprint pattern of the homozygote mutant. Gait abnormalities together with limb grasping/limb extension are suggestive of defects in nerve function.

Overall, the lack of habituation in open field, no stretch attends when first placed in the arena, a considerably long time spent in centre of the arena when first dropped in, reduced rearing activity and reduced locomotor activity are not correlated behaviours and seem to reflect a generalized deficit in the acquisition of normal adult mouse behaviour in the homozygote mouse.

To investigate defects in motor coordination and balance an accelerating rotarod was used which requires enhanced motor coordination skills. This test is sensitive to cerebellar degeneration in mice with natural mutations [Lalonde and Strazielle, 1999] as well as transgenic mice with neurofilament [Lalonde *et al*, 1999 and 2003] and muscular anomalies [Taylor, 2001; Sugarman, 2002]. Motor impairment was present in the *Opa3*$^{-/-}$ mice through the whole of testing and was statistically significantly different from the *Opa3*$^{+/+}$ ($P<0.005$ at all time points), which suggests a baseline motor coordination impairment in the *Opa3*$^{-/-}$ mice. This would point to decreased cerebellar function, which is consistent with decreased stability in rearing. In addition, a reduction in the latency to fall off the rotating rod over repeated test sessions provides a measure of cerebellar motor-learning. *Opa3*$^{-/-}$ showed no improvement in rotarod performance indicating a deficit in cerebellar-dependent motor learning.

At the end of wirehang testing there was no statistically significant difference between all three genotypes suggesting that deficits in motor-co-ordination and splayed gait are not due to muscle weakness. Muscle histology and COX-SDH also suggest no muscular defects in the *Opa3* homozygote mice. It is interesting however that during the first several testing ages the

latency to fall was considerably lower in the homozygotes when compared to the wildtypes but over time showed a dramatic improvement. There maybe several possible reasons for this (i) The wirehang is based on fear of falling from a height, as the homozygote mice are blind this paradigm may not work as well. (ii) In the home cage environment food is suspended from a wire grid cage top. This wire grid can be used for exercise by the mice. Because the homozygotes are so small they cannot reach the wire grid and therefore unlike the wildtype and heterozygotes have no previous experience of hanging from a wire grid. (iii) Or, yet again, due to a generalised deficit in the acquisition of normal adult mouse behaviour. (iv) The dramatic improvement maybe due to the homozygotes weighing considerably less than the heterozygotes and wildtypes.

Each of these methods has limitations. There are several common confounders of the rotarod test. The first is that some animals may cling to the beam, and rotate with it, rather than fall when they lose balance. The second confound relates to individual animals that refuse the test and simply fall as soon as they are placed on the rod. This is especially relevant in longitudinal assessments, during which the animals can learn over repeated tests that the consequences of falling are innocuous. This behaviour was observed in several of our animals and they had to be excluded from the test cohort. A third confound relates to mouse weight: heavy mice perform worse than light mice. Thus, genetic or lesion-induced weight loss can offset motor disability and potentially skew results. Finally, and particularly with the accelerating version of the rotarod, speed is confounded by fatigue at progressively longer latencies. However, demonstration of differential deficits at higher rotation rates in a series of fixed-speed tests can be used to ensure that a more rapid fall is indeed attributable to problems with motor coordination rather than to greater susceptibility to fatigue. Despite these confounds, the rotarod remains one of the main tests of motor function in the mouse owing to its ease of use and sensitivity.

The wirehang test lacks sensitivity, and accurate assessment of grip strength is dependent on homogeneity of mouse weight across the cohorts. In addition, the mice tend to move around when the grid has been inverted, and consequently different muscle groups are being used or rested while the animal is moving. This contrasts with testing mice on the mechanical systems, where only forelimb muscles are being strained. Mouse movement can be difficult to overcome and tends to be strain dependent; agitating the grid before inverting it partially

resolves the problem, as the animals increase their grip as the grid is shaken. The same weight problem applies to the wire hang test.

The *Opa3*$^{-/-}$ mice show no gross outward abnormalities. However, they are considerably smaller than their wildtype littermates and exhibit deficits in both motor and cognitive behaviour. Despite the small size of the *Opa3*$^{-/-}$ the differences in motor function tests are unlikely to be attributed to body mass as apart from an initial improvement in performance (probably due to either initial learning of the task or increase in muscle mass due to the young age of the mice) the variation between the wildtype and mutant strain was essentially consistent throughout the experiment.

All the above neurological and behavioural tests suggest defects in the cerebellum which is known to play an important role in motor control. It is also involved in some cognitive functions such as attention and language, and probably in some emotional functions such as regulating fear and pleasure responses. The cerebellum also is necessary for several types of motor learning, most notably learning to adjust to changes in sensorimotor relationships. The cerebellum does not initiate movement, but it contributes to coordination, precision, and accurate timing. It receives input from sensory systems and from other parts of the brain and spinal cord and integrates these inputs to fine tune motor activity. Because of this fine-tuning function, damage to the cerebellum does not cause paralysis but instead produces disorders in fine movement, equilibrium, posture, and motor learning.

High resolution three-dimensional MRI revealed that the volume of the cerebellum was significantly reduced in the homozygote mouse. This anatomical phenotype was not readily apparent from previous H&E analysis [Davies *et al*, 2008]. Cerebellar dysfunction is present in MGA-III patients but usually of a mild degree and cognitive impairments are seen in some individuals ranging from IQ of 40 upwards. Any reduction in cerebellar volume in MGA-III patients is at present unknown.

5.5 Conclusions

- The *Opa3*$^{-/-}$ mice exhibited major impairments in motor coordination as observed in the rotarod and open field which is not caused by a deficit in muscle strength as shown in the wirehang test. Therefore, the data supports the idea that absence of OPA3 contributes significantly to neurological impairment in diseases such as MGA-III.

- The wirehang test, COX-SDH staining and H&E muscle sections (Chapter IV) suggest that the *Opa3*^{L122P} mutation does not affect muscle.

- The findings suggest that *Opa3* plays a role in the mechanisms underlying complex behaviours in the adult mouse, in particular cognitive processes. The mice displayed abnormal exploratory behaviour and impaired habituation to the test environment suggesting neuropsychiatric function maybe altered. It is therefore likely to be important for normal function in the human brain. This concurs with MGA-III patients who are known to suffer from cognitive deficits.

- Cerebellum function is affected in the *Opa3*^{L122P} mice. In rotarod testing, they also exhibited poor motor learning skills, which again indicate deficits in cerebellum-dependent motor-learning tasks. A splayed gait also suggests cerebellar dysfunction. These findings of impaired cerebellar function were strengthened by preliminary data on cerebellum volumetric analysis which showed a 40% reduction in cerebellar brain mass in homozygotes.

CHAPTER VI

The *Opa3*^{L122P} mouse model of MGA-III displays profound disturbance in lipid metabolism

6.1 Introduction

Aims of chapter

- Plasma biochemistry for metabolic disturbances and analysis of 3-methylglutaconic acid to confirm our *Opa3*^{L122P} mutant mouse as a model of MGA-III.
- Assessment of decreased body fat observed in MRI scans by quantification of subcutaneous and visceral fat pads.
- Analysis of disturbed energy homeostasis by quantification of increased fat deposition in liver and bone marrow.

Increased urinary excretion of 3-methylglutaconic acid and to a lesser extent 3-methylglutaric acid is a common feature of all the MGA syndromes and they are therefore considered metabolic disorders. It was not surprising then, that in the homozygote mouse, profound disturbances in metabolic homeostasis were observed. MRI scans showed a lack of white adipose tissue (WAT) [Davies *et al*, 2008], histological sections (Chapter IV) showed G3/4 *Opa3*$^{-/-}$ C57BL/6JCrl mice with large fat deposits in the liver, and homozygote mice whilst housed separately seemed unable to maintain their body temperature and quickly die. Bio-informatics of TFBS for putative functional analysis also indicated a possible role for *Opa3* in adipogenesis. This chapter attempts to characterize the disturbance in metabolic homeostasis in our mouse model.

All work in this chapter was done in collaboration with Dr Timothy Wells, School of Biological Sciences, Cardiff University, with plasma analysis undertaken by Dr Irina Guschina, School of Biological Sciences, Cardiff University.

6.1.1 Adipose tissue in mammals

The adipose tissue pool in mammals is composed of two different types of fat: WAT and BAT, which have different physiological roles and can be distinguished by their appearance and metabolic features [Cinti, 2005]. The quantity of body fat varies widely in mammals, ranging from 2 to > 50% of body mass, but is typically 10 to 25% in mice and humans. Adipose tissue is an important metabolic organ that is crucial for whole-body energy homeostasis [Rosen and Spiegelman, 2006].

WAT is the predominant type of fat in adult humans and mice and white adipocytes are the major cellular components of visceral and subcutaneous WAT depots [Cinti, 2005]. It is the major organ for regulated storage of triglycerides for use as metabolic energy and also helps control energy homeostasis including food intake, metabolic efficiency, and energy expenditure via secreted signalling molecules, termed adipokines. Thus WAT is involved in diverse range of physiological processes.

The principal function of BAT is heat production (non-shivering or adaptive thermogenesis) this phenomenon does not exist in the absence of functional brown adipose tissue. It is the primary thermogenic mechanism for newborns and rodents to prevent hypothermia [Klingenspor, 2003]. Brown adipocytes are very rich in mitochondria that uniquely express the UCP-1. When activated, this protein dissipates proton motive force in the form of heat. Recent data has shown the presence of this tissue in healthy, adult humans [Nedergaard *et al*, 2007; Virtanen *et al*, 2009].

Mitochondria play a central role in adipose metabolism, as highlighted by mitochondrial impairment in metabolic diseases [Holloway *et al*, 2009] and neurodegenerative diseases, and in aging [Guarente, 2008 and Katic *et al*, 2007].

6.1.2 Energy homeostasis

Energy homeostasis is the process whereby bodyweight and fat mass are maintained at relatively stable levels over long periods despite day-to-day fluctuations in food intake and energy expenditure and depends on the ability of the CNS to sense and respond to changes in adiposity. A sophisticated lipoprotein transport system exists to meet the different energy demands from a variety of tissues (Fig 6.1.).

Most of the energy stored in adipose tissue comes from plasma triglycerols which are provided by dietary lipids. These dietary lipids are absorbed through the gastrointestinal tract in the form of circulating chylomicrons and very-low-density lipoprotein (VLDL), part of which is metabolized to provide energy and the rest of which enters the liver and adipose tissue for short and long term storage, respectively. As a gauge of the level of energy reserves, adipose tissues secrete several adipokines, such as leptin, which regulates energy homeostasis by signalling to the brain and peripheral tissues.

To meet increasing energy demands, or during starvation, triacylglycerol (TAG) stores are mobilised in adipose tissue, this hydrolysis of TAG into FAs and glycerol being known as lipolysis. Leaving the adipocytes, the FAs circulate in the plasma as free FAs bound to plasma albumin to be utilized principally by adipocytes (re-esterification into TAG), muscles (oxidation) and liver (oxidation and also for TAG synthesis and VLDL secretion).

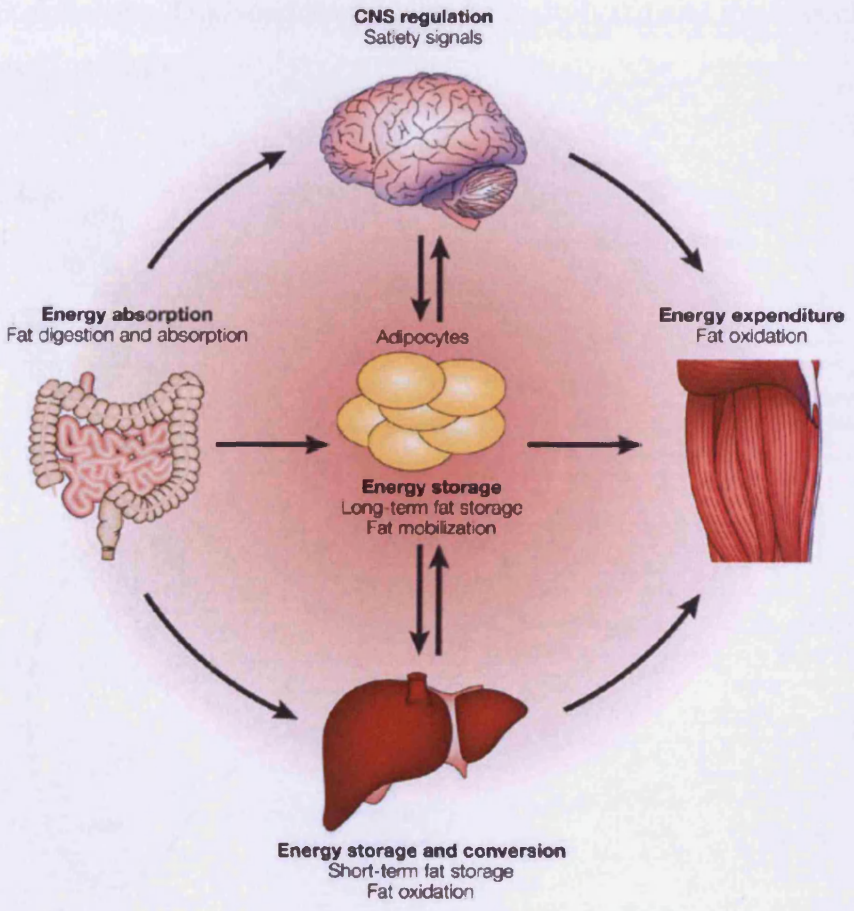

Figure 6.1. Adipose tissue, which is the main energy storage site, is responsive to both central and peripheral metabolic signals by regulating lipid storage and mobilization. [Shi and Burn, 2004]

The liver has an important role as a homeostat for transient energy fluctuation; it protects other tissues from postprandial triglyceridaemia by temporarily storing FAs from the circulation as a benign derivative, TAG, and secreting them as VLDL when the period of maximum lipid load has passed. The liver is also an important site for energy conversion, exchanging energy sources from one form to another, such as glycogen to glucose, FA to TAG and saturated FA to unsaturated FA. The potential sources of hepatic TAG include

peripheral fats stored in WAT that flow to the liver by way of the plasma free FAs pool, dietary FAs (mainly through the uptake of intestinally derived chylomicron remnants), and FAs newly made within the liver through de novo lipogenesis (Fig 6.2.). After the esterification step (conversion of FAs into TAG), TAG can then be stored as lipid droplets within hepatocytes or secreted into the blood as VLDL for storage in adipocytes and to cardiac and skeletal muscle for energy consumption. Lipoproteins are composed of triglycerides, cholesterol esters, phospholipids, and apolipoproteins, which modulate lipoprotein catabolism. Triglycerides can also be hydrolyzed and the FAs channelled towards the β-oxidation pathway.

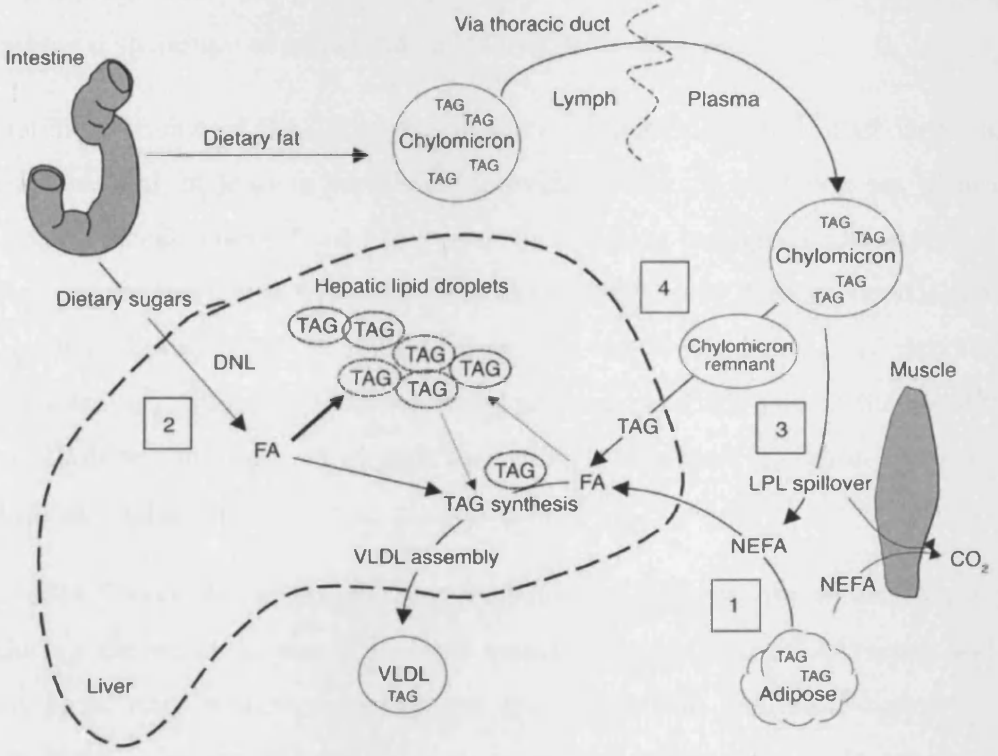

Figure 6.2. Model of lipid flux through the liver. De novo lipogenesis (DNL) indicates new fat synthesis from 2-carbon precursors (e.g., dietary carbohydrate); chylomicrons are lipoproteins made in the intestine that carry dietary fat. FA, cellular fatty acids (fatty acids not esterified to glycerol but bound to a carrier protein); LPL= lipoprotein lipase, NEFAs = nonesterified fatty. [Donnelly *et al*, 2005]

The synthesis of TAG in liver is nutritionally regulated, and its formation from simple carbohydrates requires multiple metabolic pathways, including glycolysis and pyruvate oxidation to generate acetyl-CoA for FA synthesis, NADPH generation to supply the reductive power, packaging of FAs into a glycerophosphate backbone, and finally, lipoprotein packaging to export TAG.

6.1.3 Thermogenesis

BAT has developed as an essential thermoregulatory effector in cold defence in rodents and other small mammals [Golozoubova *et al*, 2006], including infant humans. Upon cold exposure, heat production in the animals is facilitated by the splanchnic nerve-stimulated release of catecholamines, which activates thermogenesis and dissipation of the generated heat through the circulation. Heat production is accomplished by the heat-generating capacity of a significant facilitated proton leak across the extensive mitochondrial membranes of the brown adipocytes, which occurs because of the high expression of UCP-1 in BAT mitochondria [Cannon and Nedergaard, 2004]. UCP-1 is exclusively expressed in brown adipocytes, and while analysis of WAT depots displays some low level of UCP-1, it is likely due to the sparse distribution of brown fat cells throughout the tissue.

The potential significance of BAT thermogenesis in adult humans and other large mammals has been controversial, at least in part, because evidence for its existence has been lacking. However, several recent observations using positron emission tomographic scanning to assess tissue glucose uptake [reviewed by Nedergaard *et al*, 2007] have demonstrated a remarkable amount of brown adipose tissue in adult humans, and the locations of BAT depots in adult humans bear a striking similarity to those in rodents: a large BAT pad in the vicinity of the scapulae and shoulders and individual pads atop each sympathetic ganglion and surrounding the adrenal glands and kidneys.

In addition to BAT, body temperature is also regulated by shivering thermogenesis in skeletal muscles. During the rapid, repeated skeletal muscle contractions of shivering and during increases in heart rate, thermogenesis arises primarily from the inefficiency of energy utilization in cross-bridge cycling and calcium ion sequestration and, to a lesser degree, from mitochondrial membrane proton leak in the course of ATP production from fuel substrate oxidation [Rall and Woledge, 1990; Jubrias *et al*, 2008]. The muscle contractions of shivering result from rhythmic bursts of activity in the α-motoneurons innervating skeletal muscle fibres.

There are no reports of unusual WAT distribution or hepatic steatosis in MGA-III patients, but microvesicular hepatic steatosis has been observed in MGA-V patients. This chapter attempts to characterize these phenomena in our mouse model. To determine the severity of lipodystrophy, fat deposition in abdominal and visceral fat pads was quantified. Liver and bone marrow adiposity were also assessed to give a better understanding of energy

homeostasis. This together with serum chemistry quantification of metabolites and 3-methylglutaconic acid will assist in characterizing the disturbances in metabolic homeostasis in our mouse model.

6.2 Materials and Methods

6.2.1 Mice used

A cohort of twelve male 30 day old mice were used (*Opa3*$^{-/-}$ n=6, *Opa3*$^{+/+}$ n=6).

6.2.2 Tissue collection

Mice were weighed and anesthetized with isofluorane prior to decapitation. Trunk blood was collected, centrifuged and separated plasma was stored at -20°C for subsequent plasma biochemistry. Visceral (epididymal and retroperitoneal) and subcutaneous (inguinal) fat pads were excised and weighed. The right tibiae were removed, the length measured with a hand-held micro meter and treated for subsequent determination of epiphyseal plate width (EPW) and quantification of bone marrow adiposity. Liver samples excised stored at –70°C for subsequent analysis of lipid and TAG content.

6.2.3 Blood plasma biochemistry

It was not possible to obtain urine samples from the *Opa3* homozygotes mice because they produced such extremely low amounts despite not being dehydrated. Blood was therefore analysed for 3-methylglutaconic acid to confirm the mouse as a model of MGA-III.

6.2.3.1 Measurement of 3-methylglutaconic acid

50-100 µl of plasma was extracted with ethyl acetate (3x3ml) and diethyl ether (3x3ml). The combined extracts were dried under a stream of nitrogen, reconstituted in small volumes of hexane and transferred into gas chromatography vials. Pentadecanoic acid (C15:0) was added as an internal standard, the extracts were dried under nitrogen and derivatised with BSTFA (N,O-bis(trimethylsilyl)trifluoroacetamide) and pyridine (1:1, v/v) at 70°C for 30 mins. The solution was dried under nitrogen and re-dissolved into 30 µl of hexane.

Trimethylsilyl (TMS) derivatives of 3-methylglutaconic acid was analysed by GC-MS using an Agilent 6890N GC with 5973N MS and 7683 autosampler fitted with 30m X 0.25mm internal dimensions (i.d.) column (Agilent HP-5MS, phase thickness 0.25um). A 2µl sample was injected at 230°C using a 50:1 split ratio. The column was temperature programmed from 80°C to 270°C 10°C/min, then held at 270°C for 20 min; carrier gas was helium at the constant pressure of 13.43 psi. MS scanning mass to charge ratio (m/z) from 50 - 700 after 2

mins solvent delay. Characteristic ion for di-TMS of 3-methylglutaconic acid at m/z 288 was used to monitor the separation of 3-methylglutaconic acid. Quantification was made by reference to an internal standard of pentadecanoate (C15: 0).

6.2.3.2 Liver triglycerides

Lipids were extracted (from plasma and liver) by the Folch method [Kates, 1986]. Triacylglycerols and total polar lipids were separated by thin-layer chromatography and quantified by their FA contents. FA methyl esters were separated using a Clarus 500 gas chromatograph (PerkinElmer, Norwalk, CT), identified by comparing retention times with FA standards (Nu-Chek Prep., Inc., Elysian, MN) and quantified against an internal pentadecanoate standard.

6.2.4 Bone histology

Dissected tibiae were fixed in 4% PFA for five days and decalcified in 20% EDTA for three weeks. After being embedded in paraffin wax, 7-μm-longitudinal/anterior-posterior sections were taken and alternate sections stained with Masson's Trichrome [Masson, 1929] or toluidine blue (see Chapter II). EPW were measured on Masson's Trichrome-stained sections under light microscopy using Leica QWin software, with three measurements taken per section and three sections measured per bone. Bone marrow adiposity was analysed on toluidine blue sections using Image J.

6.2.4.1 Analysis of bone marrow adiposity using ImageJ

Digital images of mid-diaphyseal marrow were taken with a Leica DFC300FX digital camera mounted on a Leica DMLB microscope. A scale bar was added for image size and the image was saved as a jpeg file.

6.2.4.2 Using Image J

The images were converted to black and white. Firstly, this was done by brightness/contrast so that the white of the adipocytes is truly white, and then the image was changed to black and white using Image-type 8 bit.

Adipocytes were identified in the picture by circling in grey then all the adipocytes were filled in black. This was then checked against the original section picture to make sure all the adipocytes were filled in. The rest of the image was then removed to leave just the adipocytes

by selecting Image-Adjust-Threshold. The number of adipocytes and their area was then counted by selecting Analyze-Set Measurements and ticking Area. Then Analyze-Analyze particles were selected and range was set "from 10μm-Infinity", "Include interior holes" and "Exclude particles touching the edge". The data was then copied into an excel file and expressed as % adiposity, adipocyte number and adipocyte size. Three different sections from each bone were analysed.

6.2.5 Adiposity profiling of Liver

15μm cryostat sections of liver were stained with Oil red-O and counterstained with Mayer's haematoxylin (see Chapter II). Digital images (one image per section, three sections per mouse) were obtained with a Leica DFC300FX digital camera and a Leica DMLB microscope. Hepatic lipid droplets were measured using Q-Win.

6.2.5.1 Analysis of liver steatosis using QWin

The Leica QWin V3 software was used to analyse steatosis. The microscope was set to bright field and x 20 magnification. On the image preview page the '16-Bit/Channel' colour depth and 'Colour' image type were selected. The settings were then adjusted to:-

Exposure 2.03ms Gain x 4 Colour saturation x 2

The focus was then changed to x 40 and the zoom was used to focus the section. 'Acquire' was clicked then 'lens select for x 40' was clicked to change the pixel ratio to 0.205um

The 'colour detect' setting was then adjusted depending on the tissue type.

For normal steatosed liver i.e., wildtype mice, the setting was:

Colour detect Red 255/130 Green 110/0 Blue 50-60/0

For heavily steatosed liver ie homozygotes the setting was:

Colour detect Red 255/160 Green 60/0 Blue 50/0

Then 'measure feature' was clicked to give the number of features and the total area of the features. Colour detect levels for the heavily steatosed livers had to be set a different levels otherwise the whole field of view was marked as being fat.

6.2.6 Thermal Imaging

Using a dynamic, non-contact infrared camera (Thermo-Tracer TH7102MX, NEC San-ei), thermal images were taken of a 30 day old female and a wildtype control mouse. As variations in surface and volume ratios in organisms lead to variations in heat loss or retention

a 12 day old pup was also compared to the 30 days old homozygote female as a size matched control.

6.2.7 Statistics

Statistical analysis was carried out with SPSS 16. Results are expressed as mean ± S.E.M, differences between groups was compared using unpaired Student's *t* test. Results with $P \leq 0.05$ were considered statistically significantly different.

6.3 Results

6.3.1 General Physiology and Plasma Biochemistry of *Opa3* mutant mice

At 30 days of age the *Opa3*$^{-/-}$ mice were considerably smaller than their wildtype controls which corresponded to a 60 % reduction in body weight, accompanied by a 22 % reduction in tibiae length (Table 6.1.). The EPW of the *Opa3*$^{-/-}$ mice was 86% of the wildtype controls (P= 0.140). This would indicate that their lower body weight was due more to loss of body tissue than to a smaller skeleton.

Quantification of circulating 3-methylglutaconic acid showed a 16 fold increase confirming the *Opa3* homozygote mouse as a suitable model of Costeff's Syndrome. Serum chemistry quantification of plasma lipid, free FAs, plasma esterase (ES) and plasma ES-ARA were not significantly different from wildtype controls. Plasma ES and plasma ES-ARA are diet derived fats and indicate that the lack of WAT was not due to starvation.

	Wildtype	***Opa3* homozygote**	***P*-value**
Body Weight (g)	16.24 ± 0.47	6.46 ± 0.50	$P < 0.001$
Tibial Length (mm)	15.18 ± 0.14	11.79 ± 0.46	$P < 0.001$
Tibial epiphyseal plate width (μm)	272 ± 8	234 ± 32	$P = 0.140$
Plasma Biochemistry			
Osmolality (mOsm/kg)	295.7 ± 2.0	296.6 ± 3.4	$P = 0.202$
3-methylglutaconic acid (μg / 100μl)	0.377 ± 0.058	6.150 ± 20.325	$P = 0.000$
Total plasma lipid (μg / 100mg)	221.716 ± 18.661	182.36 ± 21.120	$P = 0.097$
Plasma free fatty acids (μg / 100mg)	11.917 ± 1.395	14.7 ± 1.665	$P = 0.286$
Plasma ES (μg / 100mg)	64.45 ± 9.217	48.42 ± 4.632	$P = 0.089$
Plasma ES-ARA (μg / 100mg)	51.15 ± 9.234	41.48 ± 10.482	$P = 0.252$

Table 6.1. General physiology and plasma biochemistry in male *Opa3*$^{-/-}$ mice.

6.3.2 *Opa3*$^{-/-}$ display profound leanness

To assess the loss of adipose tissue observed in previous MRI scans [Davies *et al*, 2008], fat depots were taken and weighed. Three fat pads were taken: one subcutaneous (inguinal) and two visceral (epididymal and retroperitoneal). Visceral adiposity was considerably decreased in the male *Opa3*$^{-/-}$ mice with both visceral depots as a percentage of body weight less than one-half that in wildtype controls (Fig 6.3A&E.). No significant difference was observed in the weight of the inguinal fat pads. Therefore, only abdominal fat depots seem to be affected.

Histological sections were taken of epididymal fat pads for adipocyte size measurements (Adipocyte size analysis by Dr Tim Wells) (Fig 6.3.). Adipocytes were 70% smaller than the wildtype controls ($P<0.001$). White adipocytes are typically larger than brown adipocytes, contain fewer mitochondria, and have a single large lipid droplet, pushing the nucleus to the cell periphery. In contrast, brown adipocyes are polygonal in shape, mitochondria-rich with multiple lipid drops scattered throughout. The nucleus is round and although eccentrically located, it is not in the periphery of the cell. Micrographs show the homozygote adipocytes to be structurally different (Fig 6.3D.) to the wildtype controls. The adipocytes in the wildtype control are typical of WAT displaying a single large lipid droplet with the nucleus at the cell periphery as seen in Fig 6.3C (arrow). However, structurally the WAT in *Opa3*$^{-/-}$ more closely resembles BAT displaying smaller cells with larger eccentrically located nuclei as seen in Fig 6.3D (arrow).

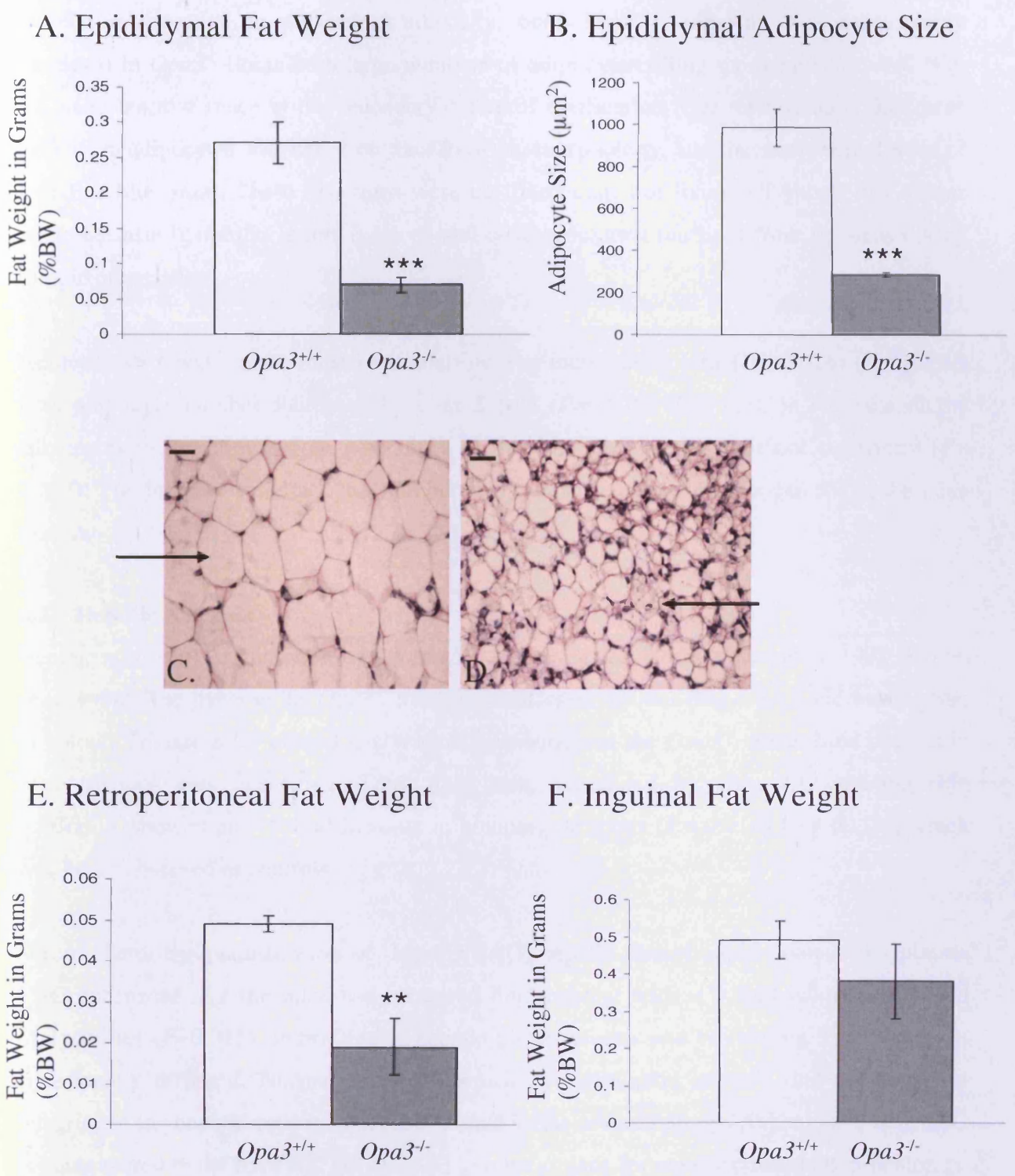

Figure 6.3. Quantification of (A) epididymal, (E) retroperitoneal and (F) inguinal WAT depots from male 30 day old *Opa3*$^{-/-}$ and age-matched control mice. (B) Graph displaying decreased adipocyte size in epididymal WAT depots in *Opa3*$^{-/-}$ compared to age-matched control mice. Representative images of epididymal fat pad sections in (C) *Opa3*$^{+/+}$ and (D) *Opa3*$^{-/-}$ are also presented (scale bar, 50 μm). Values shown are mean ± S.E.M. (*Opa3*$^{-/-}$ n=6, *Opa3*$^{+/+}$ n=6). BW, body weight. **$P < 0.01$; ***$P < 0.001$.

6.3.3 Bone Marrow adiposity

Despite a reduction in abdominal adiposity, bone marrow adiposity was considerably increased in *Opa3*$^{-/-}$ tibiae with large numbers of adipocytes filling the medullary canal (Fig 6.4.) and marrow space in the secondary centre of ossification. Our interpretation that these cells were adipocytes was based on their location, morphology, and that they were devoid of toluidine blue stain. These structures were not fixed cells but fixed cell ghosts that appear white because lipophilic agents (acetone and ethanol) extract the lipid from the cells during sample preparation.

Adiposity in *Opa3*$^{-/-}$ male mice bone marrow was increased 8 fold (P= 0.014) (Fig 59.A.) with adipocyte number increased by over 5 fold (P=0.028) (Fig 6.4C.). The size of the adipocytes in the homozygote was 158% of the wildtype but this was not significant (P= 0.087). The increase in adipocytes number suggests an increase in adipogenesis in the bone marrow.

6.3.4 Hepatic steatosis

Hepatic steatosis is common in lipodystrophic mouse models [Shimomura *et al*, 1998; Moitra *et al*, 1998]. The livers in the *Opa3*$^{-/-}$ mice were enlarged, heavier (Fig 6.5A.) and were lighter in colour. To assess for altered triglyceride distribution in the *Opa3*$^{-/-}$ mice, lipid content in liver sections was quantified. Total lipid area, visualized by Oil-red-O staining (Fig 6.5B&C.), showed an ~ 9 fold increase in homozygote livers (P= 0.018) (Fig 60.D.), which was never observed in controls.

Serum chemistry quantification of hepatic TAG, hepatic phospholipid content and plasma TAG confirmed that the mice had increased lipid content with ~ 9 fold increase in stored triglycerides (P=0.015). Interestingly, hepatic phospholipids and circulating TAG were not significantly different. Normal levels of hepatic phospholipids indicate that the structural integrity of the hepatic cells is intact and normal levels of circulating TAG suggests that TAG is being stored in the liver and not released to other organs for energy consumption or storage in adipose tissue.

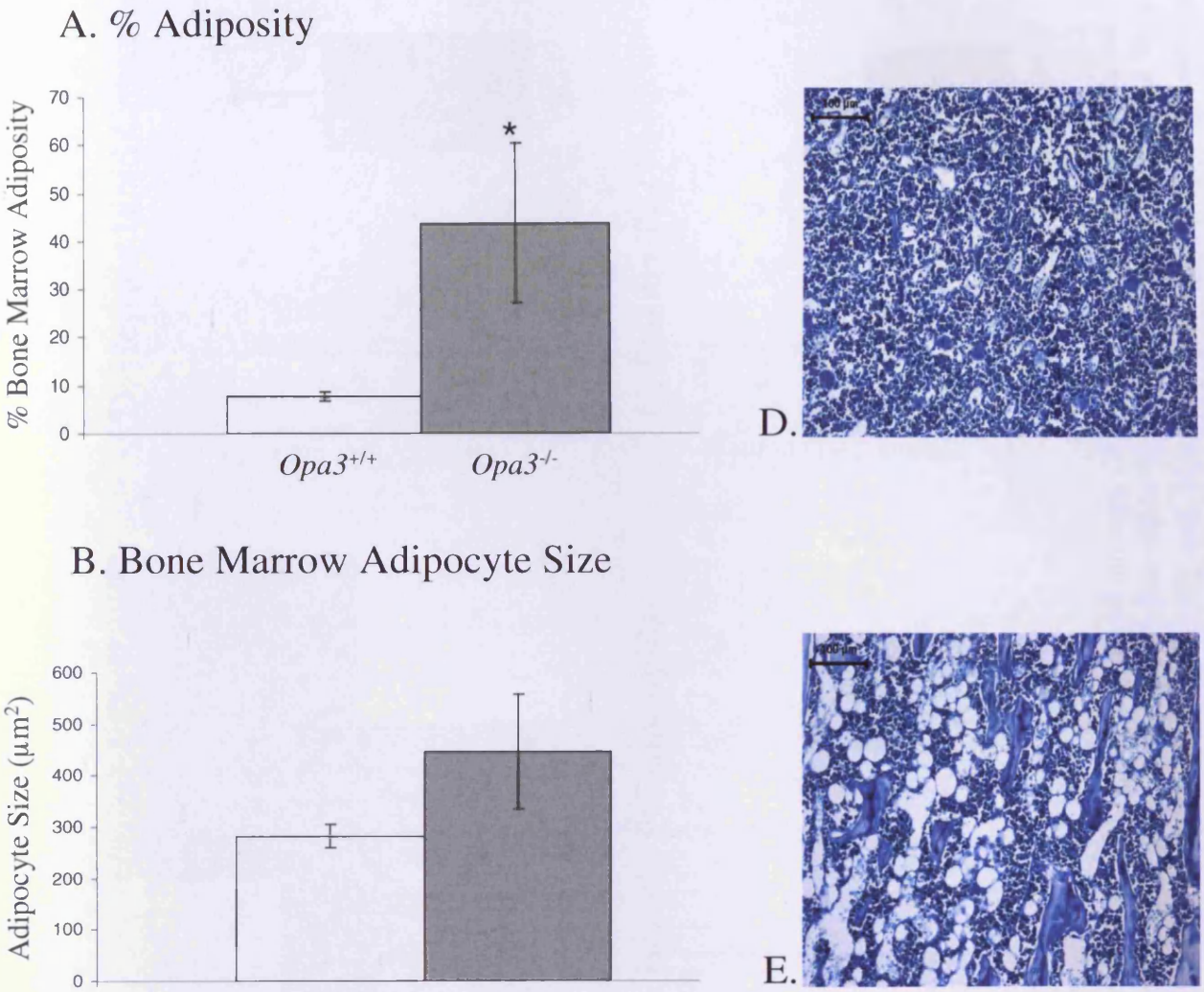

Figure 6.4. Quantification of bone marrow adiposity in toluidine blue stained proximal tibiae from male 30 day old *Opa3*$^{-/-}$ and age-matched control mice. (A) tibial bone marrow adiposity, (B) tibial marrow adipocyte size and (C) tibial marrow adipocyte number. Representative images of middiaphyseal tibial marrow sections (x20) from 30 day old (D) *Opa3*$^{+/+}$ and (E) *Opa3*$^{-/-}$ are also presented (scale bar, 50 µm). Values shown are mean ± S.E.M. (*Opa3*$^{-/-}$ n=6, *Opa3*$^{+/+}$ n=6). *$P < 0.05$.

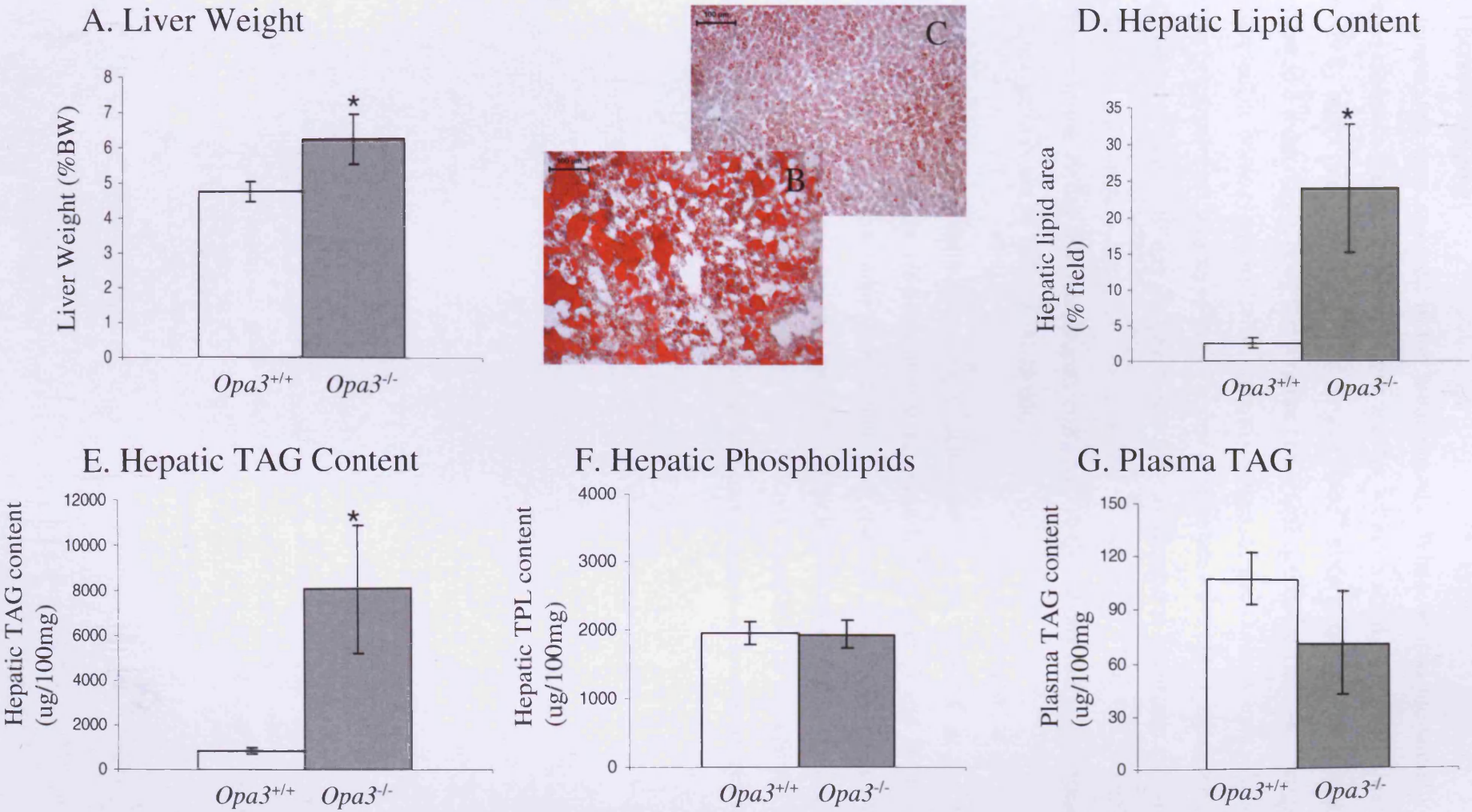

Figure 6.5. The effect of the *Opa3* mutation on hepatic TAG production and storage. (A) Liver weight. (B) Representative images of liver sections from *Opa3*$^{-/-}$ mice as compared to age-matched littermate control (C). Increased hepatic lipid content shown on (D) together with increased hepatic TAG content (E). (F) and (G) show no significant difference in hepatic phospholipids and plasma TAG respectively. Values are shown as mean ± S.E.M. *P<0.05.

6.3.5 Thermal imaging

Body temperature was assessed in the homozygotes. When housed individually they seem unable to maintain their body temperature and die within a short time. Preliminary results of surface body temperature in a 30 day old female *Opa3*$^{-/-}$ mice in the latter stages of the disease state showed a reduction in body temperature of ~4°C (Fig 6.6A.). The lower temperature was not observed in homozygote mice in the early stages of the disease state. To assess if the lower body temperature was an effect of higher surface area to volume ratio, the homozygote was also compared to a 12 day old pup (Fig 6.6B.) as variations in surface and volume ratios in organisms can lead to variations in heat loss or retention. The image shows a lower temperature in the 30 day old homozygote compared to the 12 day old pup suggesting surface area/volume ratio is not an influencing factor.

This reduction in body temperature is of particular interest as BAT in the *Opa3*$^{-/-}$ as a percentage of body weight was double that in controls (Fig 6.6C.) and BAT intrascapular adipocytes were more than three times larger than controls (Fig 6.6D.) suggesting that the reduced body temperature is due to perturbed metabolic processes rather than aberrant tissue development. However, the *Opa3*$^{-/-}$ mice were inactive compared to the control mice, which would suggest that the hypothermia maybe due in part to a lack of locomotor activity.

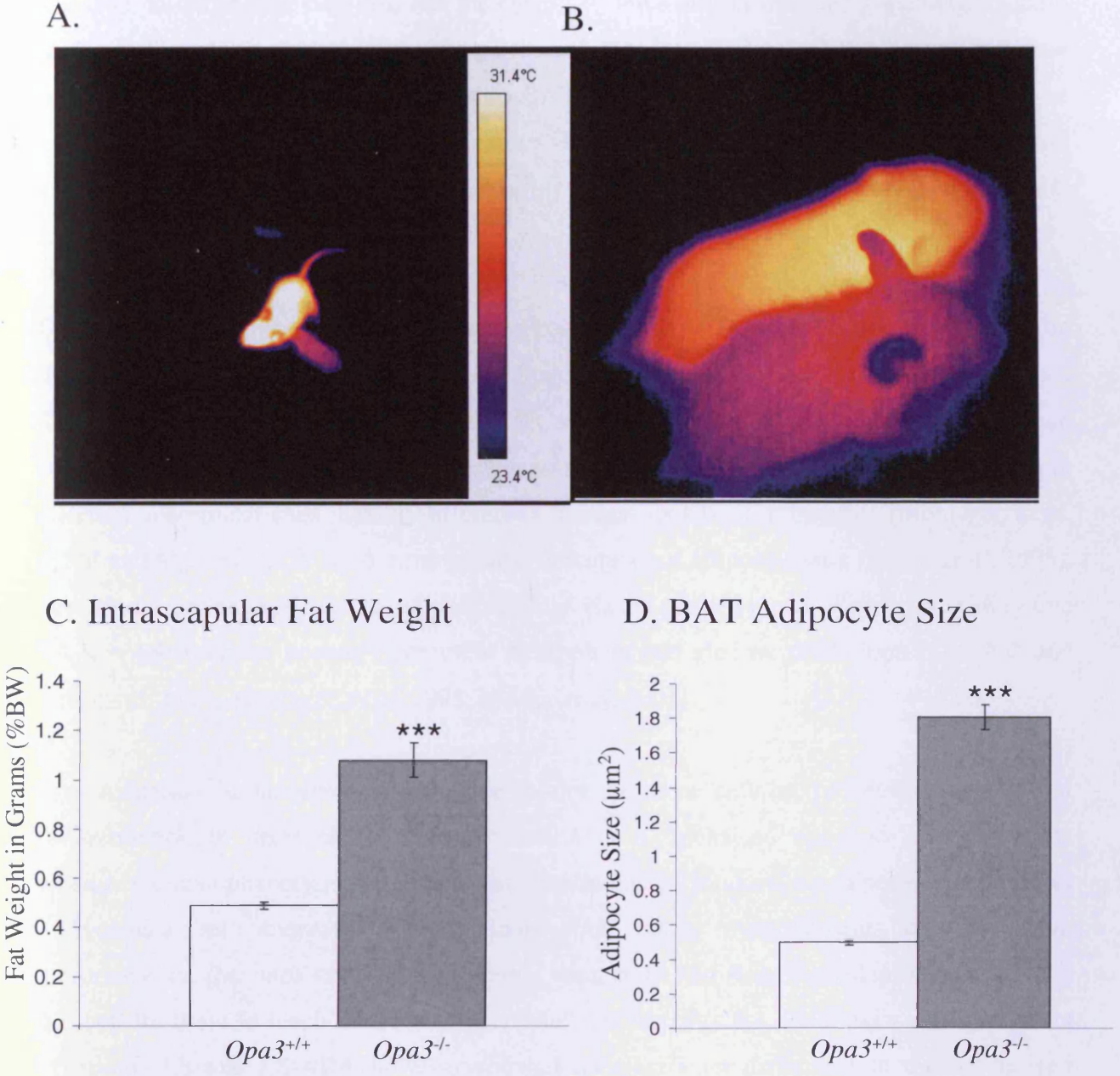

Figure 6.6. The *Opa3*$^{-/-}$ mice display defects in thermoregulation. Thermal imaging shows lower surface body temperature in a 30 day old homozygote compared to (A) age matched control and (B) 12 day old, size matched pup. (C) Quantification of intrascapular BAT depots from male 30 day old *Opa3*-/- and age-matched control mice. (D) Graph displaying increased adipocyte size in intrascapular BAT depots in *Opa3*$^{-/-}$ compared to age-matched control mice. Values shown are mean ± S.E.M. (*Opa3*$^{+/+}$ n=3, *Opa3*$^{-/-}$ n=3). BW, body weight. * *P*< 0.001.**

6.4 Discussion

The data presented here confirms that the *Opa3*^{L122P} mice display elevated 3-methylglutaconic acidemia. In addition, there is a profound reduction in intra-abdominal WAT, and what little remains appeared histologically similar to BAT. This was accompanied by an elevation in marrow adiposity and severe hepatic steatosis. Despite this fact the circulating TAG was not significantly different. In the final stages of the disease state *Opa3*$^{-/-}$ mice exhibited an ~4°C reduction in surface body temperature.

One of the hallmarks of the *Opa3* homozygote phenotype is a significant loss of adipose tissue which manifests as a reduction in abdominal fat depots but not in subcutaneous depots. This would be expected, as abdominal fat is linked to metabolic disorders more than subcutaneous fat. The difference may be due to subcutaneous and visceral adipocytes being in different anatomical sites, having differences in basal metabolic properties [Montague *et al*, 1998] and higher rates of lipid turnover than subcutaneous adipose tissue [Marin *et al*, 1996]. The venous drainage of visceral adipose tissue is via the portal system, directly providing free FA as a substrate for hepatic lipoprotein metabolism and glucose production [Kissebah and Krakower, 1994; Montague *et al*, 1998; Niesler *et al*, 2001]

This reduction in fat mass may be due to one or more cellular processes a) decreased differentiation b) decreased lipid accumulation or c) increased apoptosis. To determine whether the lean phenotype is due to a reduction in energy intake (i.e., adipocytes depleted in triglycerides but otherwise normal), daily food intake measurements can be taken. Unfortunately, the mice could not be housed separately and neurological problems made it difficult for them to reach the food hopper, thus this test was not undertaken. Measurements of plasma ES and ES-ARA however showed no significant difference in dietary derived lipids, suggesting normal food intake in homozygotes compared to wildtypes. Normally, mice with depleted adipocytes are insulin sensitive, have normal sized livers, and have normal or low liver and circulating triglycerides. In contrast, mice with ablated or malfunctioning adipocytes have insulin resistance, enlarged fatty livers and elevated circulating triglyceride levels. The *Opa3*$^{-/-}$ mice do not fall definitely into either category, as they display enlarged fatty liver but have normal circulating triglyceride levels. However, the enlarged liver, normal plasma ES and ES-ARA levels and WAT appearing histologically similar to BAT would suggest that the adipocytes are malfunctioning.

The histological sectioning of the depleted epididymal fat depots showed that the adipoctyes look structurally like brown adipocytes. Previous descriptions of fat depots have implied that white and brown adipocytes are in separate depots in distinct sites around the body. However, a very recent theory suggests that white and brown adipocytes are intermingled in fat depots [Cinti, 2009] which has led to the new concept of the adipose organ. This hypothesis of reversible physiological transdifferentiation suggests that brown and white adipocytes co-exist in fat depots and are capable of transdifferentiating into one another, to meet different energy partitioning demands. This reversible transdifferentiation can be induced by physiological stimuli, such as exposure to cold (the organ's phenotype switches from white to brown), warm exposure (the phenotype switches from brown to white), and pregnancy-lactation (part of the organ's phenotype changes from WAT to milk secreting glands), which would stem from intrinsic biological properties of the adipocytes. Therefore the brown adipocytes phenotype observed in the epididymal WAT depot of the homozygote maybe a compensatory mechanism for the observed decrease in body temperature. An increase in brown adipoctes in WAT depots has been observed in 129Sv mice kept in cold conditions (6°C) for 10 days. These mice displayed a dramatic increase in brown adipocyte content in their fat depots compared to mice maintained in near thermoneutrality conditions (28°C) for 10 days [Cinti, 2009]. It has been shown that these cold induced changes are not due to DNA replication in WAT as the total number of adipocytes does not differ from that of controls [Miller and Faust, 1982; Cousin *et al*, 1996]. There is no sign of white adipocyte degeneration or apoptosis it is therefore likely that most of the newly-formed brown adipocytes are derived from a direct transformation of white adipocytes into brown adipocytes [Murano *et al*, 2005] Emergence of brown adipocytes in WAT depots has been associated with a lean phenotype in several transgenic mouse models [Tsukiyama-Kohara *et al*, 2001; Cederberg *et al*, 2001].

Although brown and white adipocytes, in their extremes, possess opposite functional properties, mitochondrial content and lipid droplet morphology, apparent intermediate forms can exist under different conditions. In mature human adipocytes, forced expression of PGC-1α which is highly expressed in BAT but low in WAT [Lin *et al*, 2005] can induce a brown fat-like phenotype including induction of UCP-1 and other mitochondrial genes. However, the response of typical white adipocyte PPARγ targets to PPARγ agonists is not altered by PGC-1α. While this reveals a high degree of plasticity in the mature white fat cell phenotype it also argues in favour of differences in early lineage specificity as the underlying mechanism in differentiation of *bona fide* brown adipocytes. Thus, white adipocytes can attain many typical

BAT features but still maintain a white adipocyte phenotype. Interestingly a recent report by Timmons *et al*, [2007] suggest that BAT and WAT are not derived from a common preadipocyte pool as previously thought [Ailhaud *et al*, 1992] but may have different origins. BAT is apparently more closely related to muscle as brown preadipocytes appear to express myogenic specific proteins. Interestingly, differentiated WAT has been shown to acquire certain BAT-like properties and can be converted into an energy consumption organ under special conditions. It has been observed that cold-exposure or administration of β3-agonist could induce the emergence of multilocular brown adipocytes that contain high amounts of mitochondria and expresses UCP-1 in WAT depots [Bouillaud *et al*, 1984; Yoshida *et al*, 1998]. Furthermore, ablation of β3-adrenoceptor diminishes the formation of BAT in white fat in cold exposed mice [Jimenez *et al*, 2003], suggesting the requirement of β-adrenoceptor signalling for the transdifferentiation of WAT to BAT.

Lipids are essential for reproductive physiology and a lack of adipose tissue can cause leptin deficiency which is required for sexual maturation and fertility which might explain why the *Opa3*$^{-/-}$ never get bigger than a 'weaner' size and are unsuccessful at mating. However, fat is also needed for reproductive function via leptin independent mechanisms.

6.4.1 Hepatic Steatosis

Lipid accumulation in the liver is characterized as macrovesicular hepatic steatosis and is the result of an imbalance between production and utilization of triglycerides. There are three sources that may increase the hepatic FA pool: circulating free FAs from various adipose compartments, *de novo* lipogenesis within the liver and dietary factors that promote lipogenesis (Fig 6.7.).

De novo lipogenesis is dependent on acetyl Co-enzyme A, an intermediate that enables proteins and carbohydrates to be driven towards lipogenic pathways. The two main effectors that drive hepatic *de novo* lipogenesis are acetyl-CoA carboxylase and FA synthase. Dietary factors that may promote hepatic lipogenesis include exogenous FAs as well as carbohydrates which can drive triglyceride formation by way of triose phosphate as a basis for glycerol formation and by way of FA formation by acetyl-CoA. A specific dietary factor that promotes hepatic lipogenesis is fructose, which is an unregulated substrate for liver triglyceride synthesis.

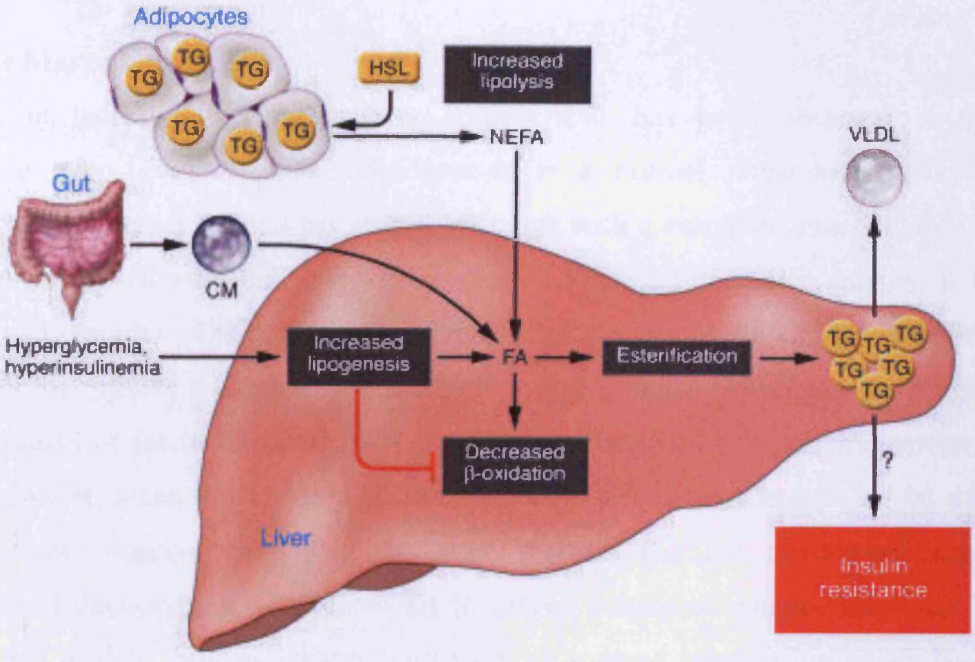

Figure 6.7. Metabolic defects leading to the development of hepatic steatosis. Different sources of fatty acids contribute to the development of fatty liver. Under conditions of insulin resistance, insulin does not adequately inhibit HSL, and lipolysis in white adipose tissue is not suppressed. Therefore peripheral fats stored in adipose tissue flow to the liver by way of plasma NEFAs. Dietary fatty acids are also taken up by the liver through the uptake of intestinally derived chylomicron (CM). In addition, the combination of elevated plasma glucose (hyperglycemia) and insulin concentrations (hyperinsulinemia) promotes de novo fatty acid synthesis (lipogenesis) and impairs β-oxidation, thereby contributing to the development of hepatic steatosis. After the esterification step (conversion of FAs into TGs) TG can then be stored as lipid droplets within hepatocytes or secreted into the blood as VLDL. Although the hepatic accumulation of lipids is widely believed to result in insulin resistance, it remains uncertain whether a causal relationship exists. Several recent studies have even showed a clear dissociation between hepatic steatosis and insulin resistance. FA, fatty acid. [Postic and Girard, 2008]

Factors that decrease the hepatic FA pool are either synthesis of triglycerides and phospholipids or FA oxidation. VLDL and chylomicron remnants have also been shown to contribute to hepatic triglyceride synthesis and storage [Parks and Hellerstein, 2006]. The rate-limiting step of mitochondrial ß-oxidation is the transfer of FAs into the mitochondria, regulated by carnitine palmitoyl acyltranferase-1 which is inhibited by insulin. The balance between lipogenesis and lipolysis in the liver is mainly affected by the ratio of insulin and glucagon. In the case of insulin resistance, fatty acid flux to the liver is increased from increased lipolysis in adipose tissue leading to increased fatty acid uptake. This in turn increases hepatic glucose output and triggers increased insulin secretion in order to maintain

euglycemia. Increased concentrations of insulin in the liver induce *de novo* lipogenesis thus creating a vicious cycle.

6.4.2 Bone Marrow Adiposity

A significant increase in bone marrow adipogenesis has been observed in the *Opa3* homozygote mice. Bone marrow adipogenesis is a normal physiologic process in all mammals and follows a defined pathway that begins with a common mesenchymal stem cell that is pluripotent [Rosen and Spiegelman, 2001]. Once adipogenesis begins, it is highly regulated and complex. The central components of this network are Cebpβ and PPARγ, two critical TFs that initiate a cascade of other factors that enhance differentiation of adipocytes. This generation of fat in the marrow is presumed to be identical to adipogenesis in other tissues. However, since the function of marrow fat is unknown, the type of fat tissue (i.e., white or brown adipose tissue) in the bone marrow has not been established. Since developmental phenotyping of marrow fat in inbred strains or mutant mice has not been accomplished to date, little is known apart from an inverse relationship exists between the amount of marrow fat, measured by spectroscopy, and bone mineral density measured by DXA or quantitative CT [Griffith *et al*, 2006].

6.4.3 Thermoregulation

The inability to maintain a normal body temperature was confirmed by thermal imaging, showing a surface body temperature around 4°C lower in the homozygote than the wildtype control. As *Opa3*$^{-/-}$ mice are leaner and have abnormal adipocytes the hypothermia seen in *Opa3*$^{-/-}$ mice may be due to the reduced lipid storage, which translates into less fuel for muscle activity.

In mammals, alert consciousness and normally patterned motor activities only occur when the temperature of the CNS is approximately 36–39°C. A fall in cellular temperature reduces enzyme efficiency and diffusion capacity, reducing cellular energy availability and membrane ion fluxes. Below-normal brain temperatures are associated with reduced alertness and with behavioural and physiological disorganization, although without physical damage to the CNS or peripheral tissues. Therefore, it should be taken into account that the moribund state seen in the homozygotes is actually hypothermia, and this may be the cause of death.

An interesting mouse model which links mitochondrial dysfunction to the metabolic defects observed in our mouse model (i.e. defective thermogenesis and WAT that histologically

resembles BAT) is the Transgenic N171-82Q mice for Huntington's disease [Weydt *et al*, 2006]. The neurodegenerative disorder Huntingtons is thought to be caused by - mitochondrial dysfunction and impaired energy metabolism [Grunewald and Beal, 1999]. This mouse model displays profound hypothermia with body temperatures dropping to ≤ 27°C and metabolic defects. It is thought that impaired thermogenesis in these Huntingtons mice stems from PGC-1α transcription interference in BAT which supports the idea that defective PGC-1α activity links mitochondrial dysfunction in neurodegeneration to thermoregulatory and metabolic defects. Also, as mentioned earlier, forced expression of PGC-1α can induce a brown fat-like phenotype. Therefore, PGC-1α expression may be worth investigating in our mouse model.

Taken together, results suggest that *Opa3* may play a role in metabolic regulation, mitochondrial activity and white adipocyte identity. Therefore, *Opa3* could serve as a potential therapeutic target for the control of obesity and diabetes.

6.5 Conclusions

- Quantification of circulating 3-methylglutaconic acid showed a 16 fold increase confirming the *Opa3* homozygote mouse as a model of Costeff's Syndrome.

- *Opa3* homozygote mice display a significant decrease in abdominal fat depots with no difference in subcutaneous fat depots which is consistent with a metabolic disorder.

- Plasma ES and ES-ARA indicate that the lack of WAT was not due to starvation. This together with increased adipogenesis in the bone marrow and epididymal adipocytes which look structurally like brown adipocytes suggest that adipocytes are abnormal rather than normal but depleted of triglycerides.

- *Opa3* homozygote mice suffer from defects in thermoregulation and their final moribund state highly resembles hypothermia. This may therefore be a contributing factor to cause of death.

CHAPTER VII

Pupillary and Visual function are dissociated in the *Opa3*^{L122P} mouse model

7.1 Introduction

Aims of chapter

- To assess and compare visual acuity in G1 and G3/4 mice.
- To determine the effect of the *Opa3*^{L112P} mutation on image-forming and non-image forming pathways.
- Use of histology to analyse the effect of the *Opa3*^{L112P} mutation on retinal architecture in adult homozygote mice.

One of the common characteristics in both patients with MGA-III and ADOAC is the reduction of visual acuity. Mutations in *OPA3* cause early-onset bilateral optic atrophy in MGA-III and optic atrophy and cataracts in ADOAC. In primary optic atrophies, the pathology largely affects the RGCs and loss of these cells leads to a reduction of optic nerve tissue and thinning of the nerve along its length. In this chapter our *Opa3*^{L122P} mutant mouse was studied for any visual impairment.

Visual impairment does not generally adversely affect the fitness of laboratory mice and animals with eye mutations are widely used as models for vision research because they are easily studied. Mice are not typically considered as visual animals, they are nocturnal and rely primarily on olfaction, audition and the use of their whiskers for sensing their environment [Pinto and Enroth-Cugell, 2000]. Although the mouse eye has many similarities to the human eye, there are a number of differences. When comparing prenatal development the major difference is that the cilary body and the iris of the developing mouse eye begin to form during the last two prenatal stages (15-19 days), whereas in the human eye the formation begins at a much later date. The adult mouse retina is also slightly different, particularly with respect to the number and distribution of the photoreceptor cells. The mouse, as a nocturnal animal, has a retina dominated by rods. In contrast, the cones are small in size and represent only 3–5% of the photoreceptors. In addition, the mouse does not have a well-defined macula and instead of three cone opsin pigments present in the human retina mice express only two types of cone opsins: the ultra violet-sensitive short wavelength opsin and the green medium wavelength opsin. This means that mice cannot see the red part of the spectrum. However, this has not stopped the generation of numerous macular degeneration models since the mouse still represents an excellent model of macular and retinal degeneration.

7.1.1 Image and non-image forming pathways

There are two visual pathways in the mammalian eye, the image forming (IF) pathway and the non-image forming (NIF) pathway. The traditional IF pathway involving the determination of the detailed form and colour of objects relies on rods and cones. This pathway is composed of photoreceptors (rods and cones) projecting to nonphotosensitive RGCs and then on to the lateral geniculate nuclei (LGN) of the thalamus. The NIF pathway (Fig 7.1.) is composed of photoreceptors projecting to melanopsin containing ipRGCs which project minimally to visual centres in the dorsal LGN, but primarily to nonvisual brain centres, including the suprachiasmatic nuclei (loci of the master circadian rhythm pacemaker) and the olivary pretectal nuclei (loci of the pupillary light response) [Hattar *et al*, 2002 and 2006].

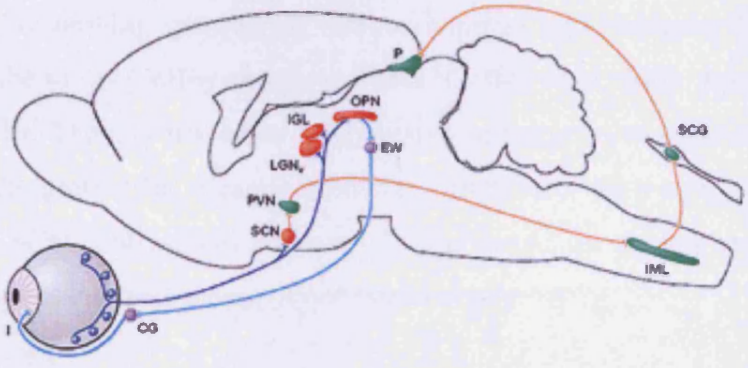

Figure 7.1. Diagram of the pathways taken by melanopsin ganglion cells to the brain. The pathway is to the suprachiasmatic nucleus (SCN) via the retinohypothalamic tract (blue) and on to the pituitary to regulate melatonin release. This circuit drives the circadian oscillator. A second pathway is through the LGN to the olivary pretectal nucleus (OPN) and to the Edinger Westaphal (EW) nucleus for control of the PLR (light blue). [Berson, 2003]

The NIF pathway controls entrainment of circadian rhythms [Freedman *et al*, 1999], photic suppression of pineal melatonin [Lucas and Foster, 1999], behavioural masking to light–dark cycles [Mrosovsky *et al*, 2001], and the PLR [Lucas *et al*, 2001; Keeler *et al*, 1927].

7.1.2 Testing the mouse visual system

There are several widely used behavioural tests for mouse vision including maze based tests, visual cliff, cued fear conditioning, optokinetic nystagmus (OKN), circadian rhythm and PLR. Due to the physical limitations of our mouse model, the maze based tests could not be used, as they require the mouse to be trained to move or swim towards visual stimuli. Some tests, such as the cued fear conditioning, require the learning of visual cues. As MGA-III patients suffer

from cognitive deficits and it is unknown as to whether our model suffers from such deficits we decided not to use any tests involving learning and memory. The running wheel for circadian entrainment was attempted but the homozygous mice never mounted the wheel. So, the most appropriate tests for our model were OKN for the IF pathway and pupillary light response for the NIF pathway.

7.1.2.1 Optokinetic Nystagmus

OKN is based on the fact that the eyes tend to follow or track the motion of one element at a time in a steadily moving display. As the tracked element moves out of sight, the eyes will 'snap back' and fixate and follow another one. The eye movements form the characteristic OKN while the less well studied head movements are often called optomotor tracking. These are thought to be subcortically mediated functions which can be tested on an optokinetic drum that can display moving gratings of various contrast and fineness. The drum was originally designed for the rat by Coffey and co-workers [Coffey *et al*, 2002; Lawrence *et al*, 2000; Lund *et al*, 2001a, b]. The absence of an OKN response suggests that the mouse does not perceive the bars in the grating as separate elements. Therefore, by varying the characteristics of a display, such as its contrast and fineness of the gratings, the researcher can measure a mouse's spatial vision e.g., contrast sensitivity or visual acuity.

7.1.2.2 Pupillary light reflex

The PLR controls the diameter of the pupil. Pupil constriction regulates the amount of light entering the eye and thus pupil diameter is negatively correlated with light intensity. At high light intensity the iris decreases the area of the pupil by 95% (full constriction) in comparison with dark-adapted conditions (fully dilated) (Fig 7.2.).

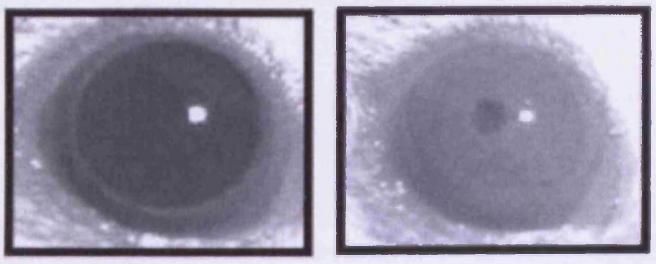

Dark adapted Bright light

Figure 7.2. Images of mouse pupils showing full dilation of pupil in dark adapted eye and full constriction of pupil in bright light.

Light-induced pupillary constriction in mice is initiated by both outer and inner retinal photoreceptors [Lucas *et al*, 2001; Hattar *et al*, 2003]. At low light intensity in which the pupil constricts by 50% or less, rod–cone input is the main signal [Lucas *et al*, 2003; Mrosovsky and Hattar, 2003]. For full pupil constriction the protein melanopsin in ipRGCs is necessary [Lucas *et al*, 2001]. Melanopsin is a blue light sensitive protein expressed specifically in ipRGCs [Berson *et al*, 2002]. In mice this represents a subset of 2% of RGCs [Provencio *et al*, 2002; Hattar *et al*, 2002]. Therefore, rods and cones are responsible for responses at lower light levels, while ipRGCs underlie pupillary constriction in brighter light [Lucas *et al*, 2003].

Mice with outer retinal degeneration or dysfunction that also lack melanopsin cannot entrain their circadian rhythms to light–dark cycles, nor do such animals show pupillary light responses [Panda *et al*, 2002; Ruby *et al*, 2002]. This suggests that the axons of melanopsin-containing ipRGCs convey the signals from both the outer and inner retinal photoreceptors that initiate pupillary constriction to the pretectum [Bailes *et al*, 2009] thus, melanopsin is required for nonvisual photoreception.

To assess whether IF functions are affected in the *Opa3* mice optokinetic responses were measured and for NIF function the PLR was assessed. Retinal thicknesses and RGC counts were also performed to assess any loss of retinal layering and/or cell types.

7.2 Materials and Methods

7.2.1 Optokinetic Nystagmus

The optokinetic response of the mice was tested using a rotating optokinetic drum. The visual tracking drum consists of a motorised drum which rotates at 2 rev/min in a clockwise or anti-clockwise direction (Fig 7.3.). The inner wall of the drum can be lined with black and white vertical stripped card of known frequency. The mouse is placed on a stationary wire platform in the centre of the drum and is not restrained. A digital video camera (JVC, GR-D250) linked to a monitor and a DVD recorder (Hitachi) was used to record any head tracking movements.

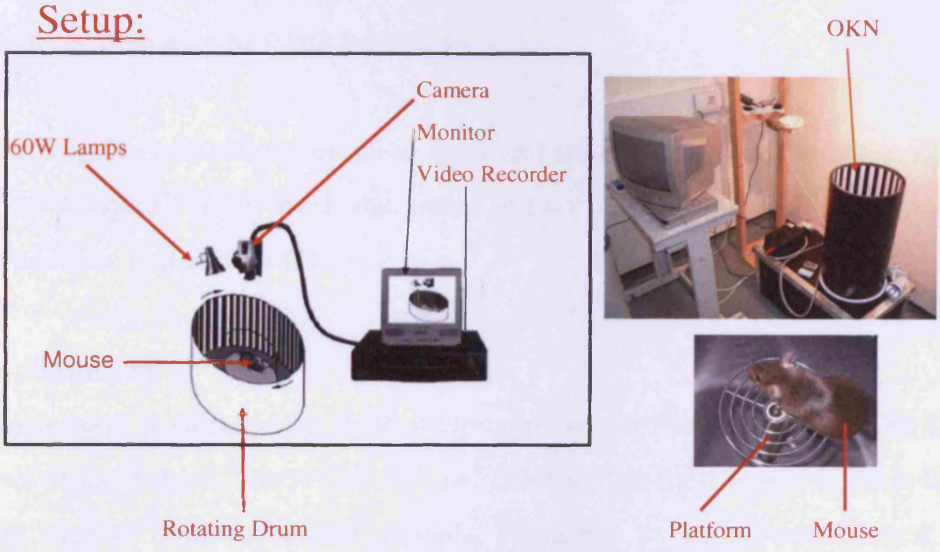

Figure 7.3. Optokinetic drum set up for visual acuity testing.

Initially, a small cohort of 21 G1 mice (*Opa3*$^{-/-}$ n=8, *Opa3*$^{+/-}$ n=8 and *Opa3*$^{+/+}$ n=5) were tested at two months of age to validate the use of the protocol on the *Opa3* mice. Briefly, mice were placed on the platform and allowed to settle for 2 mins. The drum was rotated for 1 min and the mice were observed for a head tracking response. After a 30 sec break, the drum was rotated in the opposite direction for 1 min. The mice were presented with a 1°, 2°, 4° and 8° grating (corresponding to 0.5 , 0.25, 0.125 and 0.0625 cycles/ degree respectively). Mice were tested on all gratings each day for three consecutive days, all at the same time of day. The visual acuity threshold of the C57BL/6J mouse has been measured by Schmucker *et al.* [2005] in an optomotor drum and was found to be around 0.3-0.4 cycles/degree. This corresponds to somewhere between the 1° (0.5 cycles/ degree) and 2° (0.25 cycles/ degree)

grating on our optokinetic drum. Therefore, it would be expected that all mice with normal visual acuity would see the 2° grating.

For the second test a larger cohort of 38 G3 and G4 mice (*Opa3*$^{+/+}$ n=11, *Opa3*$^{+/-}$ n=22, *Opa3*$^{-/-}$ n=5) were assessed. These mice were tested at 18, 21, 25, 28 and 31 days of age to look for onset in vision deterioration. On the first day of testing at 18 days of age the mice were presented with the 8° grating, if they could track this grating they were presented with the next smallest gratings until they reached a grating they could not see. At the next testing age the mice were presented with the lowest grating they could see on the previous test and then presented with the next grating down to see if their eyesight had improved (with visual maturation) or deteriorated (with pathology).

The heterozygotes and wildtypes were aged and tested again and the heterozygote 'founders' (*Opa3*$^{+/-}$ n=4, *Opa3*$^{+/+}$ n=4) were also tested at two years of age. Both were assessed using the same protocol as that for the G1 mice.

7.2.2 Pupillometry

Pupillometry was performed by Dr Ron Douglas and Dr Marcela Votruba on G3/4 animals at six weeks of age (*Opa3*$^{-/-}$ n=5, *Opa3*$^{+/+}$ n=5), during the light phase of their light/dark cycle. The right eyes of unanaesthetised animals, restrained by hand, were filmed under infrared illumination by an infrared-sensitive camera (Cohu, San Diego, USA) fitted with a zoom lens (giving a field of view of 8.7x6.9 mm) positioned in a plane parallel to the plane of the pupil. Various intensities of white light, filtered by a heat glass and neutral density filters and controlled by a shutter, were delivered to the eye being filmed through a fibre optic from a Leica CLS 100x light source.

The spectral irradiance at the animal's cornea for each neutral density filter was measured in 1nm steps (200-870nm) using an Ocean Optics USB2000 fibre optic spectrometer and CC3-UV cosine collector calibrated with an Ocean Optics DH-2000-Cal light source prior to measurements. Since the action spectrum of wildtype mouse pupil constriction is described by the mouse's scotopic sensitivity [Lucas *et al*, 2001], measured spectral irradiances were weighted by the spectral absorbance of the murine rod visual pigment (λmax 498nm).

After at least 1 hr dark adaptation the eye was initially filmed in infrared illumination before a light stimulus was delivered for 20 secs. The animal was then released and returned to darkness for at least 2 mins before being exposed to a brighter light for another 20 secs. In this way animals were subjected to 14 different light intensities presented in ascending order of brightness.

VHS video images were digitised and the area of the pupil, both before light exposure and in the frame showing the greatest pupillary constriction following illumination, was determined using Image J software. Pupil areas, after illumination, were corrected for individual variations in dark-adapted pupil size by expressing them relative to the area of the pupil in darkness immediately preceding the light exposure.

Irradiance response curves were constructed for each animal by plotting the minimum relative pupil size attained during light exposure against the irradiance level. Average irradiance response curves were also constructed for each genotype. The average degree of constriction at each irradiance for the homozygotes and their wildtype siblings was compared using a student's *t* test. Since multiple tests were being performed two points were only considered different if $P<0.01$. Irradiance response curves were also fitted by a four term sigmoid relationship (SigmaPlot, Systat Software Inc., San Jose, USA) of the form y=y0+a/(1+exp(-(x-x0)/b)).

7.2.3 Histology of the retina

Eyes from the mice used in the pupillometry testing (*Opa3*$^{+/+}$ n= 4 and *Opa3*$^{-/-}$ n = 4 - one of the mice had an erratic response to low light levels in pupillometry testing so was omitted from pupillometry results and histology) were taken and embedded in wax. 7μm retinal sections were cut through the optic nerve to the ora serrata then stained with H&E (see chapter II for protocol). Images were taken of each section using a Leica DMR microscope and a Leica DC500 camera. Qwin software was used for retinal layer thicknesses and Image J for RGC counts.

7.2.3.1 Quantification of thicknesses of the retina and GCL counts

The vertical thickness of all the layers of the retina in *Opa3*$^{-/-}$ and control mice used in the pupillometry were measured. Briefly, H&E-stained retinal sections that included the ora serrata and the optic nerve were used. Two regions of each retinal section were selected for

quantitative analysis, each one being 100 μm on either side of the optic nerve head. Individual retinal layer thickness was measured using the Qwin software. The thickness of the layers was determined by averaging data from four animals of each genotype. For the GCL counts, cells were counted on the whole section (ten sections per animal).

7.2.4 Statistics

Statistical analysis was carried out using SPSS 16. For the optokinetic drum testing results no statistical analysis was done due to the homozygotes showing no OKN responses. Student's *t* test was carried out on the mice undergoing pupillometry. For pupillometry testing *P* values ≤ 0.01 were considered statistically significant. GCL counts and retinal layer thicknesses were analysed by the Mann Whitney U test. *P* values ≤ 0.05 were considered statistically significant.

7.3 Results

7.3.1 Loss of visual acuity in the *Opa3*$^{-/-}$ mice

As cataracts are part of the ADOAC human phenotype the mice were checked for presence of cataract by a dilated examination on a slit lamp by Dr Marcela Votruba. No cataracts were observed in any homozygotes or heterozygotes. Heterozygote 'founders' aged to two years also did not appear to develop cataracts. Therefore, cataracts are not considered part of the disease phenotype in this animal model and any diminishment in visual acuity is not due to lens opacity.

7.3.1.1 Optokinetic drum testing on G1 cohort

The initial G1 cohort of 21 *Opa3* mice was tested at two months of age to validate the use of the optokinetic drum protocol. All mice were tested on each grating three times and at the same time on consecutive days. The mouse was said to be able to see the grating if it made at least one head tracking movement in at least one direction of drum rotation and was not able to see the grating if the mouse failed to make any head tracking movements.

The G1 *Opa3*$^{+/+}$ and *Opa3*$^{+/-}$ mice displayed good visual function with no statistical difference between them (Table 7.1.). All of the wildtypes and heterozygotes were able to track the 2° grating and all of the wildtypes and 75% of the heterozygotes were able to track the 1° grating. However, the homozygotes showed an impairment of visual acuity where none were able to track the 1° grating and only one out of the five (20%) was able to track the 2° grating. Three out of five (60%) could see the 4° and finally four out of five (80%) could see the 8° grating. Only one homozygote remained non-responsive to all of the gratings. There was a statistically significant difference between wildtype and homozygotes at 1° (P=0.001), 2° (P=0.001), 4° (P=0.034) but not 8°. When comparing the heterozygotes and homozygotes a statistically significant difference was only observed at 1° (P= 0.011) and 2° (P=0.003).

Animal	Sex	Genotype	1 deg	2 deg	4 deg	8 deg
269	f	+/+	Y	Y	Y	Y
270	m	+/+	Y	Y	Y	Y
271	m	+/+	Y	Y	Y	Y
274	f	+/+	Y	Y	Y	Y
275	f	+/+	Y	Y	Y	Y
277	f	+/+	Y	Y	Y	Y
280	m	+/+	Y	Y	Y	Y
281	m	+/+	Y	Y	Y	Y
264	f	+/-	Y	Y	Y	Y
265	f	+/-	Y	Y	Y	Y
266	f	+/-	N	Y	Y	Y
272	m	+/-	N	Y	Y	Y
282	m	+/-	Y	Y	Y	Y
283	m	+/-	Y	Y	Y	Y
284	m	+/-	Y	Y	Y	Y
304	m	+/-	Y	Y	Y	Y
267	f	-/-	N	N	N	Y
268	f	-/-	N	N	Y	Y
278	m	-/-	N	N	Y	Y
279	m	-/-	N	N	N	N
302	m	-/-	N	Y	Y	Y

Table 7.1. The visual acuity of G1 *Opa3* wildtype, heterozygote and homozygote mice on the 1°, 2°, 4° and 8° gratings at 2 months of age. A cohort of 21 mice were tested ($Opa3^{+/+}$ n=8, $Opa3^{+/-}$ n=8 and $Opa3^{-/-}$ n=5). Y = mice made at least one head tracking movement at that grating. N= mice made no head tracking movements.

7.3.1.2 Optokinetic drum testing on aged 'founders'

The colony heterozygote 'founders' and their wildtype littermates were assessed on the optokinetic drum at two years of age for any diminished visual acuity with age (Fig 7.4.). Homozygotes could not be aged and assessed as they do not survive past a few months old. Mann Whitney U showed no significant difference between heterozygous founders and their

wildtype littermates at 1° or 2° gratings. Therefore, there was no late onset disease phenotype observed in the heterozygotes 'founders'.

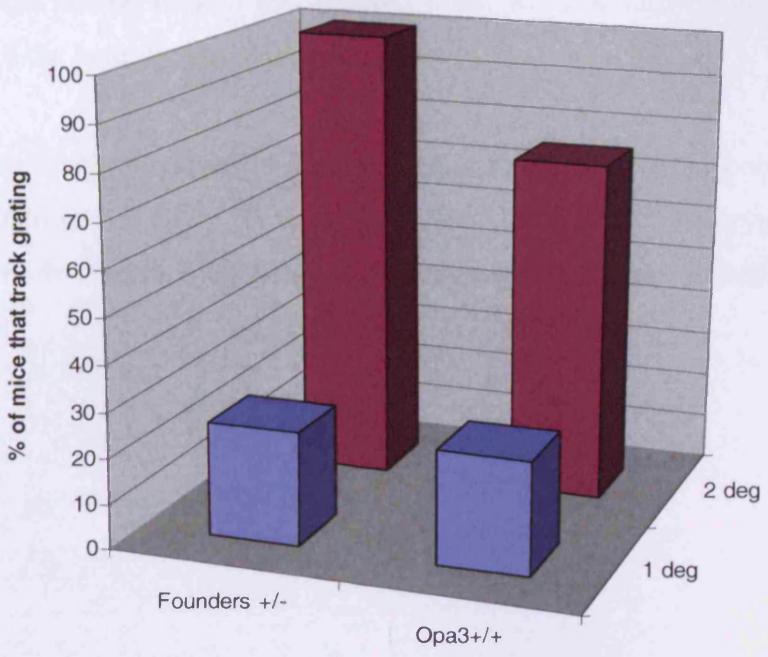

Figure 7.4. Graph showing the visual acuity of heterozygous 'founders' and their wildtype controls on the 1° and 2° grating at two years of age. A cohort of eight mice were tested (*Opa3*$^{+/+}$ *n=4* and *Opa3*$^{+/-}$ 'founders' n=4).

Due to the variability seen in the visual acuity of the G1 mice i.e. from normal visual acuity to functionally blind, further assessment of vision was undertaken on the G3/4 mice in the hope of less variability in the phenotype due to mice being more congenic. All experiments, here after, have been performed on G3/4 mice.

7.3.1.3 Optokinetic drum testing on the G3/4 cohort

Visual testing started when the mice opened their eyes at 14 days of age. However, some of the runts in the litters did not open their eyes until 15-16 days so could not be tested at 14 days. Those mice that had opened their eyes and were tested had a tendency to fall asleep on the platform during the experiment. Therefore, the 14 days of age data was not included and results only show visual acuity from 18 days onwards (Fig 7.5.).

In the G3/4 OKN testing, 100% of the *Opa3*$^{+/+}$ and *Opa3*$^{+/-}$ could see the 2° grating by 25 days of age. The ability of the *Opa3*$^{+/+}$ and *Opa3*$^{+/-}$ to see the 1° grating improved over time and by 31 days 82% of *Opa3*$^{+/+}$ and 64% of *Opa3*$^{+/-}$ could see it. This discrepancy between

percentages maybe by chance as the visual threshold of mice on an optokinetic drum is between 1° and 2° or there may be some loss of vision or delayed visual maturation in the heterozygotes. Therefore, the wildtype and heterozygotes were aged and retested to look for any late onset of visual loss in the heterozygotes. Results showed no effect of age on the visual acuity of the heterozygotes (data not shown).

None of the homozygotes tracked any of the gratings at any time points and are therefore considered functionally blind. This indicates that the visual phenotype has become more severe on the more congenic C57BL/6JCrl backgound and/or the age of onset of blindness is earlier.

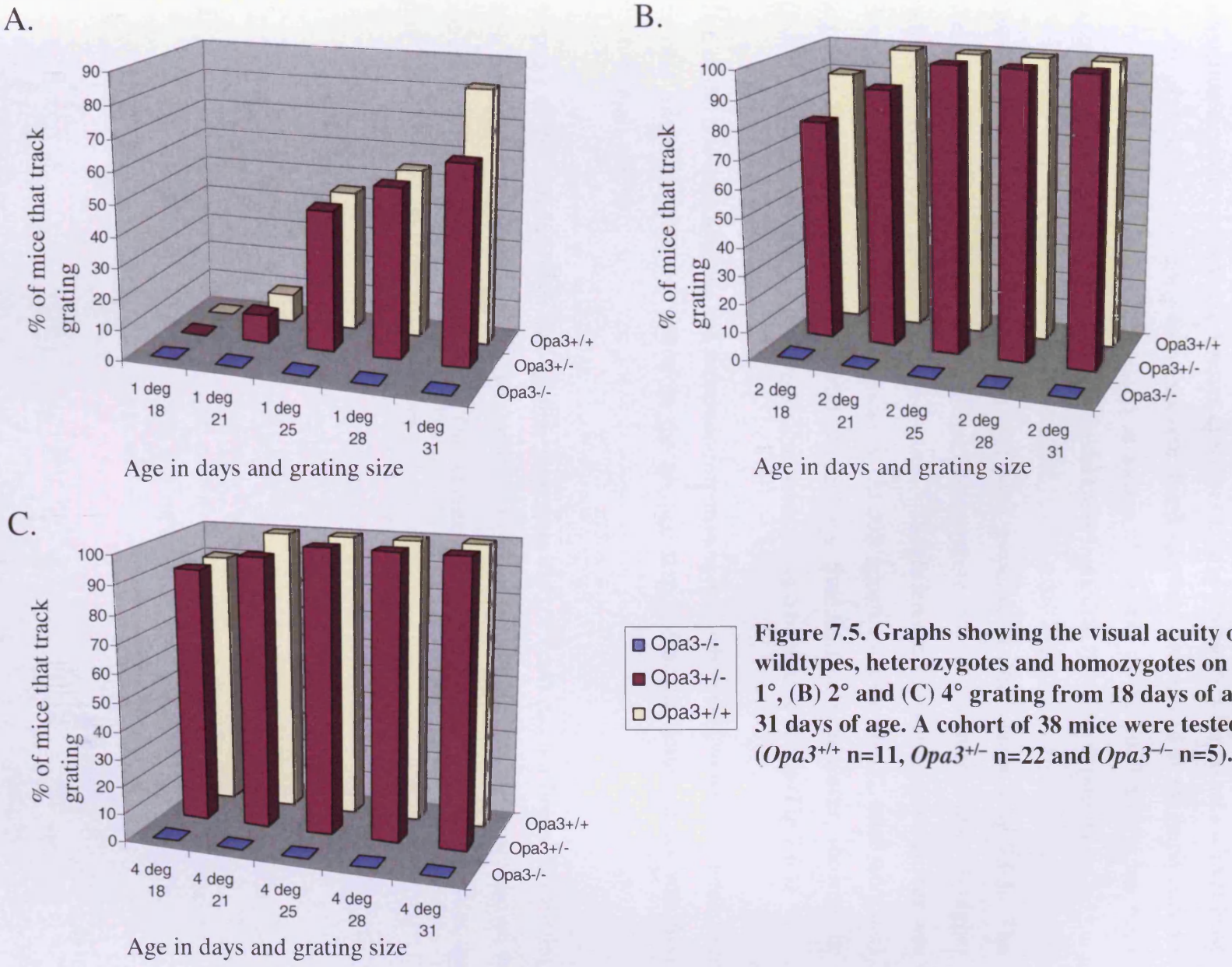

Figure 7.5. Graphs showing the visual acuity of *Opa3* wildtypes, heterozygotes and homozygotes on the (A) 1°, (B) 2° and (C) 4° grating from 18 days of age up to 31 days of age. A cohort of 38 mice were tested (*Opa3*$^{+/+}$ n=11, *Opa3*$^{+/-}$ n=22 and *Opa3*$^{-/-}$ n=5).

7.3.2 Retention of the pupillary light reflex

The right eyes of (*Opa3*$^{-/-}$ n=5 and *Opa3*$^{+/+}$ n=5) mice were tested for their pupil response to light. Heterozygotes were omitted pupillometry testing and further investigation due to no significant difference in their visual acuity compared to wildtypes. After at least 1 hr dark adaptation they were exposed to a series of increasing light intensities for 20 secs with at least 2 mins of darkness separating each exposure. Pupil size was determined as the pupil area >5 secs after illumination and is expressed as a ratio of the size of the pupil after it has been exposed to light relative to the pupil area in darkness immediately before exposure.

Opa3$^{+/+}$ and *Opa3*$^{-/-}$ mice showed a graded pupil response to illumination (Fig 7.6.). The average response intensity curve of the *Opa3* homozygote mice was displaced towards higher light levels relative to that of wildtype controls. The difference between the two curves was most apparent at lower levels of illumination. At 50% constriction the *Opa3*$^{-/-}$ mice were 0.61 log units less sensitive than their wildtype siblings. Student *t* tests, however, showed the *Opa3*$^{-/-}$ only differed from the wildtypes significantly at two irradiance levels (Fig 7.6.).

One of the five homozygotes had an erratic response to low light levels so was excluded from detailed irradiance response. Therefore the average response of the homozygotes was from three animals not four.

Scrutiny of the curves shows that all four remaining *Opa3*$^{-/-}$ (red) did not begin constricting their pupils until higher light levels than wildtypes (i.e. response/intensity curves are shifted to the left and are 'higher' for mutants). This is clearly seen when comparing averages for the four 'good' *Opa3*$^{-/-}$ and the five wildtypes.

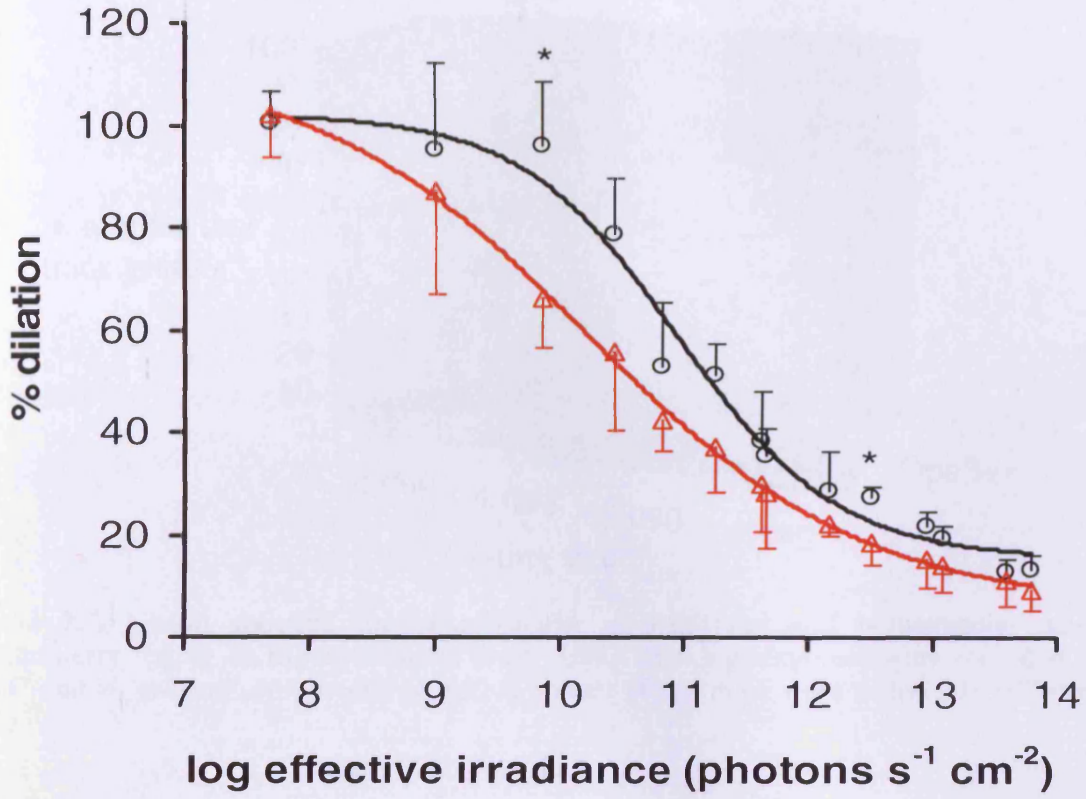

Figure 7.6. The average minimum pupil area expressed as a percentage of maximum dilation following illumination with various intensities of white light for mice homozygous for mutations of the *Opa3* gene (n=5, +1 s.d.) (solid/black symbols), compared to wildtype siblings (open/red symbols, -1 s.d.). All data is fitted with four term sigmoidal functions (solid lines) of the form y=y0+a/(1+exp(-(x-x0)/b)). The goodness of fit of these sigmoids (R2) to the data of all four genotypes is very high (*Opa3* mutants, 0.981; *Opa3* wildtypes, 0.998). The degree of constriction at each irradiance for the mutants and their wildtype siblings was compared using a Student t test. The *Opa3* mutants differed from their wildtype siblings at 2 irradiances ($P<0.01$) (indicated by *).

7.3.2.1 Optokinetic drum testing of the mice used in pupillometry

All of the G3/4 six week old mice used in the pupillometry were tested afterwards on the optokinetic drum using the protocol for the G1 mice. None of the homozygotes could track any of the gratings indicating that they were functionally blind (Fig 7.7.). This result is consistent with observations of the larger G3/4 cohort who were functionally blind from 18 days onwards.

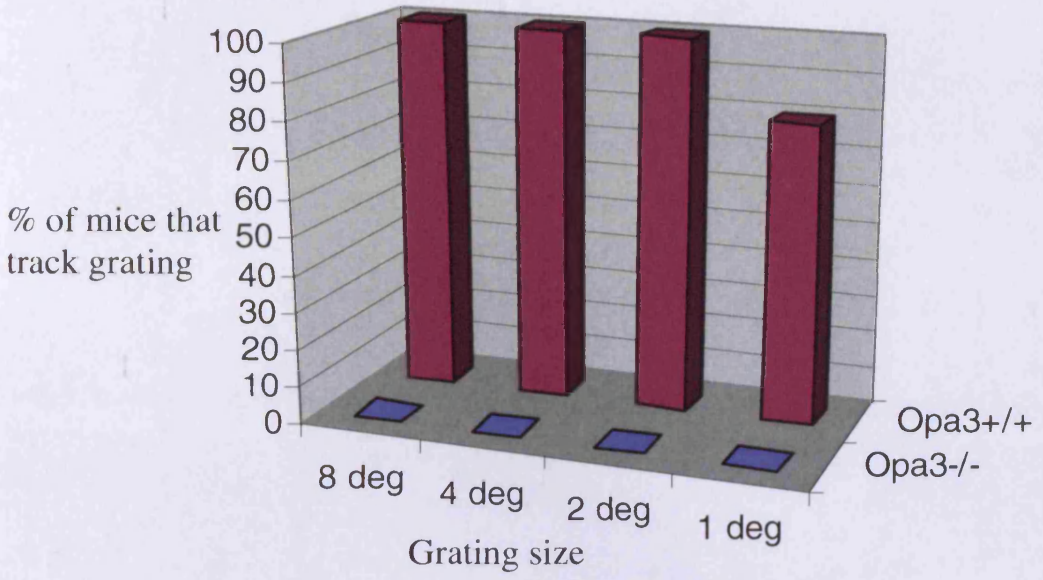

Figure 7.7. Graph showing the visual acuity of wildtypes and homozygotes used in the pupillometry testing on the optokinetic drum. Head tracking responses were recorded on the 1°, 2°, 4° and 8° gratings at 6 weeks of age. A cohort of ten mice were tested (*Opa3*$^{+/+}$ n=5, *Opa3*$^{-/-}$ n=5).

7.3.3 GCL counts and retinal layer thicknesses for mice used in pupillometry testing

Histological sections of wildtype and homozygote mice were taken (Fig 7.8A&B.). Light microscope observations of retina from adult mice used in pupillometry testing (*Opa3*$^{-/-}$ n=4 *Opa3*$^{+/+}$ n=4) revealed a statistically significant reduction in the thickness in virtually all cell layers of *Opa3*$^{-/-}$ mice (Fig 7.8D.). The whole retina, measured from retinal pigment epithelium (RPE) to NFL, was significantly thinner, with most marked differences in the combined RGC and NFL (*P*=0.005), inner plexiform layer (*P*=0.001), inner nuclear layer (*P*=0.04) and the outer nuclear layer (*P*=0.009) and the rods and cones (*P*=0.014). Layers that were not significantly affected were the outer plexiform layers (*P*=0.344) and RPE (*P*= 0.093). GCL counts from H&E stained retinal sections were statistically different between *Opa3*$^{-/-}$ and *Opa3*$^{+/+}$ mice (*P* = 0.021) (Fig 7.8C.).

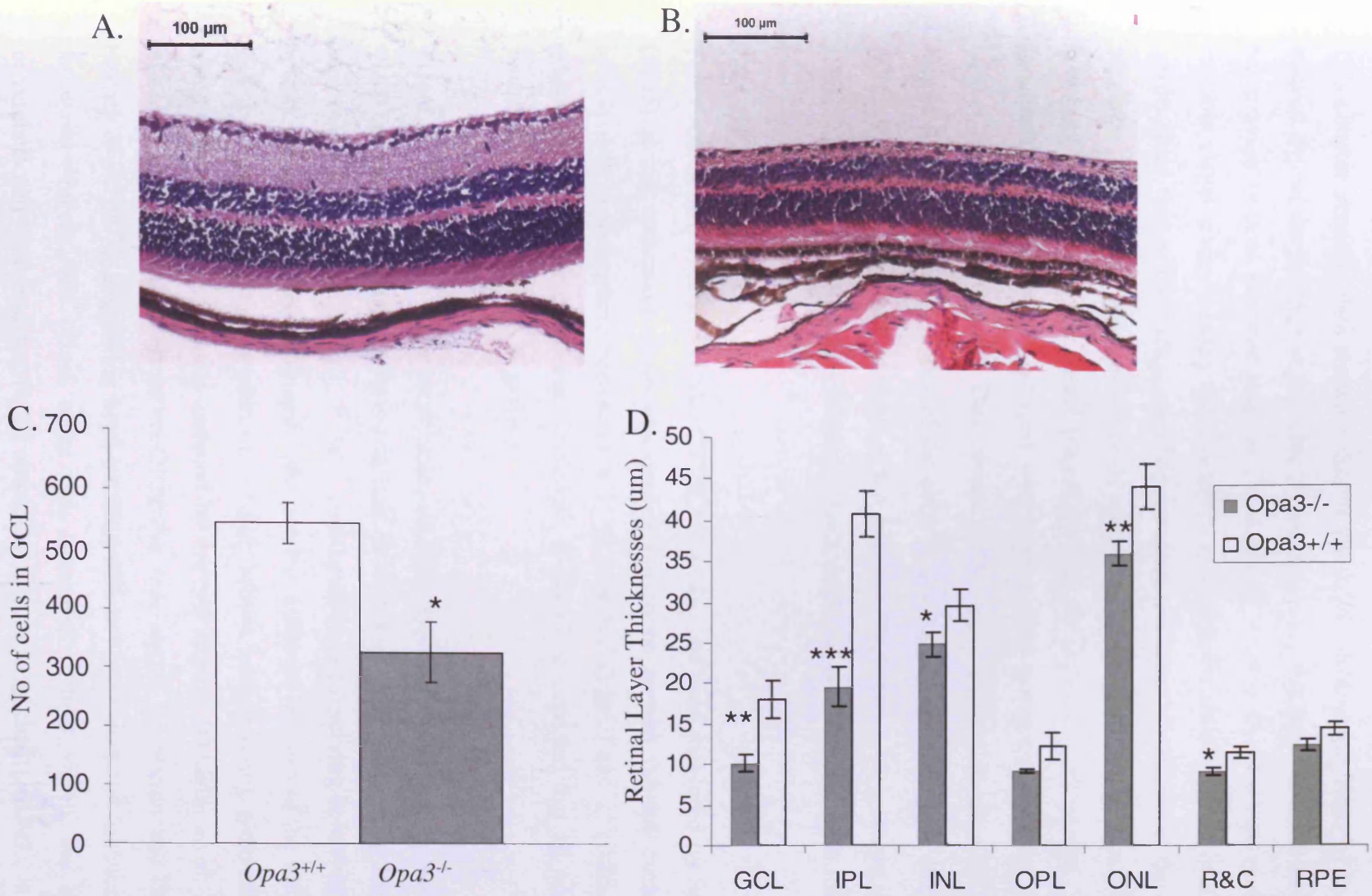

Figure 7.8 *Opa3-/-* adult mice display panretinal degeneration. Representative photomicrographs of H&E stained 7-µm sections of six week old adult (A) *Opa3*+/+ and (B) *Opa3* –/– retinas displaying thinning of all layers. (C) Graph displaying mean number of cells in GCL per retinal section in 6 week old mice (10 sections were counted per mouse). (D) Graph showing the mean thickness (µm) of the retinal layers for six week old adult *Opa3*+/+ and *Opa3*–/– mice (*Opa3*–/– n=4 and *Opa3*+/+ n=4). Values are shown as mean ± S.E.M.P*<0.05, ***P*<0.01, ****P*<0.001. GCL, ganglion cell layer; IPL, inner plexiform layer; INL, inner nuclear layer; OPL, outer plexiform layer; ONL, outer nuclear layer; R&C, outer and inner segments of rods and cones; RPE, retinal pigment epithelial layer.**

7.4 Discussion

This chapter presents data showing that in the G3/4 OKN testing none of the homozygotes tracked any of the gratings at any time points indicating that they are all functionally blind. It has previously been reported that the G1 homozygote mice tested at two months old have a variable visual acuity ranging from normal to functionally blind [Davies *et al*, 2008]. These results show that as the background became more congenic C57BL/6JCrl the age of onset of blindness was earlier and variability of onset was decreased. Comparisons with G1 retinal histology indicate that the visual phenotype did not become more severe. This finding of functional blindness was reinforced with adult retinal histology showing the homozygote retinas were 30% thinner. This thinning was most apparent in the GCL and IPL. Cell counts showed a loss of 40% of the cells in GCL. In mice, RGCs and displaced amacrine cells each constitute about one-half of the cells in GCL [Perry, 1981; Barnstable and Drager, 1984]. Therefore, the 40% loss of cells in GCL could account for an 80% loss of RGCs.

7.4.1 OKN

The visual acuity threshold of the C57BL/6J mouse has been measured by Schmucker *et al*, [2005] in an optomotor drum and was found to be around 0.3-0.4 cycles/degree. This corresponds to somewhere between the 1° (0.5 cycles/ degree) and 2° (0.25 cycles/ degree) grating on our optokinetic drum. Therefore, it would be expected that all mice with normal visual acuity would see the 2° grating.

Visual acuity is known to be more acute on other types of visual testing, such as the visual water task and the t-maze behavioural task. It is thought that there are at least two possible explanations for the discrepancy. Firstly, visual pathways subserving behavioural responses in optomotor and reinforcement-based tasks process different features of the retinal output, and therefore, reflect different measures of vision. Mouse grating acuity generated in the visual water tasks can be significantly reduced by cortical lesions [Douglas *et al*, 2005]. Cortical lesions however, have no effect on OKN eye movements [Hobbelen and Collewijn, 1971; Harvey *et al*, 1997], suggesting head-tracking thresholds measure the function of subcortical pathways whereas, the visual water task measures cortical vision. As optokinetic eye movements and head tracking in the optokinetic drum have clear parallels, it is thought that they are both driven by subcortical, low-frequency visual pathways. The second possibility is that differences in grating thresholds between optomotor and reinforcement-based tasks reflect

differences in behavioural responses. Because the optomotor response is graded with less vigorous tracking near threshold, it is possible that a weak sensory signal is present without any apparent behavioural response. In either case, the differences in the measures show that discrimination-based tasks and optomotor tasks are complimentary and not interchangeable, and prudence should be exercised when comparing threshold values generated with the different methodologies.

The difference in the visual acuity of the homozygotes in the initial G1 cohort was probably in part due to the variability of onset of the disease phenotype. The mice that could see the 2° degree grating were not suffering from any noticeable neurological defects at the time of testing whereas the mouse that did not track any of the gratings was quite ill.

In the G3/4 OKN testing, visual acuity initially improved in the wildtype and heterozygotes. At 21 days of age all of the *Opa3*$^{+/+}$ could see the 2° grating and by 25 days of age all of the *Opa3*$^{+/-}$ could see the 2° grating. This corresponds with maturity of the mouse eye around 21-25 days [Smith, 2002]. This initial improvement in visual acuity after eyes open at around P15 concurs with observations by Prusky *et al*, [2004] who measured visual acuity on the day of eye opening (P15: mean acuity, 0.031 cyc/deg) and reached a maximum (0.4 cyc/deg) by P24. This development of visual acuity suggests that although head-tracking is present on the day of eye opening, indicating that the visuomotor circuitry is already in place when high-quality visual information normally becomes available, the visuomotor circuitry requires experience to fully develop. Also development of visual thresholds could be influenced by changes in the visual system, the motor system, or both.

Only 72% of *Opa3*$^{+/+}$ and 63% of *Opa3*$^{+/-}$ could see the 1° degree grating. There are several possible reasons for this observation. 1) Their level of visual acuity on the optokinetic drum is between the 1° and 2° gratings, therefore even normal mice will have difficulty seeing the 1° grating. 2) The mice are not restrained on the platform; therefore depending where they are on the platform will alter the distance they are from the striped pattern. 3) At the smallest grating (1°) the head tracking movements are so small and for such brief periods that they are very difficult to observe and can be missed (as mentioned above for lower visual acuity on optokinetic drum compared to other visual acuity tests). These disadvantages have been shown to be obviated by replacing the mechanical drum with a virtual-reality cylinder [Prusky *et al*, 2004]. Being computer generated, the spatial frequency, contrast, and velocity of the

stimulus pattern can be changed instantaneously. Furthermore, by monitoring the position of a freely moving animal inside the system with a camera, the drum can be kept centred on the head so it is not necessary to restrain the animal.

7.4.2 Pupillometry

Although the *Opa3*$^{-/-}$ mice are functionally blind (Fig 7.5.) and show widespread retinal thinning (Fig 7.8D.), the pupil response is little affected (Fig 7.6.). Their pupillometry response was found to be diminished only slightly, i.e., at each light intensity the pupil of the homozygotes did not constrict as much as the pupils of the wildtype mice, but this was not statistically significant overall.

Non-visual ocular responses to light such as PLR and circadian rhythm are mediated by ipRGCs [Berson *et al*, 2002]. Induced ablation of melanopsin expressing ipRGCs causes complete loss of non-image forming visual responses. This suggests that axons of ipRGCs are the site of functional integration of the rod/cone and melanopsin phototransduction pathways and are the primary anatomical site for the divergence of the image and non-image forming photoresponses in mammals [Hatori *et al*, 2008]. Since *Opa3*^{L122P} has little affect on pupillary constriction but causes a large reduction in cells in the RGC layer (Fig 7.8C.) this would suggest that ipRGCs must be 'spared' while severely compromising other retinal ganglion cells projecting to the LGN.

Whereas outer retinal degenerate mice lacking melanopsin show no responses to light, mice lacking either outer retinal photoreceptors or melanopsin (but not both) show only subtle circadian entrainment phenotypes and demonstrate only partial loss of pupillary light response [Selby *et al*, 2000; Panda *et al*, 2002; Ruby *et al*, 2002; Lucas *et al*, 2003]. Melanopsin-deficient mice show behavioural masking defects primarily under bright light [Mrosovsky and Hattar, 2003]. Only when outer and inner retinal photoreceptor-specific mutations are combined do complete phenotypes emerge. Thus, there is a substantial overlap between signalling pathways from rods and/or cones and inner retinal photoreceptors to brain centres mediating nonvisual photically driven phenomena. While pupil response is affected to a lesser degree than visual acuity there is a small but significant loss of pupil sensitivity at lower light levels. As low light level pupil responses are mainly determined by rod and cone function [Lucas *et al*, 2003], this suggests that the *Opa3* ^{L122P} mutation might also be affecting function and/or viability of the rods and cones. Measurements of retinal layer thicknesses did show a

loss of cells from the rods/cones and their associated layers (Fig 7.8D.). However, pan-retinal degeneration has occurred and there was a significant thinning of the INL which might also be affecting this response at low light levels.

These findings mirror data from patients with dominant optic atrophy [Bremner *et al*, 2001] and Leber's hereditary optic neuropathy [Bremner *et al*, 1999], both degenerative diseases of RGCs linked to defective mitochondrial function which affect the pupil responses to a much lesser degree than perceptual visual function.

7.4.2.1 Why should ipRGCs be less susceptible to mitochondrial impairment than those ganglion cells going to the LGN?

It is likely that the cells least affected by loss of mitochondria are those in which energy demand is lowest. Melanopsin-containing ganglion cells are morphologically [Hattar *et al*, 2002] and physiologically [Berson *et al*, 2002] different to other ganglion cells. For example, electrophysiologically they are very sluggish [Berson *et al*, 2002]. Whether they require less energy and might thus be less affected by mitochondrial defects, however, is unclear.

From an evolutionary perspective of opsins, mouse melanopsin is most closely related to invertebrate opsins [Provencio *et al*, 1998]. Melanopsin within this class of RGC may represent a marker for an evolutionarily distinct class of RGC that is more injury-resistant (or in the case of Müller glia-derived support, more responsive) than RGCs that are not intrinsically photosensitive.

An alternative explanation for *Opa3*$^{-/-}$ mice having affected image forming vision while sparing the pupil response, is that image quality may be affected by, for example, lenticular opacities which patients with ADOAC are known to have. This would decrease acuity while leaving the pupil response relatively unaffected. However, in agreement with previous reports on the *Opa3* mice [Davies *et al*, 2008] we did not observe cataracts in any of the wildtype or mutant mice, thereby discounting this interpretation.

Pupil function seems far less affected than visual function in our mouse model of the disease. This dissociation between visual perception and pupillary function in both mouse and man implies that the RGCs subserving pupillary function are less susceptible to damage by mutations of *Opa3* than the retinogeniculate fibres underlying visual perception and/or the

melanopsin RGCs are less susceptible than non-melanopsin RGCs. At present this is being explored further by melanopsin qPCR for detection and quantification of melanopsin in *Opa3* homozygote retina compared to wildtype.

If the relationship between visual deficit and pupil deficit can vary in different diseases, then a study of pupil function in different optic neuropathies may have clinical diagnostic potential, particularly in the MGA syndromes where the detection of new clinical features would facilitate their difficult diagnosis. Therefore, the PLR could be assessed in MGA patients to confirm retention of the reflex as part of the MGA syndrome phenotype. At present the PLR is being assessed as a technique to detect asymmetric retinal damage in patients diagnosed with glaucoma [Wride *et al*, 2009] and interestingly as a possible new technique for the investigation of early cholinergic deficits, which generally lead to memory and cognitive disorders in Parkinsons and Alzheimers [Fotiou *et al*, 2009]. Moreover, the relative susceptibility of pupil afferent fibres compared with visual afferent fibres in different diseases has important implications regarding the underlying mechanisms of damage.

7.5 Conclusions

- The *Opa3* homozygous mice are functionally blind at P18 onwards. Heterozygotes displayed normal vision. Aging the heterozygote 'founders' to two years showed no onset of disease phenotype with age.

- *Opa3* ^{L122P} mutation causes pan-retinal degeneration which was most apparent in the GCL and IPL.

- Pupil function seems far less affected than visual function, suggesting that ipRGCs must be 'spared' while severely compromising other RGCs projecting to the LGN.

- Homozygote visual phenotype does not become more severe as we move to a more congenic C57BL/6JCrl background. However, the age of onset of blindness is reduced and there is less variability in onset of disease phenotype.

CHAPTER VIII

Retinal degeneration in *Opa3*^{L122P} mouse is associated with increased postnatal apoptosis

8.1 Introduction

Aims of chapter

- To assess the effect of the *Opa3*^{L122P} mutation on retinal development, GCL and INL cell counts were taken at various time points during early postnatal retinal development through to adulthood.

- TUNEL stained retinal sections were assessed for timing and region(s) of apoptotic cell loss within the retina during postnatal development and adulthood.

Apoptosis is a mechanism of programmed cell death in which the cell plays an active role in its own demise. This carefully orchestrated series of intracellular events produces a quiet death that minimises injury to adjacent cells and is important in constructive physiological processes, such as embryogenesis, and tissue remodelling [Wyllie *et al*, 1980; Gerschenson and Rotello, 1992]. This mechanism is also of considerable interest given that it is implicated in both development and degeneration of the mammalian nervous system. Neuronal death is a normal component of retinal development [Young, 1984] and maturation [Penfold and Provis, 1986], but excessive apoptosis during adult life is a pathological process that produces degeneration of the retina and causes blindness. Apoptosis is responsible for the removal of damaged cells in degenerative conditions of the retina such as retinitis pigmentosa [Li and Milam, 1995], glaucoma [Quigley *et al*, 1995], and age-related macular degeneration [Dunaief *et al*, 2002]. It has been suggested that the molecular mechanisms of apoptosis may be different under circumstances of development and degeneration, but the identity of the key regulators remains unknown [Hsu *et al*, 2004; Bahi *et al*, 2006; Donovan *et al*, 2006].

Work presented in previous chapters has shown a pan-retinal degeneration in the adult homozygous mice (Chapter VII) which supports observations in the optokinetic drum that these mice are functionally blind at P18 and onwards (Chapter VII). Blindness from such an early age could be caused by the *Opa3*^{L122P} mutation affecting retinal development or the retina develops normally and degeneration occurring afterwards. Both possibilities have been observed in other optic neuropathy mouse models. In the mouse model of Leber's congenital amarousis in which the *AIPL1* gene is mutated (as in at least 7% of Leber's congenital amarousis patients [Sohocki *et al*, 2000]) there is severe early retinal degeneration. A central-to-peripheral degeneration begins around P12 and leads to loss of almost all photoreceptors

by postnatal week 8 in the homozygote null mouse [Dyer *et al*, 2004]. This phenotype is consistent with the human disease. At the other end of the scale, in terms of time of onset and duration of cell death is the ENU induced *Opa1*^{Q285X} mouse model of ADOA [Davies *et al*, 2007]. This model has a 50% reduction in *Opa1* protein expression in the *Opa1*$^{+/-}$ mice and shows a slow onset of degeneration with retinal histology still normal at 6 months of age. Humans with *OPA1* mutations in ADOA are also heterozygous and thus have at least one functional allele.

Onset and duration of retinal degeneration in our *Opa3* mouse model is unknown. Therefore, due to the large phenotypic variation observed in other models of retinal degeneration it seemed prudent to choose a wide range of time points to cover the possibilities of early or late retinal degeneration. Although mice were chosen from P0 to 6 weeks of age this time frame does cover a large proportion of the mutant mouse lifespan. P0 was the starting point due to ease of collection and processing of retinal material.

8.1.1 Development and degeneration of the mouse retina

Mouse retinal development begins midway through embryogenesis (E10), but it proceeds well into the postnatal period until eye opening around P14 [Cepko *et al*, 1996]. Development begins with the formation of bilateral evaginations from the prosencephalon leading to the formation of an inner and an outer layer [Kaufman, 1994]. The inner layer of the optic vesicle, the neuroblastic layer, differentiates into additional layers. From approximately E17, the neuroblastic layer consists of an inner neuroblastic layer, which later gives rise to the GCL and an outer neuroblastic layer. These two layers are separated by the IPL. The outer neuroblastic layer divides at around P6 to P8 to give the ONL, in which the photoreceptor cells differentiate, and the INL, which consists of horizontal, bipolar, Müller, and amacrine cells. The outer plexiform layer (OPL) forms between these two nuclear layers.

Neurogenesis occurs in the mouse retina between E13 and P10, with exit from the cell cycle reaching a maximum at E18-P0. During this time cells in the ventricular zone undergo successive periods of proliferation and differentiation to generate seven types of retinal cells in a highly ordered fashion (six types of neurons and one glial cell type) (Fig 8.1.). RGCs are first produced followed immediately by amacrine cells, horizontal cells and cone receptor cells, in highly overlapping waves of cell differentiation. Subsequent to the formation of these early

neuronal cell types the later cell types form: bipolar cells, rod photoreceptor cells and Müller glia cells.

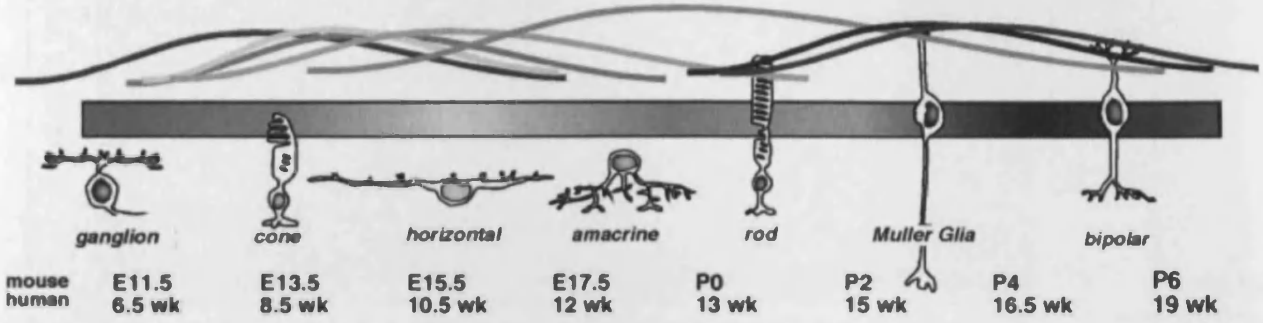

Figure 8.1. Temporal and spatial heterogeneity of developing retinal progenitor cells. Retinal formation spans approximately 2 weeks in the developing mouse and several months in the developing human. During this time, retinal progenitor cells divide and generate post mitotic cells that commit to different cell fates and differentiate to form necessary synaptic connections for proper visual signal processing. There is considerable overlap of the birth dates of different cell types, and the peak periods are represented by individual overlapping curves. [Schweers and Dyer, 2005]

Cell degeneration is also an essential part of neuronal development, including that of the retina. In many regions of the developing nervous system, neurons and their connections are produced in excess of their adult number and then are partly eliminated [Buss and Oppenheim, 2004]. Dying cells can be recognised on the basis of morphological and biochemical criteria, the former being useful for preliminary or quantitative analyses, the latter being a very powerful tool to identify specific death pathways. At the light microscope level, neurons that are dying as part of the normal developmental process exhibit condensation and breakdown of chromatin into fragments, or apoptotic bodies [Wyllie *et al*, 1980]. Cells displaying this morphology are called pyknotic.

In the developing retina two periods of cell death can be observed. Morphogenetic cell death, which takes place during early development, eliminates neuroepithelial cells and contributes to the formation of the optic vesicle, cup, fissure, and nerve. Later, histogenetic cell death removes some of the differentiated neurons.

In the postnatal (P0–P30) mouse retina pyknotic nuclei can be observed at different retinal locations [Young, 1984]. Cell death occurs primarily during the first 2 weeks after birth and is essentially complete by the end of the third week (Fig 8.2.).

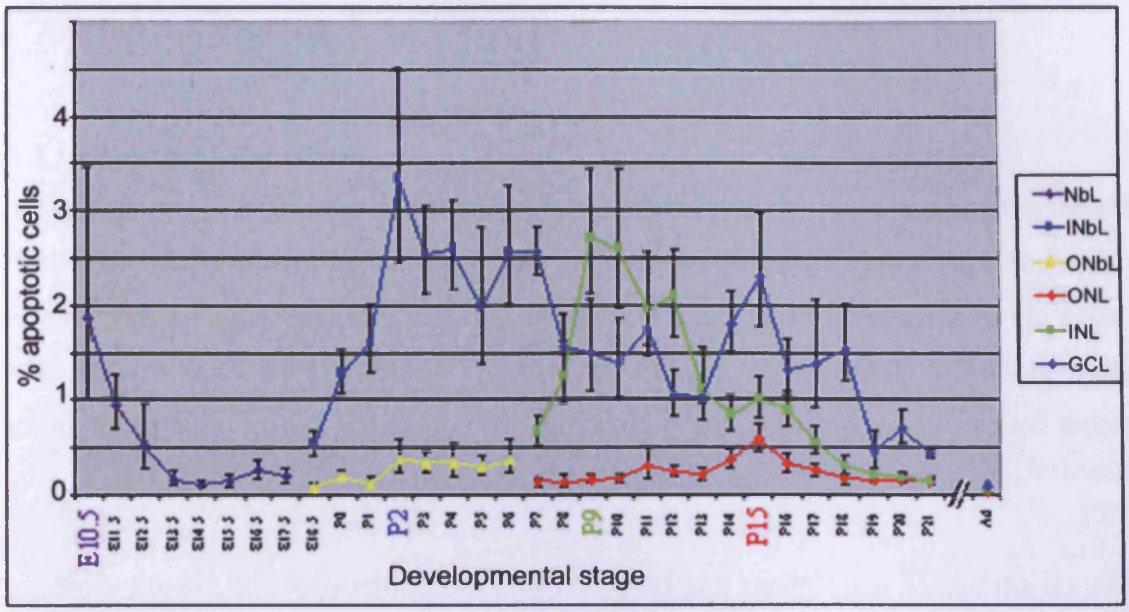

Figure 8.2. Apoptosis throughout the development of the C57BL/6J mouse retina. Each layer is shown in a different colour; each point corresponds to 1 day. Four peaks can be observed at stages embryonic day (E) 10.5, postnatal day (P) 2, P9, and P15. Error bars represent 95% confidence intervals of the percentage. NbL, neuroblastic layer; INbL, inner neuroblastic layer; ONbL, outer neuroblastic layer; ONL, outer nuclear layer; INL, inner nuclear layer; GCL, ganglion cell layer. [Péquignot, 2003]

From birth through 4 days, an increasing incidence of cell death is observed among ventricular cells. Ganglion cell degeneration is present from P0 to P11 in the GCL, with a numerical peak at P2–P4. At P9 most of the dying cells are observed in the INL and at P15 there is a peak in the loss of cells from the ONL.

This chapter represents the first in-depth histological examination of retinal tissue in the B6; C3-*Opa3*^{L122P} homozygote mouse during degeneration of the early postnatal retina.

8.2 Materials and Methods

8.2.1 Histology of the retina

The distribution of RGCs across the retina is not even. Near the optic nerve, ganglion cells are closely spaced, forming a layer two to four cells thick. A short distance from the optic nerve this becomes a single layer of cells that remains closely packed. Anterior to the equator the nuclei become more widely spaced. This can make cell counting highly inaccurate if different regions of retina are used. To over come this, only whole sections which passed through the centre of the cornea and through the optic nerve were evaluated.

Eyes from P0, P8, P12 and P26 mice (*Opa3*$^{+/+}$ n = 3 and *Opa3*$^{-/-}$ n = 3) and the six week old mice, used in the pupillometry testing (Chapter VII) (*Opa3*$^{+/+}$ n = 4 and *Opa3*$^{-/-}$ n = 4), were enucleated and embedded in wax. 7μm retinal sections were cut through the optic nerve to the ora serrata then stained with H&E (as per protocol Chapter II). Images were taken of each section using a Leica DMR microscope and a Leica DC500 camera. For the GCL and INL counts, cells were counted on the whole section (ten sections per animal) from optic nerve to ora serrata. Images were analysed using Image J.

8.2.2 Terminal deoxynucleotidyl Transferase Biotin-dUTP Nick End Labelling (TUNEL) Technique.

TUNEL is the most common technique used to study apoptosis on histolological sections. The technique is based on the detection of DNA fragments typical of apoptosis. TUNEL only indicates that a cell is apoptotic, as apposed to necrotic. It does not indicate whether the apoptosis was mediated by intrinsic (mitochondrial) or extrinsic (death receptors) pathways.

Labelling of fragmented DNA in retinal sections was carried out using ApopTag Plus Fluorescein In Situ Apoptosis Detection Kit (Chemicon) as follows.

8.2.2.1 Preparation and permeabilization of wax embedded retinas

Before commencement of TUNEL labelling, wax sections need to be deparraffinised and permeabilised. Slides were immersed three times for 5 mins each in 100% xylene. After the third wash the samples were rehydrated using a decreasing gradient of ethanol solutions. Samples were washed twice in 100% ethanol for 5 mins, then 3 mins in 95% ethanol and 3

mins in 70% ethanol. Finally, the samples were soaked in PBS for 5 mins. After the preparation steps, the slides were permeabilized by incubating for 15 mins with 100µl of 20µg/ml of Proteinase K to each slide. After incubation slides were washed twice in PBS, 2 mins for each wash.

8.2.2.2 TUNEL Assay

Subsequent to the permeabilisation step the samples were equilibrated for 2-3 mins (minimum 10 secs) with the equilibrium buffer using 75µl/5cm^3. Excess buffer was removed and the slides were incubated with working strength TdT enzyme (77µl reaction buffer plus 33µl TdT enzyme using 55µl/5cm^3) in a humid chamber for 1 hr at 37°C. Slides were then washed in stop/wash buffer (1ml stop/wash buffer and 34ml of dH_20) for 10 mins at room temperature, then in three changes of PBS for 1 min each. Excess liquid was removed and warmed anti-digoxigenin conjugate (68µl blocking solution plus 62µl anti-digoxigenin conjugate) was added to each slide using 65µl/5cm^2. Slides were then covered in aluminium foil to protect them from direct light and incubated in a humid chamber for 30 mins. After incubation the reaction was stopped by using four washes of PBS for 2 mins each. The samples were counterstained with 0.2µg/ml Hoechst 33258 (Invitrogen) and then mounted using Hydromount (National Diagnostics).

8.2.2.3 Positive Control

Rat mammary gland reference slides (Millipore) were used as a positive control. Rat mammary gland undergoes programmed cell death processes during the tissue regression that follows lactation. The same procedure was used for the control slides.

The TUNEL method was used in order to analyse the loss of retinal cells during postnatal development and adulthood. The number of TUNEL-positive nuclei in the RGC and INL, from optic nerve head to ora serrata were counted by microscopy (five sections per animal) and data from three animals in each group, at each stage, were averaged.

8.2.3 Statistics

Statistical analysis was carried out using SPSS 16. GCL and INL counts were analysed by the Mann Whitney U test. TUNEL-positive cell counts were analysed by unpaired Student's *t*-test. *P* values ≤ 0.05 were considered statistically significant.

8.3 Results

8.3.1 Postnatal and adult changes in retinal morphology

To determine onset of retinal degeneration in *Opa3*$^{-/-}$ mice, histological sections of retinal tissues from *Opa3*$^{-/-}$ and *Opa3*$^{+/+}$ controls were examined at several postnatal developmental stages (P0, P8, P12, P26 and adult), at the light microscope level (Fig 8.3A.). GCL and INL cells were counted on H&E stained sections which included the optic nerve head and ora serrata. INL cell counts were not performed on P0 retinas as the outer neuroblastic layer does not divide into the INL and ONL until around P6 to P8.

For GCL counts the homozygote mice showed no statistically significant difference compared to age-matched controls at P0 (846.1 ± 11.7 (S.E.M.) cells per section, $P = 0.707$). However, by P8 the homozygotes showed a 16% reduction in the number of nuclei compared with controls (460.6 ± 7.7 cells per section, $P = 0.002$). This gradual loss of cells continued with a significant loss at P12 (448.7 ± 19.3 cells per section, $P = 0.002$), and P26 (404.1 ± 7.3 cells per section $P = 0.000$). By six weeks of age the *Opa3*$^{-/-}$ showed a 40% loss of GCL cells (326.6 ± 51.4 cells per section, $P = 0.013$) compared to wildtypes (Fig 8.3B.).

Cell loss was also observed in the INL of the homozygotes with a 15% loss observed at P8 (3722.5 ± 73.1 cells per section, P=0.005). This increased loss continued and by six weeks of age there was a 28% loss of cells (2456.8 ± 168.6 cells per section, P= 0.021) in the homozygote compared to the wildtype (Fig 8.3C.).

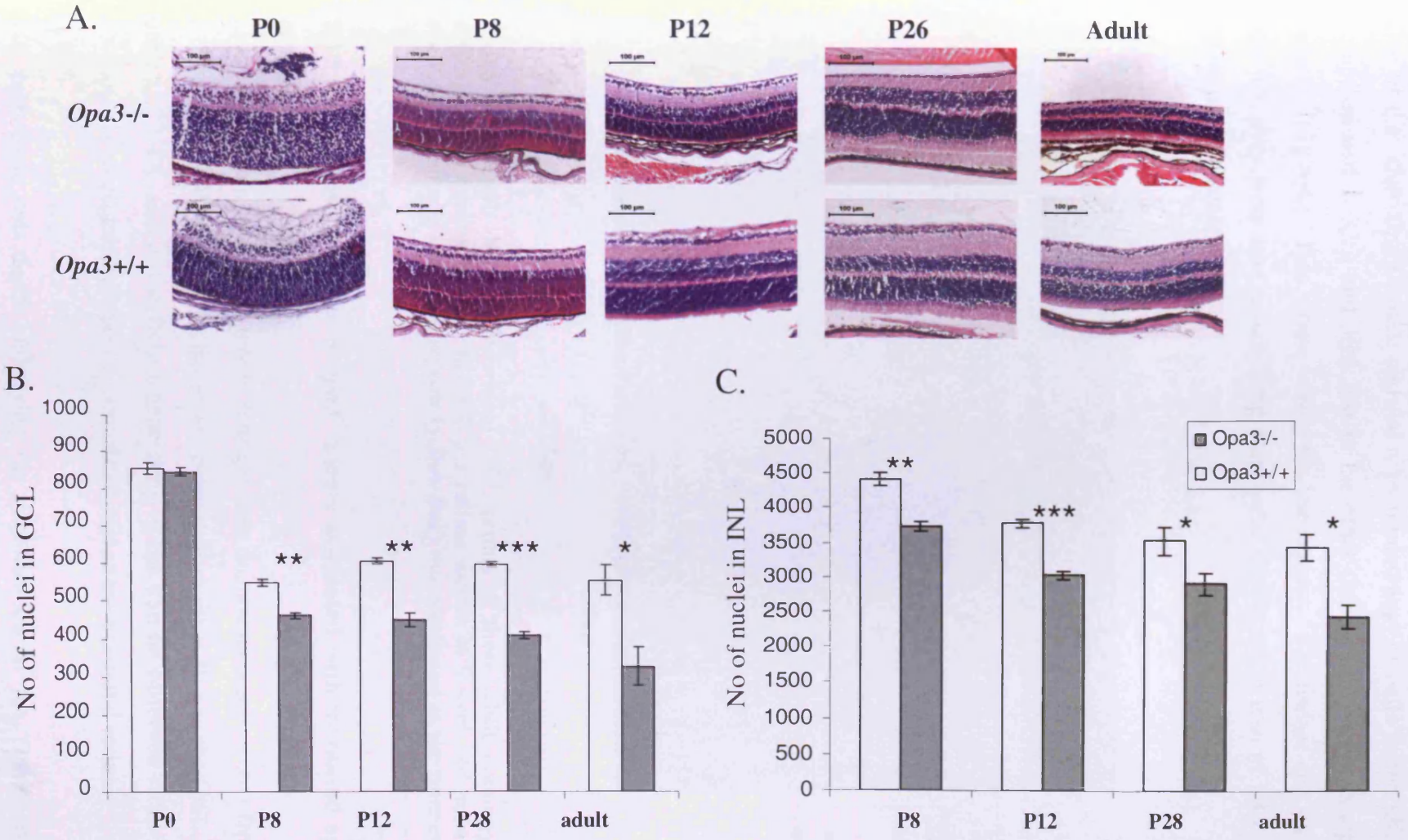

Figure 8.3. Morphological demonstrations of retinal degeneration in *Opa3*–/– mice during postnatal development. (A) Representative photomicrographs of H&E stained 7-µm sections of *Opa3*–/– and Opa3+/+ retinas at P0, P8, P12, P26 and adult (6 weeks old). Scale bar = 100 µm. Graphs displaying the average number of nuclei per section (ten sections per animal) in GCL (B) and INL (C) of mice retinas at P0, P8, P12, P26 and adult (6 weeks old) respectively (*Opa3*–/– n=3 and *Opa3*+/+ n=3). Values are shown as mean ± S.E.M.P*<0.05, ***P*<0.01, ****P*<0.001.**

One of the adult *Opa3*$^{-/-}$ mice showed a prominent loss of cells in the GCL layer of ~70% compared with a 32% and 36% loss in the other *Opa3*$^{-/-}$ mice when compared to wildtype controls (Fig 8.4.). This mouse was in the late stages of the disease and was moribund at the time the eyes were taken, indicating a dramatic escalation in loss of GCL cells in the final stages of the disease state.

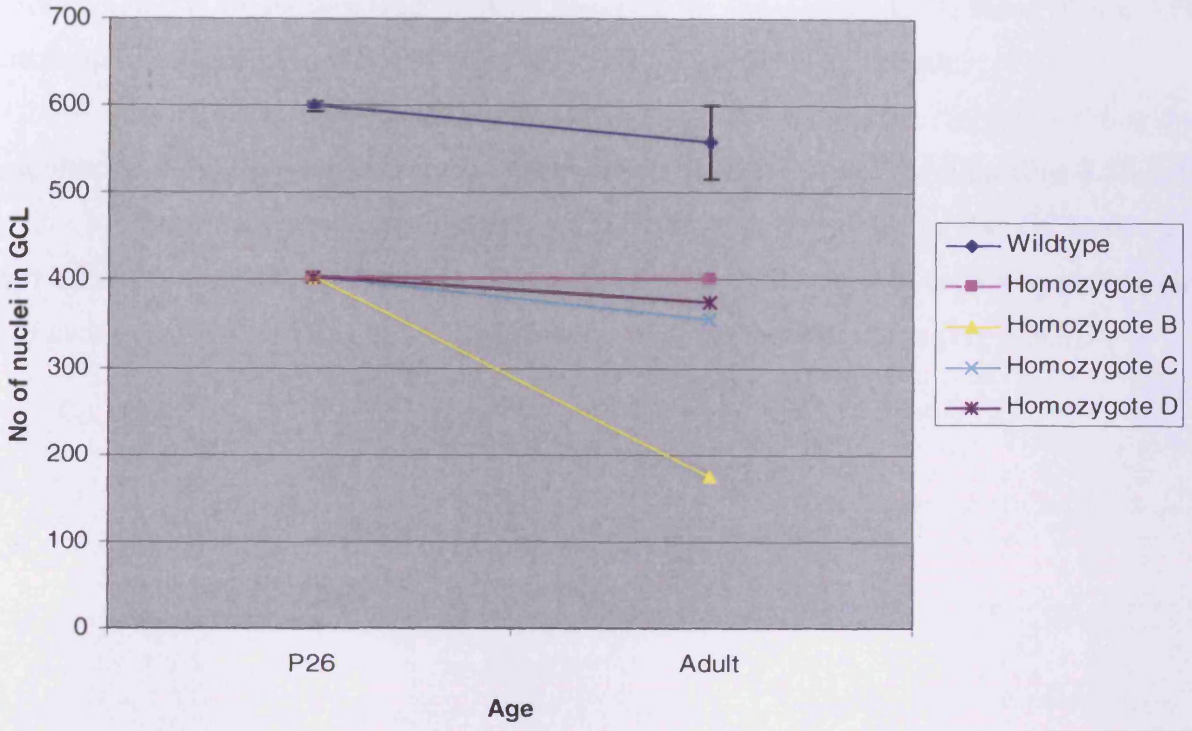

Figure 8.4. Graph displays individual GCL counts of three adult homozygote mice. Graph displays mean number of cells in GCL per retinal section in 6 week old mice (10 sections were counted per mouse). One homozygote (yellow line) was moribund at the time eyes were taken.

8.3.2 Retinal degeneration in *Opa3*$^{-/-}$ mouse associated with increased apoptosis in GCL and INL

Developmental apoptosis in mouse retina is well documented and occurs from approximately E10 through to P30. Pyknotic nuclei are present from P0 to P11 in the GCL, with a numerical peak at P2–P4, and in the INL degenerating nuclei can be observed from P0 to P18. Thus, apoptosis is an established mechanism of cell loss in the postnatal retina.

The pathologic cell death underlying the degeneration of the *Opa3*$^{-/-}$ mouse retina was examined using TUNEL which detects DNA fragmentation that is indicative of cell death. Cell death in the *Opa3*$^{-/-}$ mouse retina was investigated in comparison to wild type retina

photomicrographs of tissues (Fig 8.5A.). However, in the *Opa3*$^{-/-}$ GCL there increase in cell death and in the INL there was a 62% increase in cell death.

At adulthood, no TUNEL-reactive cells were observed in the *Opa3*$^{+/+}$ retina (F the *Opa3*$^{-/-}$ retina there was an average 1.6 TUNEL-reactive cells in the G apoptotic cells in the INL per section. The number of TUNEL-reactive cells was significant in the INL at P8 (Fig 8.5D.) and in the GCL in the adult retina (Fig 8.5

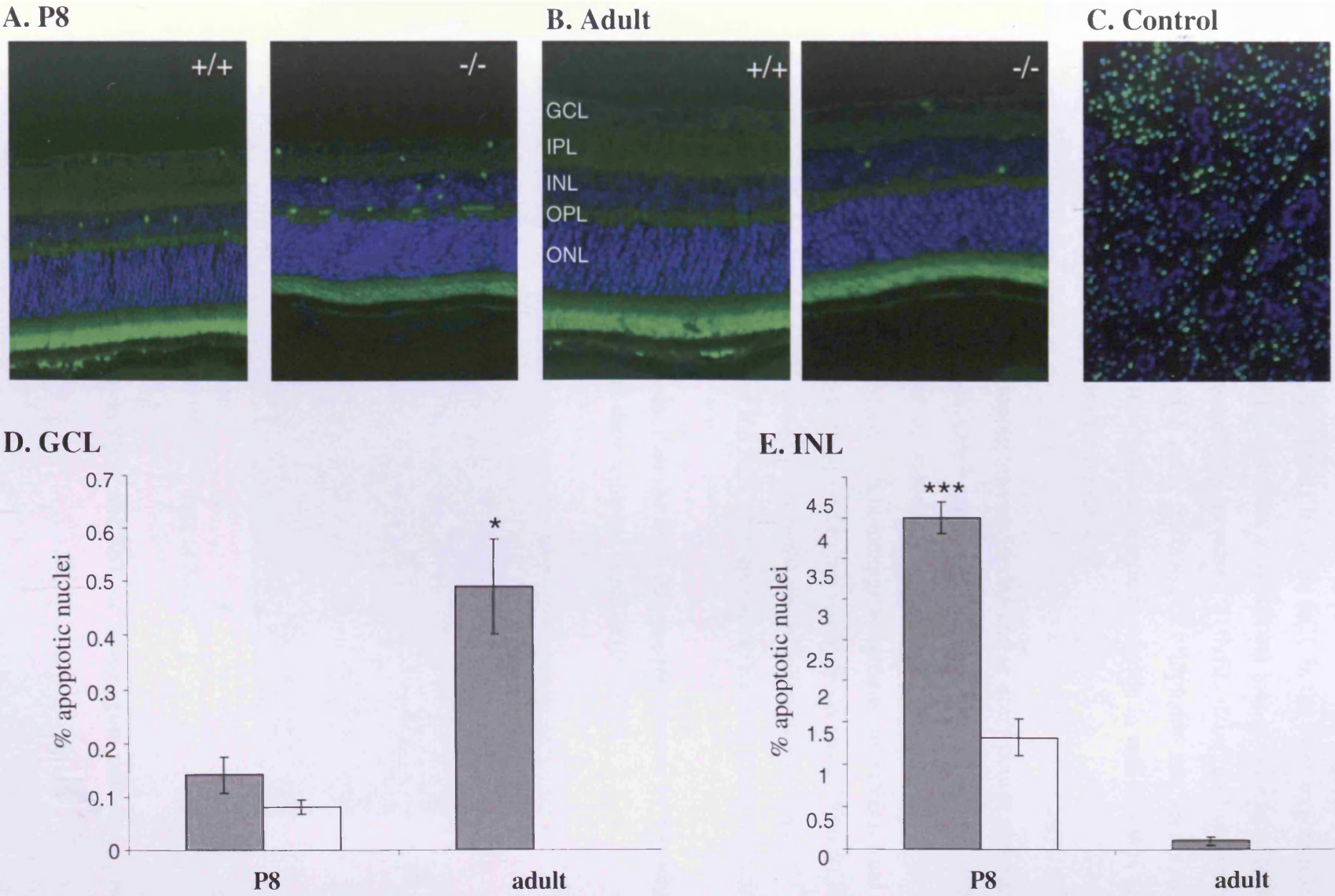

Figure 8.5. TUNEL staining in the *Opa3*$^{-/-}$ and *Opa3*$^{+/+}$ P8 and adult retina. Fluorescence photomicrographs of TUNEL positive cells in (A) P8 *Opa3*–/– and *Opa3*+/+ retina and (B) adult *Opa3*–/– and *Opa3*+/+ retina. (C) Graph displaying percentage of TUNEL positive cells per section in GCL of *Opa3*$^{-/-}$ and *Opa3*$^{+/+}$ P8 and adult retina. (D) Graph displaying percentage of TUNEL positive cells per section in INL of *Opa3*$^{-/-}$ and *Opa3*$^{+/+}$ P8 and adult retina. Apoptotic cells counts are average of five retinal sections around the optic nerve per animal. No TUNEL positive cells were observed in any of the other retinal layers. (For P8 and adult retina *Opa3*–/– n=3 and *Opa3*+/+ n=3). Values are shown as mean ± S.E.M. **P*<0.05, ****P*<0.001.

8.4 Discussion

Results showed no increased loss of cells from the GCL in the homozygote mice compared to wildtype controls at P0, but by P8 there was a significant loss of cells from both the GCL and the INL. This loss was accompanied by increased TUNEL staining observed in these layers. Loss of these cells occurs during early postnatal development and seems to continue as a gradual loss throughout life. However, a dramatic escalation in cell loss was also observed in one mouse in the final stages of the disease state.

Opa3 is expressed in the developing lens and retina and in other ocular structures, such as the extra-ocular muscles and cornea. Opa3 expression is high in the developing RGCs of the optic nerve at 14.5dpc [Powell *et al*, submitted] which is approximately the peak time for RGC neurogenesis. Cell counts in the GCL in homozygous mutants, on H&E retinal sections at P0, show no significant loss of cells compared to the wildtype controls. With RGC neurogenesis ending at approximately 18.5 dpc (around birth) this suggests that the $Opa3^{L122P}$ mutation has no effect on the neurogenesis of the RGCs but appears to have an effect on their survival.

The greatest percentage cell loss from the GCL and the INL occurs by P8, where both layers have lost ~15% more cells than their wildtype controls (Fig 8.6.).

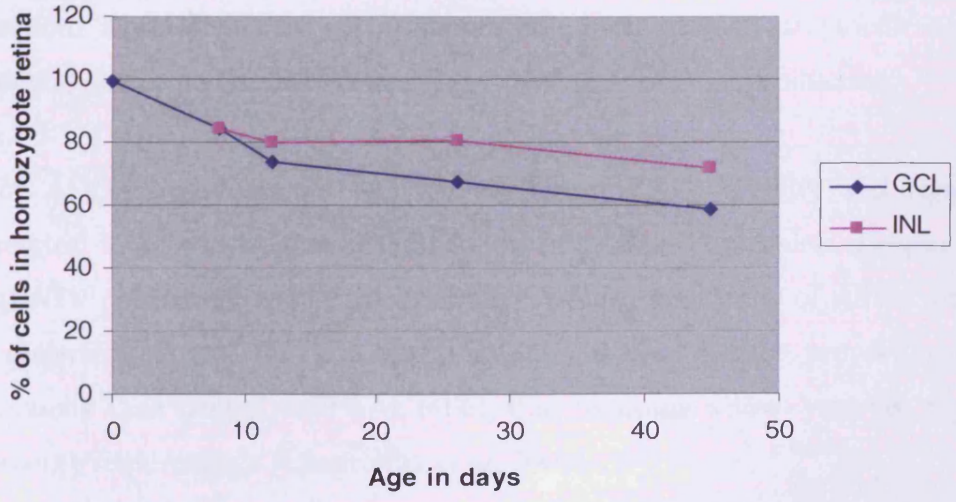

Figure 8.6. Percentage of cells in GCL and INL of homozygote mice as a proportion of the wildtype.

While increased RGC death has been well documented in optic neuropathies, the significance of increased apoptosis in the INL layer is unclear. One possible explanation for apoptosis in both layers, based on observations in ferrets [Cusato *et al*, 2001; Williams *et al*, 2001], is that elimination of the ganglion cell population by optic nerve transection, in the early postnatal period, increases apoptosis in NBL/INL. This suggests developing neuroblasts and differentiating neurons of the NBL/INL are normally dependent on the RGCs for their survival. GABAergic and glycinergic amacrine cell distribution was altered by unilateral removal at birth of the superior colliculus, pretectum, and optic tract in rats [Yamasaki *et al.* 1997]. However, no delay was observed between GCL cell death and INL cell death with both layers having lost ~15% more cells than their wildtypes by P8. This suggests that transynaptic degeneration or defects in synaptogenesis are unlikely to be the causes of retinal degeneration. It is more likely that *Opa3* is expressed in the GCL and INL and diminished metabolic capabilities of cells in these layers causes the pan retinal degeneration.

Increased cell death was also observed in these layers at P8 suggesting an increased sensitivity in the $Opa3^{L122P}$ mutant mice. This increase in cell death was observed prior to the high energy demand incurred by visually evoked potentials after eye opening, suggesting that even basal metabolic requirements of these cells are not being met.

Mitochondria play a role in promoting and regulating the apoptotic death of a cell and in energy production. The IMM is the site of apoptogenic proteins such as cytochrome *c* or the apoptosis-inducing factor and of the electron transport chain for ATP production.

Fibroblasts of ADOAC patients showed a reduction in COX activity and significantly enhanced complex V activity without modification of protein expression. Despite this the mitochondrial ATP production was normal but with reduced efficiency of ATP synthesis. In the routine respiratory state, the affected fibroblasts use a greater proportion of their respiratory capacity than controls (80% vs 60%), thus retaining a low 'reserve' capacity to face greater energy requirements [Chevrollier *et al*, 2008].

Consequences of OXPHOS dysfunction are decreased ATP production and increased ROS production, both of which have multiple simultaneous consequences at the cellular level. Compensatory mechanisms for diminished ATP production have been observed in the *Opa3* homozygote mice i.e., increased COX has been observed in the post-laminar myelinated

region of the optic nerve [Davies *et al*, 2008]. The proportion of opaque mitochondria was also significantly higher. Respiratory impairment may produce some compensatory mitochondrial proliferation in specific tissues. However, there was no increase in mitochondrial number density. 'Dark' degeneration of axons was also observed in our *Opa3*$^{-/-}$ mice, consistent with the consequences of increased mitochondrial activity. This type of degeneration is when the myelin sheath remains the same but the axons contain a dense axoplasm [Marques *et al*, 2003].

Alternatively, inefficient respiratory chain activity might increase production of ROS which can ultimately lead to apoptosis. ROS production by mitochondria can lead to oxidative damage to mitochondrial proteins, membranes and DNA, impairing the ability of mitochondria to synthesize ATP and to carry out their wide range of metabolic functions. This includes the tricarboxylic acid cycle, FA oxidation, the urea cycle, aa metabolism, haem synthesis and FeS centre assembly that are central to the normal operation of most cells. Mitochondrial oxidative damage can also increase the tendency of mitochondria to release intermembrane space proteins, such as cytochrome *c* to the cytosol by mitochondrial outer membrane permeabilization and thereby activate the cells apoptotic machinery. In addition, mitochondrial ROS production leads to induction of the mitochondrial permeability transition pore, which renders the inner membrane permeable to small molecules in situations such as ischaemia/reperfusion injury.

The small amount of apoptosis observed in the adult retina and the slope of the graph for GCL and INL cell loss (Fig 8.6.) indicates that the disease causes a gradual postnatal cell loss that continues into adulthood. The increase in cell loss observed in one mouse in the final stages of the disease state (Fig 8.6.) may be attributed, over time, to the system becoming less able to compensate for the mitochondrial energetic deficiency.

TUNEL however does not indicate which apoptotic pathway is involved. Caspases are cysteine proteases that mediate apoptotic death in a variety of cellular systems, including neurons. Caspases are activated through the extrinsic (death receptor) pathway or the intrinsic (mitochondrial) pathway. The latter is used by most neurons in most situations. However, mitochondria can also induce apoptosis in both a caspase-independent manner. Apoptogenic factors residing in the mitochondrial intermembrane space, such as apoptosis inducing factor and endonuclease G, can be released into the cytosol, translocate to the nucleus resulting in

chromatin condensation and DNA fragmentation independent of caspase activation. The caspase-independent pathway has been shown to be involved in RGC death induced by TNF-α or hypoxia [Tezel and Yang, 2004]. Apoptosis by the caspase- independent pathway has also been observed in LHON cybrids which suffered a profound ATP depletion [Zanna *et al*, 2005]. Now it is known that apoptosis is increased in $Opa3^{L122P}$ mice it would be prudent to assess the type of apoptosis involved as therapeutic strategies may need to take into account both caspase-dependent and -independent pathways.

Which apoptotic pathway is activated in the $Opa3^{L122P}$ mouse model could be explored by immunohistochemistry on retinal sections with antibodies for caspase 8 (for an initiator in the death receptor pathway) and caspase 9 in the mitochondrial apoptotic pathway. Caspase 3 could also be performed alongside TUNEL as a confirmation of apoptosis.

8.5 Conclusions

- Retinal degeneration in the *Opa3*^{L122P} mouse begins during early postnatal development and continues as a gradual loss of cells throughout life. This loss is increased as the disease severity progresses which may be attributed, over time, to the system becoming less able to compensate for the mitochondrial energetic deficiency.

- Cell counts at P0 in the GCL of the *Opa3* ^{L122P} mouse retina showed no significant difference to wildtype controls suggesting *Opa3* does not play a role in GCL neurogenesis.

- Increased cell death occurs in both the GCL and INL during early postnatal development and adulthood suggesting an increased susceptibility in these layers. This susceptibility may be due to the basal metabolic requirements of these cells not being met.

Final discussion, future work and conclusions

The scientist, by the very nature of their commitment, creates more and more questions, never fewer. Indeed the measure of our intellectual maturity, one philosopher suggests, is our capacity to feel less and less satisfied with our answers to better problems. ~G.W. Allport, *Becoming*, 1955

9. Final discussion

9.1 Summary of results - Overview of mouse phenotype

This thesis investigates the outcome of introducing an ENU induced point mutation of the *Opa3* gene into the mouse germline and compares the findings with those from clinical studies of patients with the MGA-III syndrome. The *Opa3* homozygous mouse displays a disease phenotype that can be separated into three stages as it progresses (Table 9.1.).

Early Stage	Growth retardation (smaller) Blindness Splayed gait
Middle Stage	Lower activity Tremor (mild) Higher acoustic startle response Pathological limb grasping Blanched skin colour
Late stages	Weight loss Tremor Ataxia Hunched Drop in body temperature Moribund

Table 9.1. Classification by phenotype of disease progression in the *Opa3* homozygote mouse.

In the early stages, the mice are smaller and blind, but show no neurological or behavioural deficits at this point. As the disease progresses they start to show mild neurological defects that slow their co-ordination and activity, although the mice do not seem perturbed. Time of death is variable, but certain phenotypic traits are associated with the final stage of the disease such as: a drop in body weight, lack of movement even when provoked, blanched skin colour and ataxia. Death is usually then within a couple of days. Vocalisation is sometimes present and is a sign of distress.

From the use of a range of visual, neurological, behavioural and metabolic tests it is known that in the homozygous mutant state these mice manifest a multi-systemic disease that displays variable onset. Disease characteristics include decreased weight, pan-retinal

degeneration, dilated cardiomyopathy, extra-pyramidal dysfunction, neuro-muscular defects, motor-learning deficits and severe metabolic defects including elevated blood plasma levels of 3-methylglutaconic acid and hepatic and bone marrow steatosis.

9.1.1 The Opa3^{L122P} mouse as a model of MGA- III

The Table below compares the mouse phenotype with the clinical description of human MGA-III patients, to illustrate the similarities and disparities (Table 9.2.).

Human clinical description	Mouse phenotype	Severity of mouse phenotype
ABNORMAL		
Bilateral Optic atrophy, sometimes associated with horizontal nystagmus	Bilateral optic atrophy	3
Chorea	No Chorea	0
Spastic paraplegia	Abnormal movement of back legs	1
Unstable spastic gait	Splayed gait	1
Increased tendon reflexes	Normal	0
Positive Babinski sign may be seen	Cannot be tested	/
Mild ataxia	Ataxia	2
Dysarthria	Cannot be tested	/
Cerebellar dysfunction	Cerebellar dysfunction	2
Cognitive impairment	Deficits in cerebellum-dependent learning tasks. Learning and memory were not tested.	1
Increased urinary and blood 3-methylglutaconic and 3-methylglutaric acid	Increased blood 3-methylglutaconic	3
Normal lifespan	Reduced lifespan	4
NORMAL		
Electroretinogram	Not tested	/
Sensation	Normal	0
Muscle tone	Normal muscle tone	0
No cardiac abnormalities	Cardiomyopathy	3
No structural brain abnormalities	Decreased cerebellum volume	2
Normal adiposity	Low adiposity	3

Table 9.2. Human MGA-III syndrome and the *Opa3*^{L122P} mouse model: diagnosis and phenotypic comparisons. Severity of mouse phenotype indicated by 0= normal, 1= mild, 2= moderate, 3= severe, 4= very severe.

A tabulated comparison of mice and humans that are deficient in *Opa3* activity indicates significant conservation of function. Affected mice and human patients show a similar and variable course of disease. Both show early optic atrophy, late-onset extrapyramidal dysfunction and motor-learning deficit with increase urinary excretion of 3-methylglutaconic acid. However, the mouse does display phenotypic characteristics not observed in MGA-III patients, such as craniofacial anomalies and hepatic and bone marrow steatosis. This however is not unexpected or necessarily unwanted. Due to the low number of human *Opa3* mutations found so far no genotype/phenotype correlations can be made and variations in *Opa3* phenotypes have already been observed with the clinical descriptions of MGA-III versus ADOAC. Differences observed in disease physical signs between humans and mice with *Opa3* deficiency may indeed reflect species-specific functions of the Opa3 protein. However, disease signs not reported in human MGA-III patients but present in $Opa3^{-/-}$ mice may indicate that humans most severely affected may die in gestation or in early postnatal life, whereas those least affected may reach maturity with a variable subset of disease signs. Unfortunately, exact parallels with MGA-III patients cannot be made due to the small number of human patients assessed and to the fact that no human tissues have ever been analysed.

9.2 Possible mechanisms and causes of MGA-III

9.2.1 Possible origin and effect of 3-methylglutaconic aciduria

Organic acid disorders are caused by an absence or a deficiency of one or more of the enzymes needed to complete the breakdown of dietary protein. Because the protein cannot be broken down, the body is unable to use it for growth and repair, and there is a build up of harmful substances, usually acids in the blood and urine. The increased excretion of 3-methlyglutaconic and 3-methylglutaric acid is a hall mark of the MGA syndromes and their excretion is indicative of a metabolic disturbance that impairs the body's ability to make energy in the mitochondria. The branched-chain organic acid, 3-methylglutaconic acid, is an intermediate (as the CoA thioester) in the leucine degradative pathway as well as the mevalonate shunt pathway which links isoprenoid metabolism with mitochondrial acetyl-CoA metabolism (Fig 9.1.).

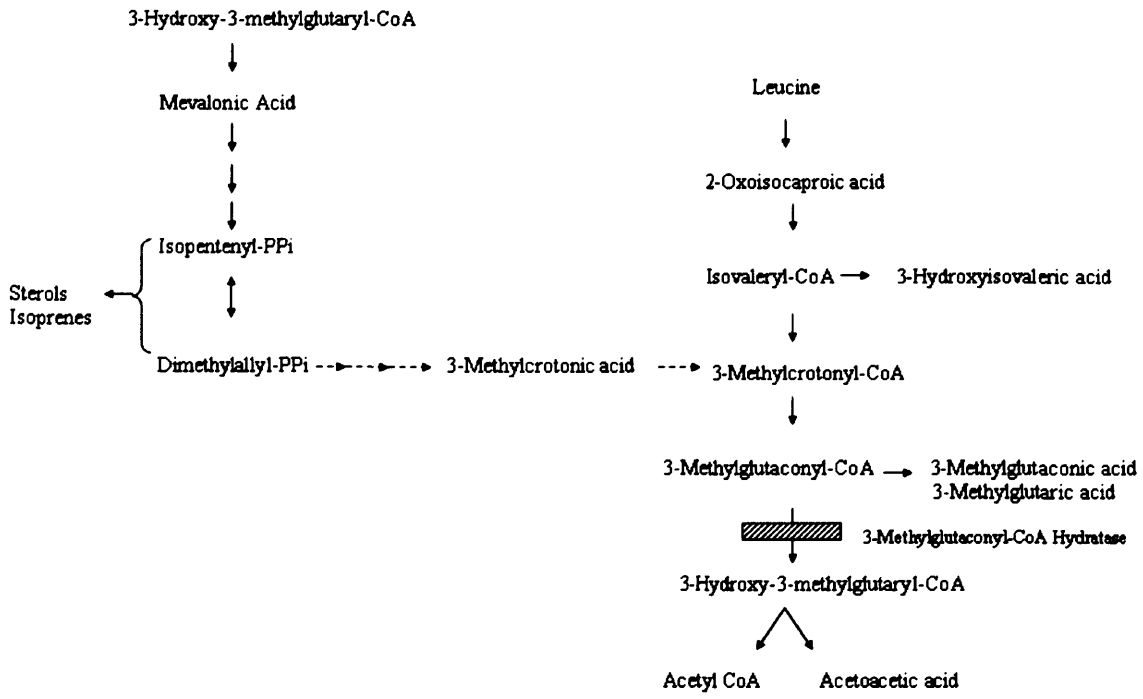

Figure 9.1. Metabolic pathway diagram showing branched-chain organic acid 3-MGC as an intermediate of leucine degradation and the mevalonate shunt pathway that links sterol synthesis with mitochondrial acetyl-CoA.
[www.ncbi.nlm.nih.gov/books/bv.fcgi?rid=gene.chapter.mga3]

The majority of patients with abnormal 3-methylglutaconic aciduria or acidemia appear to have normal leucine metabolism. This has also been seen in fibroblasts from MGA-III patients, which showed normal activity of 3-methylglutaconyl-CoA hydratase [Elpeleg, 1994]. As leucine metabolism is normal, the link between MGA and mitochondrial respiratory-chain defects likely involves the mevalonate shunt; this pathway produces 3-methylglutaconyl-CoA from mevalonate via dimethylallyl pyrophosphate [Edmond and Popjak, 1974], an intermediate in the synthesis of cholesterol and polyisoprenoids (such as ubiquinone). It has been speculated that defective ubiquinone biosynthesis could lead to increased levels of precursors (e.g. mevalonate) in the pathway, thereby increasing synthesis of 3-methylglutaconic acid [Kelley and Kratz, 1995]. However Costeff *et al*, [1989] showed no beneficial effect, on administration of an active form of ubiquinone, coenzyme Q_{10}, to three patients with MGA-III. Interestingly, a zebrafish model of MGA-III which has an antisense-based depletion of *Opa3* has shown that zebrafish *Opa3* interacts with both the leucine and mevalonate pathways [Pei *et al*, 2008]. Not all MGA-III patients have normal leucine metabolism and the zebra fish model shows *Opa3* involved in leucine metabolism.

Therefore, any therapeutic strategies for MGA-III will likely have to include the leucine degradation and mevalonate shunt pathways.

The mevalonate pathway or HMG-CoA reductase pathway or mevalonate-dependent route, is an important cellular metabolic pathway present in all higher eukaryotes and many bacteria. It is important for the production of dimethylallyl pyrophosphate and isopentenyl pyrophosphate that serve as the basis for the molecules used in processes as diverse as protein prenylation, cell membrane maintenance, protein anchoring and *N*-glycosylation. Two pathways of mevalonate metabolism are known: the major (sterol) pathway leads to cholesterol synthesis, whereas the second shunts mevalonate away from sterol production and ultimately results in its oxidation to CO_2. Edmond and Popjak [1974] found that this shunt pathway operates significantly only in tissues of ectodermal origin, such as the CNS and retina.

The shunt pathway of mevalonate metabolism is thought to begin in the cytoplasm and ends in the mitochondria. Alcohol dehydrogenase, which catalyses the oxidation of dimethylallyl alcohol to B-methylcrotonaldehyde is a cystolic enzyme. But, the steps B-methylcrotonyl-CoA to HMG-CoA, common with the leucine catabolism pathway are mitochondrial. Therefore, the shunt pathway crosses the mitochondrial membrane at the level of either B-methylcrotonaldehyde or B-methylcrotonate. It has been shown [Havre *et al*, 1977] that ethanol is converted to acetaldehyde in liver cytosol, while acetaldyhyde is oxidized to acetate mostly in the mitochondria. It is therefore likely that 3-methylcrotonaldehyde is the intermediate of the shunt pathway that crosses the mitochondrial membrane.

How this systemic metabolic disease contributes to ocular defects remains to be elucidated in MGA syndromes. Individuals affected by MGA predominantly accumulate 3-methylglutaconic acid and 3-methylglutaric acid in their tissues and body fluids, whereas 3-hydroxyisovaleric acid is also accumulated in MGA-I. Although MGA patients commonly present neurological manifestations, the pathophysiology of their symptoms is poorly established. However, it could be presumed that the increased tissue concentrations of these organic acids are associated with their neurologic symptoms, since they become worse during episodes of metabolic decompensation, in which there is a dramatic increase of the concentrations of these organic acids. Therefore, neurological defects could be due to direct toxic mechanisms of abnormal metabolic products or to accumulation of normal metabolites by errors of synthetic pathways or by deficient energy metabolism.

OPA3 may localise to the OMM [Ryu *et al*, 2010], with a C-terminus exposed to the cytosol and an N-terminal mitochondrial targeting domain. OPA3 residues 83-102 are a hydrophobic region that is predicted to be a membrane spanning segment. Deletion of these residues showed a mitochondrial localisation but no morphological changes to the mitochondria. A plausible explanation is missorting of OPA3 with deleted 83-102 residues to the mitochondrial matrix. One might hypothesis, therefore, that if OPA3 is involved in the mevalonate shunt pathway by transport of metabolites from the cytosol into the mitochondria, then the etiology of MGA-III maybe the missorting of OPA3 to the matrix causing accumulation of abnormal metabolic products or normal metabolites within the mitochondria.

.

9.2.2 OPA3 and mitochondria

A variety of degenerative diseases have now been shown to be caused by mutations in mitochondrial genes encoded by mtDNA or nuclear DNA (nDNA) (Fig 78.). And the maintenance of a finely tuned balance between mitochondrial fusion and fission processes and the generation of energy in the mitochondria via OXPHOS can now be regarded as playing important pathogenic roles in neurodegeneration. Experimental evidence has shown that the syndromes of *OPA3* can be added to the list of optic neuropathies that have a detrimental effect on both of these processes and comparisons made between these optic neuropathies reveals common themes (Fig 9.2.).

Comparisons between LHON, ADOA, ADOAC and MGA-III shows:- Firstly, in all four diseases, optic atrophy can be associated with more complex neurological signs such as dystonia or the Leigh-like syndrome in LHON, [Jun *et al*, 1994, Funalot *et al*, 2002] deafness in ADOA [Amita-Bonneau *et al*, 2003] and mild extrapyramidal signs in ADOAC and MGA-III. Second, all four diseases are caused by mutations in genes encoding proteins located in the mitochondria. LHON is mainly caused by mutation of mitochondrial DNA genes encoding respiratory chain complex I subunits; the *OPA1* gene encodes a protein anchored to the IMM facing the intermembrane space [Olichon *et al*, 2002]; and *OPA3* is known to be a mitochondrial protein although its exact location remains debatable.

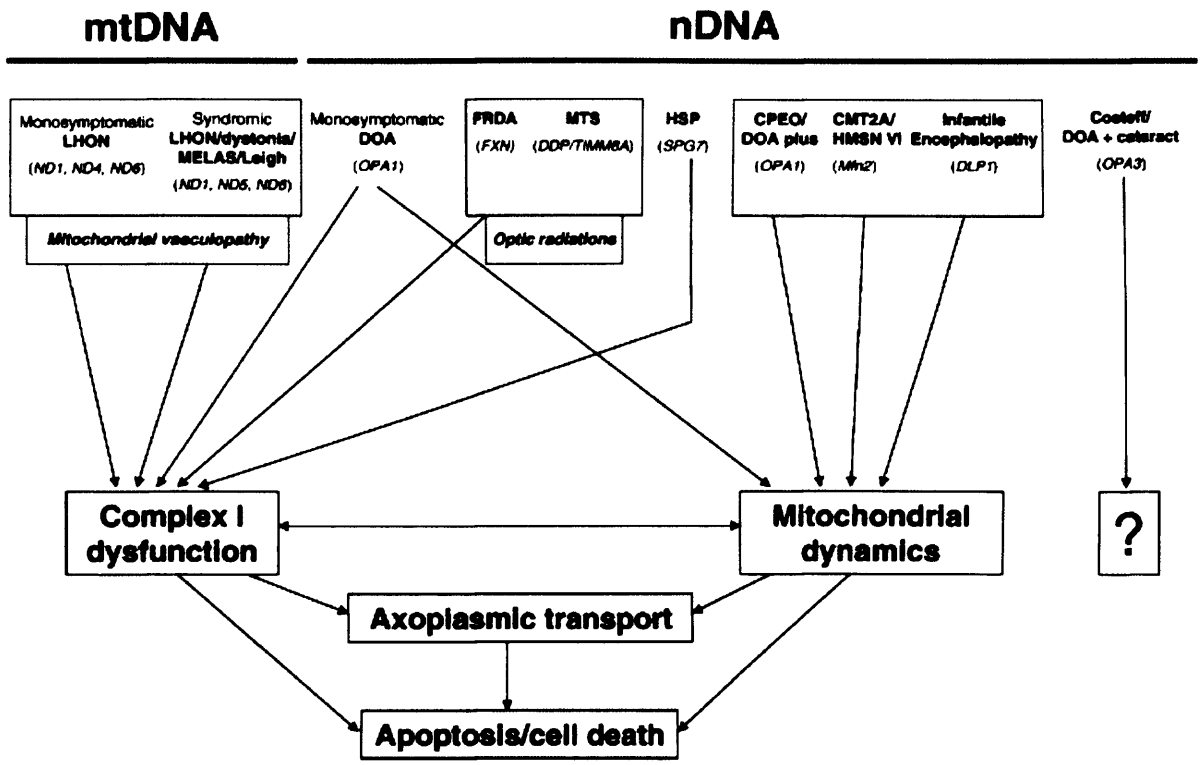

Figure 9.2. Schematic summary of the common themes linking mitochondrial optic neuropathies. [Carelli *et al*, 2009]

Third, LHON, ADOA, ADOAC and MGA-III are all associated with painless optic atrophy without inflammation, consistent with an apoptotic mechanism, which could be common to the four disorders causing RGC death culminating in optic atrophy. Indeed, it has been shown that complex I plays a key role in the permeability of transition pores [Chauvin *et al*, 2001] and that cells bearing mutations causing LHON are predisposed to apoptosis, [Danielson *et al*, 2001; Ghelli *et al*, 2002] possibly because of increased production of reactive oxygen species [Li, 2003]. Similarly, it has been shown that the silencing of *OPA1* by RNA interference in HeLa cells leads to cytochrome c release and commits cells to apoptosis [Olichon *et al*, 2003]. Reynier *et al*, in [2004] showed that fibroblast of ADOAC patients carrying the *OPA3* mutation (G93S) also has an increased susceptibility to the induction of apoptosis. Ryu *et al*, in [2010] also showed that mutant OPA3 (G93S) increased cell death and mitochondrial fragmentation in the absence of apoptotic stimuli. The further presence of cataract in ADOAC could also be explained by an apoptotic mechanism since there are several lines of evidence implicating apoptosis in cataractogenesis [Tempestini *et al*, 2003]. Experiments also revealed that overexpression of wildtype OPA3 did not induce cytochrome c release, caspase 3 activation, or Bax translocation, although OPA3-overexpressing cells were sensitised to

apoptotic stimuli. Therefore OPA3 has no pro-apoptotic effect, but rather potentiated cell death, via mitochondrial fragmentation, after apoptotic stimulation.

Some MGA patients have elevated lactic acid or citric acid cycle intermediates, as well as abnormalities of the mitochondrial electron transport chain [Ibel *et al*, 1993; Besley *et al*, 1995; Ruesch *et al*, 1996], including deficiency of the activities of respiratory chain complexes I, II, III, IV and V [Gibson *et al*, 1993; Sweetman and Williams, 2001; Gunay-Aygun, 2005; Wortmann *et al*, 2006], strongly indicating mitochondrial dysfunction.

There is also a clear link between optic neuropathies and genes of the IMM and OMM involved in fission and fusion (Fig 9.2.). The clinical relevance of maintaining a balance between mitochondrial fusion and fission processes is underscored by the fact that the pathogenesis of certain hereditary neurodegenerative disorders such as ADOA and Charcot-Marie-Tooth neuropathy type 2A (CMT2A) can now be linked to mutations in genes encoding mediators of mitochondrial fusion. Recent experimental evidence has implicated OPA3 in these fusion/fission processes. The ring-like mitochondrial fragmentation phenotype observed in OPA3 overexpression has also been observed in overexpression of major fission mediators DRP1 and FIS1. Mitochondrial morphology significantly changes in mammalian cells overexpressing wildtype or mutant (G93S) OPA3 causing ring-like mitochondrial fragmentation and cells depleted of OPA3 via RNA interference, which induced an elongated mitochondrial morphology, suggesting a role for OPA3 as a mitochondrial fission factor or an inhibitor of fusion. OPA3 was also shown to induce mitochondrial fragmentation even in the absence, via RNA interference, of DRP1 and FIS1 suggesting OPA3 might be a fission factor independent of DRP1 and FIS1.

Although overexpression of OPA3 does not itself induce spontaneous apoptotic cell death, the OPA3 induced alteration in mitochondrial morphology increased sensitivity to apoptotic stimuli. Thus, supporting a close connection between mitochondrial fragmentation and apoptotic processes. These findings substantiate the participation of *OPA3* in mitochondrial dynamics and the pathogenesis of optic atrophy. It is however, still questionable as to whether syndromes of *Opa3* are primary or secondary mitochondrial diseases although the consensus seems to be more towards secondary.

9.3 Conclusions

The cascade of events leading to neuronal death are very complex and many players will need to be considered as each taken individually e.g. axoplasmic flow or energy depletion do not give a satisfactory answer. Because of the multiplicity of mitochondrial functions, ranging from intermediate metabolism, to energy production, to apoptosis, there are many, non-mutually exclusive, potential avenues whereby damaged mitochondria can sabotage the survival of a neuronal cell. In the case of *Opa3* it is likely that mitochondrial dysfunction is the cause of neuronal death but the mitochondrial dysfunction itself maybe a downstream event of some other defect.

We should recognize that our understanding of *Opa3* function is limited and therefore be wary of making assumptions and simplifications. For example, Wolfram syndrome 1, which is another syndromic recessive optic atrophy, is associated with multiple organ abnormalities, optic nerve atrophy and diabetes. It was initially suspected as a mitochondrial disorder, but subsequent studies showed that wolframin is an integral, endoglycosidase H-sensitive membrane glycoprotein that localises to the endoplasmic reticulum [Takeda *et al*, 2001; Hofmann *et al*, 2003; Osman *et al*, 2003].

In order to help understand the function of *Opa3*, comparisons with other optic neuropathies such as LHON and ADOA are useful as they show an intriguing degree of clinical overlap. But should we expect a mechanistic overlap? LHON is caused by defects in complex I and ADOA (*OPA1*) is caused by defects in mitochondrial fusion and fission. They are therefore considered primary mitochondrial diseases. However, MGA-III is a metabolic disease, and, unlike LHON and ADOA, has a massive build up of organic acid in the tissues. The *Opa3*^{L122P} mouse model also displays phenotypic aspects that cannot be explained by mitochondrial dysfunction, such as craniofacial anomalies and bone marrow steatosis.

The most likely breakthrough now will come from animal models. Unfortunately, to date the only two published models of *Opa3* are, our B6; C3-*Opa3*^{L122P} mouse model and a zebrafish model [Pie *et al.* 2010]. This is probably due to the rarity of MGA-III/ADOAC in the human population. Overall, this thesis shows that our mouse model faithfully mimics many aspects of MGA-III and therefore is an extremely valuable tool in the study of *OPA3*. The further characterization of this model and future genetic and functional studies will eventually help

elucidate the steps that must occur from defective gene to defective mitochondria, from abnormal biochemistry to the disease state and hopefully reveal important pathophysiological pathways amenable to therapeutic interventions.

9.4 Future Work

At present the analysis of EM sections of retina, optic nerve and muscle is being undertaken to assess for any alterations in mitochondrial morphology and number. Quantitative PCR is also being undertaken to confirm that melanopsin RGCs are being preferentially spared compared to the non-photosensitive RGCs.

Future work might entail:

1) Structural description of the protein by use of small angle x-ray scattering and circular dichroism for protein tertiary structure modelling would allow for a more detailed bio-informatic analysis of structure/function correlations.

2) Increased apoptosis was observed in the retina of the *Opa3*^{L122P} mouse. Increased apoptosis can occur by caspase dependent and independent pathways. In order to be in a position to modulate retinal apoptosis therapeutically, the apoptotic pathways must be carefully defined in our mouse model.

3) Histological sections of depleted epididymal fat depots showed that the adipocytes looked structurally like brown adipocytes. To determine if these cells are brown adipocytes immunohistochemistry could be undertaken for UCP-1 which is a protein unique to brown adipocytes.

4) Assessment of putative TFBS suggested a role for Opa3 in adipogenesis. Lipodystrophy was observed in the *Opa3* homozygote mice. The reduction of adipocytes may occur via decreased growth and differentiation, increased apoptosis, or enhanced destruction as may occur in autoimmune destruction and metabolic disturbances. This suggests that transcriptional levels of PPARγ, C-EBPa+b and PGC-1α maybe altered. This could be analysed by quantitative real-time PCR.

References

Adachi S, Cross A, Babior BM *et al.* Bcl-2 and the outer mitochondrial membrane in the inactivation of cytochrome c during Fas-mediated apoptosis. *J Biol Chem.* 1997;29:21878–21882.

Ailhaud G, Grimaldi P and Negrel R. Cellular and molecular aspects of adipose tissue development. *Annu Rev Nutr.* 1992;12:207–233.

Alberts B, Bray D, Lewis J, Raff M, Roberts K, Watson JD. In: Molecular biology of the cell, Ed 2. New York: Garland Publishing, 1989.

Alexander C, Votruba M, Pesch UE *et al.* OPA1, encoding a dynamin-related GTPase, is mutated in autosomal dominant optic atrophy linked to chromosome 3q28. *Nat Genet.* 2000;26:211-215.

Altschul SF, Madden TL, Schaffer AA *et al.* Gapped BLAST and PSI-BLAST: a new generation of protein database search programs. *Nucleic Acids Res.* 1997;25:3389-3402.

Amati-Bonneau P, Odent S, Derrien C *et al.* The association of ADOA and moderate deafness may be due to the R445H mutation in the OPA1 gene. *Am J Ophthalmol.* 2003;136:1170-1171.

Andrews RM, Griffiths PG, Johnson MA *et al.* Histochemical localisation of mitochondrial enzyme activity in human optic nerve and retina. *Br JOphthalmol.* 1999;83:231–235.

Anikster Y, Kleta R, Shaag A *et al.* Type III 3-methylglutaconic aciduria (optic atrophy plus syndrome, or costeff optic atrophy syndrome): identification of the OPA3 gene and its founder mutation in Iraqi Jews. *Am J Hum Genet.* 2001;69:1218-1224.

Aparicio S, Chapman J, Stupka E *et al.* Whole-genome shotgun assembly and analysis of the genome of Fugu rubripes. *Science.* 2002;297:1283-1285.

Armoni M, Harel C, Karni S *et al.* FOXO1 represses peroxisome proliferator-activated receptor-gamma1 and -gamma2 gene promoters in primary adipocytes. A novel paradigm to increase insulin sensitivity. *J Biol Chem.* 2006;281:19881-19891.

Arn P and Funanage VL. 3-Methylglutaconic aciduria disorders: the clinical spectrum increases. *J Pediatr Hematol Oncol.* 2006;28:62-63.

Assink JJM, Tijmes NT, ten Brink JB *et al.* A gene for X-linked optic atrophy is closely linked to the Xp11.4-Xp11.2 region of the X chromosome. *Am J Hum Genet.* 1997;61: 934-939.

Badea TC and Nathans J. Quantitative analysis of neuronal morphologies in the mouse retina visualized by using a genetically directed reporter. *J Comp Neurol.* 2004;480:331–351.

Bahi N, Zhang J, Llovera M *et al.* Switch from caspase-dependent to -independent death during heart development: essential role of EndoG in ischemia-induced DNA processing of differentiated cardiomyocytes. *J Biol Chem.* 2006;281:22943–22952.

Bailes HJ and Lucas RJ. Melanopsin and inner retinal photoreception. *Cell Mol Life Sci.* 2009;67:99-111.

Barneoud P and Curet O. Beneficial effects of lysine acetylsalicylate, a soluble salt of aspirin, on motor performance in a transgenic model of amyotrophic lateral sclerosis. *Exp Neurol.* 1999;155:243–251.

Barnstable CJ and Drager UC. Thy-1 antigen: A ganglion cell specific marker in rodent retina. *Neuroscience.* 1984;11:847–855.

Barron MJ, Griffiths P, Turnbull DM *et al.* The distributions of mitochondria and sodium channels reflect the specific energy requirements and conduction properties of the human optic nerve head. *Br J Ophthalmol.* 2004;88:286–290.

Barsoum MJ. Nitric oxide-induced mitochondrial fission is regulated by dynamin-related GTPases in neurons. *EMBO J.* 2006;26:3900-3911.

Barth PG, van't Veer-Korthof ETh, van Delden L *et al.* An X-linked mitochondrial disease a.ecting cardiac muscle, skeletal muscle and neutrophil leucocytes. In Busch HFM, Jennekens FGI, Scholte HR eds. *Mitochondria and Muscular Diseases.* Beeststerzwaag: Mefar, 1981:161-164.

Barth PG. An X-linked mitochondrial disease affecting cardiac muscle, skeletal muscle and neutrophil leucocytes. *J Neurol Sci.* 1983;62:327-355.

Barth PG, Valianpour F, Bowen VM *et al.* X-linked cardio skeletal myopathy and neutropenia (barth syndrome): an update. *Am J Med Genet.* 2004;126A:349-354.

Berson DM. Strange vision: ganglion cells as circadian photoreceptors. *Trends Neurosci.* 2003;26:314-320.

Berson DM, Dunn FA and Takao M. Phototransduction by retinal ganglion cells that set the circadian clock. *Science.* 2002;295:1070–1073.

Besley GT, Lendon M, Broadhead DM *et al.* Mitochondrial complex deficiencies in a male with cardiomyopathy and 3-methylglutaconic aciduria. *J Inherit Metab Dis.* 1995;18:221-223.

Biousse V and Newman N. Hereditary optic neuropathies. *Ophthalmol Clin NA* 2001;14:547–568.

Blanchard DC, Griebel G and Blanchard RJ. Mouse defensive behaviors: pharmacological and behavioral assays for anxiety and panic. *Neurosci Biobehav Rev.* 2001;25:205-218.

Blanchette M., Bataille AR, Chen X *et al.* Genome-wide computational prediction of transcriptional regulatory modules reveals new insights into human gene expression. *Genome Res.* 2006;16:656–668.

Bolivar VJ, Caldarone BJ, Reilly AA *et al.* Habituation of activity in an open field: A survey of inbred strains and F1 hybrids. *Behav Genet.* 2000;30:285-293.

Bossy-Wetzel E and Green DR. Apoptosis: checkpoint at the mitochondrial frontier. *Mutat Res.* 1999;434:243–251.

Bouillaud F, Ricquier D, Mory G *et al.* Increased level of mRNA for the uncoupling protein in brown adipose tissue of rats during thermogenesis induced by cold exposure or norepinephrine infusion. *J Biol Chem.* 1984;259:11583–11586.

Bremner FD, Shallo–Hoffmann J, Riordan–Eva P *et al.* Comparing Pupil Function with Visual Function in Patients with Leber's Hereditary Optic Neuropathy. *Invest Ophthalmol Vis Sci.* 1999;40:2528-2534.

Bremner FD, Tomlin EA, Shallo–Hoffmann J *et al.* The pupil in dominant optic atrophy. *Invest Ophthalmol Vis Sci.* 2001;42:675-678.

Bristow EA, Griffiths PG, Andrews RM *et al.* The distribution of mitochondrial activity in relation to optic nerve structure. *Arch Opthalmol.* 2002;120:791-796.

Burge CB and Karlin S. Prediction of complete gene structures in human genomic DNA. *J Mol Biol.* 1997;268:78-94.

Burge CB and Karlin S. Finding the genes in genomic DNA. *Curr Opin Struct Biol.* 1998;8:346-354.

Buss RR and Oppenheim RW. Role of programmed cell death in normal neuronal development and function. *Anatomical science International.* 2004;79(4):191-197.

Cannon B and Nedergaard J. Brown adipose tissue: function and physiological significance. *Physiol Rev.* 2004;84:277–359.

Carelli V. Mitochondrial dysfunction as a cause of optic neuropathies. *Prog Retin Eye Res.* 2004;23:53-89.

Carelli V, La Morgia C, Iommarini L *et al.* Mitochondrial optic neuropathies: how two genomes may kill the same cell type*?* *Biosci Rep.* 2007;27:173–184.

Carelli V, La Morgia C, Valentino ML *et al.* Retinal ganglion cell neurodegeneration in mitochondrial inherited disorders. *Biochim Biophys Acta.* 2009;1787:518-528.

Carter RJ, Lione LA, Humby T *et al.* Characterization of progressive motor deficits in mice transgenic for the human Huntington's disease mutation. *J Neurol Sci.* 1999;19:3248-3257.

Cederberg A, Grønning LM, Ahre´ B *et al.* FOXC2 is a winged helix gene that counteracts obesity, hypertriglyceridemia, and diet-induced insulin resistance. *Cell.* 2001;106:563–573.

Cepko CL, Austin CP, Yang X *et al.* Cell fate determination in the vertebrate retina. *Proc Natl Acad Sci USA.* 1996;93;589–595.

Chatterjee S and Pal JK. Role of 5'- and 3'-untranslated regions of mRNAs in human disease. *Biol Cell.* 2009;101:251-262.

Chauvin C, De Oliveira F, Ronot X *et al.* Rotenone inhibits the mitochondrial permeability transition-induced cell death in U937 and KB cells. *J Biol Chem.* 2001;276:41394-41398.

Chen FC, Chen CJ, Ho JY *et al.* Identification and evolutionary analysis of novel exons and alternative splicing events using cross-species EST-to-genome comparisons in human, mouse and rat. *BMC Bioinformatics.* 2006;15:136.

Chevrollier A, Guillet V, Loiseau D *et al.* Hereditary optic neuropathies share a common mitochondrial coupling defect. *Annals of Neurology.* 2008;63:794 - 798.

Chitayat D, Chemke J, Gibson KM *et al.* 3-Methylglutaconic aciduria: a marker for as yet unspecified disorders and the relevance of prenatal diagnosis in a 'new' type ('type 4'). *J Inherit Metab Dis.* 1992;15:204-212.

Choleris E, Thomas AW, Kavaliers M *et al.* A detailed ethological analysis of the mouse open field test: effects of diazepam, chlordiazepoxide and an extremely low frequency pulsed magnetic field. *Neurosci Biobehav Rev.* 2001;25:235-260.

Christopherson KC and Bredt DS. Nitric oxide in excitable tissues:- physiological roles and disease. *J Clin Invest.* 1997;100:2424-2429.

Cinti S. The adipose organ. *Prostaglandins, Leukot Essentl Fatty Acids.* 2005;73:9-15.

Cinti S. Transdifferentiation properties of adipocytes in the adipose organ. Am *J Physiol Endocrinol Metab.* 2009;297:E977-E986.

Cipolat S, Martins de BO, Dal ZB *et al.* OPA1 requires mitofusin 1 to promote mitochondrial fusion. *Proc Natl Acad Sci USA.* 2004;101:15927-15932.

Coffey PJ. Long term preservation of cortically dependent visual function in RCS rats by transplantation. *Nat Neurosci.* 2002;5:53-56.

Costeff H. A familial syndrome of infantile optic atrophy, movement disorder, and spastic paraplegia. *Neurology.* 1989;39:595-597.

Cousin B, Bascands-Viguerie N, Kassis N *et al.* Cellular changes during cold acclimatation in adipose tissues. *J Cell Physiol.* 1996;167;285-289.

Crawley JN. What's Wrong with My Mouse? Behavioral Phenotyping of Transgenic and Knockout Mice. NY: Wiley-Liss. 2000.

Cusato K, Stagg SB and Reese BE. Two phases of increased cell death in the inner retina following early elimination of the ganglion cell population. *J Comp Neurol.* 2001;439:440-449.

DaCruz S, Xenarios I, Langridge J *et al.* Proteomic analysis of the mouse liver inner mitochondrial membrane. *J Biol Chem.* 2003;278:41566-41571.

Danielson SR, Wong A, Carelli V *et al.* Cells bearing mutations causing Leber's hereditary optic neuropathy are sensitized to Fas-induced apoptosis. *J Biol Chem.* 2001;277:5810-5815.

Dann JF, Buhl EH and Peichl L. Postnatal dendritic maturation of alpha and beta ganglion cells in cat retina. *J Neurosci.* 1988;8:1485-1499.

Davey KM, Parboosingh JS, McLeod DR *et al.* Mutation of DNAJC19, a human homologue of yeast inner mitochondrial co-chaperone, causes DCMA syndrome, a novel autosomal recessive Barth syndrome-like condition. *J Med Genet.* 2006;43:385-393.

Davies VJ, Hollins AJ, Piechota MJ *et al.* Opa1 deficiency in a mouse model of autosomal dominant optic atrophy impairs mitochondrial morphology, optic nerve structure and visual function. *Hum Molec Genet.* 2007;16:1307-1318.

Davies VJ, Powell K, White KE *et al.* A missense mutation in the murine Opa3 gene models human Costeff syndrome. *Brain.* 2008;131:368-380.

Delettre C, Lenaers G, Griffoin JM *et al.* Nuclear gene OPA1, encoding a mitochondrial dynamin-related protein, is mutated in dominant optic atrophy. *Nat Genet.* 2000;26:207-210.

DeMedinaceli L, Freed WJ, Wyatt RJ *et al.* An index of the functional condition of rat sciatic nerve based on measurements made from walking tracks. *Exp Neurol.* 1982;77:634-643.

Di Rosa G, Deodato F, Loupatty FJ *et al.* Hypertrophic cardiomyopathy, cataract, developmental delay, lactic acidosis: a novel subtype of 3-methylglutaconic aciduria. *Journal of Inherited Metabolic Disease.* 2006;29:546–550.

Doi M, Uji Y and Yamamura H. Morphological classification of retinal ganglion cells in mice. *Comp Neurol.* 1995;356:368-386.

Donnelly KL, Smith CI, Schwarzenberg SJ Sources of fatty acids stored in liver and secreted via lipoproteins in patients with nonalcoholic fatty liver disease. *J Clin Invest.* 2005;115(5):1343-1351.

Donovan M, Doonan F, Cotter TG. Decreased expression of pro-apoptotic Bcl-2 family members during retinal development and differential sensitivity to cell death. *Dev Biol.* 2006;291:154-169.

Dosztányi ZS, Fiser A and Simon I. Stabilization centres in proteins: identification, characterization and predictions. *J Mol Biol.* 1997;272:597-612.

Douglas RM, Alam NM, Silver BD *et al.* Independent visual threshold measurements in the two eyes of freely moving rats and mice using a virtual-reality optokinetic system. *Vis Neurosci.* 2005;22:677–684.

Dunaief JL, Dentchev T and Milam A. Evidence for Apoptosis in Age-Related Macular Degeneration. *Invest Ophthalmol Vis Sci.* 2002;43: E-Abstract 2817.

Duran M, Beemer FA, Tibosch AS *et al.* Inherited 3-methylglutaconic aciduria in two brothers- another defect of leucine metabolism. *J Pediatr.* 1982;101:551-554.

Dyer MA, Donovan SL, Zhang J *et al.* Retinal degeneration in Aipl1-deficient mice: a new genetic model of Leber congenital amaurosis. *Mol Brain Res.* 2004;132:208-220.

Edmond J and Popjak G. Transfer of carbon atoms from mavelonate to n-fatty acids. *J Biol Chem.* 1974;249:66-71.

Elkon R, Linhart C, Sharan R *et al.* Genome-wide in silico identification of transcriptional regulators controlling the cell cycle in human cells. *Genome Res.* 2003;13:773-780.

Elpeleg ON, Costeff H, Joseph A *et al.* 3-methylglutaconic aciduria in the Iraqi-Jewish 'optic atrophy plus' (Costeff) syndrome. *Dev Med Child Neurol.* 1994;36:167-172.

Espejo EF. Effects of weekly or daily exposure to the elevated plus-maze in male mice. *Behav Brain Res.* 1997;87:233-238.

Fernandez-Escamilla AM, Rousseau F, Schymkowitz J *et al.* Prediction of sequence-dependent and mutational effects on the aggregation of peptides and proteins. *Nat Biotechnol.* 2004;22:1302-1306.

Ferré M, Bonneau D, Milea D *et al.* Molecular screening of 980 cases of suspected hereditary optic neuropathy with a report on 77 novel OPA1 mutations. *Hum Mutat.* 2009;30(7):E692-705.

Ferrer-Costa C, Gelpi JL, Zamakola L *et al.* PMut: a web based tool for the annotation of pathological mutations on proteins. *Bioinformatics.* 2005;21:3176-3178.

Field EF, Whishaw IQ and Pellis SM. A kinematic analysis of sex-typical movement patterns used during evasive dodging to protect a food item: the role of testicular hormones. *Behav Neurosci.* 1997;111:808–815.

Fine BS and Yanoff M. Ocular Histology. A text and Atlas. Harper & Row New York. 1979;111-124.

Floyd ZE and Stephens JM. STAT5A promotes adipogenesis in nonprecursor cells and associates with the glucocorticoid receptor during adipocyte differentiation. *Diabetes.* 2003;52:308–314.

Fotiou DF, Stergioua V, Tsiptsiosa D *et al.* Cholinergic deficiency in Alzheimer's and Parkinson's disease: Evaluation with pupillometry. *Int J Psychophysiol.* 2009;73:143-149.

Frazer KA, Chen X, Hinds DA *et al.* Genomic DNA Insertions and Deletions Occur Frequently Between Humans and Nonhuman Primates. *Genome Res.* 2003;13:341–346.

Freedman MS, Lucas RJ, Soni B *et al.* Regulation of mammalian circadian behavior by non-rod, non-cone, ocular photoreceptors. *Science.* 1999;284:502-504.

Freeman HC, Hugill A, Dear NT *et al.* Deletion of nicotinamide nucleotide transhydrogenase: a new quantitive trait locus accounting for glucose intolerance in C57BL/6J mice. *Diabetes.* 2006;55(7):2153-2156.

Frezza C, Cipolat S, Martins de Brito O *et al.* OPA1 controls apoptotic cristae remodeling independently from mitochondrial fusion. *Cell.* 2006;126:177–189.

Funalot B, Reynier P, Vighetto A *et al.* A Leigh-like mitochondrial encephalopathy complicating leber's Hereditary Optic Neuropathy. *Ann Neurol.* 2002;52:374-377.

Garcin R. Sur une affection heredo-familiale associant catarate, atrophie optique, signes extra-pyramidaux et certains stigmates de la maladie de Friedreich. (Sa position nosologique par rapport au syndrome de Behr, au syndrome de Marinesco-Sjogren et a la maladie de Friedreich avec signes oculaires.). *Rev Neurol.* 1961;104:373-379.

Gerschenson FE and Rotello RJ. Apoptosis: a different type of cell death. *The FASEB Journal.* 1992; 6:2450-2455.

Ghelli A, Zanna C, Porcelli AM *et al.* Leber's hereditary optic neuropathy (LHON) pathogenic mutations induce mitochondrial-dependent apoptosis death in transmitochondrial cells incubated with galactose medium. *J Biol Chem.* 2002;278:4145–4150.

Gibson KM. Multiple Syndromes of 3-methylglutaconic aciduria. *Pediatr Neurol.* 1993;9:120-123.

Gilman S, Bloedel JR, Lechtenberg R. Disorders of the Cerebellum. (F. A. Davis Company, Philadelphia, PA) 1981.

Gimenez E and Montoliu L. A simple polymerase chain reaction assay for genotyping the retinal degeneration mutation (Pdeb(rd1)) in FVB/N-derived transgenic mice. *Lab Animal.* 2000;35:153-156.

Gish W and States DJ. Identification of protein coding regions by database similarity search. *Nat Genet.* 1993;3:266–272.

Golozoubova V, Cannon B and Nedergaard J. UCP1 is essential for adaptive adrenergic nonshivering thermogenesis. *Am J Physiol Endocrinol Metab.* 2006;291:E350–E357.

Grafstein B. Axonal transport: function and mechanisms. The Axon: structure function and pathophysiology. Oxford University Press. 1995;185-199.

Gray H .(1825–1861). Anatomy of the Human Body. 1918.

Greenlund LJS, Korsmeyer SJ and Johnson EM Jr. Role of Bcl-2 in the survival and function of developing and mature sympathetic neurons. *Neuron.*1995;14:303–315.

Griffith JF, Yeung DK, Antonio GE *et al.* Vertebral marrow fat content and diffusion and perfusion indexes in women with varying bone density: MR evaluation. *Radiology.* 2006;241:831–838.

Grunewald T and Beal MF. Bioenergetics in Huntington's disease. *Ann N Y Acad Sci.* 1999;893:203–213.

Guarente L. Mitochondria—a nexus for aging, calorie restriction, and sirtuins? *Cell.* 2008;132:171–176.

Gumucio D, Shelton D, Zhu W *et al.* Evolutionary strategies for the elucidation of cis and trans factors that regulate the developmental switching programs of the β-like globin genes. *Mol Phylogenet and Evol.* 1996;5:18-32.

Gunay-Aygun M. 3-Methylglutaconic aciduria: a common biochemical marker in various syndromes with diverse clinical features. *Mol Genet Metab.* 2005;84:1-3.

Hardison R, Slightom JL, Gumucio DL *et al.* Locus control regions of mammalian β-globin gene clusters: Combining phylogenetic analyses and experimental results to gain functional insights. *Gene.* 1997;205:73-94.

Harvey RJ, de'Sperati C and Strata P. The early phase of horizontal optokinetic responses in the pigmented rat and the effects of lesions of the visual cortex. *Vision Res.* 1997;37:1615–1625.

Hatori M, Le H, Vollmers C *et al.* Inducible Ablation of Melanopsin-Expressing Retinal Ganglion Cells Reveals Their Central Role in Non-Image Forming Visual Responses. *PLoS ONE.* 2008;3:e2451.

Hattar S, Kumar M, Park A *et al.* Central projections of melanopsin-expressing retinal ganglion cells in the mouse. *J Comp Neurol.* 2006;497:326–349.

Hattar S, Liao HW, Takao M *et al.* Melanopsin-containing retinal ganglion cells: architecture, projections, and intrinsic photosensitivity. *Science.* 2002;295:1065-1070.

Hattar S, Lucas RJ, Mrosovsky N *et al.* Melanopsin and rod-cone photoreceptive systems account for all major accessory visual functions in mice. *Nature.* 2003;424:76-81.

Havre P. Quantitation of pathways of ethanol metabolism. *Arch Biochem Biophys.* 1977;182:14-23.

Ho G, Walter JH and Christodoulou J. Costeff optic atrophy syndrome: New clinical case and novel molecular findings. *J Inherit Metab.* 2008.

Hobbelen J and Collewijn H. Effect of cerebro cortical and collicular ablations upon the optokinetic reactions in the rabbit. *Documenta Ophthalmologica.* 1971;30:227–236.

Hofmann S, Philbrook C, Gerbitz KD *et al.* Wolfram syndrome: structural and functional analyses of mutant and wild-type wolframin, the WFS1 gene product. *Hum Mol Genet.* 2003;12:2003-2012.

Hollander H, Makarov F, Stefani FH *et al.* Evidence of constriction of optic nerve axons at the lamina cribrosa in the normotensive eye in humans and other mammals. *Ophthalmic Res.* 1995;27:296-309.

Hollenbeck PJ. The pattern and mechanisms of mitochondrial transport in axons. *Front Biosci.* 1996;1:d91-d102.

Holloway GP, Bonen A and Spriet LL. Regulation of skeletal muscle mitochondrial fatty acid metabolism in lean and obese individuals. *Am J Clin Nutr.* 2009;89:455S-462S.

Hsu CD, Whaley MA, Frazer K *et al.* Limited role of developmental programmed cell death pathways in Drosophila norpA retinal degeneration. *J Neurosci.* 2004;24:500-507.

Huang TT, Naeemuddin M, Elchuri S *et al.* Genetic modifiers of the phenotype of mice deficient in mitochondrial superoxide dismutase. *Hum Mol Genet.* 2006;15(7):1187-1194.

Huizing M, Dorward H, Ly L, Klootwijk E et al. OPA3, mutated in 3-methylgluaconic aciduria type III, encodes two transcripts targeted primarily to mitochondria. *Mol Genet Metab.* 2010;100(2):149-154.

Huxlin KR and Goodchild AK. Retinal ganglion cells in the albino rat: Revised morphological classification. *J Comp Neurol.* 1997;385:309-323.

Ibel H, Endres W, Hadorn HB *et al.* Multiple respiratory chain abnormalities associated with hypertrophic cardiomyopathy and 3-methylglutaconic aciduria. *Eur J Pediatr.* 1993;152:665-670.

Ijlst L, Loupaty FJ, Ruiter JPN *et al.* 3-Methylglutaconic aciduria type I is caused by mutations in AUH. *Am J Hum Genet.* 2002;71:1463-1466.

Ishihara N, Fujita Y, Oka T *et al.* Regulation of mitochondrial morphology through proteolytic cleavage of OPA1. *EMBO J.* 2006;25:2966–2977.

Jimenez M, Barbatelli G, Allevi R *et al.* Beta 3-adrenoceptor knockout in C57BL/6J mice depresses the occurrence of brown adipocytes in white fat. *Eur J Biochem.* 2003;270:699-705.

Jones BJ and Roberts DJ. The quantiative measurement of motor in co-ordination in naive mice using an acelerating rotarod. *J Pharm Pharmacol.* 1968;20:302-304.

Jubrias SA, Vollestad NK, Gronka RK *et al.* Contraction coupling efficiency of human first dorsal interosseous muscle. *J Physiol.* 2008;586:1993–2002.

Jun AS, Brown MD and Wallace DC. Mitochondrial DNA mutation at nucleotide pair 14459 of the NADH dehydrogenase subunit 6 gene associated with maternally inherited Leber hereditary optic neuropathy and dystonia. *Proc Natl Acad Sci USA.* 1994;9:6206-6210.

Kates M. *Techniques of Lipidology: Isolation, Analysis and Identification of Lipids* (Burdon, R. H. and Van Knippenberg, P. M., eds.), Elsevier Science, Amsterdam, 1986, p. 242.

Katic M, Kennedy AR, Leykin I *et al.* Mitochondrial gene expression and increased oxidative metabolism: role in increased lifespan of fat-specific insulin receptor knock-out mice. *Aging Cell.* 2007;6:827–839.

Katz BJ, Zhao Y, Warner JE *et al.* A family with X-linked optic atrophy linked to the OPA2 locus Xp11.4-Xp11.2. *Am J Hum Genet.* 2006;140A:2207-2211.

Kaufman MH. 1994. The Atlas of Mouse Development. Academic Press, London, UK.

Kaushik S. Neuroprotection in glaucoma. *JPGM.* 2003;49:90-95.

Keeler CE. Iris movements in blind mice. *Am J Physiol.* 1927;81:107-112.

Kelly RI and Kratz L. 3-methylglutaconic aciduria in Smith-Lemli-Optiz syndrome. *Pediatr Res.* 1995;37:671-674.

Kissebah AH and Krakower GR. Regional adiposity and morbidity. *Physiol Rev.* 1994;74:761–811.

Kjer B, Eiberg H, Kjer P *et al.* Dominant optic atrophy mapped to chromosome 3q region II. *Acta Ophthalmol Scand.* 1996;74:3-7.

Kjer P. Infantile optic atrophy with dominant mode of inheritance: A clinical and genetic study of 19 Danish families. *Acta Ophthalmol Scand.* 1959;37:1-146.

Kleta R, Skovby F, Christensen E *et al.* 3-Methylglutaconic aciduria type III in a non-Iraqi-Jewish kindred: clinical and molecular findings. *Mol Genet Metab.* 2002;76:201-206.

Klingenspor M. Cold-induced recruitment of brown adipose tissue thermogenesis. *Exp Physiol.* 2003;88:141-148.

Kobzik L. Nitric oxide in skeletal muscle. *Nature.* 1994;372:546-548.

Kodadek T. Mechanistic parallels between DNA replication, recombination and transcription. *Trends Biochem Sci.* 1998;23.

Kong JH, Fish DR, Rockhill RL *et al.* Diversity of ganglion cells in the mouse retina: unsupervised morphological classification and its limits. *J Comp Neurol.* 2005;489:293–310.

Lalonde R and Strazielle C. Motor performance of spontaneous murine mutations with cerebellar atrophy. Handbook of Molecular-Genetic Techniques for Brain and Behavior Research. 1999;Elsevier, Amsterdam 627–637.

Lalonde R and Strazielle C. Motor Coordination, Exploration, and Spatial Learning in a Natural Mouse Mutation (nervous) with Purkinje Cell Degeneration. *Behav Genet.*2003;33:59-66.

Lalonde R, Dubois M, Strazielle C *et al.* Motor coordination and spatial orientation are affected by neurofilament maldistribution: correlations with regional brain activity of cytochrome oxidase. *Exp Brain Res.* 1999;126:223-234.

Lalonde R, Eyerc J, Wunderle V *et al.* Characterization of NFH-LacZ transgenic mice with the SHIRPA primary screening battery and tests of motor coordination, exploratory activity, and spatial learning. *Behav Processes.* 2003;63:9-19.

Larkin MA, Blackshields G, Brown NP *et al.* Clustal W and Clustal X version 2.0. *Bioinformatics.* 2007;23(21):2947-2948.

Lawrence JM, Sauvé Y, Keegan DJ *et al.* Schwann cell grafting into the retina of the dystrophic RCS rats limits functional deterioration. *Invest Ophthalmol Vis Sci.* 2000;41:518-528.

Leber T. Albrecht v. Graefes Arch. Ophthal. 1871;17:Abt., 249.

Li N. Mitochondrial complex I inhibitor rotenone induces apoptosis through enhancing mitochondrial reactive oxygen species production. *J Biol Chem.* 2003;278:8516-8525.

Li Z and Milam A. Degenerative diseases of the retina. New York: Plenum, 1995.

Lin J, Handschin C and Spiegelman BM. Metabolic control through the PGC-1 family of transcription coactivators. *Cell Metab.* 2005;1:361-370.

Lin MT and Beal MF. Mitochondrial dysfunction and oxidative stress in neurodegenerative diseases. *Nature.* 2006;443:787-795.

Linding R, Jensen LJ, Diella F *et al.* Protein disorder prediction: implications for structural proteomics. *Structure.* 2003a;11:1453-1459.

Linding R, Russell RB, Neduva V *et al.* GlobPlot: exploring protein sequences for globularity and disorder. *Nucleic Acids Res.* 2003b;31:3701–3708.

Loots GG, Locksley RM, Blankespoor CM *et al.* Identification of a coordinate regulator of interleukins 4, 13, and 5 by cross-species sequence comparisons. *Science.* 2000;288:136-140.

Lucas RJ. Characterization of an ocular photopigment capable of driving pupillary constriction in mice. *Nat Neurosci.* 2001;4:621-626.

Lucas RJ and Foster RG. Photoentrainment in Mammals: A Role for Cryptochrome? *J Biol Rhythms.* 1999;14:4-10.

Lucas RJ, Hattar S, Takao M *et al.* Diminished pupillary light reflex at high irradiances in melanopsin-knockout mice. *Science.* 2003;299:245-247.

Lund RD, Kwan ASL, Keegan DJ *et al.* Cell transplantation as a treatment for retinal disease. *Prog Retin Eye Res.* 2001a;20:415-449.

Lund RD, Adamson P, Sauvé Y *et al.* Subretinal transplantation of genetically modified human cell lines attenuates loss of visual function in dystrophic rats. *Proc Natl Acad Sci USA.* 2001b;98:9942-9947.

Lysen JC and Oliver AP. Four generations of blindness. *Bull Dight Inst.* 1947;5: 20-25.

Mårin P, Lönn L, Andersson B *et al.* Assimilation of triglycerides in subcutaneous and intraabdominal adipose tissues in vivo in men: Effects of testosterone. *J Clin Endocrinol Metab.* 1996;81:1018–1022.

Marques SA, Taffarel M and Blanco AM. Participation of neurofilament proteins in axonal dark degeneration of rat's optic nerves. *Brain Res.* 2003;969:1-13.

Masland RH. The fundamental plan of the retina. *Nat Neurosci.* 2004;4:877–886.

Masland RH and Raviola E. Confronting complexity: strategies for understanding the microcircuitry of the retina. *Annu Rev Neurosci.*2000;23:249–284.

Masson P. Some histological methods. Trichrome stainings and their preliminary technique. *Bull Int Assoc Med* 12: 75, 1929.

Matys V, Fricke E, Geffers R *et al.* TRANSFAC: transcriptional regulation, from patterns to profiles. *Nucleic Acids Res.* 2003;31:374–378.

McFadyen MP , Kusek G, Bolivar VJ *et al.* Differences among eight inbred strains of mice in motor ability and motor learning on a rotorod. *Genes Brain Behav.* 2003;12:214-219.

Miklyaeva EI, Martens DJ and Whishaw IQ. Impairments and compensatory adjustments in spontaneous movement after unilateral dopamine depletion in rats. *Brain Res.* 1995;681:23-40.

Miller MP and Kumar S. Understanding human disease mutations through the use of interspecific genetic variation. *Hum Mol Genet.* 2001;10:2319–2328.

Miller WH Jr and Faust IM. Alterations in rat adipose tissue morphology induced by a low-temperature environment. *Am J Physiol.* 1982;242:E93–E96.

Minckler DS, McLean IW and Tso MO. Distribution of axonal and glial elements in the rhesus optic nerve head studied by electron microscopy. *Am J Ophthalmol.* 1976;82:179-187.

Moitra J, Mason MM, Olive M *et al.* Life without white fat: a transgenic mouse. *Genes Dev.* 1998;12:3168–3181.

Montague CT, Prins JB, Sanders L *et al.* Depot-related gene expression in human subcutaneous and omental adipocytes. *Diabetes.* 1998;47:1384–1391.

Mooney SD and Klein TE. The functional importance of disease-associated mutation. *BMC Bioinformatics.* 2002;3:24-28.

Morin C and Nicolas S. Mitochondria: a target for the neuroprotective interventions of cerebral ischemia-reperfusion. *Curr Pharm Design.* 2006;12:1-19.

Mrosovsky N and Hattar S. Impaired masking responses to light in melanopsin-knockout mice. *Chronobiol Int.* 2003;20:989–999.

Mrosovsky N, Lucas RJ and Foster RG. Persistence of masking responses to light in mice lacking rods and cones. *J Biol Rhythms.* 2001;16:585–588.

Murano I, Zingaretti CM and Cinti S. The adipose organ of Sv129 mice contains a prevalence of brown adipocytes and shows plasticity after cold exposure. *Adipocytes.* 2005;1:121-130.

Naskar R and Dreyer E. New Horizons in neuroprotection. *Surv Ophthalmol.* 2001;45:S250-S255.

Neas K, Bennetts B, Carpenter K *et al.* OPA3 mutation screening in patients with unexplained 3-methylglutaconic aciduria. *J Inherit Metab Dis.* 2005;28:525-532.

Nedergaard J, Bengtsson T and Cannon B. Unexpected evidence for active brown adipose tissue in adult humans. *Am J Physiol Endocrinol Metab.* 2007;293:E444–E452.

Newman NJ. Hereditary optic neuropathies: from the mitochondria to the optic nerve. *Am J Ophthalmol.* 2005;140:517-523.

Newman NJ: Hereditary optic neuropathies, Miller NR, Newman NJ (eds). Walsh & Hoyt Clinical Neuro-Ophthalmology Williams & Wilkins, Baltimore1999, pp. 741–773.

Niesler CU, Prins JB, O'Rahilly S *et al.* Adipose depot-specific expression of cIAP2 in human preadipocytes and modulation of expression by serum factors and TNFalpha. *Int J Obes Relat Metab Disord.* 2001;25:1027–1033.

Nystuen A, Costeff H, Elpeleg ON *et al.* Iraqi-Jewish kindreds with optic atrophy plus (3-methylglutaconic aciduria type 3) demonstrate linkage disequilibrium with the CTG repeat in the 3-prime untranslated region of the myotonic dystrophy pretein kinase gene. *Hum Molec Genet.* 1997;6:563-569.

Olichon A, Landes T, Arnaune-Pelloquin L *et al.* Effects of OPA1 mutations on mitochondrial morphology and apoptosis: relevance to ADOA pathogenesis. *J Cell Physiol.* 2007;211:423–430.

Olichon A, Baricault L, Gas N *et al.* Loss of OPA1 perturbates the mitochondrial inner membrane structure and integrity, leading to cytochrome c release and apoptosis. *J Biol Chem.* 2003;278:7743–7746.

Olichon A, Emorine LJ, Descoins E *et al.*The human dynamin-related protein OPA1 is anchored to the mitochondrial inner membrane facing the inter-membrane space. *FEBS Lett.* 2002;523:171-176.

Osborne NN, Lascaratos G, Bron AJ *et al.* A hypothesis to suggest that light is a risk factor in glaucoma and the mitochondrial optic neuropathies. *Br J Ophthalmol.* 2006;90:237–241.

Osman AA, Saito M, Makepeace C *et al.* Wolframin expression induces novel ion channel activity in endoplasmic reticulum membranes and increases intracellular calcium. *J Biol Chem.* 2003;278:52755-52762.

Ovcharenko I, Loots GG, Giardine BM. Mulan: Multiple-sequence local alignment and visualization for studying function and evolution. *Genome. Res.* 2005;15.

Panda S, Sato TK, Castrucci AM *et al.* Melanopsin (Opn4) requirement for normal light-induced circadian phase shifting. *Science.* 2002;298:2213-2216.

Parks EJ and Hellerstein MK. Recent advances in liver triacylglycerol and fatty acid metabolism using stable isotope labeling techniques. *J Lipid Res.* 2006;47(8):1651-1660.

Pequignot MO, Provost AC, Salle S *et al.* Major role of BAX in apoptosis during retinal development and in establishment of a functional postnatal retina. *Dev Dyn.* 2003; 228(2):231-238.

Pei W, Bernardini I, Wassif C *et al.* Seeking the biochemical basis of type III 3-methylglutaconic aciduria through zebrafish models. *Dev Biol.* 2008;319:562.

Pei W, Kratz LE, Bernardini I *et al.* A model of Costeff Syndrome reveals metabolic and protective functions of mitochondrial OPA3. *Development.* 2010;137(15):2587-96

Peichl L. Alpha ganglion cells in mammalian retinae: common properties, species differences, and some comments on other ganglion cells. *Vis Neuroscie.* 1991;7:155-169.

Penfold PL and Provis JM. Cell death in the development of the human retina. *Graefes Arch. Clin. Exp. Ophthalmol.* 1986; 224:549–553.

Pennacchio LA and Rubin EM. Genomic strategies to identify mammalian regulatory sequences. *Nature Rev Genet.* 2001;2:100-109.

Perry VH. Evidence for an amacrine cell system in the ganglion cell layer of the rat retina. *Neuroscience.* 1981;6:931–944.

Pinto LH and Enroth-Cugell C. Tests of the mouse visual system. *Mamm Genome.* 2000;11:531-536.

Podhorna J and Brown RE. Strain differences in activity and emotionality do not account for differences in learning and memory performance between C57BL/6 and DBA/2 mice. *Genes Brain Behav.* 2002;1:96-110.

Polyak SL. The Retina. The University of Chicargo Press. 1941.

Porcelli AM, Angelin A, Ghelli A *et al.* Respiratory complex I dysfunction due to mitochondrial DNA mutations shifts the voltage threshold for opening of the permeability transition pore toward resting levels. *J Biol Chem.* 2009;284:2045–2052.

Postic C and Girard J. Contribution of de novo fatty acid synthesis to hepatic steatosis and insulin resistance: lessons from genetically engineered mice *J Clin Invest.* 2008;118(3): 829-838.

Provencio I, Cooper HM and Foster RG. Retinal projections in mice with inherited retinal degeneration: implications for circadian photoentrainment. *J Comp Neurol.* 1998;395:417-439.

Provencio I, Rollag MD and Castrucci AM. Photoreceptive net in the mammalian retina. *Nature.* 2002;415:493.

Prusky GT, Alam NM, Beekman S *et al.* Rapid quantification of adult and developing mouse spatial vision using a virtual optomotor system. *Invest Ophthalmol Vis Sci.* 2004;45:4611-4616.

Qiao X. Photoreceptor degeneration and rd1 mutation in the grizzled/mocha mouse strain. *Vis Res.* 2003;43:859-865.

Quandt K, Frech K, Karas H *et al.* Matlnd and Matlnspector: new fast and versatile tools for detection of consensus matches in nucleotide sequence data. *Nucleic Acids Res.* 1995;23:4878-4884.

Quigley HA, Nickells RW, Kerrigan LA *et al.* Retinal ganglion cell death in experimental glaucoma and after axotomy occurs by apoptosis. *Invest Ophthalmol Vis Sci.*1995;36:774-786.

Rall JA and Woledge RC. Influence of temperature on mechanics and energetics of muscle contraction. *Am J Physiol Regul Integr Comp Physiol.* 1990;259:R197–R203.

Reimold AM, Grusby MJ, Kosaras B *et al.* Chondrodysplasia and neurological abnormalities in ATF-2-deficient mice. *Nature.* 1996;379:262.

Reynier P, Amati-Bonneau P, Verny C *et al.* OPA3 gene mutations responsible for autosomal dominant optic atrophy and cataract. *J Med Genet.* 2004;41.

Rogers DC, Fisher EM, Brown SD *et al.* Behavioral and functional analysis of mouse phenotype: SHIRPA, a proposed protocol for comprehensive phenotype assessment. *Mamm Genome.* 1997;8:711-713.

Romero P, Obradovic Z, Kissinger CR *et al.* Identifying Disordered Regions in Proteins from Amino Acid Sequences. *Proc. I.E.E.E. International Conference on Neural Networks.* 1997;90-95.

Rosen ED and Spiegelman BM. PPARgamma: a nuclear regulator of metabolism, differentiation, and cell growth. *J Biol Chem.* 2001;276:37731-37734.

Rosen ED and Spiegelman BM. Adipocytes as regulators of energy balance and glucose homeostasis. *Nature.* 2006;444:847–853.

Rosenberg RN and Chutorian A. Familial opticoacoustic nerve degeneration and polyneuropathy. *Neurology.* 1967;17(9):827.

Ruby NF, Brennan TJ, Xie X *et al.* Role of melanopsin in circadian responses to light. *Science.* 2002;298:2211–2213.

Ruesch S, Krähenbühl S, Kleinle S *et al.* Combined 3-methylglutaconic and 3-hydroxy-3-methylglutaric aciduria with endocardial fibroelastosis and dilatative cardiomyopathy in male and female siblings with partial deficiency of complex II/III in fibroblasts. *Enzyme Protein.* 1996;49:321-329.

Ryu SW, Jeong HJ, Choi M *et al.* Optic atrophy 3 as a protein of the mitochondrial outer membrane induces mitochondrial fragmentation. *Cell Mol Life Sci.* 2010 Apr 8

Sadun AA. Acquired mitochondrial impairment as a cause of optic nerve disease. *Trans Am Ophthalmol Soc.* 1998;46.

Sadun AA, Win PH, Ross-Cisneros FN *et al.* Leber's hereditary optic neuropathy differentially affects smaller axons in the optic nerve. *Trans Am Ophthalmol Soc.* 2000;98:223-232.

Sandelin A. Prediction of regulatory elements. *Methods Mol Biol.* 2008;453:233-244.

Schweers BA and Dyer MA. Perspective: New genetic tools for studying retinal development and disease. *Vis Neurosci.* 2005;22(5):553-560.

Schmucker C. Grating acuity at different luminances in wild-type mice and in mice lacking rod and cone function. *Invest Ophthalmol Vis Sci.* 2005;46.

Selby CP, Thompson C, Schmitz TM *et al.* Functional redundancy of cryptochromes and classical photoreceptors for nonvisual ocular photoreception in mice. *Proc Natl Acad Sci USA.* 2000;97:14697-14702.

Shen B and Vihinen M. Conservation and covariance in PH domain sequences: physicochemical profile and information theoretical analysis of XLA-causing mutations in the Btk PH domain. *Protein Eng Des Sel.* 2004;17:267-276.

Shi Y and Burn P. Lipid metabolic enzymes: emerging drug targets for the treatment of obesity. *Nat Rev Drug Discov.* 2004;3:695-710.

Shimomura I, Hammer RE, Richardson JA *et al.* Insulin resistance and diabetes mellitus in transgenic mice expressing nuclear SREBP-1c in adipose tissue: model for congenital generalized lipodystrophy. *Genes Dev.* 1998;12:3182–3194.

Shoji Y, Takahashi T, SawaishiY *et al.* 3-Methylglutaconic aciduria type I: clinical heterogeneity as a neurometabolic disease. *J Inherit Metab Dis.* 1999;22:1-8.

Siegel GJ, Wayne Albers R, Brady S *et al.* Basic Neurochemistry: Molecular, Cellular and Medical Aspects. Elsevier Academic Press. 2006.

Simon D, Seznec H, Gansmuller A *et al.* Friedreich Ataxia Mouse Models with Progressive Cerebellar and Sensory Ataxia Reveal Autophagic Neurodegeneration in Dorsal Root Ganglia. *J Neurosci.* 2004;24:1987-1995.

Smith RS. Systematic Evaluation of the Mouse Eye: Anatomy, Pathology, and Biomethods (Research Methods for Mutant Mice Series). 2002.

Sohocki MM, Perrault I, Leroy BP *et al.* Prevalence of AIPL1 mutations in inherited retinal degenerative disease. *Mol Genet Metab.* 2000;70(2):142-150.

Stormo GD. DNA binding sites: representation and discovery. *Bioinformatics.* 2000;16:16–23.

Suen DF, Norris KL and Youle RJ. Mitochondrial dynamics and apoptosis. *Gene Dev.* 2008;22:1577–1590.

Sugarman MC, Yamasaki TR, Oddo S *et al.* Inclusion body myositis-like phenotype induced by transgenic overexpression of βAPP in skeletal muscle. *Proc Natl Acad Sci.* 2002;99:6334–6339.

Sun W, Li N and He S. Large-scale morphological survey of mouse retinal ganglion cells. *J Comp Neurol.* 2002a;451:115-126.

Sun, W, Li N and He S. Large-scale morphological survey of rat retinal ganglion cells. *Vis Neurosci.* 2002b;19:483-493.

Sunyaev S, Ramensky V, Koch I *et al.* Prediction of deleterious human alleles. *Hum Mol Gen.* 2001;10:591-597.

Susin SA, Zamzami N, Castedo M *et al.* Bcl-2 inhibits the mitochondrial release of an apoptogenic protease. *J Exp Med.* 1996;184:1331–1341.

Sweetman L and Williams JC: Branched chain organic acidurias. In: C.R. Scriver, ALB, W.S. Sly and D. Valle (Ed.), The Metabolic and Molecular Bases of Inherited Disease. McGraw-Hill, New York, 2001, pp. 2340-2342.

Takeda K, Inoue H, Tanizawa Y *et al.* WFS1 (Wolfram syndrome 1) gene product: predominant subcellular localization to endoplasmic reticulum in cultured cells and neuronal expression in rat brain. *Hum Mol Genet.* 2001;10:477-484.

Tang QQ, Jiang MS and Lane MD. Repressive effect of Sp1 on the C/EBPα gene promoter: role in adipocyte differentiation. *Mol Cell Biol.* 1999;19:4855-4865.

Taylor MD, Vancura R, Williams JM *et al.* Overexpression of neurotrophin-3 in skeletal muscle alters normal and injury-induced limb control, Somatosens. *Mot Res.* 2001;18:286–294.

Tempestini A, Schiavone N, Papucci L *et al.* The mechanisms of apoptosis in biology and medicine: a new focus for opthamology. *Eur J Opthamology.* 2003;13:S11-18.

Tezel G and Yang X. Caspase-Independent Component of Retinal Ganglion Cell Death, In Vitro. *Invest Ophthalmol Vis Sci.* 2004;45:4049-4059.

Thiselton D, Alexander C, Taanman JW *et al.* A comprehensive survey of mutations in the OPA1 gene in patients with autosomal dominant optic atrophy. *Invest Ophthalmol Vis Sci.* 2002;43:1715-1724.

Timmons JA, Wennmalm K, Larsson O *et al.* Myogenic gene expression signature establishes that brown and white adipocytes originate from distinct cell lineages. *Proc Natl Acad Sci U S A.* 2007;104:4401–4406.

Toomes C, Marchbank NJ, Mackey DA *et al.* Spectrum, frequency and penetrance of OPA1 mutations in dominant optic atrophy. *Hum Mol Genet.* 2001;10:1369-1378.

Trullas.R and Skolnick.P. Differences in fear motivated behaviours among inbred mouse strains. *Psychopharmacology.* 1993;111:323-331.

Tsukiyama-Kohara K, Poulin F, Kohara M *et al.* Adipose tissue reduction in mice lacking the translational inhibitor 4E-BP1. *Nat. Med.* 2001;7:1128–1132.

Virtanen KA, Lidell ME, Orava J *et al.* Functional brown adipose tissue in healthy adults. *N Engl J Med.* 2009;360:1518–1525.

Volker-Dieben HJ, Van Lith GHM, Went LN *et al.* A family with sex linked optic atrophy (ophthalmological and neurological aspects). *Docum Ophthal.* 1974;37(2): 307-326.

Votruba M. Clinical features, molecular genetics and pathophysiology of dominant optic atrophy. *J Med Genet.* 1998;35:793-800.

Wallace DC, Singh G, Lott MT *et al.* Mitochondrial DNA mutation associated with Leber's hereditary optic neuropathy. *Science.* 1988;242:1427–1430.

Walsh R, Conway H, Roche G *et al.* "What is the origin of 3-methylglutaconic acid?" *J Inher Metab Dis.* 1999;22:251-155.

Walsh RN and Cummins RA. The open field test: A critical review. *Psychol Bull.* 1976;83:482-504.

Wanders R. Mitochondrial oxidative phosphorylation in fibroblasts from 3-methylglutaconic aciduria patients. Paper presented at the annual meeting of the society for the study of inborn errors of metabolism. 1992;Sept 10-12.

Wang AG, Fann MJ, Yu HY *et al.* OPA1 expression in the human retina and optic nerve. *Exp Eye Res.* 2006;83:1171-1178.

Waxman SG. Prerequisites for conduction in demyelinated fibres. *Neurology.* 1978;28:27-33.

Weisstaub NV, Zhou M, Lira A *et al.* Cortical 5-HT2A Receptor Signaling Modulates Anxiety-Like Behaviors in Mice. *Science.* 2006;313:536-540.

Went LN, De Vries de Mol EC and Volker-Dieben HJ. A family with apparently sex-linked optic atrophy. *J Med Genet.* 1975;12: 94-98.

Weydt P, Pineda VV, Torrence AE *et al.* Thermoregulatory and metabolic defects in Huntington's disease transgenic mice implicate PGC-1α in Huntington's disease neurodegeneration. *Cell Metab.* 2006;4:349-362.

Williams RR, Cusato K, Raven MA *et al.* Organization of the inner retina following early ganglion cell elimination of the retinal ganglion cell population: effects on cell numbers and stratification patterns. *Vis Neurosci.* 2001;18:233–244.

Wingender E, Dietze P, Karas H *et al.* TRANSFAC: A database on transcription factors and their DNA binding sites. *Nucleic Acids Res.* 1996;24:238–241.

Wong A, Cavelier L, Collins-Schramm HE *et al.* Differentiation-specific effects of LHON mutations introduced into neuronal NT2 cells. *Hum Mol Genet.* 2002;11:431–438.

Wortmann S, Rodenburg RJ, Huizing M *et al.* Association of 3-methylglutaconic aciduria with sensori-neural deafness, encephalopathy, and Leigh-like syndrome (MEGDEL association) in four patients with a disorder of the oxidative phosphorylation. *Mol Genet Metab.* 2006;88:47-52.

Wride N, Habib M, Morris K *et al.* Clinical evaluation of a rapid, pupil-based assessment of retinal damage associated with glaucoma. *Clin Ophthalmol.* 2009;3:123-128.

Wyllie AH, Kerr JFR and Cutuue AR. Cell death: the significance of apoptosis. *Int Rev Cytol.* 1980;68:251-306.

Yamasaki E, Andrade de Costa B, Barbosa VD *et al.* Retinal ganglion depletion alters the phenotypic expression of GABA and GAD in the rat retina. *Eur J Neurosci.* 1997;9:1885-1890.

Yoshida T, Umekawa T, Kumamoto K *et al.* Beta 3-Adrenergic agonist induces a functionally active uncoupling protein in fat and slow-twitch muscle fibers. *Am J Physiol.* 1998;274:E469–475.

Youle RJ and Karbowski M. Mitochondrial fission in apoptosis. *Nat Rev Mol Cell Biol.* 2005;6(8):657-663.

Young WR. Cell death during differentiation of the retina in the mouse. *J Comp Neurol.* 1984;229:362–373.

Yu DY and Cringle SJ. Oxygen distribution and consumption within the retina in vascularised and avascular retinas and in animal models of retinal disease. *Prog Retin Eye Res.* 2001;20:175-208.

Yue P, Melamud E and Moult J. SNPs3D: candidate gene and SNP selection for association studies. *BMC Bioinformatics.* 2006;7:166-180.

Yu-Wai-Man CY, Chinnery PF and Griffiths PG. Optic neuropathies – Importance of spatial distribution of mitochondria as well as function. *Med Hypotheses.* 2005;65:1038-1042.

Yu-Wai-Man P, Griffiths PG, Hudson G and Chinnery PF. Inherited mitochondrial optic neuropathies. *J Med Genet.* 2009;46:145-158.

Zanna C, Ghelli A, Porcelli AM *et al.* Caspase-independent death of Leber's hereditary optic neuropathy cybrids is driven by energetic failure and mediated by AIF and endonuclease G. *Apoptosis.* 2005;10:997-1007.

Zanna C, Ghelli A, Porcelli AM *et al.* OPA1 mutations associated with dominant optic atrophy impair oxidative phosphorylation and mitochondrial fusion. *Brain.* 2008;131:352-367.

Zhang W, Klemm DJ, Vinson C *et al.* Role of CREB in transcriptional regulation of CCAAT/enhancer-binding protein gene during adipogenesis. *J Biol Chem.* 2004;279:4471-4478.

Appendix I

1) Chemicals and enzymes

3,3 diaminobenzidine tetrachloride (Sigma-Aldrich)
Acetic acid (Fisher Solutions, UK)
Agarose molecular biology grade (Sigma-Aldrich)
Alcian blue 8GX (Sigma-Aldrich)
Alizarin red S (Sigma-Aldrich)
Biomix red (Bioline)
Buffered formal saline
Catalase (Sigma-Aldrich)
Cytochrome c (Sigma-Aldrich)
DirectPCR Lysis Reagent (Viagen)
DNA Hyperladder IV (Bioline)
dNTPs (Bioline)
DPX permanent medium (BDH, England)
Ethanol (Fisher Solutions, UK)
Ethidium Bromide (Fisher Solutions, UK)
Eosin (Surgipath)
Formaldehyde (Sigma-Aldrich)
Glycerol (Merck)
Hydrochloric acid (Fisher Solutions, UK)
Hoechst (Invitrogen)
Isopentane (Fisher Solutions, UK)
Isopropanol (Merck)
Mayer haematoxylin (BDH, England)
Neutral buffered formalin
Newborn calf serum (Sigma-Aldrich)
Nitroblue tetrazolium (Sigma-Aldrich)
OCT (ralamb.com)
Oil-red-O (Sigma-Aldrich)
Paraformaldehyde (Sigma-Aldrich)
Phenazine methosulphate (Sigma-Aldrich)
Phosphate buffered saline (PBS) (Sigma-Aldrich)
Proteinase K (Sigma-Aldrich)
Restriction enzyme Pst1 (Promega)
RNAlater (Sigma-Aldrich)
Sodium acetate (Sigma-Aldrich)
Sodium azide (Sigma-Aldrich)
Sodium barbitone (Sigma-Aldrich)
Sodium hydroxide (Sigma-Aldrich)
Sodium succinate (Sigma-Aldrich)
Quick clean (Bioline)
Taq polymerase mastermix (Bioline)
TBE buffer (Sigma-Aldrich)
Toluidine blue powder (Sigma-Aldrich)
Xylene (Fisher Solutions, UK)

2) Kits

ApopTag Plus Fluorescein In Situ Apoptosis Detection Kit TUNEL (Chemicon)
Quantitect Reverse Transcription Kit (Qiagen)
Wizard SV Genomic DNA purification System (Promega)
RNeasy mini kit (Qiagen)

3) Solutions, buffers and media

3, 3 Diaminobenzidine tetrahydrochloride 5mM

Inject 27.77 ml of distilled water into the container of 3,3 Diaminobenzidine tetrahydrochloride. Mix until dissolved. Add 27.77 ml of 0.2M phosphate buffer pH 7.4. Adjust pH to 7.0 with 0.1M hydrochloric acid or 0.1M sodium hydroxide solution. Decant 800µl into 1.5 ml microtubes and make a small hole in the lid. Snap freeze in liquid nitrogen and store at -20°C.

Cytochrome c 500µM

Disolve 62mg of Cytochrome c in 10 ml of 0.1M phosphate buffer. Adjust to pH 7.0.

Nitroblue tetrazolium 1.875mM

Disolve 49mg of Nitorblue tetrazolium in 32 ml of 0.1M phosphate buffer. Adjust to pH 7.0. Decant 800µl into 1.5ml microtubes and store at -20°C.

Oil red-O solution

Stock solution:-
Dissolve 0.5g of Oil red-O in 200 ml of isopropyl alcohol. Warm the solution in a 56°C water bath for 1 hr and allow to cool.

Working solution:-
Prepare on day of use. Add 12 ml stock solution and 8 ml of distilled water. Mix and allow to stand for 10 mins. Filter through a filter cartridge (0.2/0.45um) or a fine filter paper (no 45 Whatman) before use.

Sodium succinate 1.3M

Disolve 3.5g of sodium succinate in 10 ml of 0.1M phosphate buffer. Adjust to pH 7.0. Decant 250µl into 0.5 ml microtubes and store at -20°C.

PBS

Dissolve 1 tablet of phosphate buffered saline (Sigma P4417) in 200 ml of distilled water. This yields a 0.01M phosphate buffer, 0.0027M potassium chloride and 0.137M sodium chloride, pH 7.4 solution

4% PFA

Measure 4g of parafolmaldehyde into a glass bottle in the fume hood. Add 100 ml of phosphate buffered saline (PBS) into the bottle and mix vigorously. Place in water bath at 65oC for 3-4 hours. Allow the solution to warm up it will turn from cloudy to clear when it is ready. When cooled it can be transferred into smaller vials and placed in the freezer for long term storage.

Phenazine methosulphate 2.0mM

Disolve 3.0634g of phenazine methosulphate in 1L of 0.1M phosphate buffer which gives 10mM phenazine methosulphate. Adjust to pH 7.0. To make 2.0mM phenazine methosulphate take 2ml of 10mM phenazine methosulphate and add to 8ml of 0.1M phosphate buffer.

0.2 M Phosphate buffer pH7.4

Add 21.8g dibasic sodium phosphate (Na_2HPO_4) and 6.4g monobasic sodium phosphate (NaH_2PO_4) to 1000 ml of distilled water. Adjust pH to 7.4.

Perfusion Fix Buffer

Perfusion fix buffer is 4% PFA in 0.1M phosphate buffer which is made up as follows:-Firstly to make up 0.2M phosphate buffer pH 7.4. Add 21.8g dibasic sodium phosphate (Na_2HPO_4) and 6.4g monobasic sodium phosphate (NaH_2PO_4) to 1000 ml of distilled water. In a separate bottle add 40g of paraformaldehyde to 500ml of distilled water. Heat to 60-65°C, solution will turn clear when ready. Then add 500ml of 0.2M phosphate buffer from the first bottle. Allow solution to cool and then filter. Adjust pH to 7.4.

Sodium azide 100mM

Disolve 3.2505g of sodium azide in 500ml of 0.1M phosphate buffer which gives 100mM phenazine methosulphate. Adjust to pH 7.0.

Toluidine Blue Solution

Sodium acetate	1.0 g
Sodium barbitone	1.5 g
Toluidine blue powder	1.5 g
Conc. Hydrochloric acid	1.0 ml
Distilled water	250 ml

Dissolve the sodium acetate and the sodium barbitone in the distilled water. Add the hydrochloric acid and adjust the pH to 5.0 using 10% HCL. Dissolve the Toluidine blue powder in this solution, filter and bottle.

4) Software

ClustalW- www.ebi.ac.uk/clustalw/
DisEmbl- www.dis.embl.de/
Ensembl- www.ensembl.org/
Globplot- www.globplot.embl.de/
MatInspector- http://genomatix.gsf.de/mat_fam;
Mulan- http://mulan.dcode.org/
NCBI- www.ncbi.nlm.nih.gov/
OMIM- www.ncbi.nlm.nih.gov/omim/
PONDR- http://www.pondr.com
PreMod- http://genomequebec.mcgill.ca/PReMod
Primer3input- http://frodo.wi.mit.edu/
Pmut- http://mmb.pcb.ub.es:8080/PMut/
PolyPhen- www.genetics.bwh.harvard.edu/pph/
SCpred- www.enzim.hu/scpred/pred.html
SNP3D- www.snps3d.org/
TANGO- www.tango.crg.es/
TFsearch- http://www.cbrc.jp/research/db/TFSEARCH.html

Appendix II

Sequencing results of murine *Opa3* exons and transcripts

1a) Mouse transcript1-2A Foward

>151008_66948_trans1-2A_trans1-2F
TGGTGGGCGCGTTCCCCATGGCGAAGCTGTTCTACTTGGGCATCCGGCAG
GTTAGCAAGCCGCTGGCCAACCGTATCAAGGATGCTGCCCGCCGCAGCGA
GTTCTTCAAGACCTACATCTGCCTACCGCCAGCCCAGCTGTACCACTGGG
TGGGAGATGCGGACGAAGATGCGCATAATGGGTTTCCGGGGCACTACCAT
CAAGCCACTGAATGAGGAGGCAGCAGCAGAGCTGGGTGCTGAGCTGCTGG
GCGAGGCCACCATCTTCATTGTGGGCGGAGGCTGCCTGGTCCTGGAGTAC
TGGCGCCACCAGACTCAGCAGCGCAATAAGGAGGAGGAACAGCGGGCAGC
CTGGAACGCTCTGCAGGATGAGGTGGGCCGCCTGGCACTGGCCTTAGAGG
CGCTGCAGGCTCAGGCACAAGCGATGCCCTCCTTGAGTGCCCTGGAGGAG
CTGCGGGAGGAGCTGCAGGAGGTGCGTGGTCAGGTCTGCAATGCTCACTG
TACTTCCAAGTGCCAGGCAGCATCTTCCAAGAAATAGCCAGCTGCTAAGG
CCTGGACTTGTTTGTGACCATGTGGCCTCCAATAGAGCCTTCTCCTCACA
CCTCCTGGCCCGGGATGCTCTGGCCTAGCAGAAACCACGAGGACCTTGAT
GTAGCTGTGACATGTGGTCACCCCTTACTGACAGGTTCTGGGCATTTCCC
CAGGGAGCACTCAGCAGAAGCCTTCAGAGCC

1b) Mouse transcript1-2A reverse

>151008_66958_trans1-2A_trans1-2R
CCTGTCAGTAAGGGGTGACCACATGTCACAGCTACATCAAGGTCCTCGTG
GTTTCTGCTAGGCCAGAGCATCCCGGGCCAGGAGGTGTGAGGAGAAGGCT
CTATTGGAGGCCACATGGTCACAAACAAGTCCAGGCCTTAGCAGCTGGCT
ATTTCTTGGAAGATGCTGCCTGGCACTTGGAAGTACAGTGAGCATTGCAG
ACCTGACCACGCACCTCCTGCAGCTCCTCCCGCAGCTCCTCCAGGGCACT
CAAGGAGGGCATCGCTTGTGCCTGAGCCTGCAGCGCCTCTAAGGCCAGTG
CCAGGCGGCCCACCTCATCCTGCAGAGCGTTCCAGGCTGCCCGCTGTTCC
TCCTCCTTATTGCGCTGCTGAGTCTGGTGGCGCCAGTACTCCAGGACCAG
GCAGCCTCCGCCCACAATGAAGATGGTGGCCTCGCCCAGCAGCTCAGCAC
CCAGCTCTGCTGCTGCCTCCTCATTCAGTGGCTTGATGGTAGTGCCCCGG
AAACCCATTATGCGCATCTTCGTCCGCATCTCCACCCAGTGGTACAGCTG
GGCTGGCGGTAGGCAGATGTAGGTCTTGAAGAACTCGCTGCGGCGGGCAG
CATCCTTGATACGGTTGGCCAGCGGCTTGCTAACCTGCCGGATGCCCAAG
TAGAACAGCTTCGCCATGGGGAACGCGCCCACCACCATCTCGGCGGCCGC
CCTGGGGCACGCGCAACCTTGC

2a) mouse transcript 1-2C Foward

>151008_66949_trans1-2C_trans1-2F
TGGTGGGCGCGTTCCCCATGGCGAAGCTGTTCTACTTGGGCATCCGGCAG
GTTAGCAAGCCGCTGGCCAACCGTATCAAGGATGCTGCCCGCCGCAGCGA
GTTCTTCAAGACCTACATCTGCCTACCGCCAGCCCAGCTGTACCACTGGG
TGGGAGATGCGGACGAAGATGCGCATAATGGGTTTCCGGGGCACTACCAT
CAAGCCACTGAATGAGGAGGCAGCAGCAGAGCTGGGTGCTGAGCTGCTGG
GCGAGGCCACCATCTTCATTGTGGGCGGAGGCTGCCTGGTCCTGGAGTAC
TGGCGCCACCAGACTCAGCAGCGCAATAAGGAGGAGGAACAGCGGGCAGC
CTGGAACGCTCTGCAGGATGAGGTGGGCCGCCTGGCACTGGCCTTAGAGG
CGCTGCAGGCTCAGGCACAAGCGATGCCCTCCTTGAGTGCCCTGGAGGAG
CTGCGGGAGGAGCTGCAGGAGGTGCGTGGTCAGGTCTGCAATGCTCACTG
TACTTCCAAGTGCCAGGCAGCATCTTCCAAGAAATAGCCAGCTGCTAAGG
CCTGGACTTGTTTGTGACCATGTGGCCTCCAATAGAGCCTTCTCCTCACA
CCTCCTGGCCCGGGATGCTCTGGCCTAGCAGAAACCACGAGGACCTTGAT
GTAGCTGTGACATGTGGTCACCCCTTACTGACAGGTTCTGGGCATTTCCC
CAGGGAGCACTCAGCAGAAGCCTTCAGAG

2b) Mouse transcript1-2C reverse

>151008_66959_trans1-2C_trans1-2R
ACCTGACCACGCACCTCCTGCAGCTCCTCCCGCAGCTCCTCCAGGGCACT
CAAGGAGGGCATCGCTTGTGCCTGAGCCTGCAGCGCCTCTAAGGCCAGTG
CCAGGCGGCCCACCTCATCCTGCAGAGCGTTCCAGGCTGCCCGCTGTTCC
TCCTCCTTATTGCGCTGCTGAGTCTGGTGGCGCCAGTACTCCAGGACCAG
GCAGCCTCCGCCCACAATGAAGATGGTGGCCTCGCCCAGCAGCTCAGCAC
CCAGCTCTGCTGCTGCCTCCTCATTCAGTGGCTTGATGGTAGTGCCCCGG
AAACCCATTATGCGCATCTTCGTCCGCATCTCCACCCAGTGGGTACAGCT
GGGCTGGCGGTAGGCAGATGTAGGTCTTGAAGAACTCGCTGCGGCGGGCA
GCATCCTTGATACGGTTGGCCAGCGGCTTGCTAACCTGCCGGATGCCCAA
GTAGAACAGCTTCGCCATGGGGAACGCGCCCACCACCATCTCGGCGGCCG
CCCTGGGGCACGCGCAA

3) Mouse exon1 dna sample 1002 foward

>031008a_66383_1002exon1_exon1F
GGGGGAGGACGGCGAGGTCGGCGGCGCCCCGCCCAGTCAGCAAGGTTGCG
CGTGCCCCAGGGCGGCCGCCGAGATGGTGGTGGGCGCGTTCCCCATGGCG
AAGCTGTTCTACTTGGGCATCCGGCAGGTTAGCAAGCCGCTGGCCAACCG
TATCAAGGATGCTGCCCGCCGCAGCGAGTTCTTCAAGACCTACATCTGCC
TACCGCCAGCCCAGCGTGAGTCTCACCCCAAGGCCTCTAGCCCTTCCATT
CCCGATCTTTCTAGTTCAGGGGAACGGA

4a) Mouse exon2 dna sample 1002 foward

>031008a_66387_1002exon2_exon2F
AGATGCGCATAATGGGTTTCCGGGGCACTACCATCAAGCCACTGAATGAG
GAGGCAGCAGCAGAGCTGGGTGCTGAGCTGCTGGGCGAGGCCACCATCTT
CATTGTGGGCGGAGGCTGCCTGGTCCTGGAGTACTGGCGCCACCAGACTC
AGCAGCGCAATAAGGAGGAGGAACAGCGGGCAGCCTGGAACGCTCTGCAG
GATGAGGTGGGCCGCCTGGCACTGGCCTTAGAGGCGCTGCAGGCTCAGGC
ACAAGCGATGCCCTCCTTGAGTGCCCTGGAGGAGCTGCGGGAGGAGCTGC
AGGAGGTGCGTGGTCAGGTCTGCAATGCTCACTGTACTTCCAAGTGCCAG
GCAGCATCTTCCAAGAAATAGCCAGCTGCTAAGGCCTGGACTTGTTTGTG
ACCATGTG

4b) Mouse exon2 dna sample 1002 reverse

>031008a_66388_1002exon2_exon2R
CCTGACCACGCACCTCCTGCAGCTCCTCCCGCAGCTCCTCCAGGGCACTC
AAGGAGGGCATCGCTTGTGCCTGAGCCTGCAGCGCCTCTAAGGCCAGTGC
CAGGCGGCCCACCTCATCCTGCAGAGCGTTCCAGGCTGCCCGCTGTTCCT
CCTCCTTATTGCGCTGCTGAGTCTGGTGGCGCCAGTACTCCAGGACCAGG
CAGCCTCCGCCCACAATGAAGATGGTGGCCTCGCCCAGCAGCTCAGCACC
CAGCTCTGCTGCTGCCTCCTCATTCAGTGGCTTGATGGTAGTGCCCCGGA
AACCCATTATGCGCATCTTCGTCCGCATCTCCACCCAGTGGGTACACTGC
AGGGGAGAAAGAGGTCAGGTGTGTTCCGAAGCTCCACCCCCAATACTT

5a) Mouse exon3 dna sample 1002 foward

>031008a_66391_1002exon3_exon3F
TGTAGTCTGGGCTTGTAATGCAGACCAAGATGCGCATCATGGGCTTCCAT
GCTGAGGCCATCAAGCCACTGAATGAGGATGCAGCGACTGAGCTGGGTGC
GAACCTGCTGGGTGAAGCCATCATCTTTGCTGCTGCGGGCAGCTGTCTGC
TGCTGGAGTTCTGGCGCCAGAAGTCATCGAAACACCGCAGGGAAGTGGCG
CAGGTGGCCACGGTGCTGTCGCTGCGGGAGGATGTGGAATACCTGGAGAA
CATGCTGGACGAGGTGCAGGTGCAGGTGCAGGCAGCATTGCCCAGGAACT
CACTGGATGAGCTGCGGGCAGAGCTGCGGGCAGAGCTGCGGGCGGAGCTG
CGGACAGAGTTGCAAGCAGAGTTGCGGGCAGAGCTTCAAGATGAGCTACA
GAAGTTCAGAACCCAGATCTGTAAAGATTGCTATGAGCCAGAGCTTAAGC
CTGAACTCCAGTGTCCTGAGGCCCCCAAGGAGTAGAGGCCGCAGGACTCT
GGCCTTGGACGTGGACTGTTGTCTGGGCTTGT

5b) Mouse exon3 dna sample 1002 reverse

>031008a_66392_1002exon3_exon3R
AAGCTCTGGCTCATAGCAATCTTTACAGATCTGGGTTCTGAACTTCTGTA
GCTCATCTTGAAGCTCTGCCCGCAACTCTGCTTGCAACTCTGTCCGCAGC
TCCGCCCGCAGCTCTGCCCGCAGCTCTGCCCGCAGCTCATCCAGTGAGTT
CCTGGGCAATGCTGCCTGCACCTGCACCTGCACCTCGTCCAGCATGGTTC
TCCAGGTATTCCACATCCTCCCGCAGCGACAGCACCGTGGCCACCTGCGC
CACTTCCCTGCGGTGTTTCGATGACTTCTGGCGCCAGAACTCCAGCAGCA
GACAGCTGCCCGCAGCAGCAAAGATGATGGCTTCACCCAGCAGGTTCGCA
CCCAGCTCAGCCGCTGCATCCTCATTCAGTGGCTTGATGGCCTCAGCATG
GAAGCCCATGATGCGCATCTTGGTCCGCATCTCTAGCCAGTGGTACACTA
CAGGGAAGAAGAGAGGAGTCGGAGTTTGCTTTGGCCAGGGACGCTCCTCA
CCCCACTGCAAACAC

5c) Reverse compliment of 1002exon3_exon3R

GTGTTTGCAGTGGGGTGAGGAGCGTCCCTGGCCAAAGCAAACTCCGACTC
CTCTCTTCTTCCCTGTAGTGTACCACTGGCTAGAGATGCGGACCAAGATG
CGCATCATGGGCTTCCATGCTGAGGCCATCAAGCCACTGAATGAGGATGC
AGCGGCTGAGCTGGGTGCGAACCTGCTGGGTGAAGCCATCATCTTTGCTG
CTGCGGGCAGCTGTCTGCTGCTGGAGTTCTGGCGCCAGAAGTCATCGAAA
CACCGCAGGGAAGTGGCGCAGGTGGCCACGGTGCTGTCGCTGCGGGAGGA
TGTGGAATACCTGGAGAACCATGCTGGACGAGGTGCAGGTGCAGGTGCAG
GCAGCATTGCCCAGGAACTCACTGGATGAGCTGCGGGCAGAGCTGCGGGC
AGAGCTGCGGGCGGAGCTGCGGACAGAGTTGCAAGCAGAGTTGCGGGCAG
AGCTTCAAGATGAGCTACAGAAGTTCAGAACCCAGATCTGTAAAGATTGC
TATGAGCCAGAGCTT

6a) Mouse exon2 dna sample 1003 foward

>031008a_66389_1003exon2_exon2F
GGGGCACTACCATCAAGCCACTGAATGAGGAGGCAGCAGCAGAGCTGGGT
GCTGAGCTGCTGGGCGAGGCCACCATCTTCATTGTGGGCGGAGGCTGCCT
GGTCCTGGAGTACTGGCGCCACCAGACTCAGCAGCGCAATAAGGAGGAGG
AACAGCGGGCAGCCTGGAACGCTCTGCAGGATGAGGTGGGCCGCCTGGCA
CTGGCCTTAGAGGCGCTGCAGGCTCAGGCACAAGCGATGCCCTCCTTGAG
TGCCCTGGAGGAGCTGCGGGAGGAGCTGCAGGAGGTGCGTGGTCAGGTCT
GCAATGCTCACTGTACTTCCAAGTGCCAGGCAGCATCTTCCAAGAAATAG
CCAGCTGCTAAGGCCTGGACTTGTTTGTGACCATGTG

6b) Mouse exon2 dna sample 1003 reverse

>031008a_66390_1003exon2_exon2R
CCGCAGCTCCTCCAGGGCACTCAAGGAGGGCATCGCTTGTGCCTGAGCCT
GCAGCGCCTCTAAGGCCAGTGCCAGGCGGCCCACCTCATCCTGCAGAGCG
TTCCAGGCTGCCCGCTGTTCCTCCTCCTTATTGCGCTGCTGAGTCTGGTG
GCGCCAGTACTCCAGGACCAGGCAGCCTCCGCCCACAATGAAGATGGTGG
CCTCGCCCAGCAGCTCAGCACCCAGCTCTGCTGGCTGCCTCCTCATTCAG
TGGCTTGATGGTAGTGCCCCGGAAACCCATTATGCGCATCTTCGTCCGCA
TCTCCACCCAGTGGGTACACTGGCAGGGGAGAAAGAGGTCAGGTGTGTTC
CGAAGCTCCACCCCCAATACTT

7a) Mouse exon3 dna sample 1003 foward

>031008a_66393_1003exon3_exon3F
TCGCTGCGGAGGATGTGGAATACCTGGAGAACATGCTGGACGAGGTGCA
GGTGCAGGTGCAGGCAGCATTGCCCAGGAACTCACTGGATGAGCTGCGGG
CAGAGCTGCGGGCAGAGCTGCGGGCGGAGCTGCGGACAGAGTTGCAAGCA
GAGTTGCGGGCAGAGCTTCAAGATGAGCTACAGAAGTTCAGAACCCAGAT
CTGTAAAGATTGCTATGAGCCAGAGCTTAAGCCTGAACTCCAGTGTCCTG
AGGCCCCCAAGGAGTAGAGGCCGCAGGACTCTGGCCTTGGACGTGGACTG

7b)Mouse exon3 dna sample 1003 reverse

>031008a_66392_1002exon3_exon3R
AAGCTCTGGCTCATAGCAATCTTTACAGATCTGGGTTCTGAACTTCTGTA
GCTCATCTTGAAGCTCTGCCCGCAACTCTGCTTGCAACTCTGTCCGCAGC
TCCGCCCGCAGCTCTGCCCGCAGCTCTGCCCGCAGCTCATCCAGTGAGTT
CCTGGGCAATGCTGCCTGCACCTGCACCTGCACCTCGTCCAGCATGGTTC
TCCAGGTATTCCACATCCTCCCGCAGCGACAGCACCGTGGCCACCTGCGC
CACTTCCCTGCGGTGTTTCGATGACTTCTGGCGCCAGAACTCCAGCAGCA
GACAGCTGCCCGCAGCAGCAAAGATGATGGCTTCACCCAGCAGGTTCGCA
CCCAGCTCAGCCGCTGCATCCTCATTCAGTGGCTTGATGGCCTCAGCATG
GAAGCCCATGATGCGCATCTTGGTCCGCATCTCTAGCCAGTGGTACACTA
CAGGGAAGAAGAGAGGAGTCGGAGTTTGCTTTGGCCAGGGACGCTCCTCA
CCCCACTGCAAACAC

7c) Reverse compliment of 1002exon3_exon3R

GTGTTTGCAGTGGGGTGAGGAGCGTCCCTGGCCAAAGCAAACTCCGACTCC
TCTCTTCTTCCCTGTAGTGTACCACTGGCTAGAGATGCGGACCAAGATGCG
CATCATGGGCTTCCATGCTGAGGCCATCAAGCCACTGAATGAGGATGCAGC
GGCTGAGCTGGGTGCGAACCTGCTGGGTGAAGCCATCATCTTTGCTGCTGC
GGGCAGCTGTCTGCTGCTGGAGTTCTGGCGCCAGAAGTCATCGAAACACCG
CAGGGAAGTGGCGCAGGTGGCCACGGTGCTGTCGCTGCGGGAGGATGTGGA
ATACCTGGAGAACCATGCTGGACGAGGTGCAGGTGCAGGTGCAGGCAGCAT
TGCCCAGGAACTCACTGGATGAGCTGCGGGCAGAGCTGCGGGCAGAGCTGC
GGGCGGAGCTGCGGACAGAGTTGCAAGCAGAGTTGCGGGCAGAGCTTCAAG
ATGAGCTACAGAAGTTCAGAACCCAGATCTGTAAAGATTGCTATGAGCCAG
AGCTT

8a) Mouse exon3 dna sample 1003 reverse

>061008_66528_1003exon3_exon3R
AAGCTCTGGCTCATAGCAATCTTTACAGATCTGGGTTCTGAACTTCTGTA
GCTCATCTTGAAGCTCTGCCCGCAACTCTGCTTGCAACTCTGTCCGCAGC
TCCGCCCGCAGCTCTGCCCGCAGCTCTGCCCGCAGCTCATCCAGTGAGTT
CCTGGGCAATGCTGCCTGCACCTGCACCTGCACCTCGTCCAGCATGGTTC
TCCAGGTATTCCACATCCTCCCGCAGCGACAGCACCGTGGCCACCTGCGC
CACTTCCCTGCGGTGTTTCGATGACTTCTGGCGCCAGAACTCCAGCAGCA
GACAGCTGCCCGCAGCAGCAAAGATGATGGCTTCACCCAGCAGGTTCGCA
CCCAGCTCAGCCGCTGCATCCTCATTCAGTGGCTTGATGGCCTCAGCATG
GAAGCCCATGATGCGCATCTTGGTCCGCATCTCTAGCCAGTGGTACACTA
CAGGGAAGAAGAGAGGAGTCGGAGTTTGCTTTGGCCAGGGACGCTCCTCA
CCCCACTGGCAAAC

8b)Reverse compliment of 1003exon3_exon3R

GTTTGCCAGTGGGGTGAGGAGCGTCCCTGGCCAAAGCAAACTCCGACTCCT
CTCTTCTTCCCTGTAGTGTACCACTGGCTAGAGATGCGGACCAAGATGCGC
ATCATGGGCTTCCATGCTGAGGCCATCAAGCCACTGAATGAGGATGCAGCG
GCTGAGCTGGGTGCGAACCTGCTGGGTGAAGCCATCATCTTTGCTGCTGCG
GGCAGCTGTCTGCTGCTGGAGTTCTGGCGCCAGAAGTCATCGAAACACCGC
AGGGAAGTGGCGCAGGTGGCCACGGTGCTGTCGCTGCGGGAGGATGTGGAA
TACCTGGAGAACCATGCTGGACGAGGTGCAGGTGCAGGTGCAGGCAGCATT
GCCCAGGAACTCACTGGATGAGCTGCGGGCAGAGCTGCGGGCAGAGCTGCG
GGCGGAGCTGCGGACAGAGTTGCAAGCAGAGTTGCGGGCAGAGCTTCAAGA
TGAGCTACAGAAGTTCAGAACCCAGATCTGTAAAGATTGCTATGAGCCAGA
GCTT

9) Mouse transcript1-3 foward

>151008_66951_trans1-3A_trans1-3F
GCAGGTTAGCAAGCCGCTGGCCAACCGTATCAAGGATGCTGCCCGCCGCA
GCGAGTTCTTCAAGACCTACATCTGCCTACCGCCAGCCCAGCTGTACCAC
TGGGCTTGTAATGCAGACCAAGATGCGCATCATGGGCTTCCATGCTGAGG
CCATCAAGCCACTGAATGAGGATGCAGCGACTGAGCTGGGTGCGAACCTG
CTGGGTGAAGCCATCATCTTTGCTGCTGCGGGCAGCTGTCTGCTGCTGGA
GTTCTGGCGCCAGAAGTCATCGAAACACCGCAGGGAAGTGGCGCAGGTGG
CCACGGTGCTGTCGCTGCGGGAGGATGTGGAATACCTGGAGAACATGCTG
GACGAGGTGCAGGTGCAGGTGCAGGCAGCATTGCCCAGGAACTCACTGGA
TGAGCTGCGGGCAGAGCTGCGGGCAGAGCTGCGGGCGGAGCTGCGGACAG
A

10a) Human exon3 dna sample 486 foward

>151008_66950_humanE3486_humanE3F
GGTTTCAATGCCGCTGCCATCAAGCCGCTGAACGAGGGTGCAGCCGCCGA
GCTGGGCGCGGAGCTGCTGGGCGAGGGCATCATCTTCATCACCGCCTGCA
GCTGCCTGATGCTGGAGTATTGGCGCCACCAGTTGCAGCAGCGCCGCAAG
GAAAAGGAGCGACGTGTTGCCAGGGAGGCGCTGCGGGGCGAGGTGGGCCA
CTTGGGGCTGGCGCTCGAGGAGTTGCAGGCGCAGGTGCAGGCGACGTCGA
CGCAGCTCGCCCTGGAGGAGCTGCGCGCTCAGCTGCAGGAGGTGCGAGCC
CACCTCTGCCTCCGAGACCCGCCGCCTGCACCCCCAGTTGCGCCGGCGTC
CGAGAAATAGGAGGTCTCGGGGCCCTGGTCTTG

10b) Human exon3 dna sample 486 reverse

>151008_66960_humanE3486_humanE3R
GGGTGCAGGCGGCGGGTCTCGGAGGCAGAGGTGGGCTCGCACCTCCTGCA
GCTGAGCGCGCAGCTCCTCCAGGGCGAGCTGCGTCGACGTCGCCTGCACC
TGCGCCTGCAACTCCTCGAGCGCCAGCCCCAAGTGGCCCACCTCGCCCCG
CAGCGCCTCCCTGGCAACACGTCGCTCCTTTTCCTTGCGGCGCTGCTGCA
ACTGGTGGCGCCAATACTCCAGCATCAGGCAGCTGCAGGCGGTGATGAAG
ATGATGCCCTCGCCCAGCAGCTCCGCGCCCAGCTCGGCGGCTGCACCCTC
GTTCAGCGGCTTGATGGCAGCGGCATTGAAACCCATGATGCGCATTTTGG
TCCGCATCTCCAGCCAGTGGTACACTGGCAGGAAAAGACAGGAGT

11a) Human exon3 dna sample 487 foward

>151008_66951_humanE3487_humanE3F
AAAATGCGCATCATGGGTTTCAATGCCGCTGCCATCAAGCCGCTGAACGA
GGGTGCAGCCGCCGAGCTGGGCGCGGAGCTGCTGGGCGAGGGCATCATCT
TCATCACCGCCTGCAGCTGCCTGATGCTGGAGTATTGGCGCCACCAGTTG
CAGCAGCGCCGCAAGGAAAAGGAGCGACGTGTTGCCAGGGAGGCGCTGCG
GGGCGAGGTGGGCCACTTGGGGCTGGCGCTCGAGGAGTTGCAGGCGCAGG
TGCAGGCGACGTCGACGCAGCTCGCCCTGGAGGAGCTGCGCGCTCAGCTG
CAGGAGGTGCGAGCCCACCTCTGCCTCCGAGACCCGCCGCCTGCACCCCC
AGTTGCGCCGGCGTCCGAGAAATAGGAGGTCTCGGGGCCCTGGTCTTG

11b) Human exon3 dna sample 487 reverse

>151008_66961_humanE3487_humanE3R
GGTGCAGGCGGCGGGTCTCGGAGGCAGAGGTGGGCTCGCACCTCCTGCAG
CTGAGCGCGCAGCTCCTCCAGGGCGAGCTGCGTCGACGTCGCCTGCACCT
GCGCCTGCAACTCCTCGAGCGCCAGCCCCAAGTGGCCCACCTCGCCCCGC
AGCGCCTCCCTGGCAACACGTCGCTCCTTTTCCTTGCGGCGCTGCTGCAA
CTGGTGGCGCCAATACTCCAGCATCAGGCAGCTGCAGGCGGTGATGAAGA
TGATGCCCTCGCCCAGCAGCTCCGCGCCCAGCTCGGCGGCTGCACCCTCG
TTCAGCGGCTTGATGGCAGCGGCATTGAAACCCATGATGCGCATTTTGGT
CCGCATCTCCAGCCAGTGGTACACTGGCAGGAAAAGACAGG

Appendix III

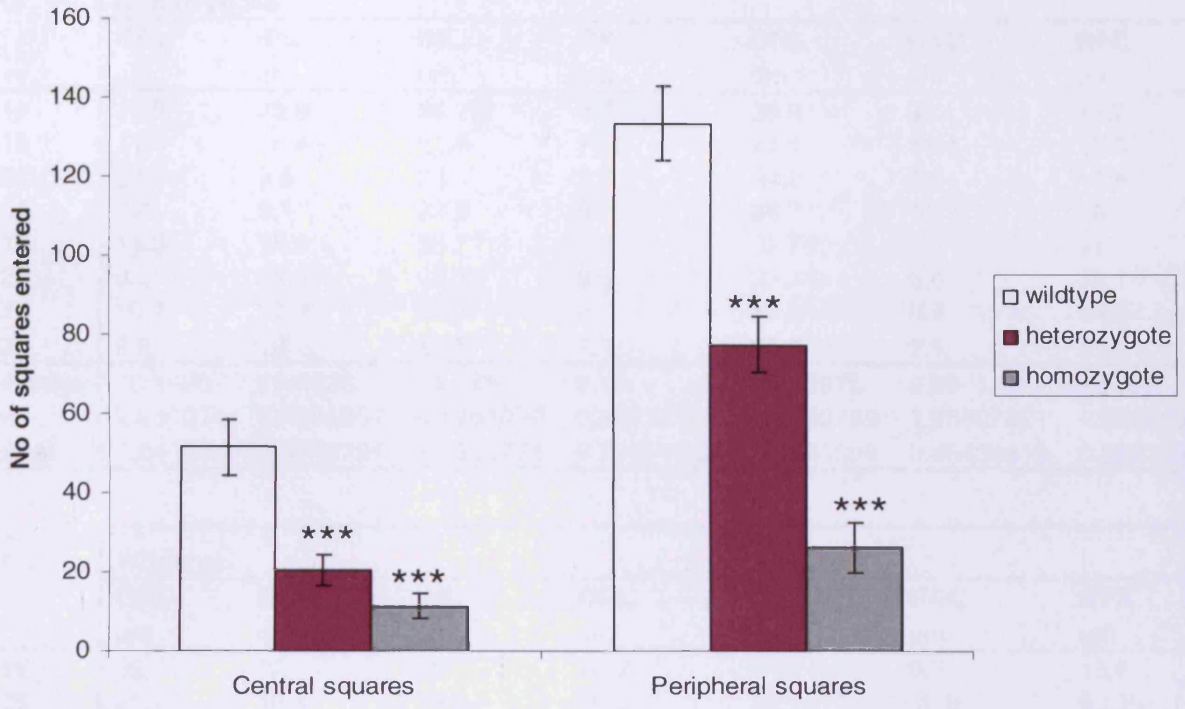

Figure 10.1. Total number of central and squares entered during 5 mins of *Opa3*$^{-/-}$ and *Opa3*$^{+/-}$ and *Opa3*$^{+/+}$ mice in open field testing. Data expressed as mean ± S.E.M. (*Opa3*$^{+/+}$ n = 9, *Opa3*$^{+/-}$ n =10, *Opa3*$^{-/-}$ n =9). ***$P < 0.001$.

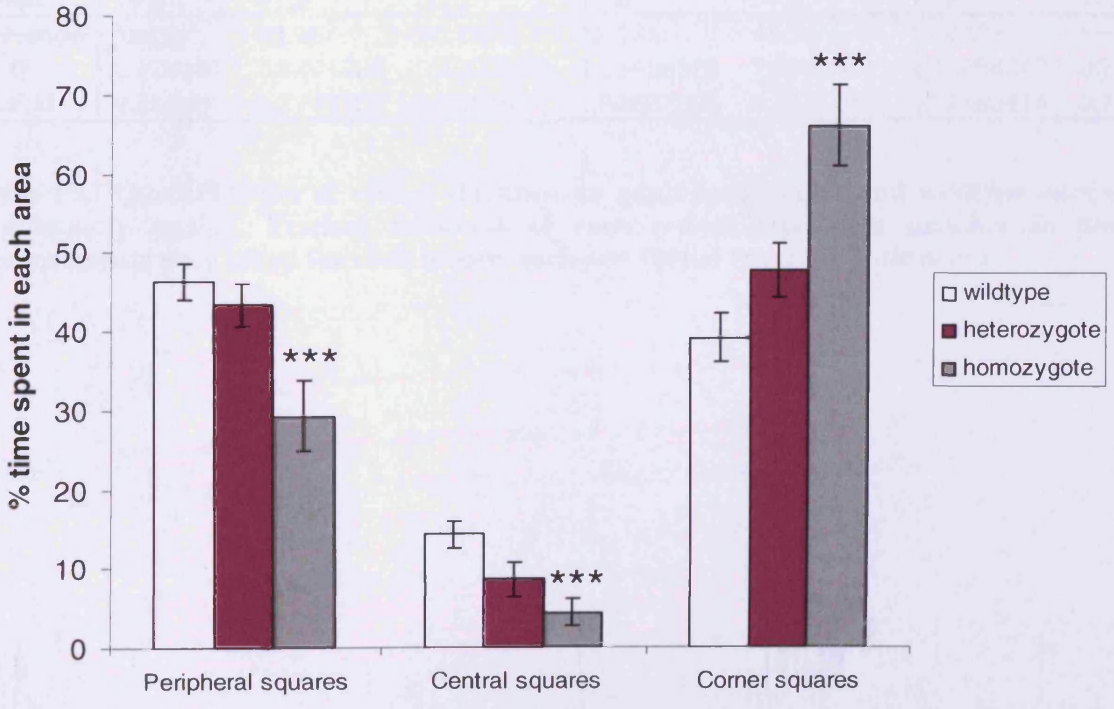

Figure 10.2. Percentage of time spent in various areas of the arena (after the mice had reached the periphery) of *Opa3*$^{-/-}$ and *Opa3*$^{+/-}$ and *Opa3*$^{+/+}$ mice in open field testing. Data expressed as mean ± S.E.M. (*Opa3*$^{+/+}$ n = 9, *Opa3*$^{+/-}$ n =10, *Opa3*$^{-/-}$ n =9). ***$P < 0.001$.

A.

	Homozygote						
	GCL	**IPL**	**INL**	**OPL**	**ONL**	**R&C**	**RPE**
	um	um	um	um	um	um	um
618	15.8	25.6	28.7	8.5	38.8	9	13.2
618	11.4	26.4	31.5	10.5	44.1	11.4	15.8
654	6.9	9.6	24	9.6	34.2	9.8	11.4
654	6.4	9.1	23.6	9.1	35.7	7.9	10
628	11.3	18.9	25.7	9.3	32.75	9.2	11
628	9.6	19.8	22.5	9.5	33.14	8.6	12.1
637	10.7	27.3	23.7	9	37.8	9.4	14.3
637	9.2	19	17.7	7.7	29.9	7.1	11.2
average	10.1625	19.4625	24.675	9.15	35.79875	9.05	12.375
S.D	2.950514	7.0964654	4.1365099	0.82114902	4.4020789	1.28507921	1.92928558
S.E.M	1.043164	2.5089794	1.4624771	0.29032002	1.5563699	0.45434411	0.68210546

B.

	Wildtype						
	GCL	**IPL**	**INL**	**OPL**	**ONL**	**R&C**	**RPE**
	um	um	um	um	um	um	um
636	25	52	35	16.3	41.1	9.3	15.6
636	31.1	48.4	33.3	16.3	39.1	10.8	13.1
1108	14.9	38.9	23.2	7.9	40.9	11.5	12.7
1108	14.4	35.2	28.7	10.9	40.7	9.4	11.1
1124	13.9	30.6	23.8	6.2	40.5	11	13.3
1124	12.9	33.3	28.8	7.1	38.7	10.4	15.2
1083	17.7	48	38.2	16.1	61.1	16	17.3
1083	14.5	41.2	35.3	16.6	51.9	12.9	17.1
average	18.05	40.95	30.7875	12.175	44.25	11.4125	14.425
S.D	6.528181	7.8401895	5.5300316	4.63488326	7.9962491	2.18268347	2.21859029
S.E.M	2.30806	2.7719256	1.9551614	1.63867869	2.827101	0.77169514	0.78439012

Table 10.1 Quantification of retinal thickness in adult homozygote and wildtype mice used in pupillometry testing. Vertical thickness of each retinal layer was measure in μm. Two measurements were taken for each mouse, each one 100μm from the optic nerve.

A.

	Homozygote						
	GCL	IPL	INL	OPL	ONL	R&C	RPE
	%	%	%	%	%	%	%
618	11.3	18.34	20.56	6.08	27.8	6.45	9.45
618	7.45	17.47	20.95	6.95	29.19	7.54	10.45
654	6.54	9.1	22.75	9.1	32.42	9.29	10.8
654	6.29	8.94	23.2	8.94	35.06	7.75	9.82
628	8.9	14.88	20.24	7.33	32.75	7.24	8.66
628	7.81	16.12	18.32	7.74	33.14	7.01	9.86
637	8.09	20.65	17.93	6.81	28.6	7.11	10.81
637	9.04	18.67	17.38	7.56	29.37	6.98	11
average	8.1775	15.52125	20.16625	7.56375	31.04125	7.42125	10.10625
S.D	1.600533	4.3634306	2.1655348	1.03414475	2.6202914	0.84947778	0.80696853
S.E.M	0.565874	1.5427057	0.7656322	0.36562538	0.9264129	0.30033575	0.28530646

B.

	Wildtype						
	GCL	IPL	INL	OPL	ONL	R&C	RPE
	%	%	%	%	%	%	%
636	12.87	26.77	18.02	8.38	21.15	4.78	8.03
636	16.19	25.2	17.34	8.48	20.35	5.62	6.82
1108	9.93	25.93	15.46	5.27	27.27	7.67	8.47
1108	9.57	23.41	19.08	7.25	27.06	6.25	7.38
1124	9.98	21.97	17.08	4.45	29.07	7.9	9.55
1124	9.46	24.42	13.78	5.21	28.37	7.62	11.14
1083	8.3	22.38	17.81	7.5	28.5	7.45	8.06
1083	7.65	21.74	18.63	8.76	27.39	6.81	9.02
average	10.49375	23.9775	17.15	6.9125	26.145	6.7625	8.55875
S.D	2.764494	1.8977863	1.7469075	1.69634692	3.4066573	1.12287577	1.35262113
S.E.M	0.977396	0.6709688	0.6176251	0.5997492	1.2044353	0.39699654	0.47822379

Table 10.2 Percentage thickness of retina in adult homozygote and wildtype mice used in pupillometry testing. Each measurement was taken as a percentage of the whole retina. Two measurements were taken for each mouse, each one 100μm from the optic nerve.